

Diss. ETH No. 24743

# **Infrared Thermography for Endwall Heat Transfer Measurements**

A thesis submitted to attain the degree of

**DOCTOR OF SCIENCES OF ETH ZURICH**  
(Dr. sc. ETH Zurich)

presented by

**SEBASTIANO LAZZI GAZZINI**

Laurea Specialistica in Ingegneria Meccanica  
Università degli studi di Roma “la Sapienza”, Italy  
born April 11<sup>th</sup>, 1987  
citizen of Italy

accepted on the recommendation of

Prof. Dr. Reza S. Abhari, examiner  
Prof. Dr. Hyung Gyu Park, co-examiner  
Dr. Anestis I. Kalfas, co-examiner

2017





# Acknowledgements

It is surprisingly hard, I find, having reached the conclusion of five remarkable years at the Laboratory for Energy Conversion of ETH Zurich, to express in full the gratitude I owe to so many.

I cannot start but by thanking my supervisor, Prof. Dr. Reza S. Abhari, who has done much more than guiding my research effort with his invaluable experience and knowledge. He himself with his drive for excellence and the fertile environment he has created at the LEC over the years have fostered my professional and personal growth. I owe it primarily to him if – looking back to the day he interviewed me in his office – I can barely recognize myself.

Dr. Anestis I. Kalfas has been a steady and comforting presence throughout the whole duration of my stay at the lab. His availability at all times has always been deeply appreciated, together with his precious advice on both the secrets of the rig – some of which only he holds – and on how to express oneself in writing.

Prof. Dr. Hyung Gyu Park honors me by co-examining my work. I am thankful for his time and effort in reviewing the present thesis.

The research project the key achievements of which are summarized in the work that follows would not have been possible without the technical and financial support of the two industrial partners MTU Aero Engines AG and Siemens AG.

Especially, I must acknowledge the greatly constructive contributions of Dr. Ewald Lutum, Dr. Jochen Gier, Dr. Gregor Schmid, Dr. Sebastian Hohenstein and Dr. Tilman auf dem Kampe.

My daily experience in the laboratory has been enriched by the presence of a wealth of brilliant people.

First of all, my predecessor Dr. Benoit Laveau. With great patience and with his determination for success he has guided my first steps and taught me daily for two years. It has been a blessing to learn from such a talent.

From Dr. Kai Regina I learnt method and order, besides how to assemble a turbine and how aerodynamic measurements work. His presence in the control room has made testing days a warmer experience.

Dr. Patrick Rebholz committed himself to the success of this project as much as if it were his own. His remarkable engineering made electronic equipment spin safely and operate inside the rig. I will never forget how much of his thought and effort went into making this happen on time for our first rotor campaign.

Rainer Schädler has been the column on which the project could stand steadily. His shoulders have borne the load (at times literally) of the design and commissioning of parts and maintenance of the rig on top of his already demanding experimental work. Even under great pressure, Rainer never forgot his kindness or his patience. His comradeship has been a gift.

My gratitude also goes to Dr. Ilias Bosdas for his thorough proof-reading of the papers that resulted from this work and for being of constant support from the very start; to Dr. Michel Mansour for sharing with me his knowledge on thin film deposition and so many other things, always smiling; to Flori Alickaj for missing his train so often because his skills were the only thing between me and missing a deadline; to Marlene Hegner for never moving me from my beloved office, for the support on any organizational matter and for the pleasant conversations in front of the coffee machine; to Altug Basol, Asad Raheem and Ilias Pappagiannis for their help on any CFD issue and the co-supervision of students working in their field; to Dr. Chokani for his kind words of encouragement during the first, difficult times; to Dylan Barratt for the endless, valuable conversations on the global trends that helped put things in perspective; to Marco Weber and Markus Brandstätter for dropping whatever they would be doing any time I had a question for them; to Luna Bozinova for the fun talks in the office; to Dominic Hänni for having kept listening even well after I had lost my train of thought; to Mevluet Polat (a.k.a. Polat) and Ben Newton for their prompt help respectively on IT and website issues; to Rolf Rüttiman and Thomas Künzle for their excellent craftsmanship in machining the parts needed – often on short notice.

All the members of the lab contributed to my experience in their own way. I hope whomever I did not mention explicitly will not assume I did not value sharing my time with him or her. Stay assured it is not so.

Finally, I would like to thank my parents for watching closely on me from far away and my close friends for being there for me – especially Ania, Micol and Stefano for the coffees, the frequent phone calls and the texts.

Ylenia, grazie per le cene calde in laboratorio e per aver aspettato che uscissi da lavoro finché hai potuto.

# Abstract

The importance of gas turbines in the energy market is forecast to increase in the near future, as they present sufficient operational flexibility and efficiency to complement the variable availability of renewable energy sources.

The increasing requirements in terms of efficiency coming from environmental constraints are typically met by increasing the maximum temperature of the thermodynamic cycle of the engine, thus exposing the hot section of the engine, and particularly the rotating organs, to harsher thermo-mechanical loads.

The current work aims at measuring the thermal loads on the endwalls of the second stator and the rotor of the rotating research turbine LISA at the Laboratory for Energy Conversion at ETH Zurich.

Measurements on the stator endwall are performed at three operating conditions: the rated one and two off-design points with reduced and increased rotor loading.

Heat transfer patterns for design point are related to the three-dimensional flow features in the passage by means of unsteady CFD simulations and aerodynamic probe data.

Variations in the patterns with operating condition are related to secondary flows coming from the upstream rows, Reynolds number effects and boundary layer relaminarization.

Measurements on the rotor endwall are performed for two operating conditions: the nominal operating point of the machine and a part-load condition with reduced mass flow rate and pressure ratio, resulting in a negative incidence on the rotor blade of  $-12.3^\circ$ .

The expected reduction in heat transfer coefficient is observed due to the decrease in Reynolds number.

Comparisons with CFD predictions suggest that unsteady effects play a non-negligible role in determining the rate of convective heat transfer in turbomachinery.

An increase in the injection ratio of the rim seal leakage flow typically results in an enhancement of the signature of the secondary flows on the Nusselt number distribution and in a drop in adiabatic wall temperature at the inlet of the passage towards the suction side.

A novel, non-axisymmetric design of the rim seal cavity was tested under the same operating conditions, aiming at increasing the circumferential component of velocity of the purge flow, thus reducing the mixing losses and the negative incidence of the purge flow on the rotor blade.

At design point, the heat transfer results show for this configuration a higher effectiveness of the purge air as endwall coolant, while the secondary flows seem not to be strengthened by the injection of purge flow as much as in the configuration with axisymmetric cavity design.

At part-load condition, the purge control features are not as effective in spreading evenly the rim seal leakage flow over the endwall: the purge flow again exits the cavity in the proximity of the suction side of the passage and secondary flows are strengthened comparably as with the axisymmetric cavity.

The main achievements of the current work cover the both the methodological and experimental aspect of the measurements on the rotating frame on one hand and the interpretation of the newly acquired data on the other.

For the first time to the best of the author's knowledge, infrared thermography of rapidly moving objects of arbitrarily complex shape was performed. This required, in particular, the development of: a custom-made heat transfer platform to be integrated in the rotor of the turbine and carrying a directly deposited, laser-cut film heater; quantitative, frequency-based image reconstruction tools and a novel method to measure the heat flux locally produced by a surficial source.

The transient step-wise heat flux calibration has the potential of reducing the uncertainties of any heat transfer measurement setup relying on an iso-energetic or a quasi-iso-energetic boundary condition.

The interpretation of the results acquired by means of the newly developed tools and methodologies developed in this work underlines the importance of performing unsteady computations in order to accurately predict heat transfer distributions, rather than relying on steady-state simulations, thus incurring in errors of as much as 30%.

# Riassunto

Si prevede che – nel prossimo futuro – saranno le turbine a gas a complementare l’offerta di energie rinnovabili nel mix energetico, data la loro flessibilità operativa ed efficienza.

L’incremento della temperatura massima del ciclo termodinamico è il tipico espediente per soddisfare ai requisiti di efficienza posti dai sempre più stringenti limiti alle emissioni inquinanti. A ciò conseguono carichi termomeccanici più severi sugli organi della sezione “calda” dell’impianto motore – la turbina – e, in particolare, sulle sue parti rotanti.

Scopo di questo lavoro è la misurazione dei carichi termici sulla piattaforma alla radice delle pale del secondo statore e del rotore della turbina sperimentale LISA del Laboratory for Energy Conversion, presso il Politecnico Federale di Zurigo.

Le misurazioni sulla parete dello statore sono effettuate operando la macchina alle condizioni nominali, a carico parziale e con incidenza positiva sul rotore.

Le distribuzioni osservate alle condizioni nominali sono messe in relazione al flusso tridimensionale nel vano palare tramite simulazioni CFD non stazionarie e dati sperimentali da sonde aerodinamiche.

Le variazioni alle altre condizioni di misura sono dovute all’effetto congiunto dei flussi secondari generati nelle schiere palari precedenti il secondo statore, alla riduzione del numero di Reynolds, ed alla rilaminarizzazione dello strato limite.

Le misurazioni sulla parete del rotore sono effettuate per due condizioni: la nominale ed una a carico parziale con flusso in massa e rapporto di espansione ridotti, con conseguente incidenza negativa sul rotore di  $-12.3^\circ$ .

La riduzione del coefficiente di scambio termico convettivo è giustificata dal decremento del numero di Reynolds.

Il confronto con simulazioni CFD suggerisce che la non stazionarietà del flusso svolga un ruolo rilevante nel determinare lo scambio di calore convettivo in flussi di interesse turbomacchinistico.

Un aumento nel flusso in massa dell’aria iniettata dalla tenuta tra statore e rotore ha l’effetto di rinforzare la traccia dei flussi secondari sulla distribuzione del numero di Nusselt e contemporaneamente di ridurre la temperatura adiabatica di parete all’ingresso del vano palare, verso la superficie in depressione.

Un disegno della tenuta tra rotore e statore di nuova concezione reduce il deficit di velocità circonferenziale del flusso da lí iniettato e conseguentemente riduce le relative perdite aerodinamiche e l'incidenza negativa sul rotore.

Alle condizioni nominali, questa configurazione mostra anche una maggiore efficacia di raffreddamento della piattaforma palare, mentre i flussi secondari non sono altrettanto rinforzati che con la tenuta assialsimmetrica.

A carico parziale, tuttavia, la geometria di nuova generazione non è piú altrettanto efficace nel distribuire il refrigerante sulla piattaforma. Il comportamento è conforme a quanto riscontrato con la tenuta assialsimmetrica a pari condizioni.

Due tecniche sperimentali distinte sono necessarie per le due schiere palari: una basata su una condizione al contorno isoterma per lo statore, una su una condizione al contorno isoenergetica per il rotore.

La prima è stata adattata per il presente studio da lavori precedenti.

La seconda ha richiesto, invece, lo sviluppo di dispositivi e strumenti di calcolo appositi quali: una piattaforma di misura per il trasferimento di calore integrata nel rotore della macchina e munita di un riscaldatore di spessore sottile in materiale direttamente depositato sulla sua superficie e tagliato al laser; strumenti di ricostruzione quantitativa di immagini basati su analisi di frequenza e, infine, un nuovo metodo di misura del flusso di calore localmente prodotto da una fonte superficiale.

Questi dispositivi e strumenti di calcolo consentono di misurare il trasferimento convettivo di calore su oggetti in movimento e su superfici di geometria qualsivoglia complessa.

La calibrazione del flusso di calore con tecnica transitoria a gradino può ridurre l'incertezza di qualunque misura di trasferimento di calore basata su condizione al contorno isoenergetica o quasi-isoenergetica.

Il contributo del presente lavoro si compone dell'aspetto metodologico-sperimentale delle misurazioni sulle superfici rotanti da un lato e della lettura dei dati sperimentali acquisiti con i nuovi mezzi sviluppati dall'altro.

Il presente lavoro avanza lo stato dell'arte della termografia infrarossa conseguendo per la prima volta – per quanto a conoscenza dell'autore – misurazioni su superfici di geometria arbitrariamente complessa, in rapido movimento. Ciò ha richiesto, in particolare, lo sviluppo di: una piattaforma di misura per il trasferimento di calore integrata nel rotore della macchina e munita di un riscaldatore di spessore sottile in materiale direttamente depositato sulla sua superficie e tagliato al laser; strumenti di ricostruzione quantitativa di immagini basati su ana-

lisi di frequenza e, infine, un nuovo metodo di misura del flusso di calore localmente prodotto da una fonte superficiale.

La calibrazione del flusso di calore con tecnica transitoria a gradino puó ridurre l'incertezza di qualunque misura di trasferimento di calore basata su condizione al contorno isoenergetica o quasi-isoenergetica.

L'interpretazione dei risultati potuti acquisire grazie agli strumenti e ai metodi sviluppati in questo lavoro illustrano l'importanza di condurre simulazioni di carattere transitorio onde predire accuratamente i carichi termici, anziché avvalersi di calcoli stazionari incorrendo in errori fino al 30%.





*“These instruments have play’d me so many tricks that I have at last found them out in many of their humours and have made them confess to me what they would have concealed, if I had not with such perseverance and patience courted them.”*

Sir Frederick William Herschel to Alexander Aubert, 1781

# Contents

<b>1. Introduction.....</b>	<b>1</b>
1.1 Motivation.....	1
1.1.1 Trends in Energy Markets.....	2
1.1.2 Trends in Air Transportation .....	4
1.1.3 Trends in Turbomachinery.....	5
1.1.4 Need for Experimental Validation of CFD Prediction Tools ...	7
1.2 Aerodynamics in a Turbine Passage.....	9
1.2.1 Secondary Flows in Cascades.....	9
1.2.2 Secondary Flows in a Rotor Passage .....	11
1.2.3 Non-Axisymmetric Endwall Contouring .....	12
1.2.4 Rim Seal Leakage Flows.....	13
1.3 Endwall Heat Transfer .....	18
1.3.1 Cascade Endwall Heat Transfer.....	19
1.3.2 Measurements on the Rotating Frame .....	20
1.4 Research Objectives.....	22
1.5 Key Achievements .....	22
1.6 Outline.....	23
<b>2. Experimental Methods.....</b>	<b>26</b>
2.1 Infrared Thermography .....	26
2.1.1 Basics of Radiative Heat Transfer .....	27
2.1.2 Infrared Transparent Materials.....	29
2.1.3 Atmospheric Infrared Transmissivity .....	31
2.1.4 High-Emissivity Coating.....	31
2.1.5 IR Imaging Devices.....	32
2.2 Image Processing.....	42
2.3 Heat Transfer Measurement Principle.....	53
2.3.1 Theoretical Background.....	53

---

<b>3. Measurement Methodology for Heat Transfer Measurements on the Stationary Frame</b> .....	<b>59</b>
3.1 The Rotating Axial Gas Turbine Research Facility LISA.....	59
3.1.1 Similitude in LISA and Operating Conditions of the Rig .....	62
3.2 Mechanical Integration of a Stator 2 Heat Transfer Platform.....	65
3.2.1 Design of the Stator 2 Heat Transfer Platform.....	65
3.2.2 Instrumentation.....	73
3.2.3 Insulating Layer and High-Emissivity Coating.....	74
3.3 Thermal Management of the Heat Transfer Platform.....	76
3.4 Traversing System .....	77
3.4.1 In-Situ Camera Calibration.....	78
3.5 Measurement Procedure.....	79
<b>4. Measurement Methodology for Heat Transfer Measurements on the Rotating Frame</b> .....	<b>81</b>
4.1 Mechanical Integration of a Rotor Heat Transfer Platform.....	83
4.1.1 Thermo-mechanical FEM Analyses .....	87
4.2 Design of Electrical Endwall Heaters.....	89
4.3 Manufacturing of Film Heaters for Contoured Endwalls .....	92
4.3.1 Physical Vapor Deposition .....	92
4.3.2 3D Laser Ablation.....	98
4.4 Rotating Data Acquisition System .....	101
4.4.1 PT100 Arrangement .....	103
4.5 Step-Wise Transient Heat Flux Calibration .....	104
4.5.1 Impact of Heat Flux Non-Uniformities on Heat Transfer Measurements .....	105
4.5.2 Theory and Principle.....	106
4.5.3 Experimental Setup for Step-Wise Transient Heat Flux Calibration .....	107
4.5.4 Data Elaboration.....	108
4.5.5 Point-Wise Heat Flux Distribution.....	111
4.5.6 Characterization of the Substrate .....	113
4.6 Measurement Procedure.....	116

4.6.1	Summary .....	117
<b>5.</b>	<b>Uncertainty Analysis.....</b>	<b>119</b>
5.1	Uncertainty Analysis for the Stator Endwall Heat Transfer Measurements.....	119
5.1.1	In-Situ Calibration of the Infrared Camera.....	119
5.1.2	Non-Uniformity in the Aluminum Temperature.....	121
5.1.3	Non-Uniformity of the Thermal Resistance of the Insulation.....	124
5.1.4	PT100 Calibration Error .....	133
5.1.5	Final Uncertainty Distributions for Stator Endwall Results.....	133
5.2	Uncertainty Analysis for the Rotor Endwall Heat Transfer Measurements.....	139
5.2.1	Errors in Surface Temperature.....	140
5.2.2	Errors in the determination of the electrical heat flux provided at the endwall .....	144
5.2.3	Errors in the determination of the conductive losses through the insulating substrate.....	145
5.2.4	Final Uncertainty Distributions for Rotor Endwall Results.....	149
5.2.5	Geometry Errors due to Manufacturing Tolerances .....	153
<b>6.</b>	<b>Heat Transfer Measurements on the Stator Endwall .....</b>	<b>155</b>
6.1	Nominal Operating Point and Comparison to CFD.....	156
6.1.1	Numerical Setup.....	159
6.1.2	CFD Results.....	162
6.2	Off-Design Conditions .....	167
6.2.1	Reduced Reynolds Number and Rotor Incidence .....	167
6.2.2	Reduced Reynolds Number with Increased Rotor Incidence.....	173
6.3	Summary .....	176
<b>7.</b>	<b>Heat Transfer Measurements on Contoured Rotor Endwalls.....</b>	<b>177</b>
7.1	Heat Transfer Measurements at Nominal Operating Condition.....	178
7.1.1	Comparison with CFD Predictions.....	180
7.2	Effect of Off-Design Operation.....	184
7.3	Effect of Roughness .....	190
7.4	Summary .....	192

---

<b>8. Effect of Purge Air Injection on the Heat Load Distributions .....</b>	<b>195</b>
8.1 Definitions .....	196
8.2 Effect of Purge Air Injection on the Heat Load Distributions at Design Point	198
8.3 Effect of Unitary Density Ratio .....	203
8.4 Effect of Purge Air Injection on the Heat Load Distributions at Off-Design Conditions .....	204
8.5 Summary .....	214
<b>9. Rim Seal Cavity Exit Shaping and its Effects on Coolant Distribution</b>	<b>215</b>
9.1 Design Principles of Rim Seal Cavity Exit Shaping .....	216
9.2 Effects of Rim Seal Cavity Exit Geometry on endwall Cooling at Design Condition .....	217
9.3 Effects of Rim Seal Cavity Exit Geometry on endwall Cooling at Off-Design Condition .....	222
9.4 Integral Cooling Effectiveness Comparison of Purge Control Features and Axisymmetric Cavity Geometry .....	225
9.5 Summary .....	227
<b>10. Summary, Conclusions and Outlook .....</b>	<b>229</b>
10.1 Summary .....	229
10.2 Concluding Remarks and Main Contributions .....	234
10.2.1 Stator Endwall Heat Transfer .....	234
10.2.2 Rotor Endwall Heat Transfer .....	234
10.3 Outlook .....	235
<b>Bibliography .....</b>	<b>237</b>
<b>A. Nomenclature .....</b>	<b>249</b>
<b>B. List of Publications .....</b>	<b>253</b>
<b>C. Curriculum Vitae .....</b>	<b>255</b>



# 1. Introduction

## 1.1 Motivation

Gas turbine engines account for a substantial amount of the energy production with fossil fuels and are the prime mover of choice for the aeronautical sector. With the rising global population and the increase in mobility on one hand and the ever more stringent environmental requirements necessary to combat climate change on the other, industry and academia are jointly striving to achieve higher engine efficiencies. The technology goes in the direction of increasing the maximum temperature of the thermodynamic cycle (see section 1.1.3 ), but this poses structural challenges and calls for more refined, experimentally validated design tools (see section 1.1.4 ).

A gas turbine engine (Figure 1.1) schematically consists of:

- a compressor: provides mechanical energy to the working fluid (air) and increases its pressure, temperature and speed;
- a combustion chamber: provides an environment suitable for stable combustion to take place. The chemical energy of the injected fuel is released in the form of heat increasing the temperature of the working fluid;
- a turbine: here the working fluid expands providing useful work pushing against the airfoils of a rotor. Mechanical power is harvested from the rotor shaft to drive the compressor upstream;
- a nozzle to accelerate the fluid and provide thrust (aero-engine) or a power turbine to extract the remaining work (land-based gas turbine for power production);
- inlet and exhaust manifolds: provide suitable aerodynamic conditions for the intake and outtake of the working fluid from and to the environment.

Compressors and turbines are themselves composed of several stages, each alternating rotors and stators, and typically grouped in high, intermediate and low-pressure sections.

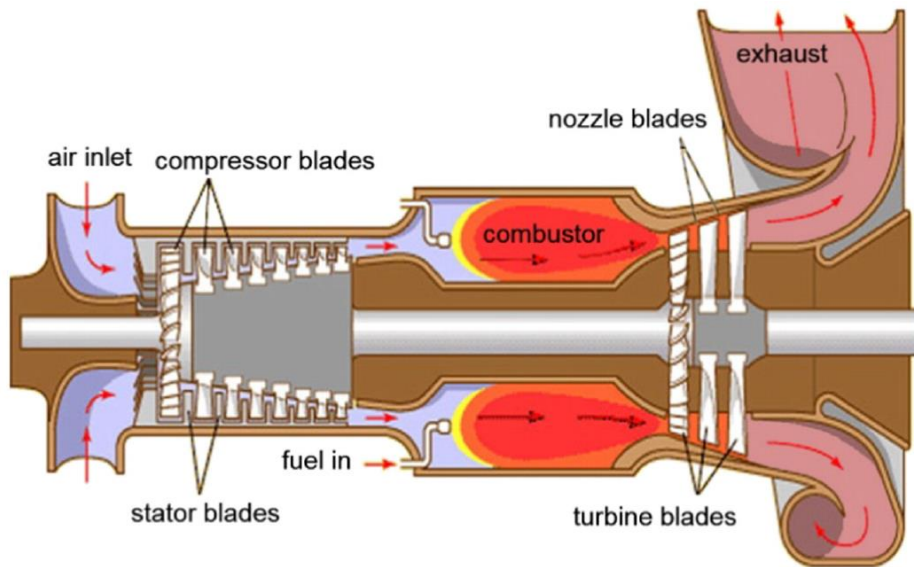


Figure 1.1: schematic of a land-based gas turbine engine for power production from Salehnasab et al. [1].

### 1.1.1 Trends in Energy Markets

According to the 2016 World Energy Outlook of the International Energy Agency (IEA) [2], global energy demand is expected to rise by 30% between 2016 and 2040. This estimation is based on the conservative, yet desirable scenario in which the Paris agreement pledges are respected in order to limit global warming to  $2^{\circ}\text{C}$  compared to pre-industrial levels. Even so, more than half a billion people will still be left with no electricity to cover their basic energy needs. More room is therefore left for the expansion of the energy market. The growth in energy demand is driven by the increase in global population and the development of third world countries, especially India and China. In this scenario, fossil fuels are still used for the production of more than half of the global energy supply ( $\sim 57\%$ ), but while coal consumption stays constant in absolute levels, natural gas consumption grows by about a third from 2012 levels (Figure 1.2). It is therefore required of the traditional technologies, i. e. gas and steam turbine power plants, to become more efficient, consume less fuel and produce lower amounts of greenhouse gases (i. e.  $\text{CO}_2$ ) and pollutants such as  $\text{NO}_x$ .



Furthermore, the increased penetration of highly variable renewable energy sources also contributes to the growth of the share of gas turbines in the power mix.

In 2040, renewables – particularly wind and solar – will cover together about 16% of the global energy demand.

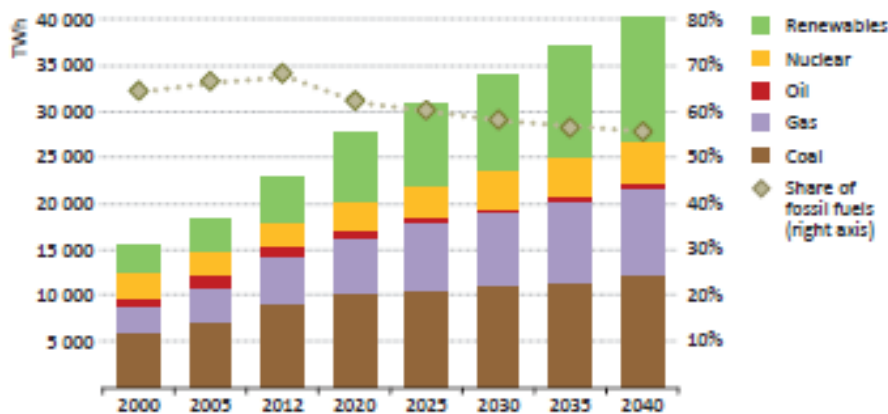


Figure 1.2: historical trends and projections in global primary energy demand by type according to the reference case as reported in the IEA World Energy Outlook 2014 [3]. Thousands TWh vs. year.

This requires developing power plants able to dispatch on short notice to integrate the availability of these two renewable energy sources.

Gas turbines – often integrated as topping plant in a combined cycle with a steam turbine – offer the most suitable technology for this application thanks to their low mechanical and thermal inertia. For this reason, it is estimated that gas turbine power plants will be accountable for about 70% of the added electricity production capacity by 2040 [3].

### 1.1.2 Trends in Air Transportation

In parallel to power production, mobility is also expected to grow strongly, as a consequence of the globalization of the economy and population growth. In particular, air traffic is expected to more than double globally, again driven by Asian countries [4]. The same trend is independently forecast by Airbus, as represented in Figure 1.3.

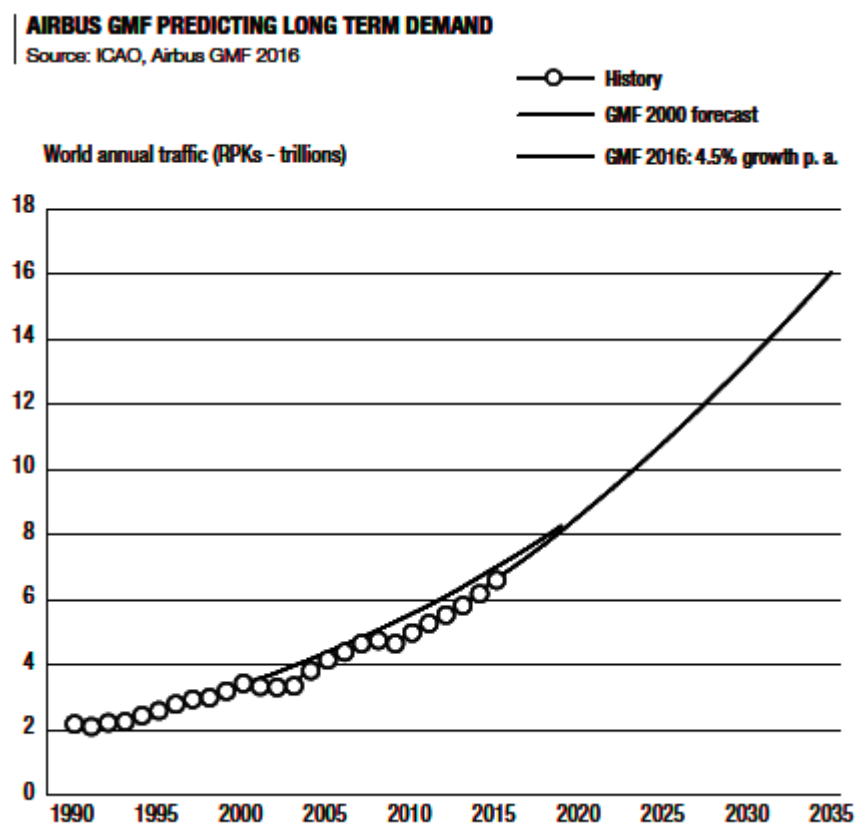


Figure 1.3: historical data and forecast for yearly revenue passenger kilometers (RPKs) from the Airbus Global Market Forecast 2016-2035 [5].

The growth of the market poses severe environmental concerns: the aviation sector currently accounts for about 12% of the total transportation-related CO<sub>2</sub> emissions. This share is expected to grow up to 23% by 2050 if no measure is taken. It is therefore necessary to make air travel more efficient by jointly acting on airframe aerodynamics, operation and engine performance.

For this reason, the airline industry is targeting to improve the fuel efficiency by 1.5% annually, achieve carbon-neutral growth until 2020 and cut CO<sub>2</sub> emissions by half until 2050 compared to 2005 levels (IATA Annual Review 2016 [6]).

Moreover, there is an obvious economic incentive for the air carriers to reduce fuel costs. Despite the reduction in oil price from more than 100USD to about 50USD in 2014, fuel still accounts for around 27% of the total costs.

### 1.1.3 Trends in Turbomachinery

Gas turbine engine efficiency is typically improved by increasing the maximum temperature of the thermodynamic cycle, bringing it closer to the adiabatic flame temperature of the fuel. This is easily demonstrated by recalling that the thermal efficiency  $\eta_B$  for an ideal Joule-Brayton cycle operating between two given temperatures  $T_t > T_a$  and is given by:

$$\eta_B = 1 - \left(\frac{T_a}{T_t}\right)^{\frac{\gamma-1}{\gamma}} \quad (1.1)$$

This trend is well documented by the increasing Turbine-Entry Temperatures (TETs) of commercially available engines over the years (Han et al. [7]), now reaching 1900 °C in aeronautical engines (especially military) and 1400 °C in land-based applications (Chen [8]). It is estimated that a TET 1750 °C will be required of future coal-gas turbines to meet the performance goal mandated by U. S. fossil energy policy. Industry is expected to keep this direction (Dunn [9]), pushing the boundaries of material science to produce advanced materials able to withstand the increasing thermal loads. A recent example of the advances in material science and manufacturing technology are the Ceramic Matrix Composites (CMCs) found in the CFM Leap engine. This engine is jointly developed by GE and Snecma and scheduled for entry into service by 2017 [10].

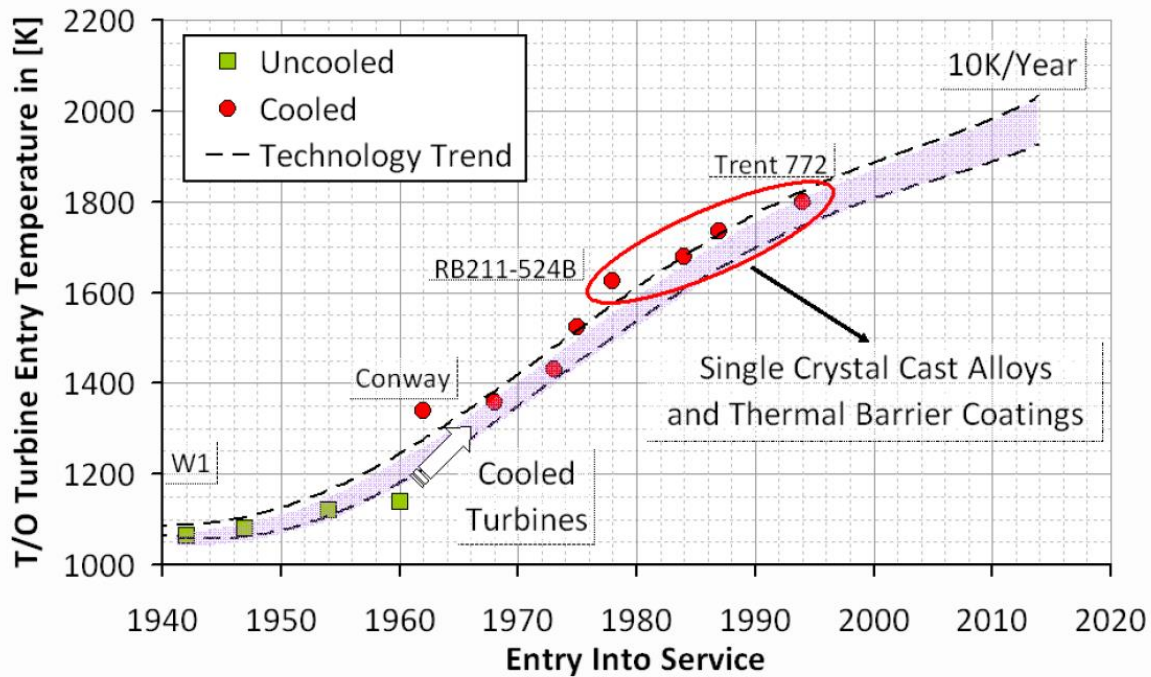


Figure 1.4: historical and projected trend of turbine entry temperatures against year of introduction of the engine (from Kyprianidis [11]).

Additive manufacturing constitutes a disruptive innovation in the production of parts for the hot section of the engines, allowing for far more elaborate cooling schemes than the ones achievable by means of traditional technologies, and its application to full rotating parts is reaching maturity, with the first 3D-printed rotor blades successfully tested in an actual engine at full load in early 2017 by Siemens AG [12]. However, the introduction of the last major technological change with the widespread use of single crystal casting and thermal barrier coating is more than 20 years old and the achievable increases in entry temperature have ever since been brought about by incremental improvements in prediction tools and cooling effectiveness. It is therefore still of crucial interest for designers to minimize the quantity of bypass air needed for the thermal management of the components to the benefit of efficiency. In this regard, finding ways to selectively cool critical locations rather than improving the overall cooling performance is key (Bunker [13]).

### 1.1.4 Need for Experimental Validation of CFD Prediction Tools

The increasingly demanding levels of thermo-mechanical stress arising from the growing total inlet temperatures (see previous section 1.1.3 ), together with the advance of complex blade and endwall geometries and aerodynamics, put the designers in need of more advanced and reliable prediction tools in order to be able to estimate accurately the metal temperatures of the components in the hot path. These prediction tools – Computational Fluid Dynamics (CFD) codes – are by no means exact, since – as explained by Denton [14] – they are subject to errors deriving from:

- finite differences approximation resulting in numerical error propagation;
- modeling errors. Particularly, turbulence and transition modeling play a significant role in high-pressure turbine computations (Schobeiri and Abdelfattah [15], Dunn [9]);
- uncertainty in the prescribed boundary conditions;
- uncertainty in the geometry of the domain, arising from manufacturing technology or alteration of the actual engine geometry due to erosion or deposition of particles on the surfaces;
- steady flow assumptions.

In the specific case of turbomachinery applications, the behavior of the secondary flows can be strongly influenced by the numerical setup [16] and grid refinement and the effects of wall roughness play a relevant role in the absolute values of heat transfer and are not always faithfully captured in presence of strong accelerations (Lutum et al. [17]).

Computation of heat transfer quantities is even more demanding than purely aerodynamic predictions. First of all, because the temperature gradient at the wall is what drives the heat transfer to the metal, the requirement for grid refinement at the wall is much higher than what customarily used for surface pressure calculations. Typically, the requirement is for the first cell height to be at most within one viscous unit. The computational cost for faithful heat transfer simulations is therefore significantly higher.

The typical Reynolds-Averaged Navier-Stokes-based (RANS) solvers, furthermore, are unable to capture fully the complexity of the unsteady, three-

dimensional flow in turbomachinery passages (Duchaine et al. [18]), even in their unsteady form (URANS). This is why Large Eddy Simulations are being introduced to turbomachinery applications (Tucker [19]), but the more faithful representation of the flow physics and the lower sensitivity to turbulence modeling also come with a much higher computational cost and still cannot eliminate the need for experimental validation.

It follows that:

- a) at the present state, CFD predictions shall not be used as absolute predictors, but rather as a comparative tool. As an example, the reader should consider the very advanced conjugate CFD-CHT simulations for meshes of up to 200 million nodes carried out by Rodriguez et al. [20], that still present errors in metal temperatures of more than 5% compared to experimental data ( $\sim 50\text{K}$ );
- b) tuning of the CFD solvers based on experimental data is essential.

On the other hand, even when validation data is available, it must be born in mind that the provenience of such data has to be scrutinized.

First of all, agreement between aerodynamic predictions and experimental data does not guarantee accurate heat transfer predictions. Schobeiri et al. [21] recently show how discrepancies in adiabatic effectiveness are one order of magnitude greater than the ones in aerodynamic efficiency.

Secondarily, most of the available commercial solvers are validated against flat-plate or cascade data, which fail to fully represent the highly unsteady, three-dimensional flow of turbomachinery, let alone the representative turbulence levels and body forces (Dunn [9]).

Measurements on advanced blade and endwall geometries, especially for rotating components in full-scale demonstrators, are lacking due to the intrinsic challenges in the measurement practice and, when available, often are limited to discreet measurement points rather than high resolution maps. A validation performed on full maps of heat transfer coefficient and adiabatic wall temperature can more thoroughly confirm the accuracy of the prediction tools used. Additionally, resolving the thermal gradients enables the evaluation of the local material stresses acting on the part. A review of the open literature on experimental heat transfer in turbomachinery, with particular reference to research carried out in rotating facilities, is given in section 0.

## 1.2 Aerodynamics in a Turbine Passage

### 1.2.1 Secondary Flows in Cascades

The complex aerodynamics of turbine passages has been object of study since the early 1950s with pioneering works such as the one from Hansen et al. [22]. As explained in detail by Langston et al. [23] and further reported in the review by Simon and Piggush [24], the incoming boundary layer rolls up and separates in correspondance of a saddle point between 20 and 50% of the pitch (moving from pressure side to suction side). The newly formed boundary layer is swept in the passage flow that originates due to the pressure gradient between the pressure side of the passage and the suction side. The strength of the passage flow increases with the turning of the blades.

After having reached the pressure side of the passage, the passage flow is entrained by the pressure leg of the horseshoe vortex originated by the presence of a bluff body (the blade) protruding from the endwall. Size and strength of the horseshoe vortex is thus enhanced. The new and thin boundary layer downstream of the separation contributes to the enhancement of the heat transfer in addition to the acceleration of the flow towards the throat of the passage.

Additionally, the passage flow induces a rotation in the stream surfaces which produces a vortical structure in itself: the passage vortex.

This structure finally includes the pressure leg of the horseshoe vortex and carries a Lamb-Oseen vortex in its core.

The suction leg of the horseshoe vortex climbs the suction surface and is dissipated by viscosity.

On top of these main vortical structures, smaller but still strong corner vortices originate in correspondance of the leading edge of the blade and a counter-rotating wall vortex is induced by the passage vortex on the suction surface.

A simplified schematic of the turbine passage flow is given by Langston [25] (Figure 1.5).

Secondary flows are most relevant in High-Pressure Turbines (HPTs) due to the lower aspect ratio (span over chord) of their blades, typically between 1 and 2 [26].

In HPTs, the low aspect ratio and the higher turning angle of the flow results in stronger secondary flows affecting a wider portion of the passage. With 40-50% of loss, secondary flows are the major contributor to the efficiency drop in HPTs [21]. HPTs are a perfect example of complex 3D flow in presence of secondary vortices, adverse pressure gradients and wake-boundary layer interactions. Because of these reasons, accurate simulation of the flow through these components is challenging, while at the same time being crucial for a reliable design due to the extreme conditions to which they are typically exposed.

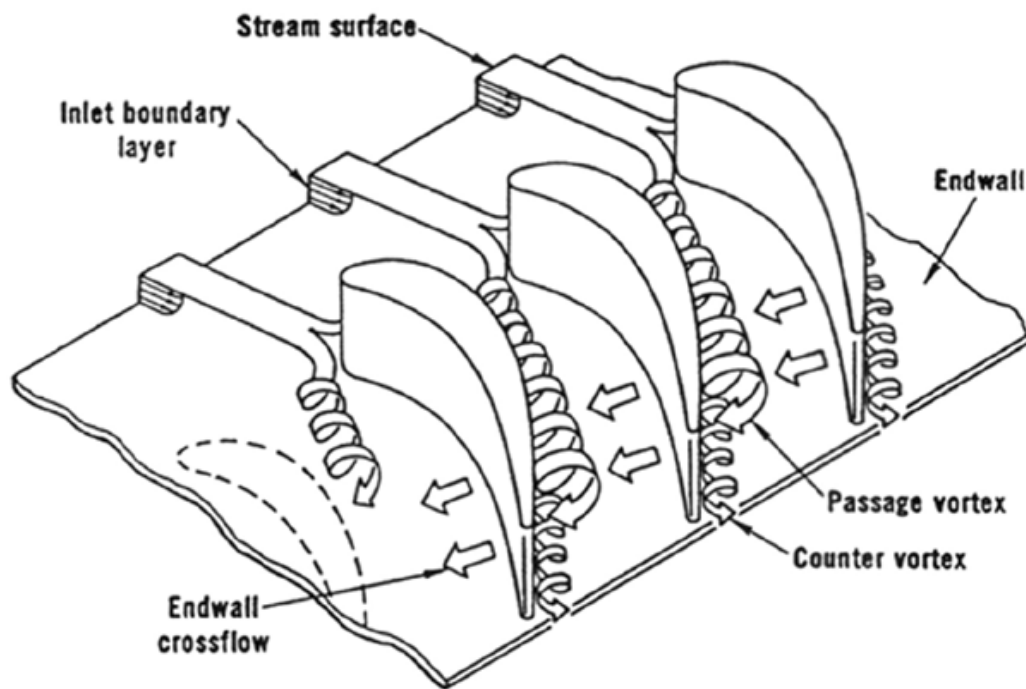


Figure 1.5: schematic overview of the secondary flows in a turbine passage (from Langston [25]).



### 1.2.2 Secondary Flows in a Rotor Passage

In the rotating frame and in the presence of unsteady stator-rotor interactions, the model defined in cascades is oversimplified. The behavior of the flow through the rotor passage is intrinsically unsteady and pulsatile due to the interaction of the wake shed by the upstream stator vanes with the rotating potential field of the rotor blade.

Moreover, the secondary flows formed in the passage of the first stator affect the generation of the vortical structures in the rotor passage. The rotor secondary flows increase their vorticity due to stretching through the rotor blade passage. Furthermore, centrifugal effects (centrifugal and Coriolis forces and relative eddy) promote the migration of the flow towards higher spanwise locations. Schlienger et al. [27] show how the wake of the first stator rolls up under the influence of the indigenous rotor vortices and affects itself the formation of the rotor secondary flows. His schematic representation of the phenomenon is shown in Figure 1.6.

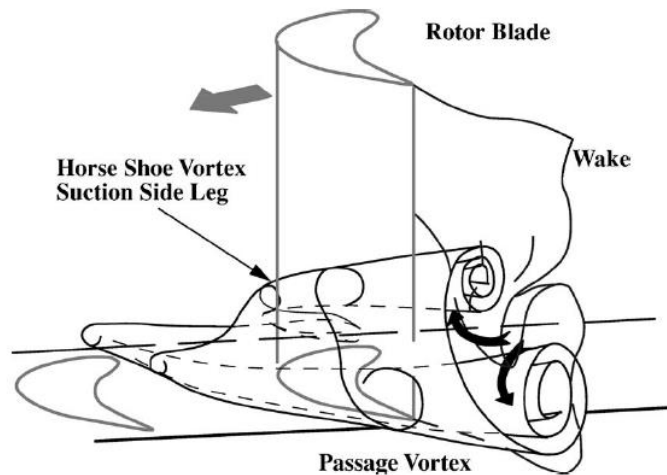


Figure 1.6: secondary flows in a rotor passage according to Schlienger et al. [27].

Additionally, the suction side leg of the horseshoe vortex migrates radially due to centrifugal effects and – when present – purge flow injection, as confirmed by Jenny [28] (see 1.2.4 ).

The radial flow is caused – according to Dring and Joslyn [29] – by the so-called relative eddy: an inviscid phenomenon originating from the axial component of vorticity that the flow carries when observed from the rotating frame of reference. Its effect on the migration of the secondary flows on the rotor blades is visualized in their work (Figure 1.7).

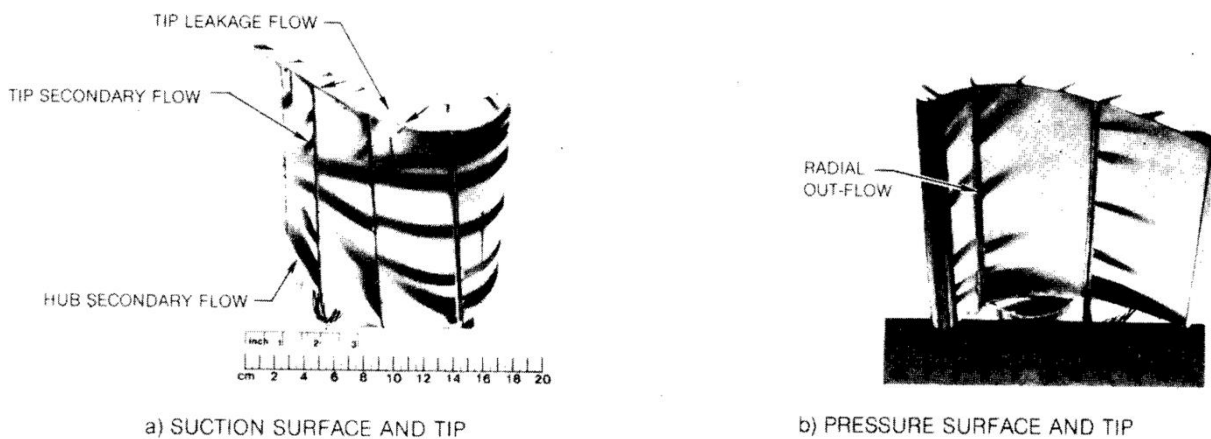


Figure 1.7: visualization of secondary flows and effect of relative eddy on the rotor flow field (Dring and Joslyn [29]).

### 1.2.3 Non-Axisymmetric Endwall Contouring

Advanced aerodynamic designs have recently incorporated the practice of non-axisymmetric endwall contouring to manage secondary flows and reduce the losses associated to them. The principle is to counteract the cross-wise pressure gradient in the passage by accelerating the flow close to the pressure side (therefore reducing its static pressure) and decelerating it towards the suction side (enhancing its pressure), respectively by means of hills and troughs on the endwalls. Despite having been invented in 1965 by Rioulet [30], this approach has

only been proven effective in reducing the strength and size of the passage vortex in the early 2000s.

The earliest studies on the matter, in fact, observed an increase in losses when applying endwall profiling due to boundary layer separation. This was itself induced by the interaction between endwall and blade (Morris and Hoare [31], Atkins [32]). After Rose demonstrated computationally the possibility of reducing in-passage pressure non-uniformities by means of non-axisymmetric endwall contouring [33], actual reduction in losses (Hartland et al. [34]) and their relationship to an alteration of the secondary flows (Ingram et al. [35]) were measured by the same group in the Durham Cascade facility. The interest of the turbomachinery community in the impact of non-axisymmetric endwall profiling on aerothermal performance is still of relevance today, with the focus shifting towards the effects on heat load redistribution (Mahmood and Acharya [36], Saha and Acharya [37], Laveau et al. [38]) and film cooling. In fact, a new test facility has recently been developed at the Karlsruhe Institute of Technology for this specific purpose (Kneer and Puetz [39, 40]).

#### 1.2.4 Rim Seal Leakage Flows

Purge air or rim seal leakage flow is a necessary evil in turbomachinery. By-pass air is bled from the compressor upstream and fed to the rotor drum in order to be leaked through the turbine seals. The purpose of this practice is twofold:

- a) to cool the rotor disks;
- b) to prevent hot gas from entering the hub cavity and reaching delicate organs such as the shaft and bearings.

An example of how this is practically accomplished in an actual aeronautical engine is provided in the schematics of Figure 1.8.

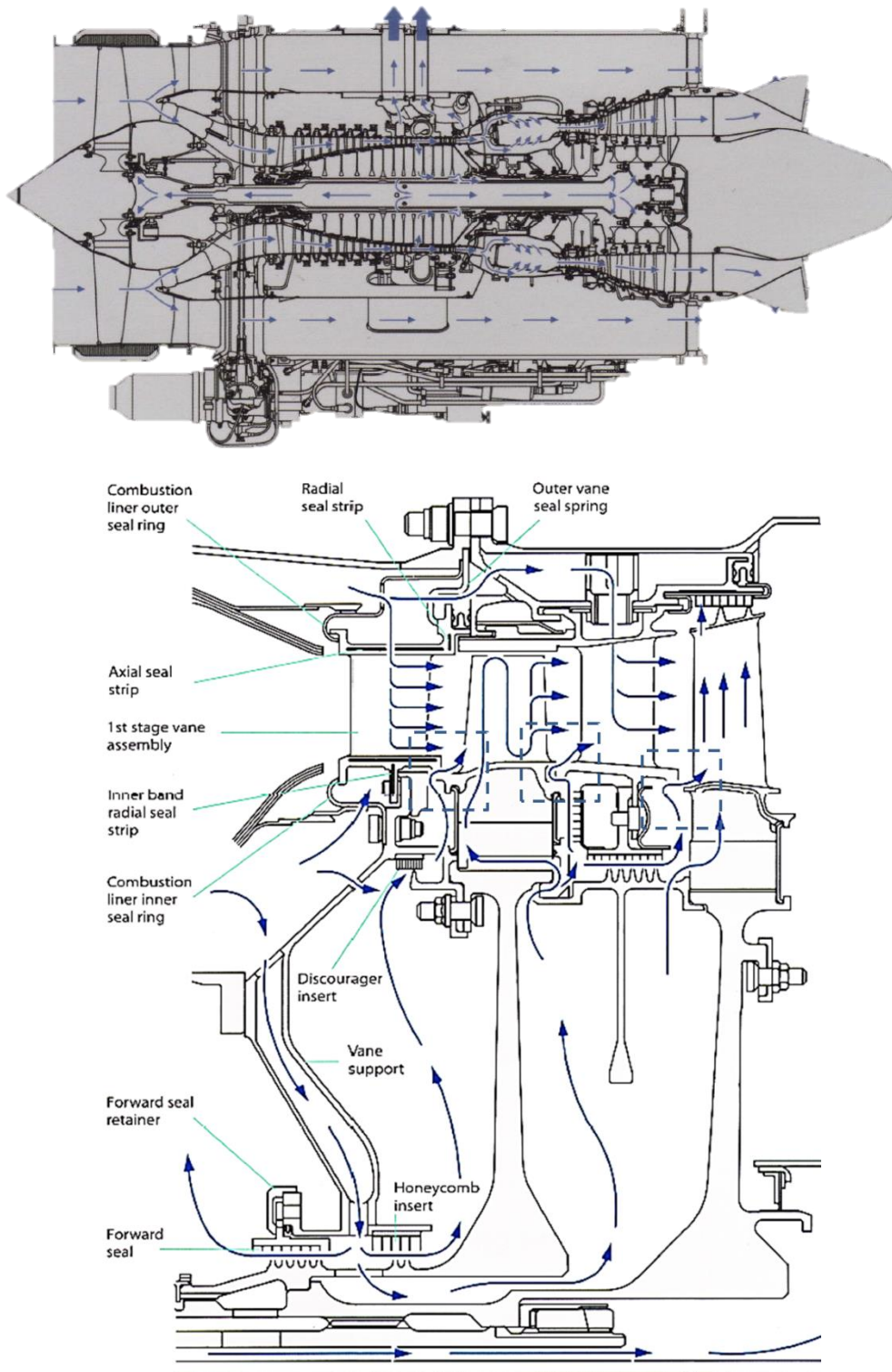


Figure 1.8: secondary air system of the Rolls-Royce aero engine AE3700 (top). Detail of the internal air flow path for the first two stages of the high-pressure turbine. The dashed blue boxes highlight the endwall purge flow between stators and rotors [41].

The importance of avoiding hot gas ingestion below the hub of the turbine rotor derives from its possible impact on the reliability of the whole engine. It has been estimated (Johnson et al. [42]) that even minor quantities of hot gases coming from the main flow path, if able to reach the disks, can reduce the life of the parts by half.

On the other hand, this practice introduces efficiency penalties because of several reasons:

1. the by-pass air, after having gained energy at the expense of compressor work is left flowing idly within the machine;
2. once the purge flow enters the main flowpath, it carries lower momentum and temperature than the main flow and, consequently, introduces mixing losses in the rotor passage decreasing the incidence on the rotor blades (Reid et al. [43], Ong et al. [44]);
3. the strength and size of the secondary flows in the passage are increased by the interaction with the purge flow, which additionally promotes the lift-off of the hub passage vortex from the endwall (Paniagua and Dénos [45], Schüpbach et al. [46], Jenny et al. [47]);
4. the blockage introduced by the low-momentum fluid affects the mass flow distribution all across the span of the blade altering significantly the aerodynamic coupling of the complete blade if not taken into account during the design process (Green et al. [48]).

Concerning point 3, Jenny shows how each percentage of mass flow rate injected from the purge cavity displaces the core of the hub passage vortex by an additional 10% span.

Even at the design injection ratio of 0.8%, depending on the exit position of the fluid particle, its spanwise position at rotor exit can vary between 20, 30 or 40% span and, most importantly, it may part from the rotor endwall between 10 and 40% of their path.

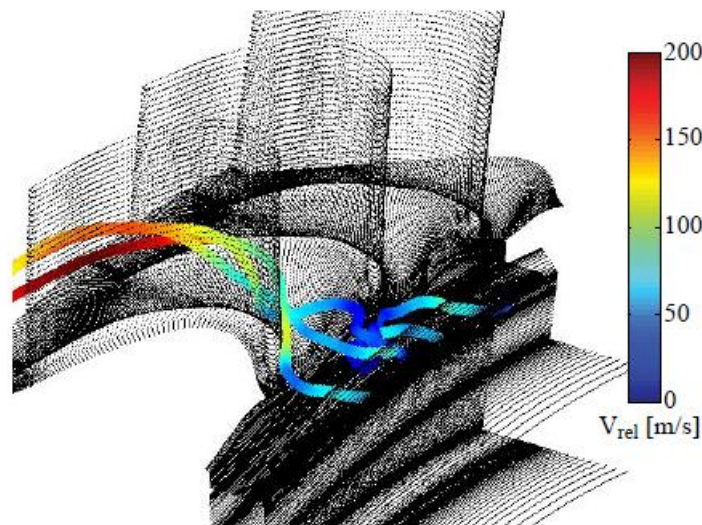


Figure 1.9: the three typical fluid particle paths from the purge flow cavity. Their migration towards higher spanwise positions is evident and is strongly dependent on the location of their exit from the cavity and interaction with the secondary flows of the passage (Jenny [28]).

Furthermore, the attention on the effect of leakage flows on performance and heat transfer has grown in the recent years due to the change in the operation of gas power plants from base-load in the 1990s to intermediate-load in the 2000s (Balling [49]) and peaking load nowadays.

The higher penetration of renewables in the energy mix (section 0), with their inherent variability in available power, requires an unprecedented operational flexibility of traditional power plants. Among the numerous technical challenges in decreasing the start-up times for gas turbines (together with rotor inertia and tip clearance control) the control of axial clearance between rotating and stationary organs plays a crucial role. The thermal transient during start-up produces a differential expansion of the organs of the hot section that needs to be accounted for in the design process. The gaps between rotor and stators become consequently larger than what would be aerodynamically optimal to provide the desired amount of purge flow at design point.

Parametric studies on wheel space gaps have shown how sensitive designs can be to varying rim seal geometries (Popovic and Hodson [50]), making it even harder to obtain accurate predictions of performance and heat load while the geometry of the gaps is altered by thermal effects.

In particular, the practice of optimizing the aerodynamic design by including the secondary air system in the 3D simulations has only recently been included in the engine design process thanks to the improvements in computational resources and modeling. Recently, it has been shown that capturing accurately the dynamics of leakage flows – including low-frequency pressure perturbations – requires full-annular simulations. Only so is it possible to avoid artificial damping of these low frequencies because of periodic boundary conditions (Basol et al. [51], Rebholz et al. [52], Schädler et al. [53]).

For these simulations, the typical mesh size is such that parallelization on multiple Graphics Processing Units (GPUs) is required as opposed to regular Central Processing Units (CPUs) to contain the run time of the solvers.

Despite these recent efforts, CFD simulations are still far from being considered reliable predictors both of performance and heat transfer patterns, especially because of the sensitivity of their results to the accurate modeling of the wheel-space gaps. In particular, the endwall static pressure field and streamlines are strongly affected even by slight variations of the secondary air path and are completely mispredicted if cavities are not included at all (Turner [54], Hunter and Manwaring [55]). In particular, Ong et al. [44] find the evolution of the hub passage vortex – one of the flow features leaving strong signatures on the endwall heat transfer patterns – to be very sensitive to the distribution of leakage flow on the endwall.

### **Effect of Purge Flow on Endwall Heat Load**

Several experiments – mainly from linear cascades – are documented in the open literature, offering data on the cooling effectiveness of the rim seal leakage flow and its impact on heat transfer. One of the earliest works in this regard was published by Blair [56]. In this study, coolant is observed to be swept towards the suction side of the passage. The resolution of the method was later improved by Graziani et al. [57]. Gao et al. [58] demonstrate that purge flow can be effective in cooling the front portion of the passage and visualize the leakage flow moving towards the suction side of the blade, consistently with Blair’s findings. Similar observations are made by Wright et al. [59].

High-resolution data from a cascade presenting endwall contouring is provided by Lynch and Thole [60] by means of IR Thermography. They report an increase of the heat transfer on the suction side of the passage with higher leakage flow injection. The technique is similar to the one used in the present paper, as it relies on a contoured endwall heater (developed in Lynch et al. [61]) and on infrared imaging.

Data from rotating facilities is not as readily available due to the technical challenges of measuring on the rotating frame. Blair [62] uses iso-flux foils and arrays of thermocouples to measure heat transfer contours in a low-speed facility. Time-resolved heat transfer and film cooling measurements in short-duration facilities are found in literature, but are often taken at discrete locations (e. g., by means of heat flux gauges: Abhari et al. [63, 64] and Dunn et al.[65, 66]).

More recently, Dénos and Paniagua [67] find a reduction in gas temperature due to purge flow injection, again on the suction side of the passage.

A recent study by Rezasoltani et al. provides high-resolution cooling effectiveness measurements for purge air on the rotor platform of a rotating facility [68] with and without endwall contouring. They find significant improvement in the aerothermal performance with the non-axisymmetric endwall shape and better coverage of the endwall when off-loading the rotor.

However, the aforementioned technique cannot provide a quantification of the local Nusselt number to complement the cooling effectiveness information.

$$\text{Nu} = \frac{h \cdot L}{\kappa} \quad (1.2)$$

### 1.3 Endwall Heat Transfer

Endwall heat transfer is particularly difficult to predict because of the highly three-dimensional nature of the endwall flow (section 1.2). For this reason, and because accuracy of predictions plays a crucial role in part lifing (an error of 50K



in metal temperature can lead to a reduction of the life of the components by half, see Han et al. [7]), research and design engineers reserve most of the attention to this particular area of the passage. The request for experimental validation of CFD codes under conditions the most engine-representative possible is therefore pressing. A brief literature review on experimental endwall heat transfer is offered in the following sections.

### 1.3.1 Cascade Endwall Heat Transfer

Multiple studies have followed in the steps of the early work of Blair [56] in 1974, focusing on the heat transfer distribution in linear cascades. These setups, despite typically lacking when it comes to matching engine-like levels of unsteadiness and body-forces effects, still provide valuable insight in the relationship between endwall aerodynamics and corresponding heat loads. The findings of Blair were later confirmed by Graziani et al. [57] and Goldstein and Spores [69]. More recently, a systematic study of the effects of Reynolds number and boundary layer thickness on endwall heat transfer was offered by Boyle and Russell [70]. In a later paper by Kang et al. [71], their results were confirmed.

The main features appearing in the distributions of heat transfer coefficient in cascades are:

- a) a high heat transfer region towards the leading edge and pressure side of the blade, which is attributed to the presence of the stagnation point and the formation of the pressure side leg of the horseshoe vortex;
- b) a wedge-like region pointing downstream, at the inlet of the passage, where the heat transfer coefficient reflects the one observed in turbulent boundary layers on flat plate;
- c) an increase in heat transfer coefficient due to the downwash motion of the hub-passage vortex, followed by a region of lower heat transfer coefficient because of the blockage induced by the migration of this vortical structure towards the suction side of the passage;
- d) as the flow expands and accelerates through the passage, the heat transfer coefficient increases.

According to the experiments of Laveau et al. [38, 72], these signatures left by the flow features on the heat transfer patterns are still observable in annular cascades.

### 1.3.2 Measurements on the Rotating Frame

Experimental data from rotating machinery is required if the effects of rotor-stator interaction, centrifugal and Coriolis forces are to be taken into account. Several challenges arise when attempting the measurement of heat transfer quantities on the rotating frame and often data is shown only for discrete locations in the passage or on the airfoils. Nonetheless, experiments on the rotating frame have been performed since the early 1990s.

Once again, Blair's work [62] is one of the first attempts to measure heat transfer in rotating facilities. His technique employed foil heaters and arrays of thermocouples soldered to their surface to measure airfoil and endwall heat transfer on a large-scale, low-speed rotating facility. Contours of heat transfer coefficient and adiabatic wall temperature were determined by interpolating the values measured at the thermocouple locations. In presence of local effects – such as in the leading edge region – data from liquid crystals complemented the measurements. Heat flux gauges have been successfully and reliably employed in short-duration facilities. de la Loma et al. [73] provide a concise list of works of this kind. In particular, Abhari [64] finds that the unsteadiness plays a significant role in the effectiveness of the cooling of the rotor airfoils, specifically, the heat transfer decreases by 12% on the suction surface of the airfoil and by 5% on the pressure side compared to cascade data for the same cooling configuration. The effect of unsteadiness on heat transfer will be considered when comparing steady and unsteady predictions to the rotor endwall heat transfer data (section 7.1.1).

Dunn [65, 66] concludes that the boundary layer transitions to turbulence early on the NGVs and the flow is essentially turbulent on the downstream rotor surfaces. A case is made in this work concerning the possibility of relaminarization of the boundary layer due to flow acceleration in the second stator downstream of the first stage (see section 6.2.1).

Despite the advantage of heat flux gauges of providing time-resolved data (Abhari et al. [63]) at representative engine conditions (especially at representative temperature ratios between main flow and cooling flows), they can only measure the heat transfer coefficient at discrete locations. It is therefore difficult to assess the local effect of flow features on the heat load distribution, particularly on the endwalls. For this purpose, a high-resolution measurement technique is required.

Moffat [74] describes broad-band liquid crystals thermography and infrared thermography as the only two experimental techniques able to provide full maps of heat transfer coefficient and adiabatic wall temperature. Significant improvements have been made in the accuracy and speed of commercially available infrared imaging systems, especially after the introduction of 3rd generation infrared detectors in the early 2000s (Rogalski [75]). Nowadays, it is possible to purchase devices capable of measuring temperatures with integration times in the order of tens of microseconds in the long-wave infrared range (see section 2.1.5). Still, signal to noise ratio limitations restrict the possibility of applying such devices for the measurements of heat transfer in the rotating frame of reference of “cold” (i.e. close to ambient temperature) high-speed or even moderate speed turbine facilities.

Essentially, the main challenges of measuring on the rotor of a turbine by means of infrared thermography can be summarized as follows:

- limitations on the integration time of the camera under the contrasting requirements of a sufficiently high signal-to-noise ratio and of being able to acquire a sharp image of a rapidly moving object;
- implementation of an accurately known thermal boundary condition with instrumentation able to withstand the centrifugal loads.

The present work deals with the development of a measurement technique overcoming the aforementioned difficulties and the results obtained from measurements in a rotating axial turbine research facility.

## 1.4 Research Objectives

The current work aims at contributing to the joint industrial and academic effort in increasing the efficiency and operational flexibility of gas turbine engines – both for power production and aircraft propulsion – without compromising the reliability of their operation and, possibly, enhancing the components' life and reducing maintenance costs.

Specifically, the research presented here focuses on providing experimental evidence of heat load variation under changing operating conditions in one of the regions in the machine with the most complex aerothermodynamics: the rotor hub endwall. The data collected is analyzed to provide suggestions for the operation and design of the machines with the goal of protecting the rotor endwall from overheating.

In particular, the effects of the following factors are studied:

- changes in the overall operating condition of the turbine (full load/part-load);
- variation in mass flow rate of rim seal leakage flows;
- advanced rim seal cavity shaping.

These effects are observed in an aerodynamically optimized 1.5-stage rotating machine, with fully three-dimensional blade and endwall design.

## 1.5 Key Achievements

For the first time, to the best of the author's knowledge, quantitative infrared thermography is performed on rapidly moving objects with a resolution of 0.32mm/pixel. In order to do so and fulfil the research objectives outlined in the previous section 1.4, the combination of frames acquired with multiple integration times was achieved for the first time in the open literature preserving quantitative information on the recorded temperatures (section 2.2). A calibration technique is also developed eliminating the necessity for iso-energetic hypotheses or complex methodologies to evaluate the uniformity of a surface heat source (section 4.5.5 ). A manufacturing process for the production of robust surficial heat sources for employment on arbitrarily complex geometries is described (section 4.3).

From the turbomachinery design perspective, the data acquired with the newly developed tools and methods enable the following observation: unsteady effects cannot be neglected when aiming at faithful predictions of the heat loads.

## 1.6 Outline

### Chapter 1

The first chapter presents the general motivation for the current piece of research and provides a brief literature review on the main topics addressed in the following chapters, with particular reference to endwall heat transfer and aerodynamics, purge flow aerodynamics and impact on heat transfer, experiments in the field of turbine endwall heat transfer and rim seal leakage flow.

### Chapter 2

The second chapter summarizes the experimental methods and techniques employed in the experiments performed and describes the theoretical background underlying each. Remarks on the practical limitations and applicability of the methods are given to underline the necessity of the developments carried out in this work. In this chapter, the quantitative image processing tools and procedure enabling the combination of frames acquired with different integration times while retaining the temperature information are described in detail. Such tools constitute part of the main contribution of this piece of work.

### Chapter 3

The specifications, the development, manufacturing and integration of the instrumentation used for the second stator endwall heat transfer measurements are presented in this chapter. Details are given on the thermal and mechanical design of the stator heat transfer platform and the multiple view image acquisition system.

## **Chapter 4**

The specifications, the development, manufacturing and integration of the rotating instrumentation used for the current experiments are presented in this chapter. Details are given on the mechanical integration of the rotor heat transfer platform, the directly deposited film-heaters and the rotating, on-board data acquisition system. The manufacturing process developed in the framework of this thesis and described here allows experimentalists in the field to produce a known thermal boundary condition on complex three-dimensional geometries.

The theoretical background and the practical application of the step-wise transient heat flux calibration are also described. The uncertainty of the method is assessed and its importance for the correct evaluation of the endwall heat load is explained. Such newly developed calibration methodology enables the measurement of the locally produced heat flux in a quick and inexpensive way and with high levels of accuracy and repeatability.

## **Chapter 5**

Details are given on the sources of measurement error and their impact on the final results both for the stator and for the rotor measurement techniques.

## **Chapter 6**

The experimental results from the stator endwall heat transfer measurements are presented for three operating conditions. The patterns observed at the rated operating condition of the machine are related to the flow structures predicted by unsteady CFD simulations.

The variations are explained in terms of Reynolds number effects, secondary flows, rotor loading and turbulence in the boundary layer.

## **Chapter 7**

The first experimental results from the rotating frame are presented in this chapter and analyzed with reference to literature and simulations performed by

Siemens. The possible reasons for discrepancy are addressed. The effects of the part-load operation are observed and analyzed.

One of the main conclusions of this work is drawn here, concerning the necessity of using unsteady simulations to accurately predict the endwall heat loads.

### **Chapter 8**

The effect of variations in the mass flow rate of purge air on endwall heat transfer is analyzed in this chapter for both full load and part-load operation.

### **Chapter 9**

The effect of a novel rim seal cavity design enhancing the circumferential component of momentum of the purge flow is observed experimentally for both full load and part-load operation.

### **Chapter 10**

This chapter summarizes the key findings of the work and provides suggestion for future research.

## 2. Experimental Methods

This chapter presents the physical principles underlying the measurement technique, starting from the basics of infrared thermography (section 2.1) to include image processing tools (section 2.2) and the measurement principle of the heat transfer quantities (section 2.3).

### 2.1 Infrared Thermography

Infrared thermography is a versatile, non-intrusive temperature measurement technique returning remarkable data density. It has been employed in very diverse applications, such as medical science, non-destructive testing and environmental science, as exhaustively reported by Meola et al. [76] and Carlomagno et al. [77]. In the field of thermo-fluid-dynamics, infrared thermography is used to measure convective heat transfer both at a fundamental level (Scherer et al. [78]) and in more application-oriented contexts (Schulz [79]). Application of the technique to rotating machinery or components is of interest for a variety of fields (fundamental fluid mechanics, Cardone et al. [80]; automotive, Lyons et al. [81]; railway engineering, Siroux et al. [82]), but limitations in the acquisition speed of the detector typically allow quantitative measurements only in a circumferentially averaged fashion. An attempt to reconstruct a full temperature map of a rapidly rotating disk was reported in 2002 by Astarita et al. [83]. The objective of their work is to visualize and count the spiral vortices formed by the rotation of the surface of the disk. Their ingenious, purely geometrical reconstruction provides enough qualitative detail of the temperature field to visualize the signatures of the vortices, but cannot be used to infer quantitative heat transfer measurements due to the smearing of the temperature profiles. In fact, quantitative information on the surface heat loads on a similar setup, but with the addition of a jet is provided later in 2008 by the same group still in an azimuthally averaged fashion (Astarita et al. [84]).



### 2.1.1 Basics of Radiative Heat Transfer

Any grey body at a temperature superior to absolute 0 (i. e. 0K) emits energy in the form of radiation, following the Stefan-Boltzmann law:

$$j^* = \sigma \cdot \varepsilon \cdot T_s^4 \quad (2.1)$$

with  $j^*$  being the radiant emittance or the energy emitted across all wavelengths per unit surface area per unit time by the grey body,  $\sigma$  is the Stefan-Boltzmann constant equal to  $5.670373 \cdot 10^{-8} \frac{W}{m^2 \cdot K^4}$ ,  $0 \leq \varepsilon \leq 1$  is the emissivity of the grey body and  $T_s$  is its thermodynamic temperature. The spectral radiance  $B_\lambda(\lambda, T_s)$  or the energy emitted by the body per unit time, per unit area, per unit solid angle and per unit wavelength, changes according to Planck's law:

$$B_\lambda(\lambda, T_s) = \frac{2 \cdot h \cdot c^2}{\lambda^5} \cdot \frac{1}{e^{\frac{h \cdot c}{\lambda \cdot k_B \cdot T_s}} - 1} \quad (2.2)$$

where  $\lambda$  is the wavelength,  $h = 6.626070040 \cdot 10^{-34} J \cdot s$  is Planck's constant,  $c = 299'792'458 \frac{m}{s}$  is the speed of light in vacuum (assuming that it is, indeed, a constant [85]),  $k_B = 1.38064852 \cdot 10^{-23} \frac{J}{K}$  is the Boltzmann constant.

The relation between spectral radiance and radiant emittance is given by the following:

$$j^* = \int_0^\infty d\lambda \int_{2\pi} B_\lambda(\lambda, T_s) d\Omega \quad (2.3)$$

That is, the radiant emittance  $j^*$  is the integral of the spectral radiance  $B_\lambda(\lambda, T_s)$  over all wavelengths and over a full hemisphere (solid angle  $2\pi$ ).

The wavelength  $\lambda_{\max}$  at which the spectral radiance reaches its maximum value increases with the temperature of the radiating body (see Figure 2.1) according to Wien's displacement law:

$$\lambda_{\max} = \frac{b}{T_s} \quad (2.4)$$

where  $b = 2.8977729 \cdot 10^{-3} \text{ m} \cdot \text{K}$  is Wien's displacement constant.

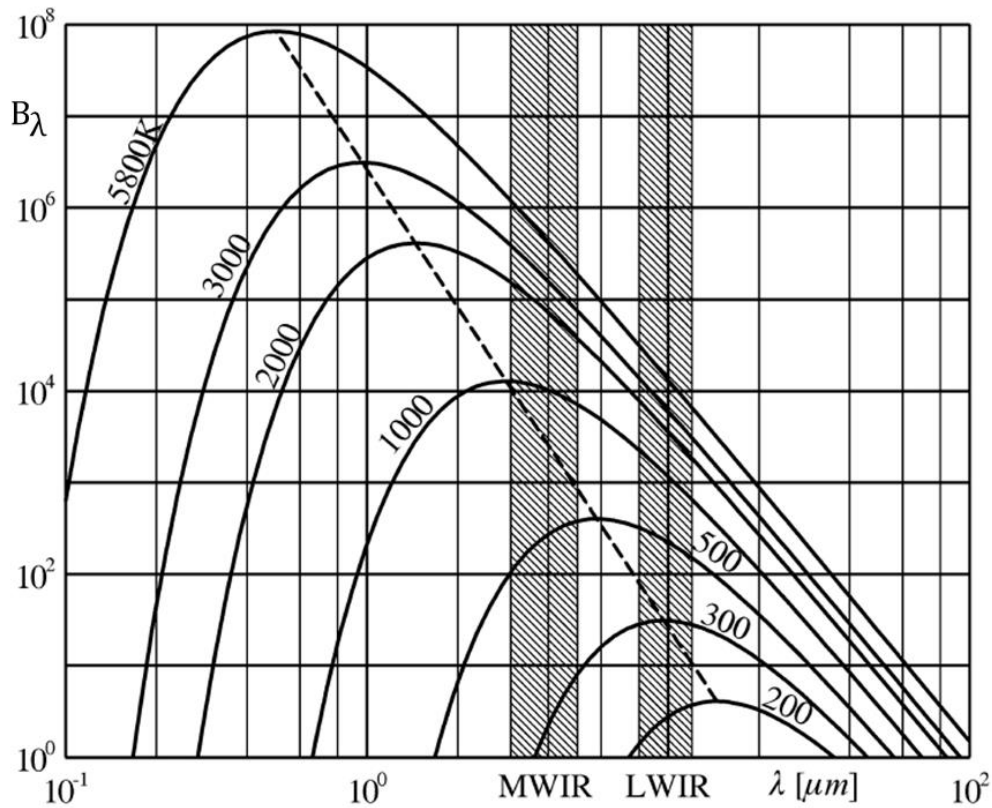


Figure 2.1: spectral hemispherical black body emissive power [ $\text{W/m}^2\mu\text{m}$ ] in vacuum for several absolute temperatures as a function of wavelength  $\lambda$  [86].

The relationship between the temperature of the body and the spectrum of the emitted radiation poses a requirement on the spectral range of the sensors depending on the expected temperature values one wishes to measure. Typically, the infrared spectral band is sub-divided in five, conventionally specified regions depending on the wavelength, as summarized in Table 1.

Table 1: conventional sub-division of the infrared spectral range based on wavelength intervals.

Spectral Band Name	Abbreviation	Wavelengths [ $\mu\text{m}$ ]	Temperatures [ $^{\circ}\text{C}$ ]
Near-infrared	NIR	0.75-1.4	3'590-1800
Short-wavelength infrared	SWIR	1.4-3	1800-690
Mid-wavelength infrared	MWIR	3-8	690-90
Long-wavelength infrared	LWIR	8-15	90- -80
Far-infrared	FIR	15-100	-80 - -270

The MWIR and LWIR bands are of particular interest for thermal measurements and most of the commercial thermal imaging devices are sensitive in this range. The two combined constitute the so-called “thermal infrared” band.

Thermal imaging finds its use mainly in military and industrial applications.

### 2.1.2 Infrared Transparent Materials

Optics for infrared measurements must be produced out of materials with appropriate transmissivity in the infrared range of interest. If the radiometric measurements are to be made in the LWIR range, the choice typically falls on the following materials:

- Sodium Chloride (NaCl): transparent in a wide spectral range from the near infrared to the LWIR, has the drawback of being water soluble. It requires careful control of the humidity of the air to avoid degradation of the optics;

- Germanium (Ge): suitable for MWIR and LWIR applications, presents lower transmissivity than ZnSe;
- Zinc-Selenide (ZnSe): is more transparent than NaCl in the same band of wavelengths. Despite its cost, brittleness and toxicity when broken, it is the preferred material for MWIR and LWIR application;
- some acrylic polymers can offer a low cost alternative if transmissivity requirements and homogeneity of the transmission over the wavelength range are not stringent.

Figure 2.2 shows the value of transmissivity of several materials. The values in the chart can be enhanced up to 98% by depositing anti-reflective coating on the optics. For the current study, ZnSe windows with anti-reflective coating are integrated in the casing of the facility for IR optical access to the rotor endwall (Chapter 1).

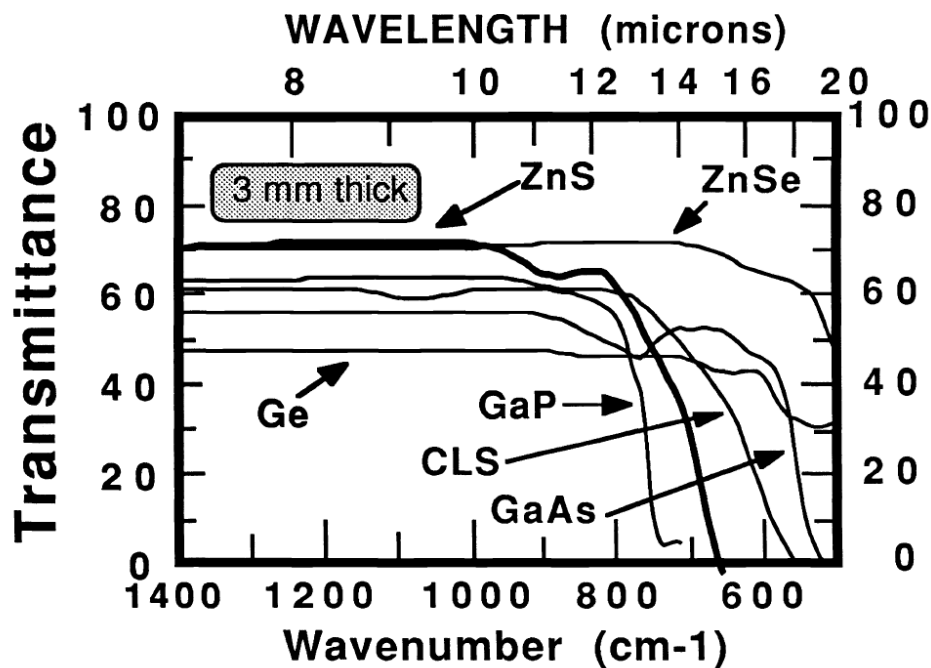


Figure 2.2: transmittance of several 3mm-thick slabs from different infrared transparent materials. It can be seen how uncoated ZnSe presents the highest transmissivity over the widest range [87].

### 2.1.3 Atmospheric Infrared Transmissivity

Two regions of the infrared spectrum are well transmitted by the Earth's atmosphere, corresponding to the adopted bands for MWIR and LWIR (section 2.1.1 ). In these so-called atmospheric windows, the transmittance of a 1km-thick atmospheric layer reaches values of beyond 80%. It follows that the atmospheric absorption of infrared radiation is negligible when dealing with thicknesses of the order of 1m as is often the case in laboratory experiments.

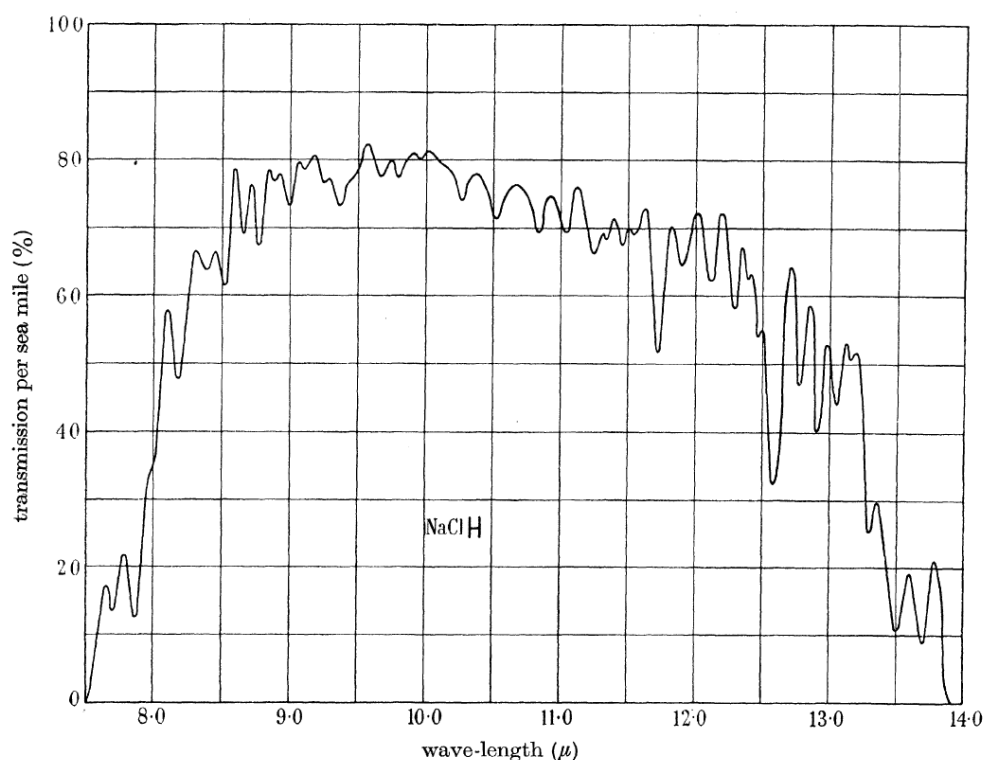


Figure 2.3: atmospheric transmittance in the LWIR window as reported by Gebbie et al. [88].

### 2.1.4 High-Emissivity Coating

It is beneficial for the emitting surface to present a high value of emissivity in the wavelength range of interest for the surface temperature measurements, so to increase the signal collected by the infrared images devices. This can be achieved by coating the surface with substances with values of emissivity close to 1. The simplest way to achieve this is by spraying the surface with high-

emissivity paint such as the NEXTEL<sup>®</sup> Velvet Coating 811-21 by Mankiewicz used for this study. The emissivity of this coating is thoroughly characterized by Lohrengel and Todtenhaupt [89] for all wavelengths and as a function of the angle to the local normal. It is found that the spectral emissivity of the coating is  $\sim 97\%$  in the long-wavelength infrared range and its total directional emissivity is constant up to  $60^\circ$  from the normal (see Figure 2.4 from Gegenbach et al. [90]). Given the geometrical arrangement used in the study, this allows to neglect variations in emissivity due to the viewing angle.

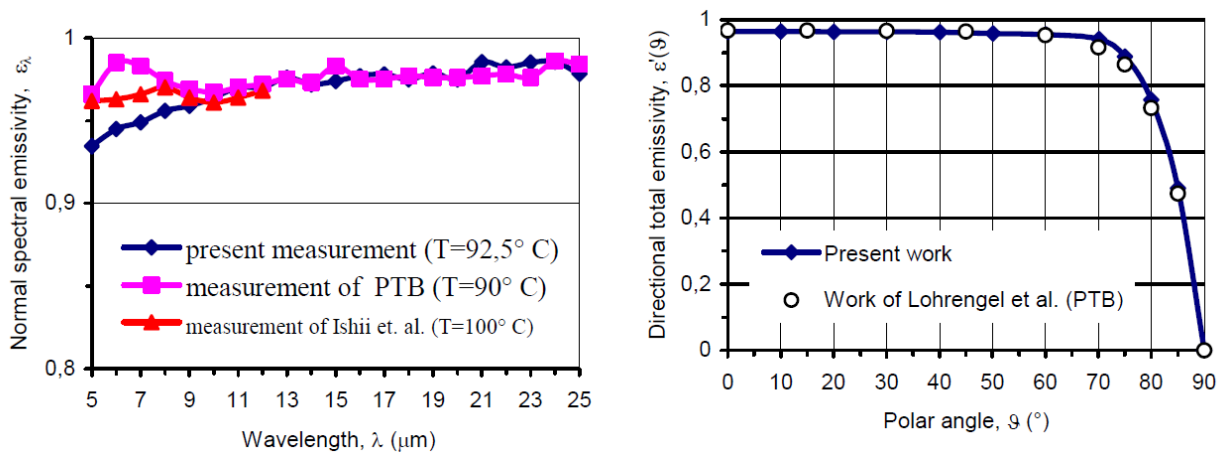


Figure 2.4: spectral emissivity (left) and directional total emissivity (right) as measured by Gegenbach et al. [90], in good agreement with previous results from Lehrengel and Todtenhaupt

### 2.1.5 IR Imaging Devices

Typically, a thermal imaging device consists of:

- a focal plane array (FPA) of infrared-sensitive elements;
- a read-out electronic circuit translating the output of the pixels of the FPA in digital signals;
- an optical system able to focus the infrared radiation coming from the environment onto the focal plane where the FPA lies.

Depending on the technology used, the focal plane array may require cooling. In that case, thermoelectric elements or Stirling cooler are generally used to drop

the temperature of the sensing element down to 77K (boiling point of nitrogen at atmospheric pressure) to enhance its sensitivity.

### Infrared Detectors

The readers is referred to Astarita and Carlomagno [86] for further details on the basics and general applications of infrared thermography. There are essentially two kinds of infrared detectors:

- thermal detectors;
- photon detectors.

Thermal detectors date back to when infrared radiation was first discovered in 1800 by Sir F. W. Herschel [91]. Material science and miniaturization made it possible to integrate these devices in a focal plane array.

The functioning principle is very simple: a slab of material changes its temperature as a result of incident radiation. Its temperature can be measured either by means of a thermocouple (thermopile) or by measuring its electrical resistance as a function of temperature (bolometer).

The time response of the detector is driven by its thermal capacity  $C$  and the conductance  $G$  of its support, which should minimize the conduction losses.

The time constant  $\tau$  of this system is then proportional to the ratio of the thermal capacity  $C$  and the conductance  $G$ :

$$\tau \propto \frac{C}{G} \quad (2.5)$$

The order of magnitude of the response time of these detectors nowadays is of the order of 10ms, and this makes them unsuitable for imaging rapidly moving objects, based on the requirements that will be defined in the later sections.

### Photon Detectors

In photon detectors, electrons move to the conductive band of the detector's material due to the energy coming from incident photons on the array. A change in resistance (photoconductive detectors) or a voltage difference (photovoltaic detectors) is produced, the magnitude of which is linear with the incident radiation

and its wavelength. Being the output signal proportional to the incident radiation, it is also linear with the integration time when imaging a source at constant temperature.

The most commonly used types of photon detector materials are: mercury cadmium-telluride (HgCdTe or MCT), indium antimonide (InSb), and the quantum well photodetector (QWIP). In particular, the infrared camera used in the current work is equipped with a MCT detector. The composition of the material is tuned to make it sensitive in the LWIR band (7.7-9.3 $\mu\text{m}$ ): the amount of CdTe (a semiconductor with bandgap of  $\sim 1.5\text{eV}$  at room temperature) relative to the amount of HgTe (a semimetal, therefore having a null bandgap) determines the bandgap of the mixture. The MCT detector can work both as a photoconductive detector and as a photovoltaic one, but needs to be cooled at 77K to achieve the required sensitivity.

### Performance of Infrared Detectors

The performance of all infrared detectors is noise-limited, as noise determines the minimum detectable temperature difference [92]. The key figure quantifying IR detector performance is therefore expressed in terms of signal-to-noise ratio as proposed by Jones in 1959: with the normalized detectivity  $D^*$ :

$$D^* = \frac{\sqrt{\Sigma \cdot \Delta f}}{\text{NEP}} \quad (2.6)$$

In the definition 2.6,  $\Sigma$  represents the active surface area of the detector,  $\Delta f$  its equivalent noise bandwidth, and the NEP (Noise-Equivalent Power) is the amount of incident radiative power for which an output signal equal to the detector noise is generated. The measurement unit of the normalized detectivity  $D^*$  is the Jones [ $\text{cm} \cdot \sqrt{\frac{\text{Hz}}{\text{W}}}$ ]. It represents the amount of noise generated by 1W of radiation incident on a sensor with a unitary active surface area when measured with a bandwidth of 1Hz.



Detectivity is a valuable parameter for comparing the performance of different technologies across all wavelengths as shown in Figure 2.5.

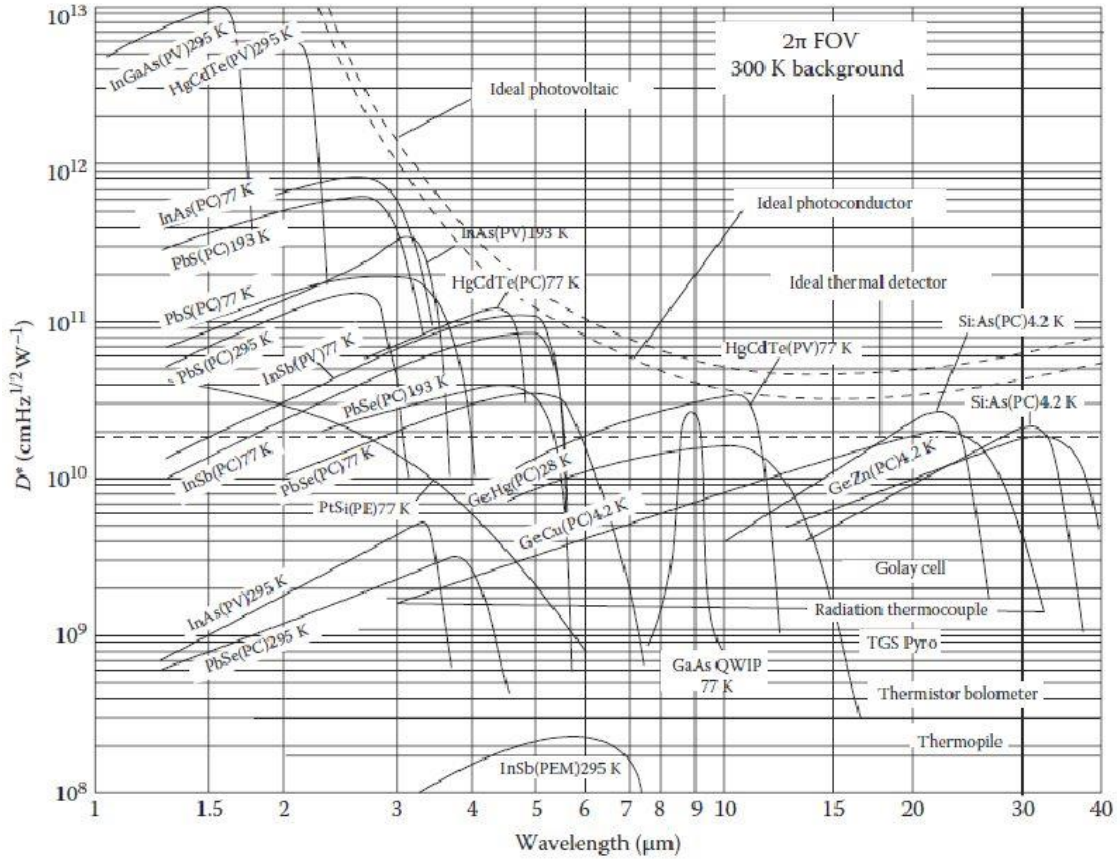


Figure 2.5: normalized detectivity  $D^*$  (eq. 2.6) for different infrared detectors cross the infrared spectral range.

It can be seen how the MCT detector shows the highest detectivity of all detectors in the LWIR range, of interest in this study.

Aside from the performance of the detector, also read-out electronics, data transfer and elaboration, optics and calibration play a role in the overall performance of the imaging system. Significant improvements have been made in the accuracy and speed of commercially available infrared imaging devices, especially after the introduction of 3rd generation infrared detectors in the early 2000s (Rogalski [75]). These detectors enable acquisition and storage of data from the whole FPA simultaneously, rather than scanning the array pixel by pixel, thus dramatically reducing the time needed for the acquisition of a single frame. The additional

noise produced by read-out electronics and analog-to-digital converters also affects the rapidity of the acquisition: the higher the amount of energy collected by the detector, the higher the signal, the lower the relative contribution of the aforementioned noise sources. Nowadays it is possible to purchase devices capable of measuring temperatures with integration times in the order of tens of microseconds in the LWIR range, the least energetic in the thermal IR band, thanks to the low noise levels of detectors and electronics.

### FLIR SC7300L IR Camera

For the current study, a FLIR SC7300L infrared camera is used. The SC7300L is a LWIR camera, equipped with a 256x320pixel MCT detector, cooled by a Stirling refrigerator at 77K and with a pixel size of 30 $\mu$ m. Because of the high sensitivity of the detector, its integration time – analogous to the exposure time of the film or sensor in a regular camera – can be as low as 3 $\mu$ s. The gain of the detector can be set to either 1 or 3.

In order to use the maximum possible responsivity of the detector for a given integration time, the gain is kept at the maximum factor of 3 during the whole campaign. Nevertheless, the minimum integration time that can be used to measure temperatures in the expected range of operation of the turbine research rig (between the mass-averaged relative total flow temperature  $T_{t,rel} = 40.7^{\circ}\text{C}$  and the maximum operating temperature of the endwall heaters  $T_s < 100^{\circ}\text{C}$ ) cannot be lowered below  $IT = 50\mu\text{s}$  (see Figure 2.6).

Table 2: performance indicator for the FLIR SC7300L camera used in this study

Performance Indicator	Test Parameters	Measured Value
FPA Temperature	20 ° C background	77K
Electronic Noise	25 ° C BB	1.94DL
NETD	IT = 400ms	16.39mK
Sensitivity	25-26 ° C	8.44mK/DL

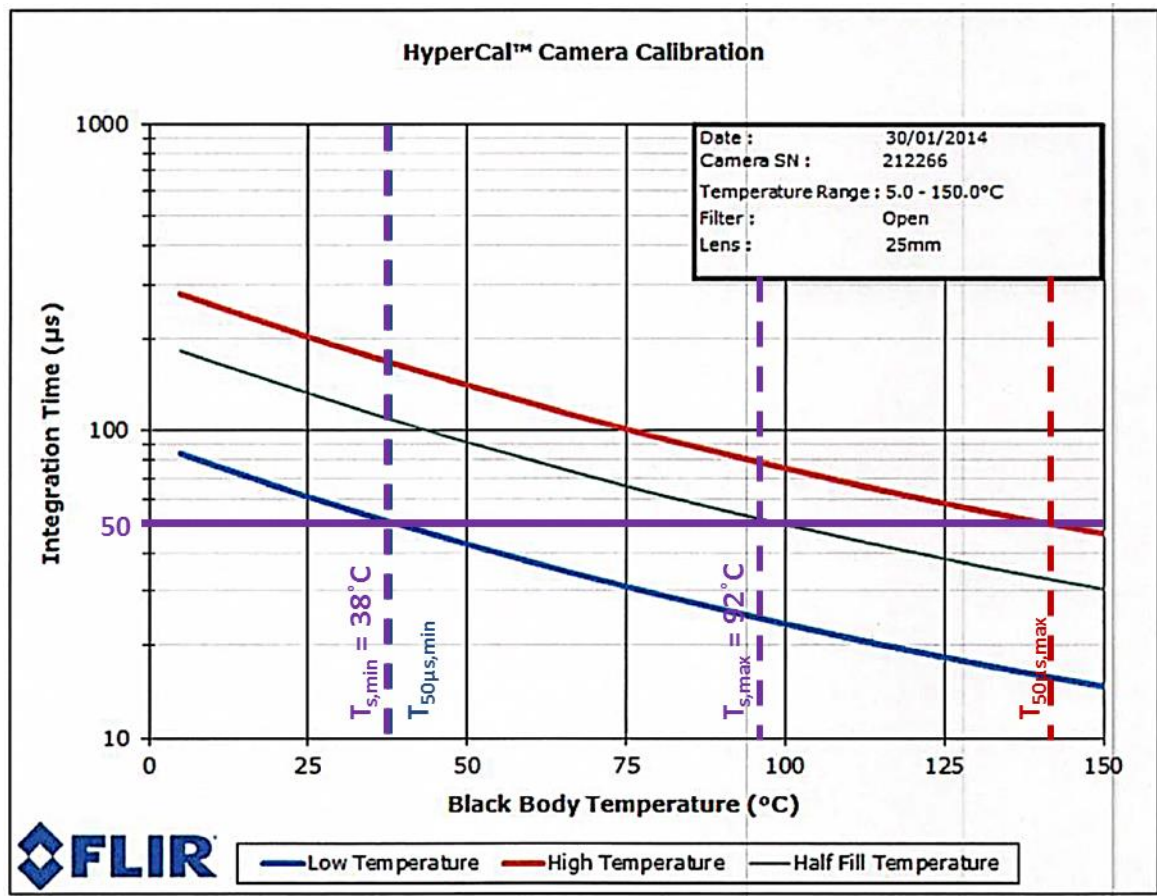


Figure 2.6: recommended temperature range for a specific integration time. Best detector performance is obtained for the half-fill temperature (digital levels of the detector correspond to half of its saturated level). Operating temperature range of the endwall heaters is indicated. Courtesy of FLIR.

If the camera is operated in the recommended range and, specifically, in proximity of the half-fill level of the detector, the error in measured temperature is less than 0.2K, as proven by the quality checks performed by the manufacturer and reported in the following Table 3.



Figure 2.7: a FLIR SC7300L camera (courtesy of FLIR).

Table 3: temperature error as a function of the object temperature with half-filled detector (\*value for 100 °C is interpolated: value measured at 150C is 0.45 °C).

$T_{BB}$ [°C]	$\delta T$ [°C]
5	-0.19
15	-0.12
75	-0.12
100	0.19*

In the following section 2.2 it will be clarified how the measurements were performed combining data acquired with a 50 $\mu$ s integration time, which lies within the specified operating range of the camera, with a lower integration time of 10 $\mu$ s, which instead allows to acquire thermograms of the moving rotor endwall with a higher spatial resolution.

Despite operating the camera at such low integration time is not recommended, the performance of the instrument under these conditions was still investigated (see next section).

### Limitations of the FLIR SC7300L IR Camera

Based on tests performed on a black body IR source, it is found that, for an integration time of 10 $\mu$ s, the root mean square error in temperature over a frame at 60 °C is of 0.25 °C, with peak-to-peak oscillations of  $\pm 1$  °C.

For the purpose of this study, two requirements are set for successful heat transfer measurements on the rotor endwall of the turbine facility:

- a maximum movement of the rotor endwall of 1mm during the acquisition of a frame. This requirement translates into a maximum allowable integration time of 10 $\mu$ s, based on the radius of the rotor at the hub and on the rotational speed of the turbine during the measurements;
- a maximum error in the measured temperature of 0.5K.

The first constraint ensures that the smearing of the temperature contours does not exceed an extent of 3 pixels, given the spatial resolution of the optical setup used during the measurements (0.32mm/pixels). This is equivalent to the effect of the superposition of the 1000 frames acquired per sequence (sect. 4.2), which is done with a minimum tolerance on the rotor displacement of  $\pm 1$  pixel.

The uncertainty on wall temperature has been described as the main driver of global heat transfer uncertainties for iso-energetic setups in previous works (Lynch et al. [61]). This is why the second constraint strictly limits its value to match the order of magnitude indicated by Lynch et al. themselves for their own experiment and by Laveau et al. [38, 72] when performing IR-based heat transfer measurements in the same facility and with similar wall temperature ranges as in the present study. It is therefore evident that it is not possible to satisfy both requirements with a 10 $\mu$ s-long integration time. Satisfactory temperature accuracy can be obtained by increasing the integration time to 50 $\mu$ s. With this setting, the noise-induced error in temperature decreases by a factor of 5. Temperature profiles (Figure 2.8(b)) extracted from thermograms of the high-emissivity hot plate of Figure 2.8(a) provide a representative example of the impact of noise in the temperature readings at low integration times.

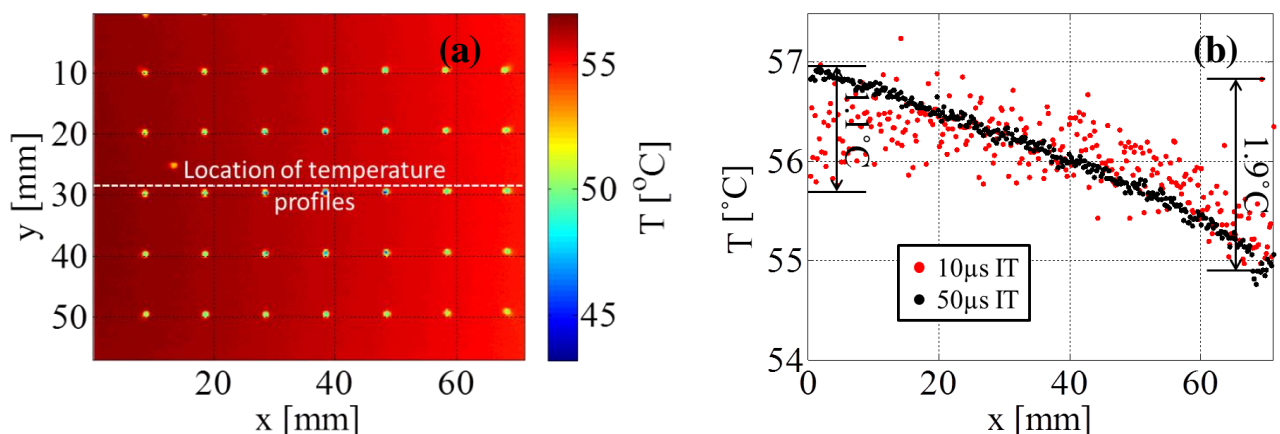


Figure 2.8: thermogram of a high-emissivity hot plate (a) with location of extraction of temperature profiles highlighted with a white dashed line. The extracted temperature measurements shown in (b) are taken with two different integration times: 10 $\mu$ s and 50 $\mu$ s. The former shows high noise-induced fluctuations and differences up to 1.9 $^{\circ}$ C to the latter.

On the other hand, the movement of the rotor endwall during the integration is 5 times bigger. The rotor, in fact, spins with a rotational speed of 2700rpm, corresponding to a linear speed at the hub endwall of 93m/s. The camera is installed at a distance of 370mm (hub endwall to FPA), resulting in an image resolution of 0.32mm/pixel. It follows that during a 50 $\mu$ s-long integration, the rotor hub endwall moves by 4.7mm, equal to 14.6 pixels. Considering for reference that the throat section of the rotor hub passage is of about 7mm, it is clear that the averaging occurring due to the smearing effect of the temperature contours would result in a coarse spatial resolution. No integration time setting can be found returning contemporarily a satisfactory image quality and a temperature sensitivity compatible with the target measurement uncertainties. The solution applied in this study is to combine the information collected in two data sets acquired with a different integration time (namely, 10 $\mu$ s and 50 $\mu$ s) by means of the image restoration procedure described in the later sections.

### **Calibration of the IR Camera**

The temperature calibration of the infrared camera is performed on a test bench replicating the optical setup used in the facility – i.e, the ZnSe window and camera arrangement, respecting the relative distances within  $\pm 1$ mm –, by replacing the endwall heater with an isothermal black body (ISOTECH® Graybody Source 975) presenting a temperature stability of  $\pm 0.005$  ° C. Measurements are performed every 15 ° C in the range from 30 ° C to 120 ° C, thus including the full range of temperatures experienced during the turbine testing. This semi in situ calibration method resembles the one suggested by Ochs et al. [93].

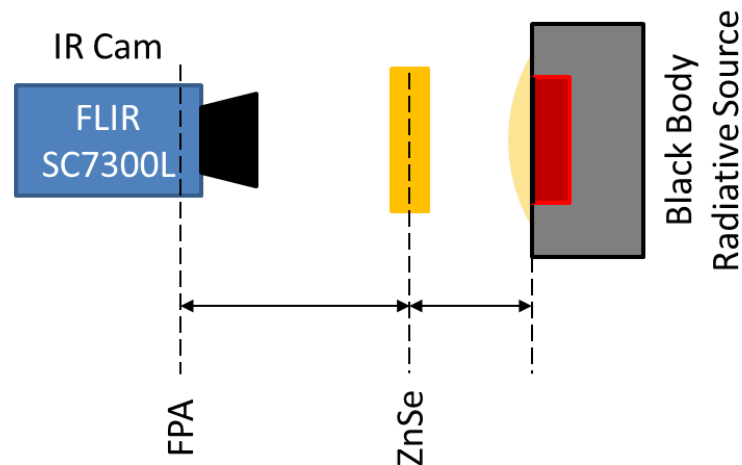


Figure 2.9: schematic of the semi in situ camera calibration setup. Distances between elements of the optical path are kept the same on the test bench than in the final experimental setup. The method resembles the one suggested by Ochs et al. [93]

The calibration curve is given a 4<sup>th</sup> order polynomial form in accordance with the Stefan-Boltzmann law. In fact, the digital levels read out from the MCT detector are proportional to the incident radiation. The calibration curve for a 50s integration time at detector gain x3 is shown in Figure 2.10. Sources of error arising from the camera calibration are discussed in section 0.

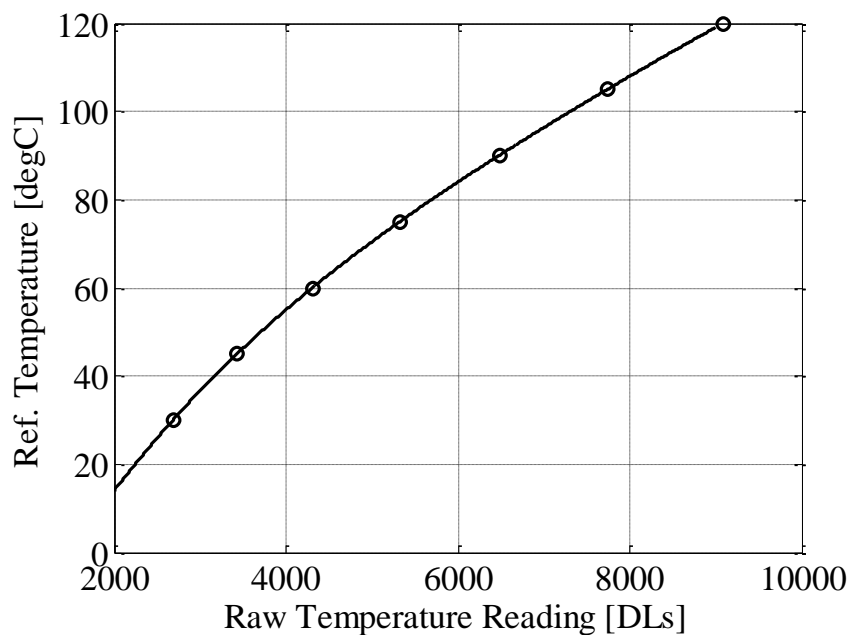


Figure 2.10: 4<sup>th</sup> order polynomial calibration curve for 50 $\mu$ s integration time at detector gain x3.

## 2.2 Image Processing

Due to the contrasting requirements of high spatial resolution and high temperature sensitivity, the thermal imaging of a moving object (i.e. the turbine rotor endwall) in the LWIR range necessitates a complex image restoration procedure. Images are taken with two different detector integration times,  $50\mu\text{s}$  and  $10\mu\text{s}$ , during which the rotor moves respectively by 14.6pixels and 2.9pixels. The two sets are then combined into a single temperature map through the following steps:

- registration of the images to account for jittering in the rotor trigger signal;
- deblurring of the  $50\mu\text{s}$  integration time thermograms;
- scaling of the  $10\mu\text{s}$  integration time thermograms to match the same digital level range as the  $50\mu\text{s}$  integration time set;
- frequency analysis of the difference between the two newly obtained data sets and individuation of the characteristic frequency of the ringing introduced by deblurring;
- application of band-pass filters to the two data sets, based on the frequency analysis performed at the previous point;
- combination of the two resulting thermograms into one hybrid data set.

A schematic overview of the image processing procedure after registration is provided in Figure 2.11. For validation of the procedure, images taken with a still rotor are used. In this case, the original  $50\mu\text{s}$  integration time frame is artificially blurred by convolution with a blur kernel  $\mathbf{k}$  to simulate the motion blurring during operation.

Each of the involved steps is described in the following subsections.

An evaluation of the uncertainty in the temperature reading resulting from the complete procedure is also provided.



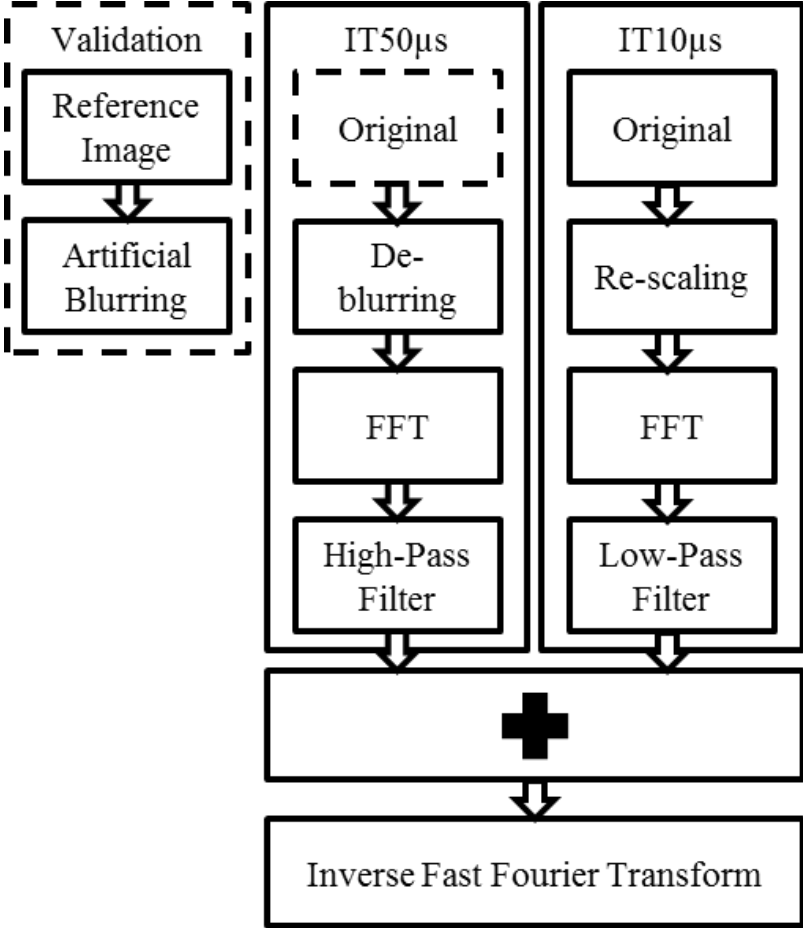


Figure 2.11: schematic overview of the image reconstruction procedure. For validating the procedure the original 50ms image is substituted with an artificially blurred version of the reference image of the still rotor.

### Image Registration.

The acquisition of each frame is triggered by a photodetector monitoring the revolution of the turbine axis. Jittering in the trigger signal controlling the acquisition of a frame can result in misalignment of the pictures. An image registration algorithm is employed to realign the frames of a sequence by recognizing the edges of the heated platform. If the misalignment is found to be greater than  $\pm 1$  pixel, the frame is discarded.

At least 25% of the acquired frames are generally accepted, meaning that the averages are computed from at least 250 images (see Figure 2.12).

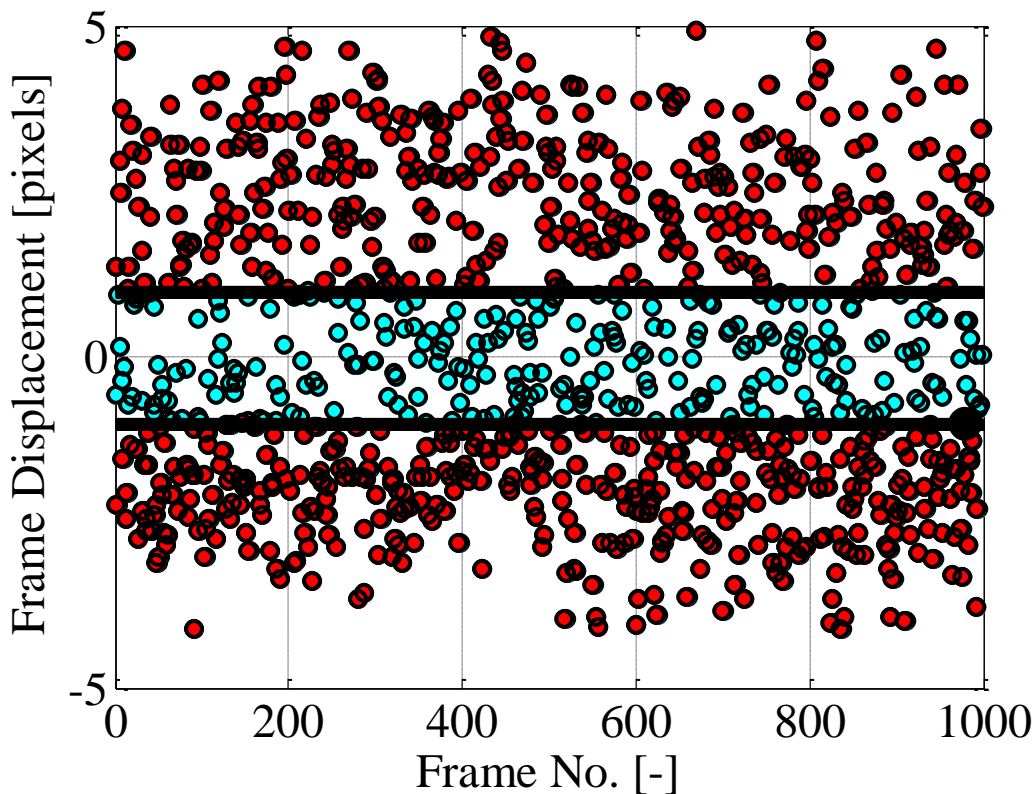


Figure 2.12: frames in a sequence are discarded if their measured displacement is greater than 1 pixel in both directions. Blue dots represent accepted frames, red dots are discarded frames. Thick black solid lines are the threshold of  $\pm 1$  pixel. For the sequence shown, the success rate is of 27%.

### Deblurring of the $50\mu\text{s}$ integration time thermograms

The motion of the rotor during the  $50\mu\text{s}$ -long signal integration results in smearing of edges and temperature contours.

Analytically, any blurred image  $\mathbf{y}$  can be represented as the convolution between a sharp image  $\mathbf{I}$  and a blur kernel  $\mathbf{k}$ :

$$\mathbf{y}=\mathbf{k}\otimes\mathbf{I} \tag{2.7}$$

Several techniques can be found in literature to recover a sharp version of the blurred images. An accelerated Richardson-Lucy [94, 95] algorithm (the built-in “deconvblind” function of MATLAB R2013a, for details on the algorithm the reader is referred to [96] and [97]) is used to recover a maximum-likelihood estimation of  $\mathbf{I}$ , given an initial guess of the blur kernel  $\mathbf{k}$ , based on the measured image resolution and the velocity of the rotor endwall. In the case of the current experiment, an initial guess can be given for the blur kernel  $\mathbf{k}$ , as the motion of the rotor in terms of pixels is known.

It can be shown that the Richardson-Lucy algorithm converges to the maximum likelihood solution as a special case of the expectation maximization algorithm [95], [98].

The deblurring restores an isotropic image resolution of 0.32mm/pixel. Prior to deblurring, an edge tapering treatment is applied to reduce ringing. Nonetheless, the presence of strong thermal gradients in the cropped image still results in ringing patterns that are treated by means of band-pass filters.

Ringing is defined as the introduction of artifacts in the reconstructed image at specific frequencies. The frequencies of the artifacts correspond to the zeros of the Fourier transform of the point-spread function [96]. As shown in Figure 2.13(c), ringing can result in temperature oscillations of up to  $\pm 1$  °C. Band-pass filters can be used to suppress this effect as shown in the later sections.

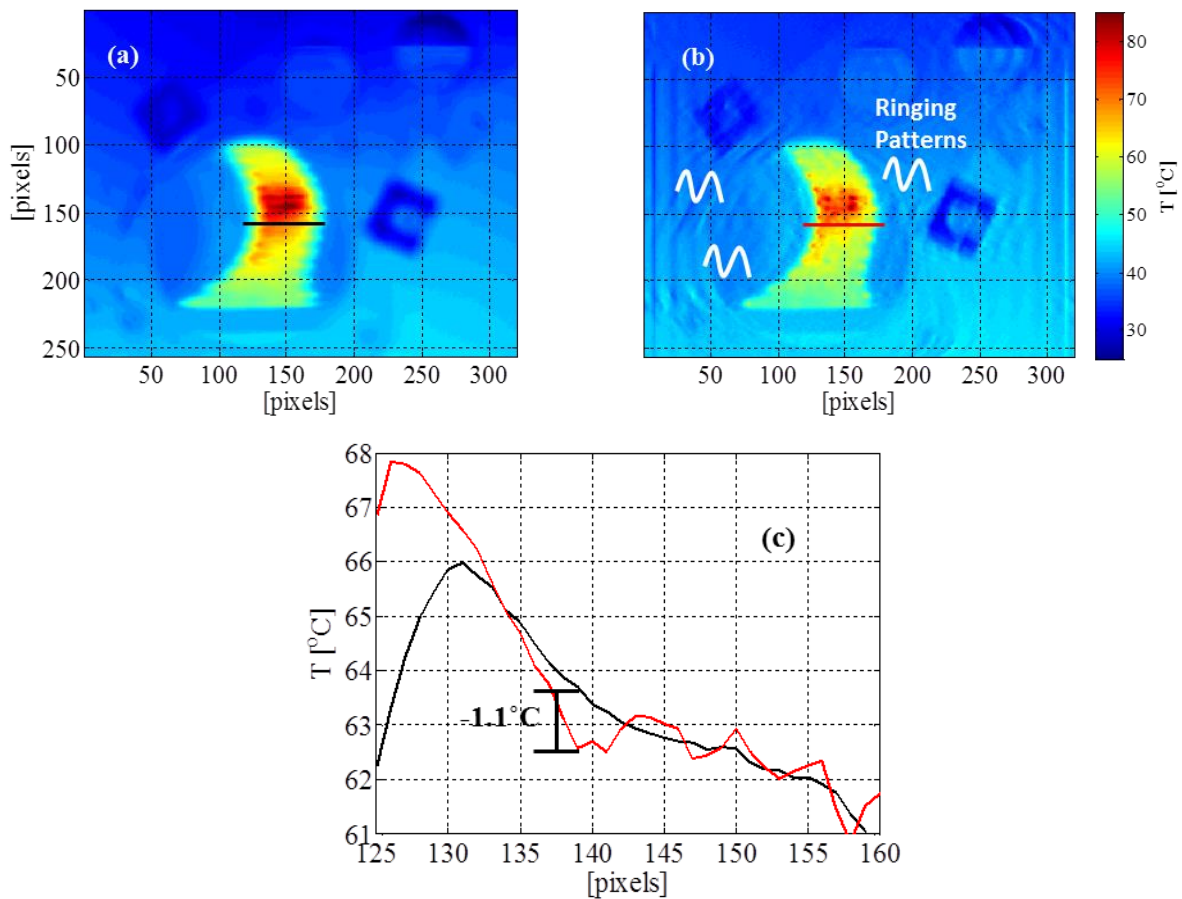


Figure 2.13: original thermogram acquired with a  $50\mu\text{s}$ -long integration time (a); resulting thermogram deblurred with a blind deconvolution method. Ringing patterns are evident (b); temperature profiles extracted from the locations indicated in (a) and (b). Ringing results in oscillations of up to  $\pm 1^\circ\text{C}$  (c).

### Frequency-based image combination for two integration time settings

It is possible to identify the frequency range of the ringing phenomenon by studying the two-dimensional, discrete Fourier transform of the difference between the deblurred,  $50\mu\text{s}$  integration time frame and the sharp,  $10\mu\text{s}$  integration time frame, provided that the latter is rescaled to match the dynamic range of the former. Rescaling is done on the physical grounds that the MCT detector returns a raw signal in voltage that is proportional to the absorbed radiative energy. It follows that, when that the same radiative power insists on the detector – as it happens when observing the same scene – the signal is directly proportional to the integration time (section 2.1.5 ). This is verified experimentally by plotting the temperature readings obtained from the  $10\mu\text{s}$  integration time frame versus the values in the  $50\mu\text{s}$  integration time frame (Figure 2.14).

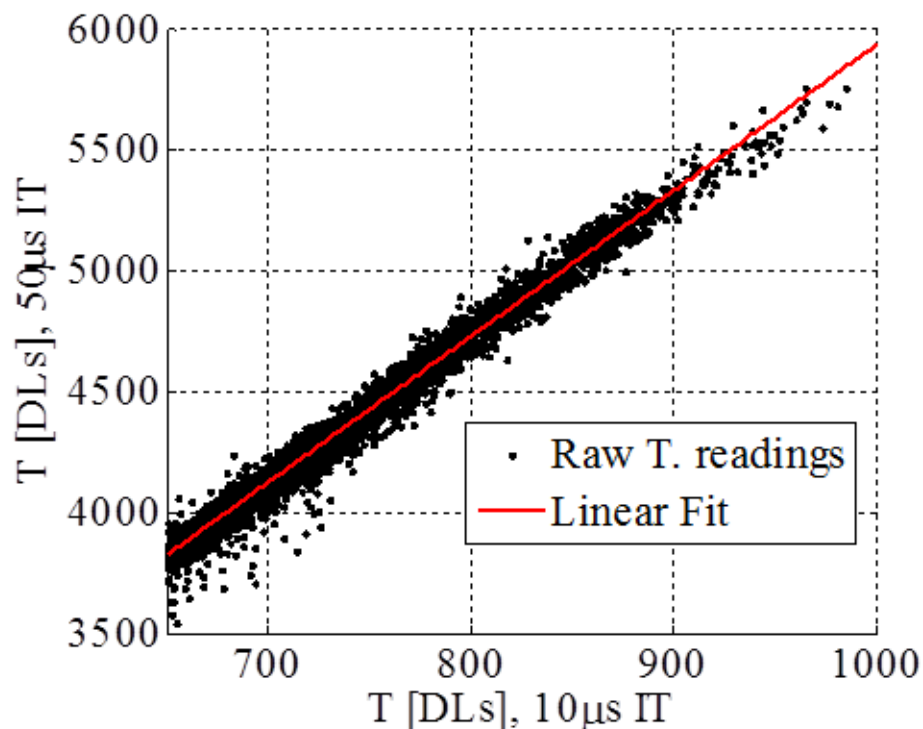


Figure 2.14: Temperature readings in Digital Levels (DLs) of the same scene for two different integration times ( $10\mu\text{s}$  and  $50\mu\text{s}$ ).

A linear fit is calculated for each scene, starting from the values detected on the heaters.

In order to reduce the impact of potential non-linearities of the analog to digital conversion, only the pixels corresponding to the heated endwall are considered, since they provide the highest well fill of the sensors and are the only ones of relevance in the frame. The fits are calculated with a 95% confidence bound.

The value stored in each pixel of each 10 $\mu$ s integration time thermogram is then rescaled based on the calculated fit. Now the direct comparison of the 10 $\mu$ s and 50 $\mu$ s integration time datasets is possible, particularly in the form of the pixel-by-pixel difference between the two and of its 2D discrete frequency spectrum, calculated according to the following discrete Fourier transform:

$$F(u,v) = \frac{1}{M \cdot N} \cdot \sum_{m=0}^{M-1} \sum_{n=0}^{N-1} I(m,n) \cdot e^{-i \cdot 2 \cdot \pi \cdot \left( \frac{u \cdot m}{M} + \frac{v \cdot n}{N} \right)} \quad (2.8)$$

Having indicated with  $I(m,n)$  the intensity of the  $M \times N$  pixel image,  $m$  and  $n$  go through all the pixels in the image  $I$ ,  $u$  and  $v$  being the wave numbers. The rescaling of the 10 $\mu$ s integration time frames amplifies artificially the raw signal and the noise, which is the main limiting factor in the accuracy of the temperature measurement at low integration times [92]. The ringing affecting the accuracy of the temperature readings in the 50 $\mu$ s integration time frames occurs at much lower spatial frequencies (10-15 pixels wavelength) than the noise degrading the accuracy of the 10 $\mu$ s integration time frames. It is therefore possible to apply a high-pass filter to the former – thus eliminating the contribution of ringing – while applying the complementary low-pass filter to the latter, to reduce the impact of noise. An image with the same dynamic range as the original can be obtained by summing the resulting frequency spectra and inverting the discrete Fourier Transform:

$$I(m,n) = \frac{1}{\sqrt{M \cdot N}} \cdot \sum_{u=0}^{M-1} \sum_{v=0}^{N-1} F(u,v) \cdot e^{i \cdot 2 \cdot \pi \cdot (\frac{u \cdot m}{M} + \frac{v \cdot n}{N})} \quad (2.9)$$

One parameter to be chosen is the size of the filter. This is done in the following section, where it is found that a filter size corresponding to 10% of the global signal power of the difference between the rescaled 10 $\mu$ s integration time frame and the deblurred 50 $\mu$ s integration time frame gives the minimum error compared to a sharp reference acquired with 50 $\mu$ s integration time.

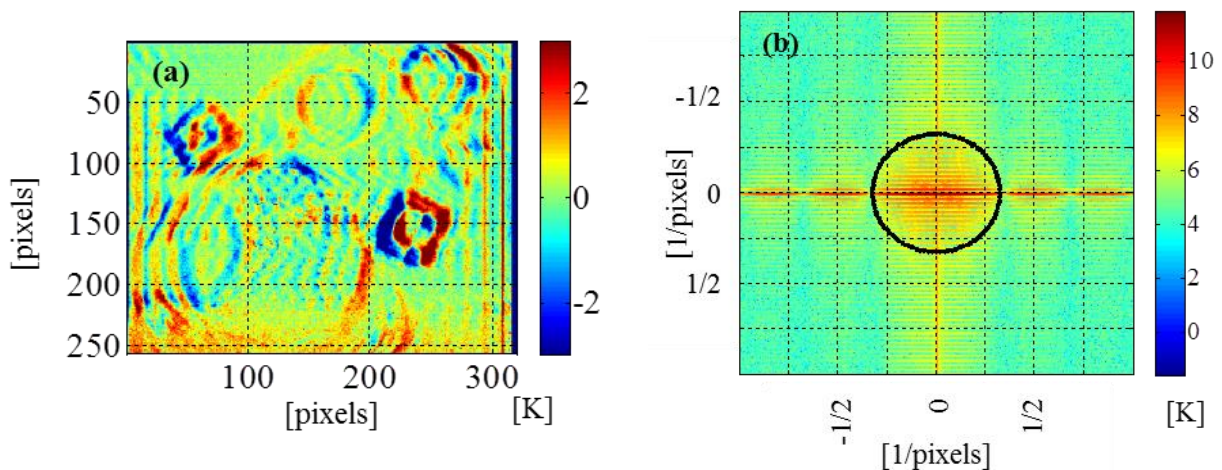


Figure 2.15: temperature differences between the rescaled 10 s integration time frame and the deblurred 50 $\mu$ s integration time frame. Fluctuations are in the order of  $\pm 1.5$   $^{\circ}$  C (a). 2D discrete frequency spectrum of figure (a). The black circle indicates the 10% power threshold used to identify the size of the frequency filter (b).

### Validation of the Image Restoration Procedure

The image restoration procedure is validated against test images taken with a still rotor. The images are acquired with the same optical setup and acquisition parameters as during the measurements, but the resulting images are naturally sharp with all integration times and, in particular, even with the 50 $\mu$ s integration time. The sharp 50 $\mu$ s integration time frame can therefore be taken as the reference against which to quantify the error in temperature reading introduced by the restoration procedure. First of all, an artificially blurred frame is created

from the reference by convolution with the blur kernel  $\mathbf{k}$  (see section above). The blind deconvolution algorithm is then applied to the artificially blurred frame for a variable number of iterations. A mean value of structure similarity index (**MSSIM**) is then calculated to quantify the resemblance of the deblurred frame to the original sharp reference. The structure similarity index (**SSIM**) is defined in [99] as:

$$\text{SSIM}(s, y'_n) = \frac{(2\mu_s\mu_{y'_n} + C_1)(2\sigma_{sy'_n} + C_2)}{(\mu_s^2 + \mu_{y'_n}^2 + C_1)(\sigma_s^2 + \sigma_{y'_n}^2 + C_2)} \quad (2.10)$$

In the previous equation,  $\mu_s$  and  $\mu_{y'_n}$  indicate respectively the mean intensity of the sharp image  $\mathbf{s}$  and of the output image of the R-L algorithm at the  $n$ -th iteration  $\mu_{y'_n}$ ,  $\mu_s$  and  $y'_n$  represent the contrast of the two images (estimated by means of their standard deviations);  $\sigma_{sy'_n}$  is the correlation of the two images. The constants  $C_1$  and  $C_2$  ensure the stability of the calculation and their value is determined based on the dynamic range of the image. The number of iterations  $n$  giving the maximum value of **MSSIM** is chosen for the processing of the measurement data. It is found that, for a repeated take of the same frame, the number of iterations maximizing the **MSSIM** varies of  $\pm 1$ , as it happens for the two different camera positions. The variation of **MSSIM** with the number of iterations of the deblurring algorithm is given in figure Figure 2.16.



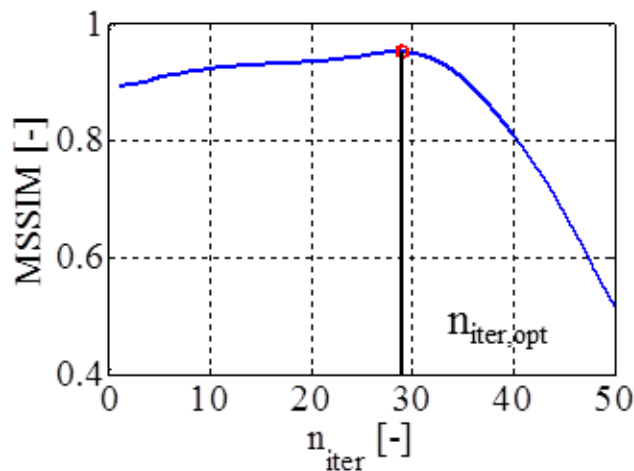


Figure 2.16: mean structure similarity index variability with number of iterations of the blind deconvolution algorithm for a typical frame. The maximum value is highlighted in red.

Once the number of iterations returning the maximum value of **MSSIM** is identified for both camera positions, the artificially blurred frame is deblurred by blind deconvolution. The  $10\mu\text{s}$  integration time frame is rescaled as explained earlier. Two complementary filters are applied to the deblurred  $50\mu\text{s}$  integration time frame and to the  $10\mu\text{s}$  integration time frame: respectively, a high-pass filter to the former and a low-pass filter to the latter. The cutoff frequency is varied in the range 0-256 pixels. The resulting spectra are summed and transformed back into an image by an inverse fast Fourier transform algorithm. The similarity of the resulting image to the reference frame is then assessed in terms of root mean squared error over the portion of the image containing the endwall information (Figure 2.17).

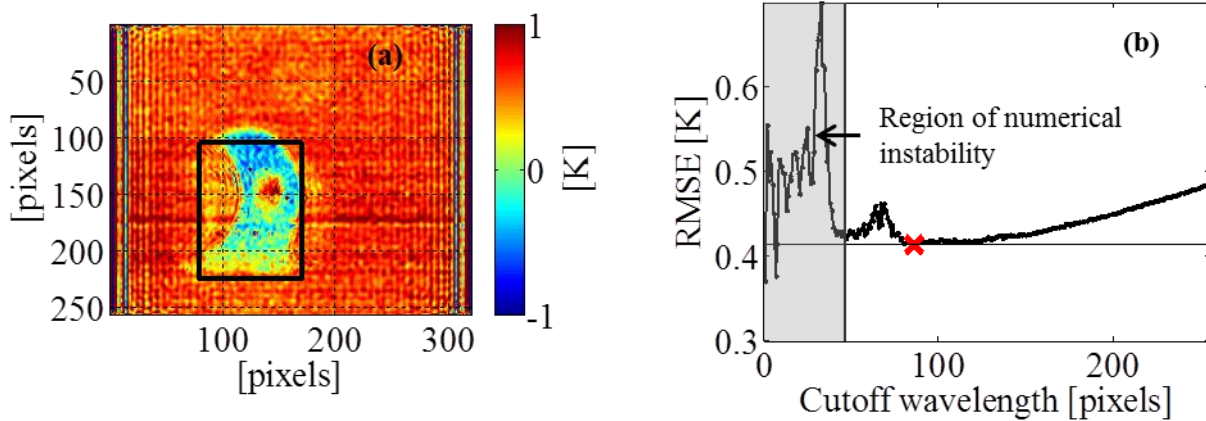


Figure 2.17: temperature difference between hybrid image and reference image with highlighted region of interest (a); root mean square error in temperature over the region of interest as a function of the filter cutoff wavelength. The minimum error (red cross), after a region of high instability of the result, is given by the filter size determined in Figure 2.15(b).

It is found that the filter size returning the minimum root mean squared error is the one containing 10% of the power of the spectrum of the difference between the deblurred 50 $\mu$ s integration time frame and the rescaled 10 $\mu$ s integration time frame. This filter is shown in Figure 2.15(b). The minimization of the root mean square error with respect to the 50 $\mu$ s integration time image of the still rotor is shown in Figure 2.17(b). For the uncertainty analysis, the error in the surface temperature is conservatively assumed to be  $\pm 0.46$ K, which is the highest obtained for all positions considered.

### Geometrical reconstruction of Images

The image reconstruction tools developed by Laveau [72, 100], based on the theory of projective geometry as described in [101] are adapted to the geometry of the rotor components. The reader is referred to these works for further details. Points of lower emissivity are drawn with silver ink on the black coating of the hub endwall, as a means of referencing the thermograms to the CAD model of the turbine. Digital pictures of the painted and marked PEEK platforms are acquired as geometrical reference. An algorithm compares the 3D coordinates of reference points extracted from a CAD model of the platform-jig assembly with the points of the 2D digital pictures selected by the user (Figure 2.18).

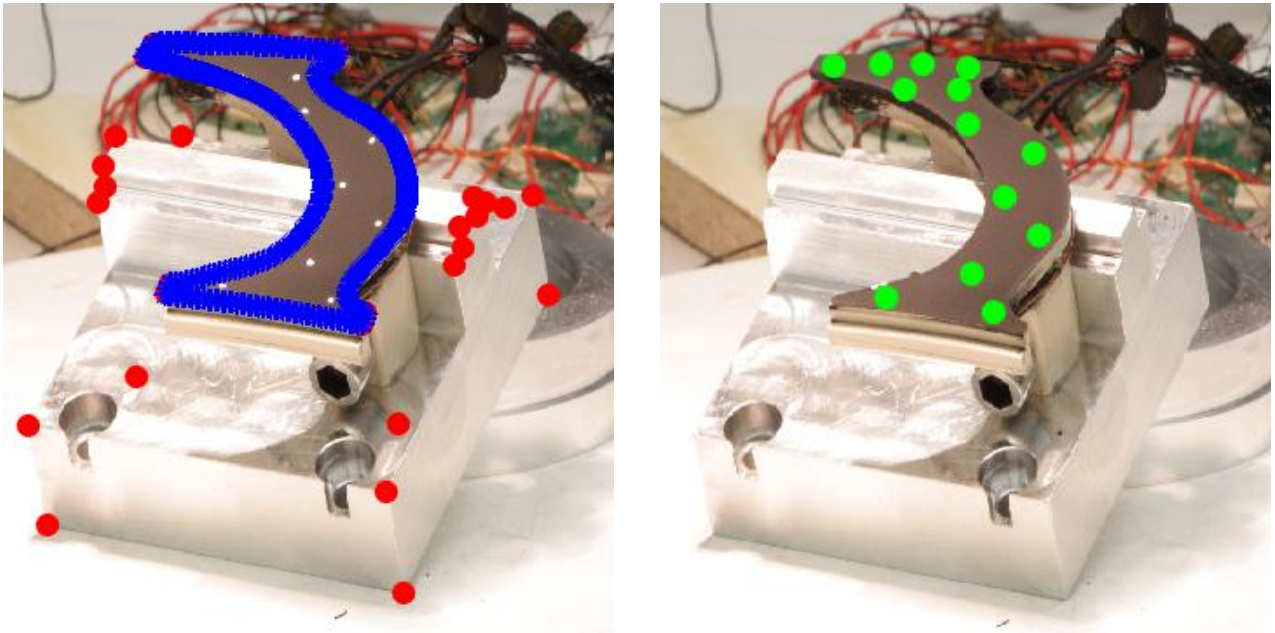


Figure 2.18: left, reference digital picture of the heat transfer platform with projected CAD points superimposed; Right, locations of infrared markers are highlighted in green.

A geometrical transformation is obtained and used to reconstruct the 3D coordinates of the IR markers in the CAD frame of reference.

The coordinates obtained are used to calculate the geometrical transformation relating the thermograms acquired during the measurements to the three-dimensional CAD model of the rotor hub endwall. The method has been shown to return an error in position within 0.3mm (Laveau [100]).

## 2.3 Heat Transfer Measurement Principle

### 2.3.1 Theoretical Background

The heat exchange between a surface and a fluid in motion grazing it can be expressed as the conductive heat transfer in the fluid slab adhering to the wall because of no-slip and impermeability boundary conditions:

$$\dot{q}''_{\text{conv}} = \kappa_{\text{fluid}} \frac{\partial T}{\partial n} \quad (2.11)$$

Where  $\kappa_{\text{fluid}}$  is the thermal conductivity of the fluid and  $\frac{\partial T}{\partial n} = \nabla T \cdot \hat{\mathbf{n}}$  is the component of the fluid temperature gradient locally normal to the surface. The convective heat flux  $\dot{q}''_{\text{conv}}$  is experimentally found to be proportional to the temperature difference between the wall and the local adiabatic wall temperature, the proportionality factor being the heat transfer coefficient  $h$ :

$$\dot{q}''_{\text{conv}} = h \cdot (T_w - T_{\text{aw}}) \quad (2.12)$$

The proposed definition, based on the adiabatic wall temperature, has the advantage of returning a value of heat transfer coefficient that is purely a function of fluid properties, geometry and flow field (Moffat [74]). The adiabatic wall temperature  $T_{\text{aw}}$  is defined as the temperature the wall would need to have in order to be in thermal equilibrium with the flow. Because of the practical difficulty of resolving with sufficient accuracy the temperature gradient at the wall, it is more convenient to exploit eq. 2.12 to determine experimentally the local heat transfer coefficient  $h$  and the adiabatic wall temperature  $T_{\text{aw}}$ , once the wall temperature  $T_w$  corresponding to a controlled value  $\dot{q}''_{\text{conv}}$  of convective heat flux is known. This can be achieved either by controlling the substrate temperature and deriving the corresponding, local convective heat flux, or by controlling the local heat flux directly. In both cases, the corresponding local wall temperature must be measured. Depending on which of the two approaches is chosen, the measurement technique is normally termed respectively iso-thermal or iso-energetic, relying under the assumption that the wall is either kept at a uniform temperature level, or that the heat flux provided to the flow is uniform over the surface. In the present study, the technique makes use of an experimentally de-

terminated distribution of wall heat flux produced by non-uniform Joule heating. On a point-wise basis, the approach reflects the one used in iso-energetic setups.

### Iso-Thermal Setups

As anticipated in the previous section, in iso-thermal setups the reference thermal boundary condition is provided by controlling the temperature of the bulk material constituting the component either by means of electrical coil heaters or by thermally controlled water flowing into the material. Some authors (Werschnik et al., [102]) refer to the technique as the “auxiliary wall method”, since an insulating layer covers the highly-conductive, isothermal substrate to ensure a detectable, flow-induced surface temperature difference. The setup is schematically illustrated in Figure 2.19. The calculation of the heat transfer quantities in this case starts from the following energy balance:

$$\dot{q}''_{\text{cond}} - \dot{q}''_{\text{rad}} = \dot{q}''_{\text{conv}} \quad (2.13)$$

In which, the different contributions on the left side can be quantified as follows:

$$\dot{q}''_{\text{cond}} = \frac{\kappa}{d} \cdot (T_w - T_{\text{sub}}) \quad (2.14)$$

$$\dot{q}''_{\text{rad}} = \varepsilon \cdot \sigma \cdot (T_w^4 - T_f^4) \quad (2.15)$$

Known the thermal properties of the substrate and the auxiliary wall (Kapton®, adhesive and high-emissivity coating) and measured the temperatures of the substrate, the wall and the total temperature of the flow, equations 2.14 and 2.15 can be solved.

By changing the solid temperature  $T_{\text{sub}}$  in steps and recording point-wise the convective heat flux  $\dot{q}''_{\text{conv}}$  and surface temperature  $T_w$  over the area of interest, it is possible to perform a linear fit to determine both local adiabatic wall tem-

perature (intercept with the  $0\text{W}/\text{m}^2$  axis) and the heat transfer coefficient (slope of the fit). The principle is equivalent as the one used in the iso-energetic setup described in the next section and is exemplified in Figure 2.20.

In the setup used in this work, the auxiliary wall is formed by patches of polyimide (Kapton® by DuPont™) and pressure-sensitive adhesive glued to a CNC-machined Aluminum stator segment. Kapton® is chosen for its high dimensional accuracy, which directly relates to the uncertainty in the final results (section 3.2.3 ).

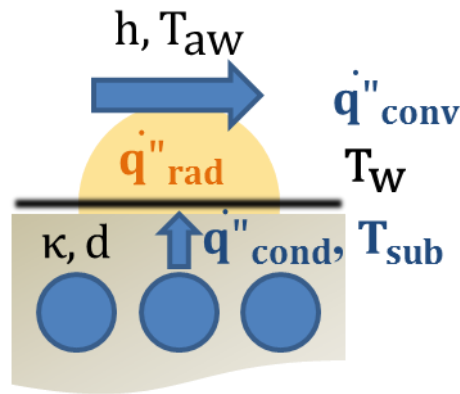


Figure 2.19: schematic of an iso-thermal setup. Thermally controlled water ensures the substrate is quasi iso-thermal. At steady state, the conductive heat flux from the substrate to the auxiliary Kapton® wall equals the sum of the radiative losses and the convective heat flux.

### Iso-Energetic Setups

In iso-energetic setups, rather than controlling the substrate's temperature, a prescribed wall heat flux is provided at the surface. The energy balance 2.13 is altered to account for the surface heat flux  $\dot{q}''_{\text{BC}}$  as in the following 2.16:

$$\dot{q}''_{\text{BC}} - \dot{q}''_{\text{cond}} - \dot{q}''_{\text{rad}} = \dot{q}''_{\text{conv}} \quad (2.16)$$

That is, the heat flux  $\dot{q}''_{\text{BC}}$  provided as a wall boundary condition by the experimental setup is balanced by the heat lost at the surface by convection  $\dot{q}''_{\text{conv}}$

and by radiation  $\dot{q}''_{\text{rad}}$  and the conductive losses through the solid  $\dot{q}''_{\text{cond}}$ . The balance is schematically illustrated in Figure 2.20.

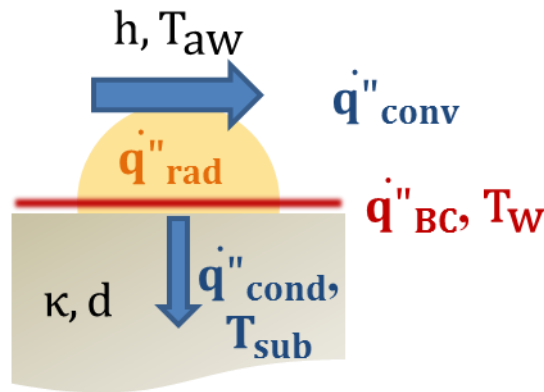


Figure 2.20: schematic of an iso-energetic setup. The wall provides a controlled heat flux  $\dot{q}''_{\text{BC}}$ , part of which is lost by conduction through the substrate or by radiation to the surrounding environment. The most part, however, is convected by the flow.

If the wall temperature  $T_w$  is measured (e. g. by means of an array of thermocouples, thermochromic liquid crystals or infrared thermography), the substrate temperature  $T_{\text{sub}}$  is also monitored (e. g. by means of PT100 RTDs) and the flow temperature  $T_f$  is known, conductive and radiative contributions can be estimated as follows:

$$\dot{q}''_{\text{cond}} = \frac{\kappa}{d} \cdot (T_w - T_{\text{sub}}) \quad (2.17)$$

$$\dot{q}''_{\text{rad}} = \varepsilon \cdot \sigma \cdot (T_w^4 - T_f^4) \quad (2.18)$$

In equation 2.17,  $\kappa$  is the thermal conductivity of the substrate and  $d$  is the depth within the substrate where the solid temperature is measured.

The heat flux  $\dot{q}''_{\text{BC}}$  is prescribed by the experimental setup (e. g. by means of electrical foil or film heaters) and is therefore to be considered known. Details on how the wall heat flux is experimentally determined point by point for the current study are given in chapter 4.54.5.

Finally, it is possible to compute the convective heat flux  $\dot{q}''_{\text{conv}}$  according to equation 2.16.

By changing the wall boundary condition in steps it is possible to measure multiple pairs of corresponding values of convective heat flux and wall temperature. A linear fit of wall temperature and convective heat flux can eventually be used to derive the heat transfer coefficient (the slope of the curve) and the adiabatic wall temperature (its intercept on the  $\dot{q}''_{\text{conv}}=0$   $\frac{\text{W}}{\text{m}^2}$  axis), as exemplified in Figure 2.20.

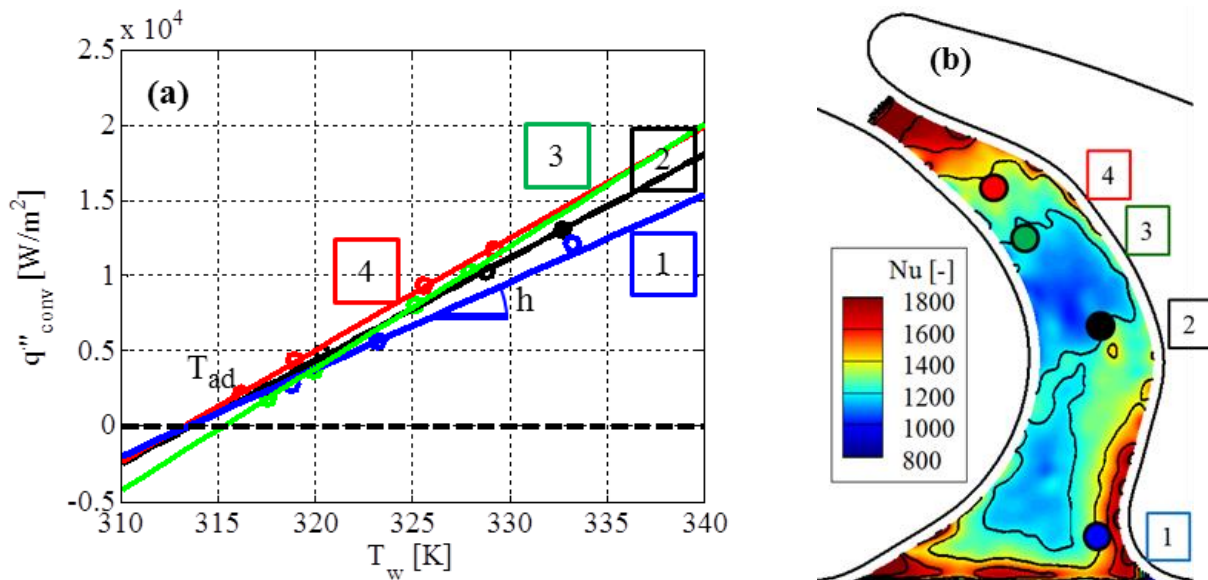


Figure 2.21: the linear fit procedure is illustrated for specific points in the passage, the heat transfer coefficient is given by the slope of the fit, while the adiabatic wall temperature by the intercept (a). Locations 1-4 of the passage for which the fit is performed are indicated in the distribution of Nusselt number at design point, IR0.8% (b).



# 3. Measurement Methodology for Heat Transfer Measurements on the Stationary Frame

The setup for the heat transfer measurements on the second stator endwalls of the axial turbine facility LISA (section 3.1) is an adaptation of the one designed and realized by Laveau and described in detail in his doctoral dissertation [100].

Minor modifications were necessary to integrate the heat transfer platform in the second stator instead of in the first one, mainly for different space constraints, thermal boundary conditions during operation and optical accessibility.

Additionally, a different approach for the application of Kapton® on the contoured endwall was used compared to the study of Laveau (section 3.2.3 ), with the goal to reduce the potential for detachment of the auxiliary wall from the substrate with the consequent alteration of the thermal properties of the multi-layer and degradation of the accuracy of the results.

## 3.1 The Rotating Axial Gas Turbine Research Facility LISA

The axial turbine research facility LISA of the Laboratory for Energy Conversion (LEC) at ETH Zürich is a long-duration, moderate-speed, low-temperature rotating facility. It consists of a quasi-closed air loop including a centrifugal compressor, a two-stage heat exchanger, a 3m-long flow conditioning stretch for flow uniformity upstream of the turbine, the turbine itself and a calibrated Venturi nozzle for mass flow measurements. The flow accelerates upstream of the turbine stage, thus reducing further the impact of any non-uniformities left after the conditioning stretch. The heat exchanger controls the turbine inlet total temperature  $T_{t,in}$  to an accuracy of  $\pm 0.3K$

A DC generator, coupled to the turbine shaft via a gearbox, acts as break by converting the mechanical power produced by the turbine into electrical power, which is fed back to the grid. The rotational speed is controlled with an accuracy of  $\pm 0.02\%$  ( $\pm 0.5$  rpm). A torque meter is installed on the vertical shaft between the turbine and the gearbox. At the exit of the test section, two successive rows of deswirl vanes recover the static pressure of the flow before its going through the venturi nozzle and back to the compressor. For more details on the rig the reader is referred to Schüpbach et al. [46]. A 1.5 stage, high work turbine configuration is installed in the test section of the facility. Both airfoils and endwalls have a complex 3D geometry optimized for minimizing the aerodynamic losses. The main characteristics of the blading are summarized in the following Table 3.1, while an illustration of the endwall contouring of the stator hub is shown in Figure 3.2.

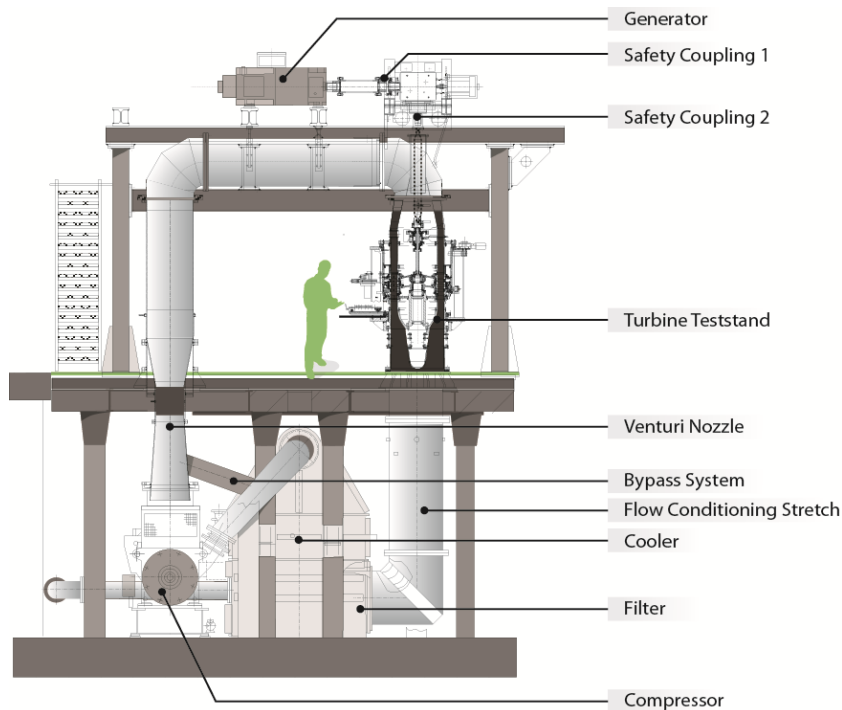


Figure 3.1: Schematic of the rotating axial turbine facility LISA, Laboratory for Energy Conversion, ETH Zurich.

Table 3.1: Geometrical Characteristics of the instrumented turbine configuration.

		NGVs	Rotor	Stator 2
Blade count	[-]	36	54	36
Aspect Ratio AR	[-]	0.89	1.21	0.83
Solidity	$\sigma$ [-]	1.23	1.35	1.32

The aggressive, non-axisymmetric endwall contouring designed for the management of the secondary flows poses challenges in the application of the polyimide insulating layer required by the iso-thermal setup.

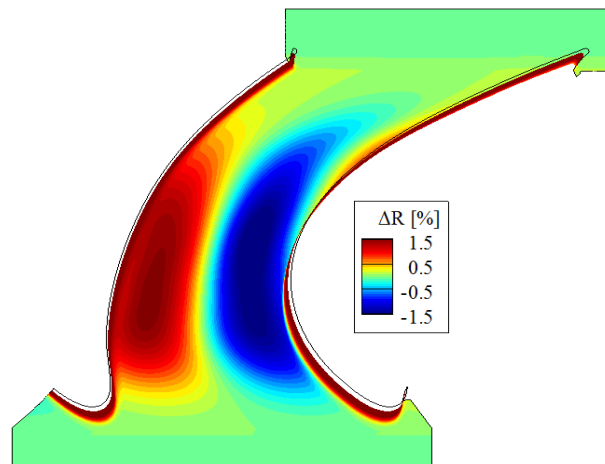


Figure 3.2: visualization of non-axisymmetric endwall contouring on the stator 2 in terms of % difference of nominal radius. The aerodynamically optimized shape is designed to reduce the strength of the secondary flows, but poses challenges in the application of the necessary insulating layer for the iso-thermal setup.

Air is spilled from the main air loop upstream of the flow conditioning stretch and fed to the stator/rotor cavity through the first stator vanes. The amount of by-pass flow “B” (see Figure 3.3) is measured via a standard Venturi nozzle. The purge flow mass flow rate is calculated as the difference between the total by-pass mass flow rate “B” and the secondary leakage flow following the path through the drum, labeled “S” in Figure 3.3, also measured by means of a Venturi nozzle. The injection ratio IR is then defined as:

$$IR = \frac{\dot{m}_B - \dot{m}_S}{\dot{m}_{MAIN}} \cdot 100 \quad (3.1)$$

where  $\dot{m}_S$  is measured by another standard nozzle. The error on the injection ratio IR is of  $\pm 0.01\%$ . A  $45^\circ$  chamfer on the rotor platform ensures that the purge flow presents an axial component of velocity, relevant for endwall cooling purposes (Paniagua [103]). Further details on the purge injection system are found in Regina et al [104] and Schädler et al. [53].

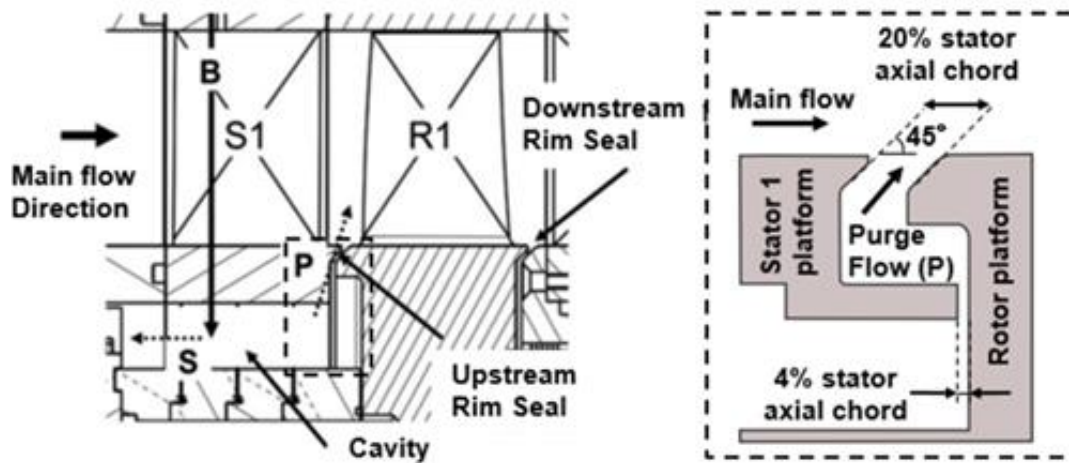


Figure 3.3: view from an axial plane of the purge flow path (left). Detail of the stator-rotor rim seal cavity (right) [105]

### 3.1.1 Similitude in LISA and Operating Conditions of the Rig

The turbine is operated at engine-representative corrected speed and mass flow rate. The matching of the corrected speed, given the low total inlet temperature of the rig, is ensured by a lower rotational speed and mass flow rate than in an actual engine. The main non-dimensional parameters of interest are summarized in Table 3.2 for both nominal and part-load operating conditions.

Table 3.2: operating conditions of the LISA facility during heat transfer measurements

	Design Point	Part Load
$T_{t,in}$	$(313.8 \pm 0.3)K$	$(317.2 \pm 0.3)K$
$\beta$	$1.65 \pm 0.4\%$	$1.33 \pm 0.4\%$
$\frac{\dot{m} \sqrt{T_{t,in}}}{p_{t,in} n}$	$151.3 \pm 0.1 \frac{kg \cdot \sqrt{K}}{s \cdot bar}$	
$\frac{n}{\sqrt{T_{t,in}}}$	$2.49 \pm 0.05 \frac{rps}{\sqrt{K}}$	$2.53 \pm 0.05 \frac{rps}{\sqrt{K}}$
$Re_{Cax} S1/R/S2$	710k/380k/510k	520k/310k/460k
$n$	$(2700 \pm 0.5)rpm$	$(2700 \pm 0.5)rpm$
$\dot{m}$	11.7kg/s	8.3kg/s
IR	$(0.0/0.8/1.2 \pm 0.01)\%$	$(0.0/0.8/1.2 \pm 0.01)\%$
$\psi$	2.3	1.9
$\phi$	0.56	0.48
$i$	$0^\circ$	$-12.3^\circ$

The two operating conditions lie at the extremes of the characteristic of the rig (see Figure 3.4) for a constant turbine speed of 2700rpm. The capabilities of the centrifugal compressor limit the achievable pressure ratio and mass flow rate.

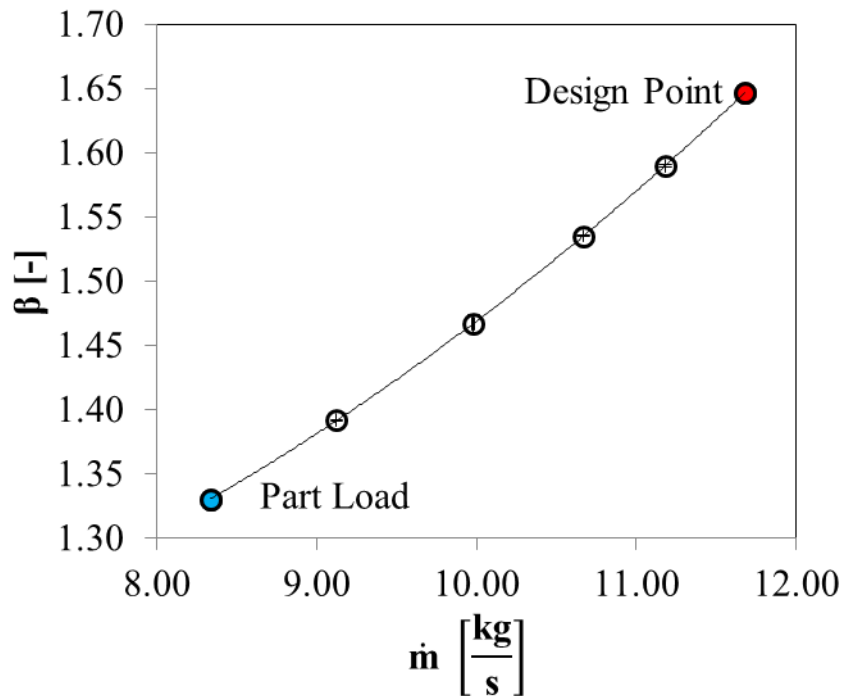


Figure 3.4: turbine characteristic at a constant rotational speed of 2700rpm. The two operating conditions, labeled as “Design Point” and “Part Load” are at the extremes of the measurable characteristic curve of the rig, limited by the compressor capabilities.

Compared to the design point, the off-design condition presents lower mass flow rate with identical rotational speed and total inlet temperature.

The rig does not allow the temperature ratio between the main flow and the rim seal leakage flow to match engine-representative values. The consequences of this on the aerodynamics of the purge flow are discussed in section 8.3.

## 3.2 Mechanical Integration of a Stator 2 Heat Transfer Platform

### 3.2.1 Design of the Stator 2 Heat Transfer Platform

The stator 2 heat transfer platform is to be fit in the region highlighted in Figure 3.5, with minimum alterations to the adjacent components to limit the complexity and the cost of the design.

In particular, the requirements can be summarized as follows:

- fit within the inner and outer radii and the axial extent of the adjacent stator 2 segments, so not to require modification of the surrounding support rings;
- 4 vanes width for quasi-periodicity of the thermal boundary condition at the region of interest: the central hub endwall (endwall and vanes adjacent to the measurement area also thermally managed);
- present thermal insulation on all surfaces in contact with thermally conductive materials (minimum thickness  $\sim 4\text{mm}$ );
- be manufactured in highly conductive material (Aluminum) to grant thermal uniformity of the bulk;
- a minimum wall thickness at all locations of no less than  $0.8\text{mm}$  (a stringent requirement for the design of the internal water channels);
- water tightness to avoid corrosion and damage of the surrounding components of the facility and embedded instrumentation (PT100 RTDs).

A schematic of the modified test section is provided by the axial cut of Figure 3.5.

Essentially, minor modifications of the two downstream rings and one upstream ring are put in place to fit the required thickness of the thermal insulation. Additionally, an opening is cut into the supporting ring at the outer diameter to allow optical accessibility to the endwall and water feed-through.

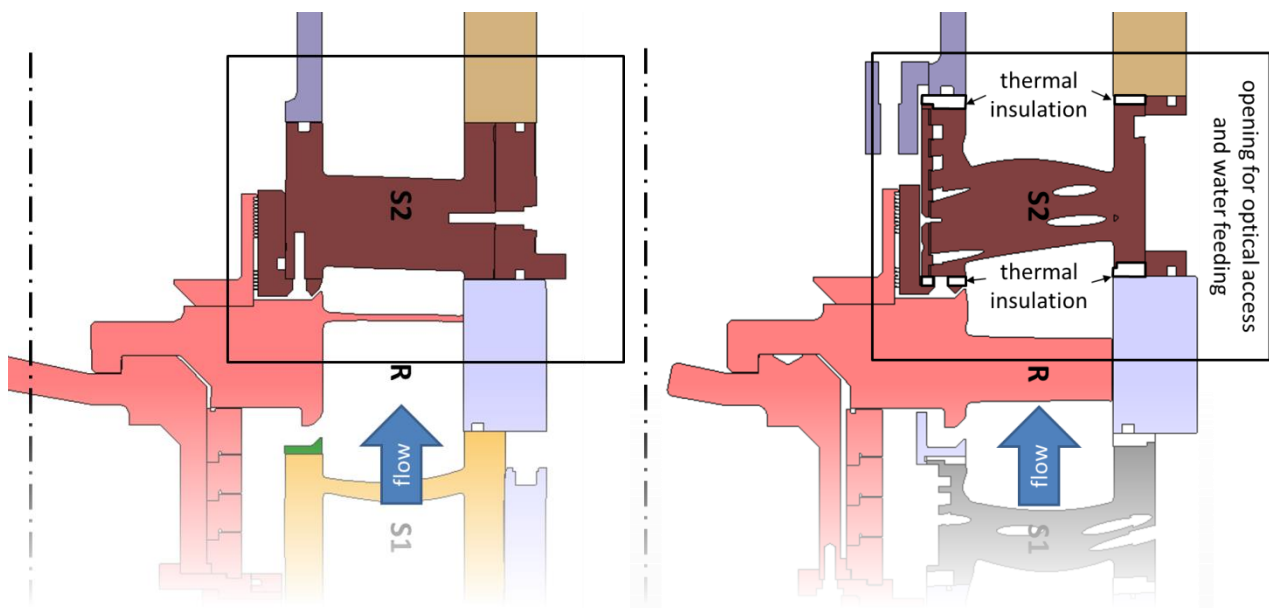


Figure 3.5: modification of the surrounding components to fit the thermally managed stator 2 platform are highlighted in the schematic on the left, compared to a reference case on the right.

## Thermal Design

The complex geometry of the stator segment with three-dimensional blading and non-axisymmetric endwall contouring (Figure 3.2) implies heavy reliance of the thermal design on Finite Elements Analyses.

At first, simplified two-dimensional models of the hub platform and airfoils are studied to evaluate size and position of the water channels supplying the thermally controlled water.

The 2D model of the hub endwall includes:

- an axial section of the contoured endwall extracted from the CAD of the part to have representative thickness variations of the substrate material (Aluminum);
- the upstream insulating ring in POM-C;



- the steel support ring holding the heat transfer platform and the adjacent stator 2 segments;
- six water channels.

The channels, originally square in cross-section, are modified on the top and bottom surfaces to keep a constant depth with reference to the endwall, despite its aggressive contouring.

The meshed model is illustrated in Figure 3.6. The triangular unstructured mesh is automatically generated and refined in the Partial Differential Equation solver of MATLAB (PDETool) and consists of 27'055 nodes.

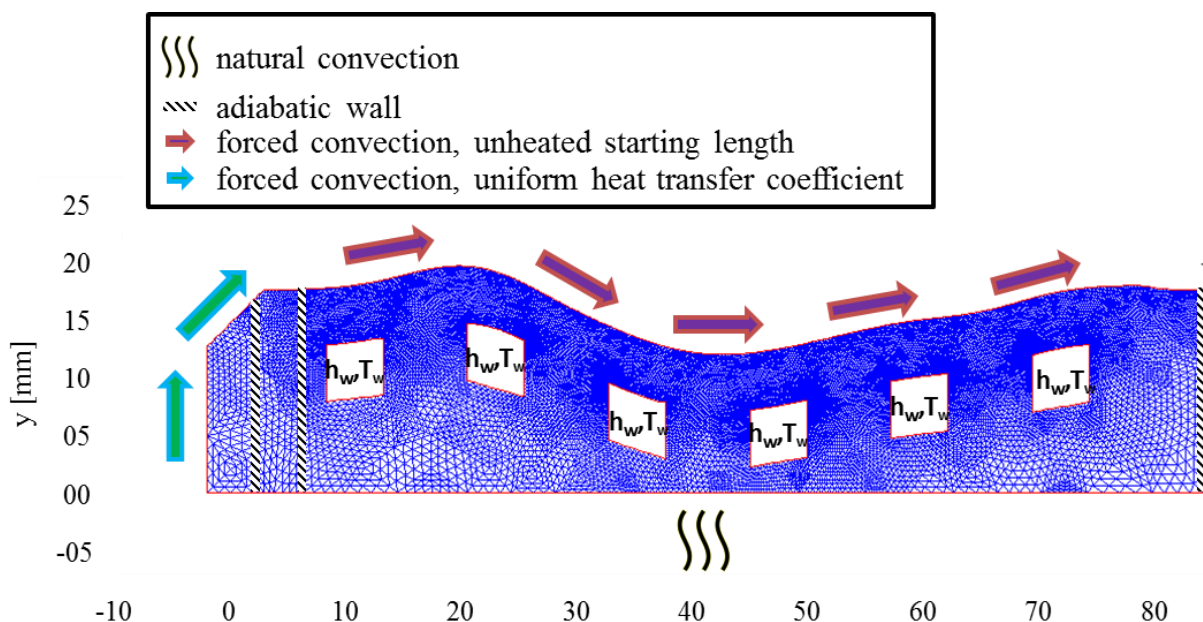


Figure 3.6: simulation domain used in the PDETool of MATLAB with the thermal boundary conditions highlighted. A triangular, unstructured mesh of 27055 nodes is automatically generated.

The thermal boundary conditions are all of Neumann's type (the value of the second derivative, i. e. the heat flux at the wall is imposed) and based on experimental values and 1D correlations.

In particular, the convective heat flux over the endwall is derived from the correlation for a constant free-stream velocity flow along a semi-infinite plate with constant surface temperature (Kays et al. [106]):

$$\text{St} \cdot \text{Pr}^{0.4} = 0.0287 \cdot \text{Re}_x^{0.2} \quad (3.2)$$

A heat transfer coefficient for the water channel is estimated based on their hydraulic diameter, the head provided by the circulating pump of the water loop and the pressure loss along the feeding lines. The resulting value is of  $\sim 10 \text{ kW/m}^2\text{K}$ . Their depth is changed at each simulation to evaluate whether thermal disuniformities are observable on the surface due to their presence.

The results for two cases are shown in Figure 3.8, one for a depth of the water channel of 2mm, the second one for a depth of 5mm.

The temperature profile clearly shows oscillations due to the water channels being too close to the surface when a depth of 2mm is set. On the contrary, no oscillations in the temperature profile can be seen if a 5mm depth is chosen (see Figure 3.8).

Also, no significant improvement in the temperature drop at the leading edge of the platform is brought by channels closer to the surface. A depth of 5mm is therefore chosen for the final design.

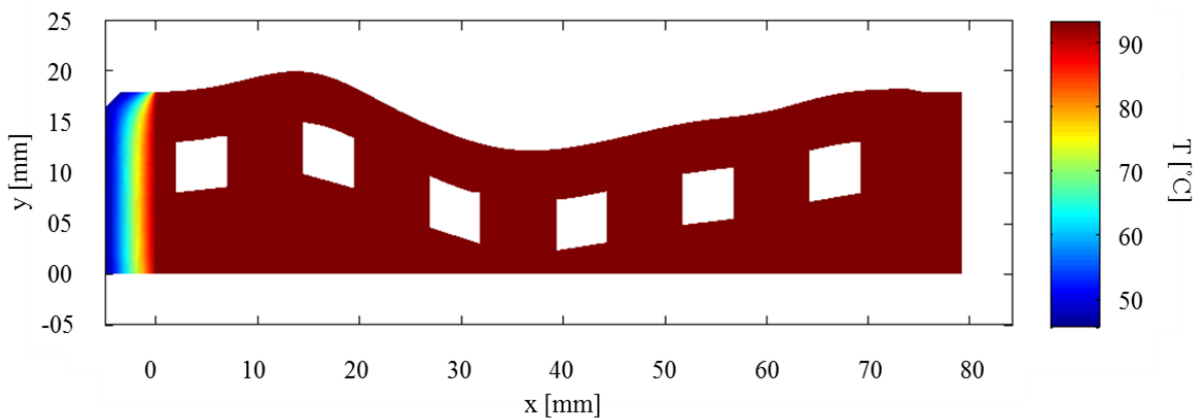


Figure 3.7: temperature distribution for water channels 5mm below the endwall. Temperature uniformity within the bulk of the material is satisfactory (less than  $\pm 0.5^\circ \text{C}$ )

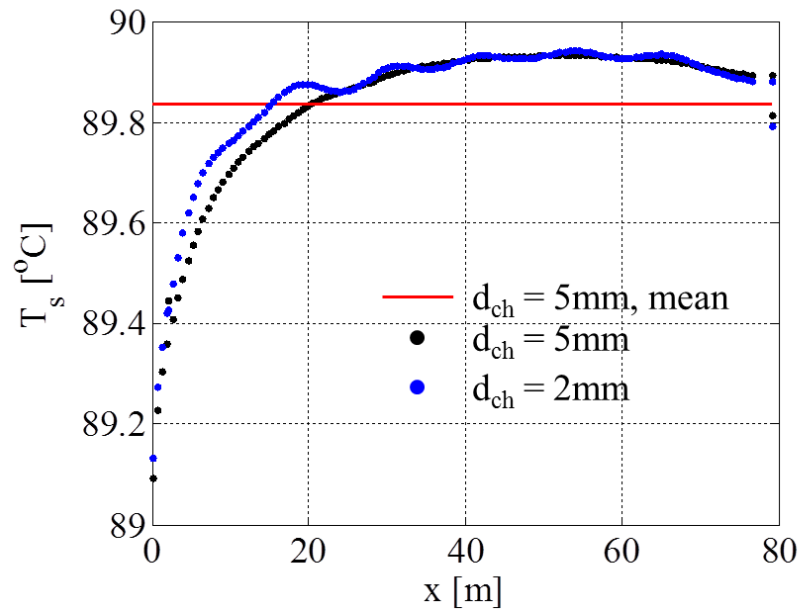


Figure 3.8: when comparing the results of the FEM analysis for water channels 5mm deep (black) or 2mm deep (blue), it is evident that the latter case produces undesired surface temperature oscillations. Due to the higher heat transfer at the leading edge of the platform, a drop in surface temperature is observed in this area.

Similarly, an optimization is run for three different spanwise locations in the vanes to choose the position of the water channels providing the highest temperature uniformity at the surface of the airfoil.

Sections are extracted at 10, 50 and 90% of the span. The resulting channel positions define their path within the vane and are respected during the mechanical design of the heat transfer platform unless manufacturing reasons require adjustments.

The target function of the optimization is the difference in surface temperature between pressure side and suction side. The maximum temperature differences are recorded at  $s = 5\text{mm}$  and  $s = 25\text{mm}$  and correspond to  $0.4^\circ\text{C}$ . However, on average the difference is less than  $0.15^\circ\text{C}$ .

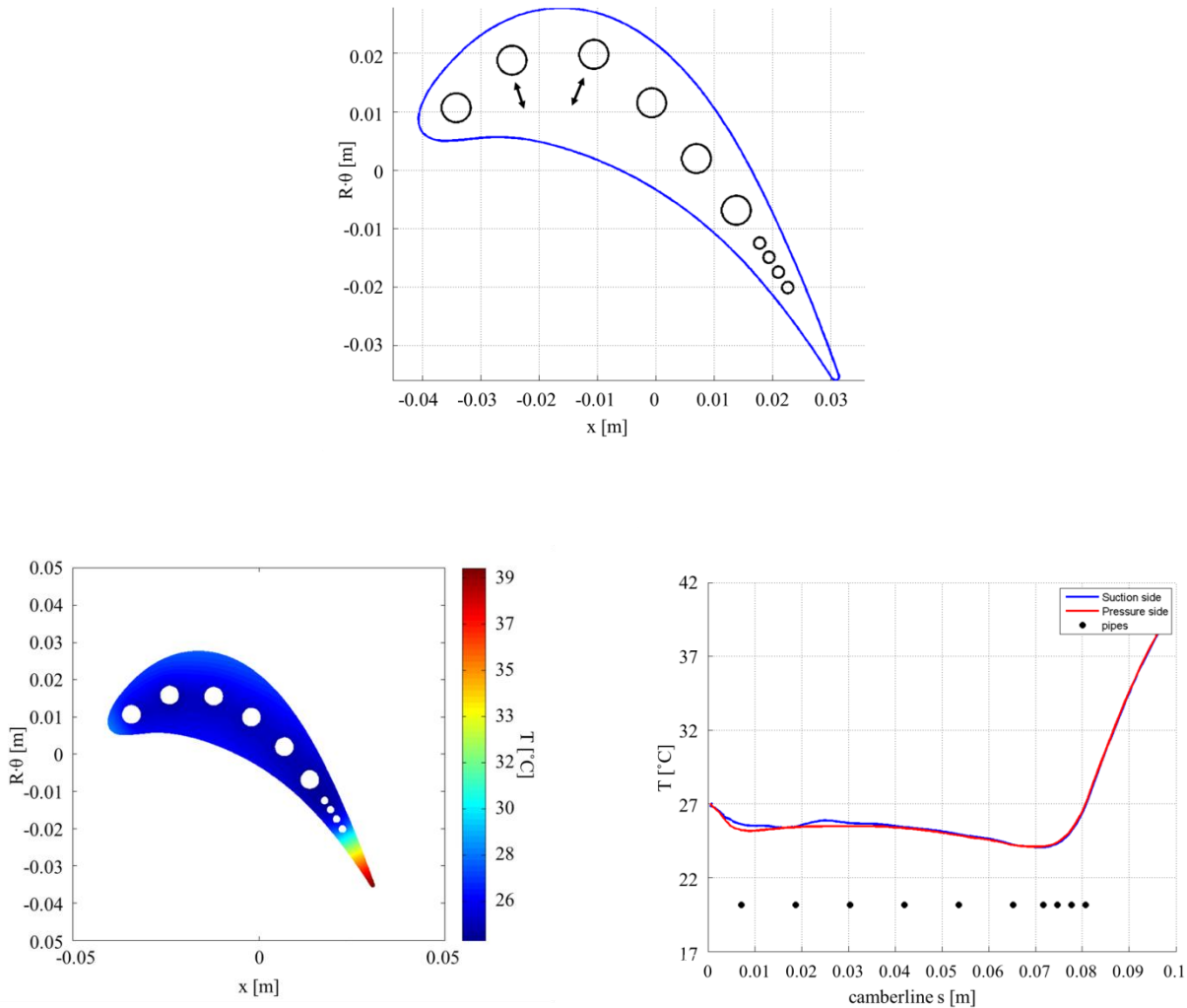


Figure 3.9: the positions of the tubes are iteratively modified (top), the temperature field within the vane's section is evaluated in the Partial Differential Equation solver of MATLAB (bottom left) with the target of minimizing the temperature difference between suction and pressure side (bottom right).

The thermal boundary conditions for the 2D vane simulations are derived from a steady state CFD simulation performed in ANSYS CFX with a triangular mesh of 65'127 nodes and 126'688 elements.

### Mechanical Design

Manufacturability issues must be addressed when designing the 3D component according to the specifications defined by the preliminary 2D simulations (see previous section).

First of all, the swept, bowed and leaned shape of the vanes prevent from drilling straight channels in a single operation from tip to hub. It is therefore necessary to grant access to the drilling machine from both sides of the work piece and at customizable angles, in order to drill “V-shaped” circular water channels in the vanes. The minimum wall thickness of 0.8mm is required for mechanical integrity and machining tolerance reasons.

This poses an additional challenge: that to seal the hub side of the vane channels after drilling (Figure 3.11a)). The central vanes are, in fact, separately controlled and no communication should be there between the hub water channels and the mid-vane channels, as clarified by the schematic in Figure 3.10 (Laveau, [100]).

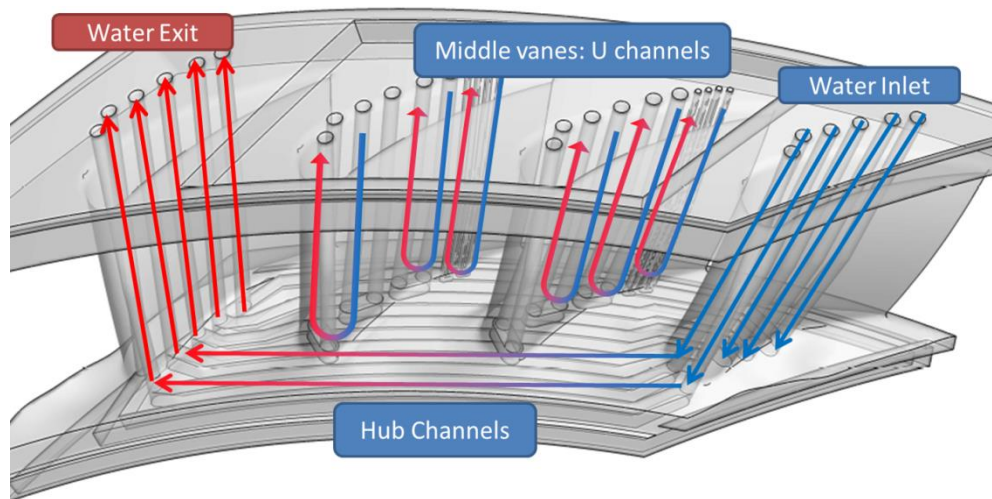


Figure 3.10: schematic of the desired water flow in the stator heat transfer platform (Laveau [100]). The channels in the middle vanes do not communicate with the hub channels.

The insertion of aluminum plugs into the hub is required, followed by laser welding of the parts (Figure 3.11b)).



The plugs, however, can only be put in place if no separation is present between the 6 hub channels. These separations are necessary for adjusting the flow rate of the individual channels according to the temperature field. Therefore, 5 additional aluminum parts are manufactured, again to be laser welded in the hub to define the side surfaces of the channels (Figure 3.11c) and d)).

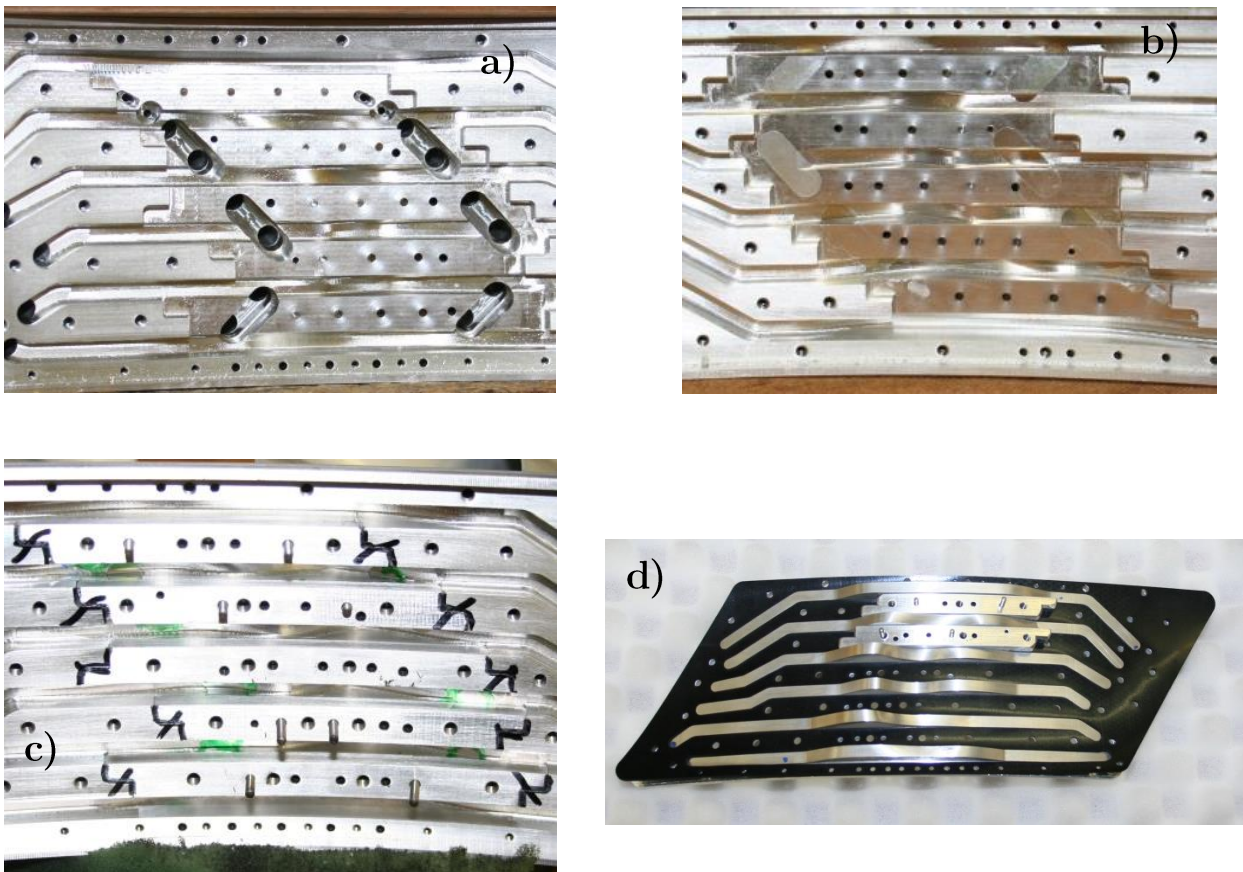


Figure 3.11: steps in the assembly of the hub section of the stator 2 heat transfer platform.  
 a) the inner part of the hub seen from the inner radius. Separations between channels are absent to allow the insertion of the sealing plugs in the channels of the middle vanes;

b) the plugs are inserted to seal the channels of the middle vanes;

c) the separations restore the side-walls of the hub channels;

d) the aluminum cover with the sealing rubber gasket can be put in place. Notice the contoured bottom walls of the hub channels carried by the cover.

Laser welding is also used to seal the tubes and flanges connecting the channels to the water distributor (Figure 3.12).

In total, the complete assembly of the stator 2 segment consists of 58 parts, excluding the sensors and sensor housings.

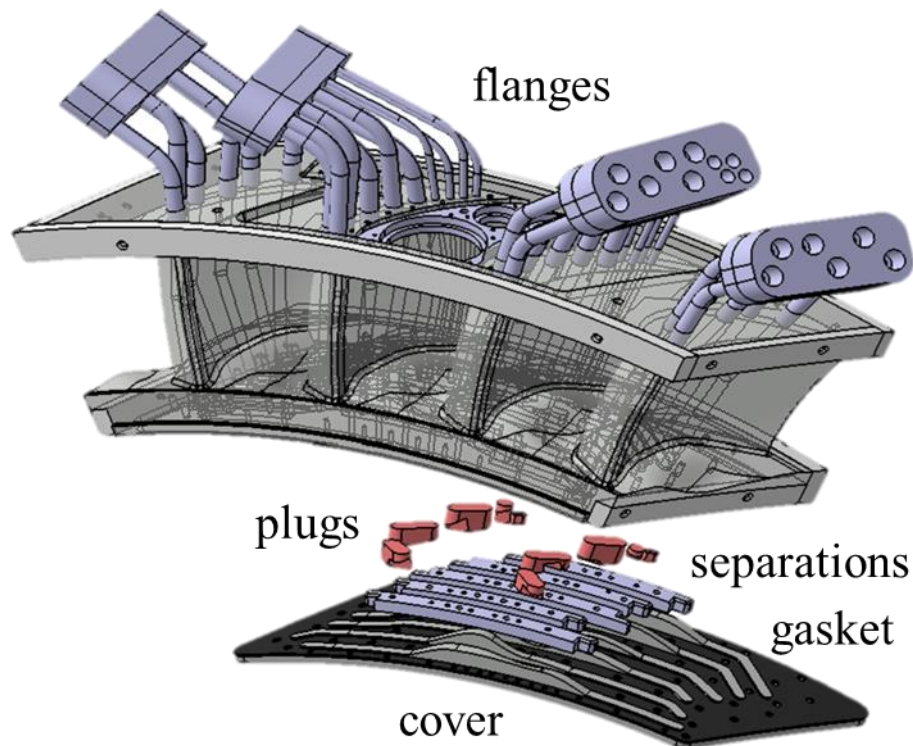


Figure 3.12: exploded view of the 3D stator 2 heat transfer platform CAD model. 58 components, excluding instrumentation, compose the assembly.

### 3.2.2 Instrumentation

The stator 2 heat transfer platform is completed by the installation of more than 30 PT100 RTDs to monitor the temperature of the Aluminum solid. Most of the sensors (22) are housed in the hub, between the water channels, in order to resolve the temperature field directly below the measurement area.

As such, these temperature transducers require special protection from water infiltrations and are therefore glued to a protective steel shaft, leaving only the sensing element exposed, but still protected by a film of glue.

All the sensing elements in the hub are placed 1mm below the endwall surface. Their calibration is performed after installation in the segment in the calibration oven of LEC. Further details can be found in section 5.1.4 .

### 3.2.3 Insulating Layer and High-Emissivity Coating

The iso-thermal setup requires an insulating layer over the highly-conductive Aluminum substrate: the “auxiliary wall”. The purpose of this layer is to preserve the uniformity of the bulk temperature when the part is exposed to the flow; reduce the convective heat loss; maximize the thermal gradients on the endwall surface, thus allowing for a more accurate resolution of the convective heat transfer patterns.

Moreover, the uncertainty on the thermal properties of this layer directly reflects on the uncertainty on the final results.

For this reason, commercial grade polyimide (Kapton® by DuPont™) is chosen, for the accurate thickness control during its production process ( $\sim 7\%$ ). The polyimide sheet is laminated on the thinnest commercially available pressure sensitive adhesive (3M 467MP,  $50\mu\text{m}$ ) in order to minimize the relative contribution of the adhesive thickness uncertainty ( $\sim 20\%$ ) to the overall uncertainty.

Because of the highly three-dimensional shape of the flow path, the sheet is cut in several patches to approximate as closely as possible the non-developable geometry.

In particular, in order to reduce the risk of air entrainment between the polyimide/adhesive layer and the metal especially in the measurement area (Laveau [38]), the layer is glued in adjacent stripes disposed crosswise to the flow.

The approach is successful in approximating better the endwall surface, characterized by an aggressive, non-axisymmetric endwall contouring. However, the varying thermal properties of the layer in proximity of the edges will affect the quality of the data. For this reason, an area of 1mm of width around the cuts is blanked (chapter 6).



Because the whole surface is covered in the rough Nextel Velvet coating for emissivity reasons, the cuts do not affect the development of the boundary layer. They are, in fact hidden by the roughness elements of the coating ( $R_a = 8.3\mu\text{m}$ ,  $R_z = 59.5\mu\text{m}$ ), as shown in Figure 3.13.

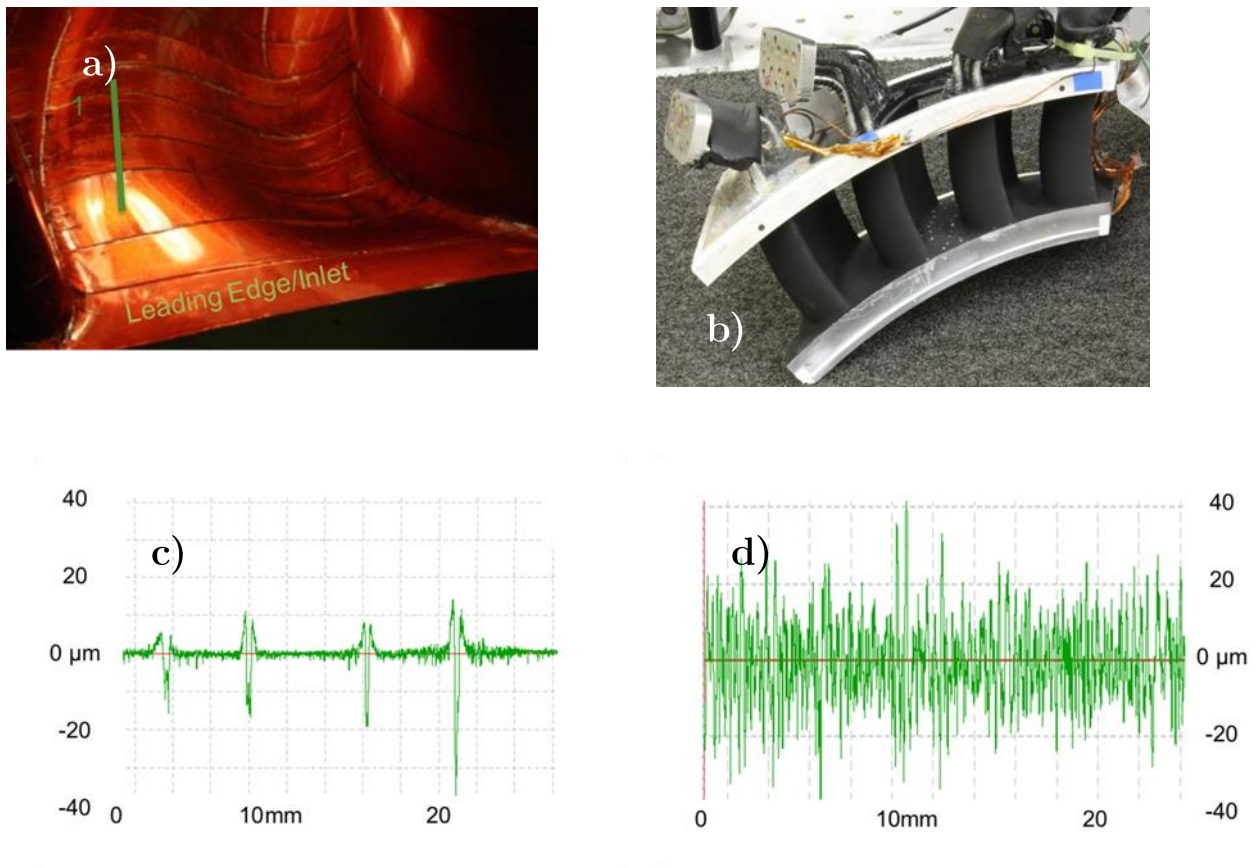


Figure 3.13: detail of the hub endwall covered in polyimide patches; b) the fully assembled and coated stator 2 heat transfer segment; c) and d) surface roughness before and after coating the polyimide with high-emissivity paint. The cuts in the polyimide, visible before, are completely hidden by the paint d).

### 3.3 Thermal Management of the Heat Transfer Platform

The heat transfer platform is connected to a water loop including a centrifugal pump, two water/water heat exchangers and a water distributor separating the main flow in 16 different sub-loops, each monitored for pressure, temperature and flow rate. The flow rate of each channel can be adjusted individually by means of a manual valve in order to maximize the temperature uniformity in the solid during operation. The 22 PT100 sensors embedded 1mm below the endwall are read in real time during the experiments. It is therefore possible to observe the effect of the change in flow rate through one or more channels on the end-wall temperature distribution.

The system also includes fast-acting electronic valves to bypass the stator 2 in case of necessity and two manual valves to evacuate the distributor.

The system is schematically illustrated in Figure 3.14 (Laveau [100]).

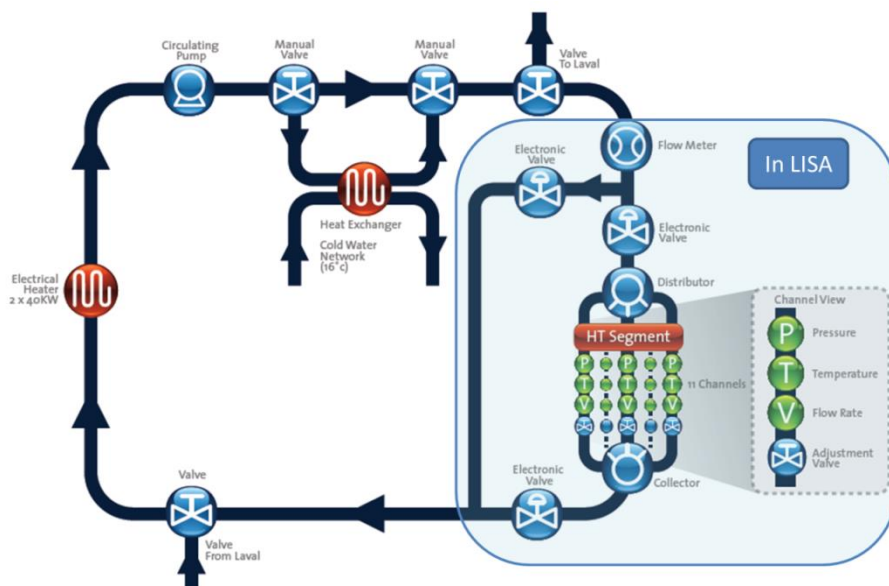


Figure 3.14: schematic of the water network providing thermally controlled water to the stator 2 heat transfer segment as shown in Laveau [100].

## 3.4 Traversing System

Due to the limited optical accessibility of the endwall through the stator casing, the acquisition of multiple views is necessary to reconstruct the whole temperature distribution on the measurement area.

For this purpose, a 6 degree-of-freedom robot arm by Stäubli (RX-60) is used to traverse the camera through 48, CAD-defined positions covering the whole end-wall surface and aiming the InfraTec VarioCam IR camera at the endwall through the different windows. The robot has a repeatability of 0.015mm.

The coverage of the surface of interest is first checked in the CAD model itself and then verified by testing the traversing the camera in the facility and processing the preliminary test-images.

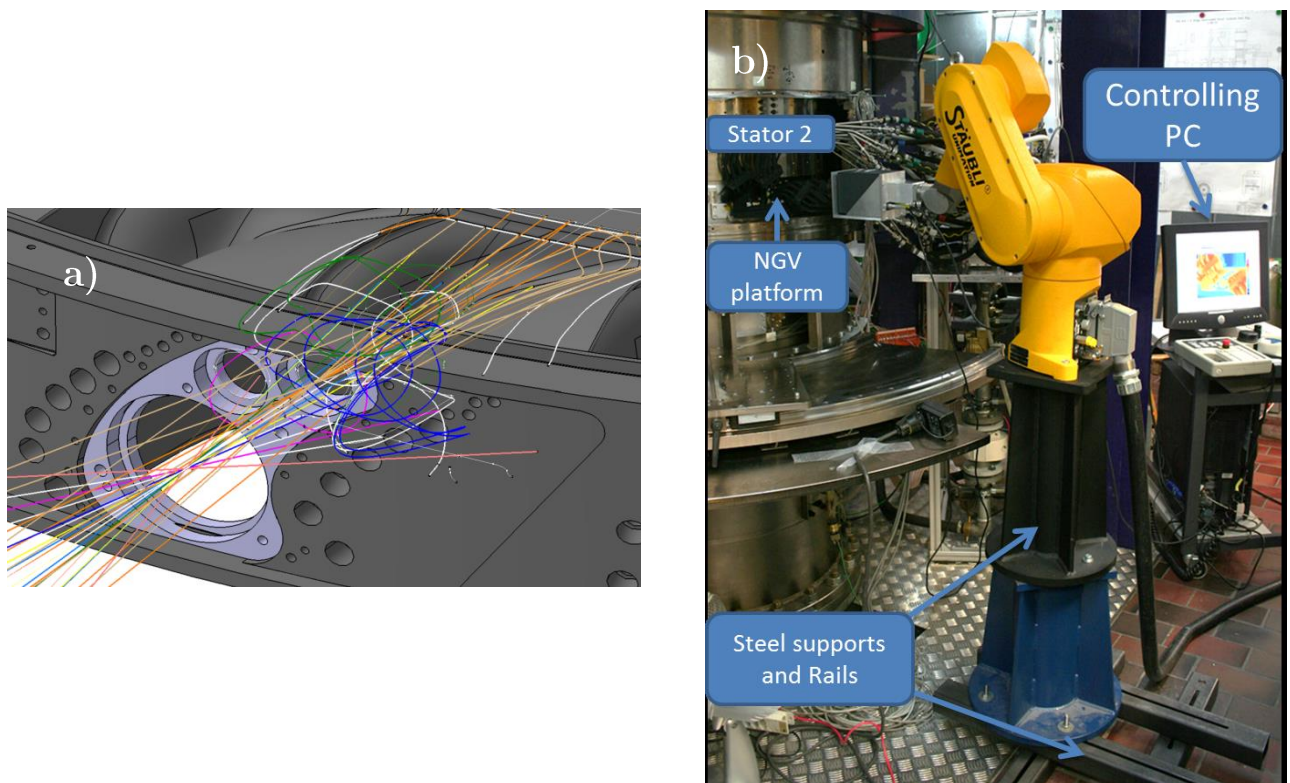


Figure 3.15: a) ray tracing in CATIA V5 and projected window contours on the endwall. The coverage of the measurement area is thus assessed prior to assembly; b) view of the complete setup in the facility as portrayed by Laveau [100].

The coordinates characterizing each position are stored in a table with six values per row and a number of rows equal to the number of camera positions needed.

Three of the six values give the camera center in the CAD reference system, while the remaining three correspond to the end vertex of the unitary vector starting from the camera center and pointing towards the endwall. A Matlab program, based on J-Y Bouguet's code [107] is able to calculate a transformation matrix between the CAD reference system and the Robot's reference system, after an in-situ spatial calibration procedure of the robot-camera system is performed.

### 3.4.1 In-Situ Camera Calibration

After the robot is placed in the facility and screwed firmly to the floor, a reference heated target with infrared markers is mounted to the stator casing.

The target consists of a square piece of Aluminum, precisely fixed to the stator casing with reference pins and bolts. The surface of the target is coated with high-emissivity paint and a square pattern of dots 10mm apart is CNC machined on the surface, covering an area of  $200 \times 200 \text{mm}^2$  (see Figure 3.16).

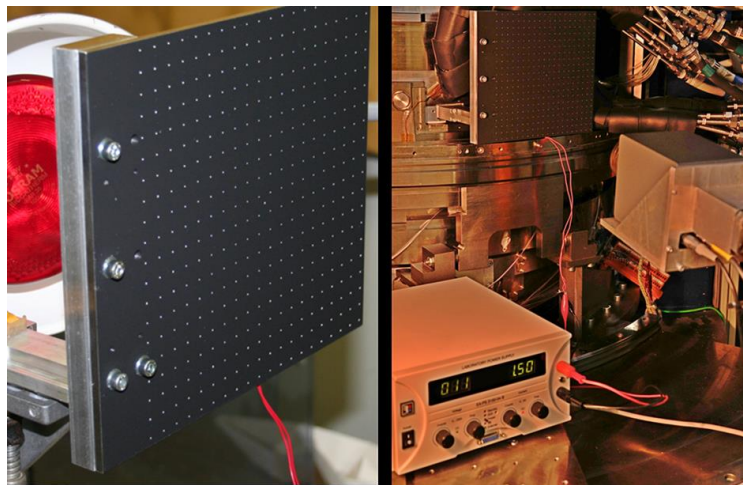


Figure 3.16: the infrared reference target before (left) and after (right) assembly in the LISA facility.

The position of the target and the location of the markers are known in the CAD model. The location of each marker in the IR images acquired by the robot is cross-referenced to its set of coordinates in the CAD model and to the 6 coordinates returned by the robot's controller.

The procedure is repeated twice: a first time, a coarse set of pictures at about 10 different robot positions are taken. A second time, an automatically generated set of robot/camera positions is provided by the script, resulting in a more accurate calculation of the transformation matrix.

## 3.5 Measurement Procedure

Data collection requires the thermal steady state to be reached both at a turbine level (total inlet temperature stationary within  $\pm 0.3$  °C) and at a platform level (steady bulk temperature). The procedure is therefore structured as follows: the turbine is started with a cold stator 2 heat transfer platform. Once the temperatures of the main flow and the inlet and outlet cavities have reached steady state, the first set point is input to the water temperature controller. 35-40 minutes are necessary for the bulk temperature of the stator 2 heat transfer platform to stabilize. After this time, it is possible to start the image acquisition for this set point. The water and solid temperatures (all of the 43 embedded RTDs), the water flow rate, the temperature of the water plenum of the distributor and the pressure of the feeding lines are constantly monitored. The Stäubli RX60 robot arm automatically goes through a set of 48 positions designed and tested to cover the complete endwall surface. After having reached each position, the controller of the robot sends a signal to the computer to start the IR camera and acquire 50 thermograms with a frame rate of 50frps. Once the sequence of images is completed, the camera confirms the successful acquisition and triggers the computer to move the robot arm to the following position. The whole image acquisition requires about 15minutes. Overall, including the waiting time for steady state, each water temperature step requires about 1 hour to complete.

A total of 26'400 infrared images are acquired and averaged per test case.





# 4. Measurement Methodology for Heat Transfer Measurements on the Rotating Frame

The instrumentation specific to the heat transfer measurements can be classified into stationary and rotating.

The stationary instrumentation consists of a fast infrared camera mounted on a traversing system, the power supply units to the rotating instrumentation, the power monitoring system and a data acquisition computer. Optical access to the rotor endwall is granted by three Zinc-Selenide (ZnSe) windows mounted in the rotor casing. More views of the hub can be acquired by traversing the camera so to cover a wider portion of the endwall surface. Details on the infrared camera are provided in section 2.1.5 .

The instrumentation mounted on the rotor includes a 2-channel slip ring for power transmission, a set of 9 Wi-Fi data acquisition boards and a special hub platform insert carrying a film heater and 9 embedded PT100 RTDs. A schematic of the complete setup is provided in Figure 4.1.

The facility LISA has been described in section 3.1, while the main parameters describing the operating conditions investigated during the measurements are summarized in Table 3.2.

The facility is set up for heat transfer measurements on the rotor by adapting the infrared-based technique used by Laveau et al. [72] for stationary parts. In particular, an optical access was obtained through the rotor casing and a heat transfer platform was inserted between the rotor blades, as schematically indicated in Figure 4.1. The blading for the rotor heat transfer campaign is newly optimized for efficiency and includes non-axisymmetric endwall contouring (Figure 4.2). The variations in radius being contained within  $\pm 0.3\%$  of the nominal cylindrical radius at the hub, the profiling can be considered as mild.

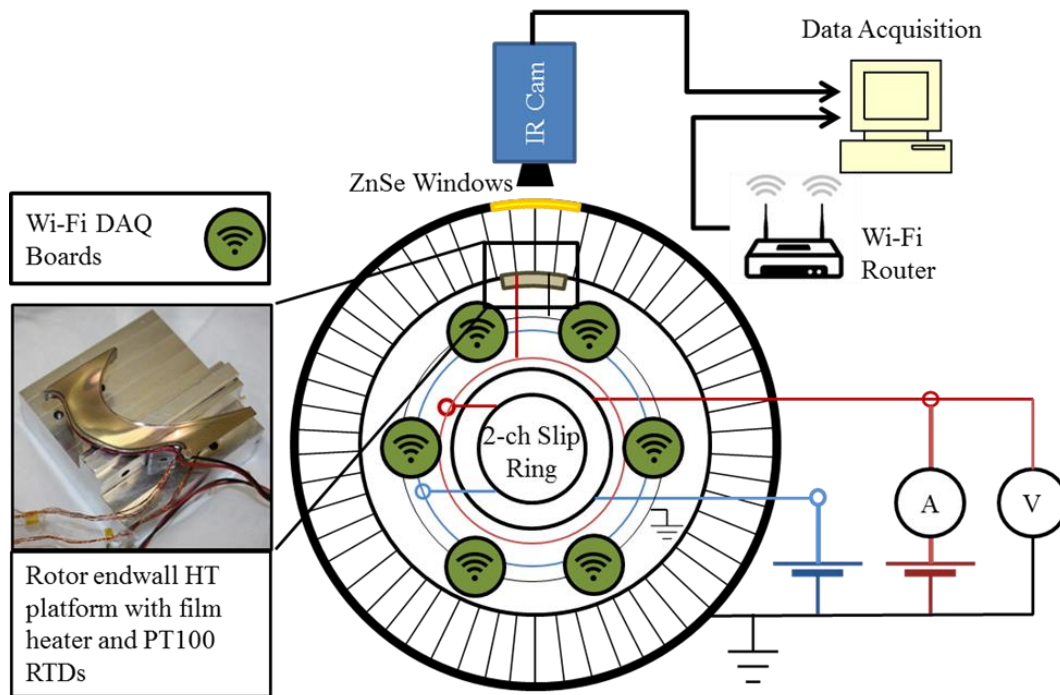


Figure 4.1: schematic of the heat transfer measurement setup.

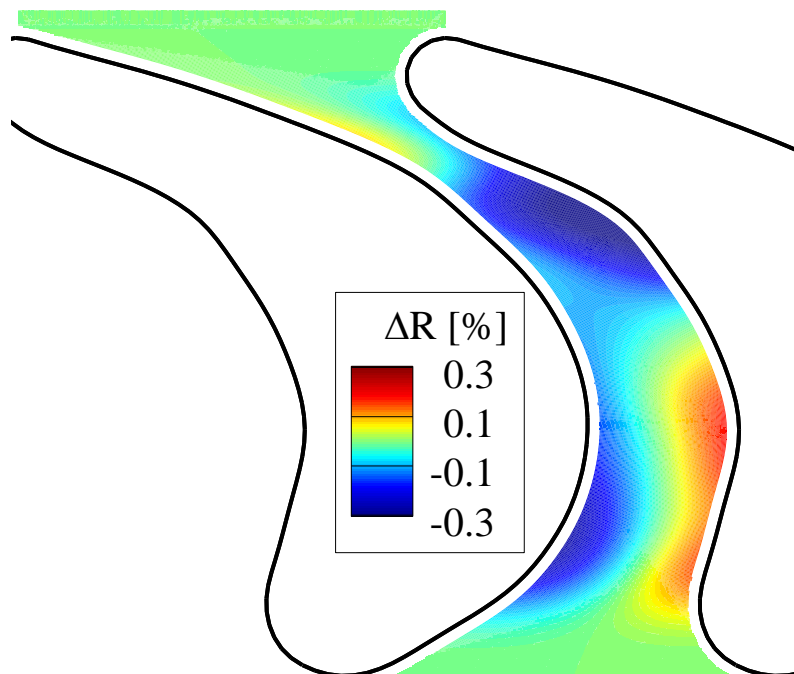


Figure 4.2: non axi-symmetric rotor endwall contouring for the case studied. Variations in terms of % of nominal radius.



## 4.1 Mechanical Integration of a Rotor Heat Transfer Platform

The conceptual development of a rotating platform equipped for heat transfer measurements must take into account several constraints of very different nature, addressing mechanical, thermal, and system-level concerns to ensure a successful outcome of the campaign.

### Material properties

A suitable material for the construction of a heat transfer platform must present physical properties ensuring mechanical integrity, satisfactory thermal management and ease of fabrication and instrumentation.

Preferably, for the sake of simplicity and robustness of calibration, data reduction and modeling, all properties should be homogeneous within the substrate material and the material should behave isotropically.

- Mechanical properties: the material suitable for this application should present resilience and ductility to prevent catastrophic, sudden failure during operation. Given the centrifugal load during operation over a broad range of temperatures, the material should present sufficiently high elastic modulus to produce small deformations and not alter the shape of the flow path. Clearly, the yield strength must be sufficient to bear the expected loads. To minimize the stresses on the fixation system, it is crucial that the material is lightweight, unless a full-blisk solution is implemented (that is, a solution imposing the thermal management of the complete rotor as a single block of material). A good level of machinability is a must, in order to contain the manufacturing costs and satisfy the required geometrical tolerances to simplify data elaboration and reduce the uncertainties.
- Thermal properties: the candidate material must present a thermal expansion coefficient compatible with the ones of the surrounding materials (metallic blisk, glues, polymers) to avoid build-up of stresses due to differential thermal expansion during operation. Depending on whether an iso-thermal (bulk-

heating) approach is selected as opposed to an iso-energetic (surface-heating) one, the thermal conductivity of the candidate material should respectively be high (e.g. Cu, Al) or low (e. g., polymers, ceramic). Beneficially, all properties should be constant or mildly varying with temperature.

- Chemical properties: the substrate material must tolerate the solvent of the high-emissivity paint and the glues used for instrumentation and installation on the rotor. It must also be chemically stable in the temperature range of interest, not just during operation, but also during the manufacturing and assembly process, including the temperature variations required for curing of adhesives and glues or the ones experienced during the film-heater deposition (if – as in this case – a surface-heating approach is chosen).

### **Instrumentation**

The design of the heat transfer platform must ensure ease of instrumentation and calibration. Specifically:

- easy handling of the part is required to allow equipping the platform with temperature (or other kinds of) transducers. It is preferable for the part to be compact and removable from the blisk assembly also for calibration and maintenance/repair purposes;
- if a surface-heating approach is chosen, vacuum compatibility is required to be able to carry out Physical Vapor Deposition of the film heater. Evacuating layers of adhesive is also recommended during instrumentation.
- accuracy of thermal boundary condition: either bulk heating or surface heating should provide a well-known boundary condition, respectively in terms of substrate temperature field and surface heat flux. Ideally, for simplicity of calculation, the thermal boundary condition should be uniform.

### **System Integration**

The requirements for a successful integration of the heat transfer platform with the rest of the system include the following.

- For safety reasons, it is preferable for the power requirements of the thermal management system to fall in a low current/low voltage range;
- mechanical containment of all parts must be ensured in case of catastrophic failure of the platform during operation;
- in order to preserve the flow field from disturbances, seamless surface junctions are required in the flow path between the heat transfer platform and the surrounding components.

Solutions requiring the instrumentation and heating of the whole rotor blisk are discarded because of cost, complexity in calibration and instrumentation and excessive power requirements. Two rival concepts are devised based on the constraints above and techno-economic considerations:

- an iso-thermal setup based on a highly conductive, metallic insert heated by means of cartridge heaters with a directly deposited, polymeric auxiliary wall;
- a surface-heating based setup relying on a low-conductive, plastic insert heated with directly deposited film heaters.

While the first option offers reliance on more established manufacturing techniques and instrumentation and replicates the approach used in the past for stator measurements, the much higher power requirements ( $\sim 20$  times) and weight of the components (more than 2 times higher) pose challenges in terms of safety of the assembly and power system so high, that the development of a new manufacturing technique for the production of a three-dimensional, directly deposited film heater is considered the conservative option.

Direct deposition of film heaters on non-conductive substrates presents the following advantages for the application on the rotating frame:

- the low weight per unit area of the film heaters dramatically reduces centrifugal loads compared to bulk-heating devices (e. g. cartridge heaters);
- the insulating substrates can be fabricated out of light, polymeric material, as opposed to the conductive – therefore metallic – substrates required by iso-thermal, bulk-heated setups. This solution is, therefore, even more convenient from a mechanical standpoint;

- ~20 times lower power requirements for reaching the desired endwall temperatures under the expected convective conditions compared to isothermal solutions requiring the heating of a solid piece of conductive material;
- applicability of the technique to virtually any endwall geometry.

Furthermore, the simple construction and strong adhesion limit the chances of failure under centrifugal loads.

The insulating substrate is shaped as a 3D hub insert to be fit in a pocket cut out between two rotor blades to complete the hub platform (Figure 4.3). This allows instrumentation and calibration of the part prior to its installation on the rotor.

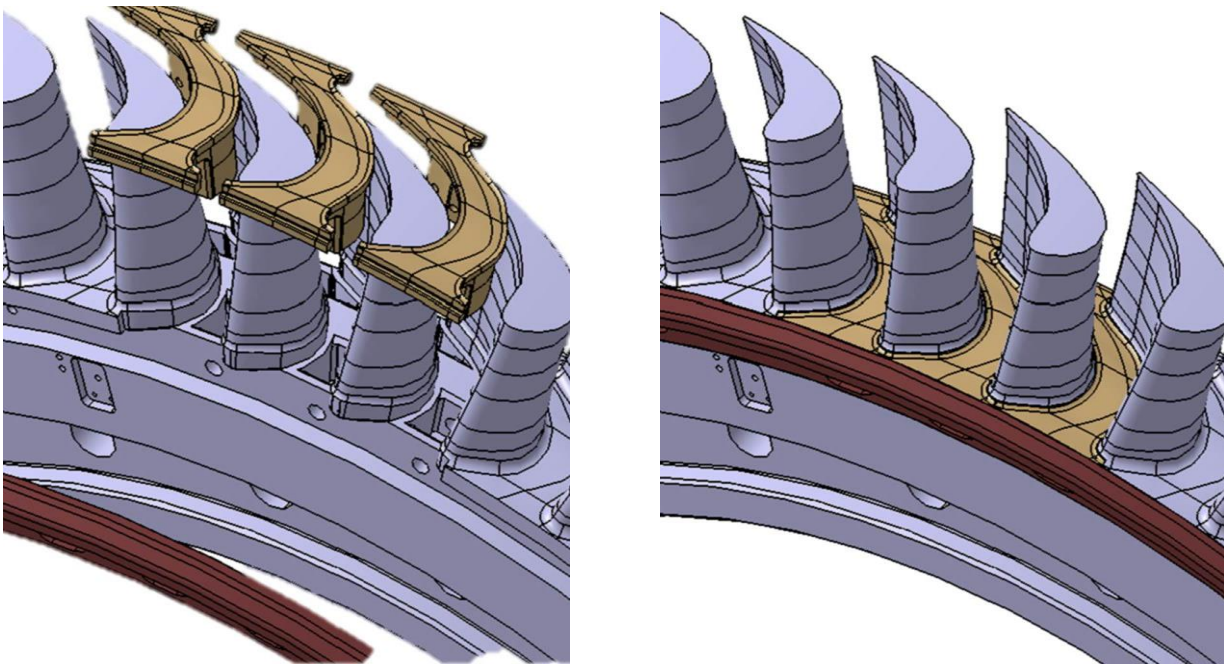


Figure 4.3: left, exploded view of the main structural components of the blisk assembly: blisk (grey), heat transfer platform inserts (brown), rim seal cavity retaining ring (dark red). Right, assembled components.

The platform insert is bolted to the rotor blisk (in aluminum). A step on the upstream face of the insert fits into a circumferential groove cut out of the inner face of the exchangeable ring defining the rim seal cavity geometry on the rotor side. The modularity of the assembly allows testing of multiple rim seal cavity

geometries. Results for an advanced shaping of the cavity will be shown in a later chapter (chapter 9).

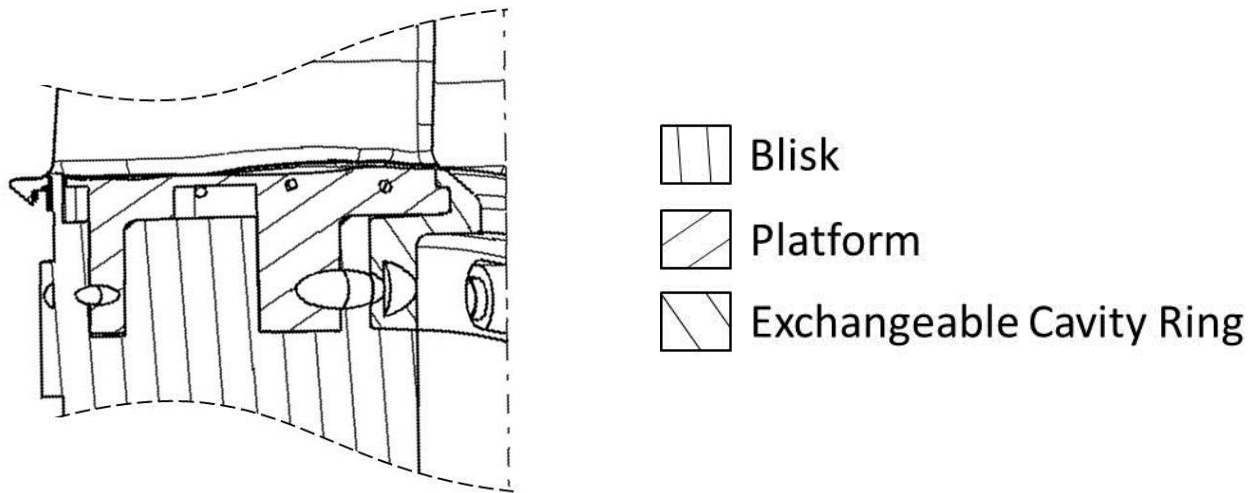


Figure 4.4: an axial cut of the rotor assembly. The heat transfer platform is bolted to the aluminum blisk. Additional containment in the radial direction is provided by the exchangeable ring defining the geometry of the rim seal cavity on the rotor side.

The material chosen for the construction of the hub insert is PEEK (Poly-ether-ether-ketone). Its low thermal conductivity ( $\kappa = 0.25 \frac{\text{W}}{\text{m}\cdot\text{K}}$ ) is favorable as it contains the conduction losses through the substrate, while the good machinability allows the fabrication of pieces with complex shapes. Additionally, the material presents sufficiently high yield strength (90MPa), which makes it suitable for the expected loads under rotation, as verified by means of FEM analyses shown in the following section 4.1.1 . A thorough material characterization is conducted and results are presented in section 4.5.6 .

#### 4.1.1 Thermo-mechanical FEM Analyses

FEM analyses are performed to verify the suitability of the design during operation. The setup includes the rotor blisk, the PEEK platform, the steel bolts used to fix the platform to the blisk and representative boundary conditions in terms of endwall heat load. For a conservative estimate, the simulations are performed

by imposing a  $\sim 10\%$  overspeed on the rotor, which is spinning at 3'000rpm rather than at the nominal 2'700rpm. Assuming linearity of the loads with centrifugal acceleration, this results in an additional 20% increase in the estimated loads.

Stresses of up to 11MPa are found in the region of the fixation of the platform to the blisk, still offering a safety factor of more than 8.

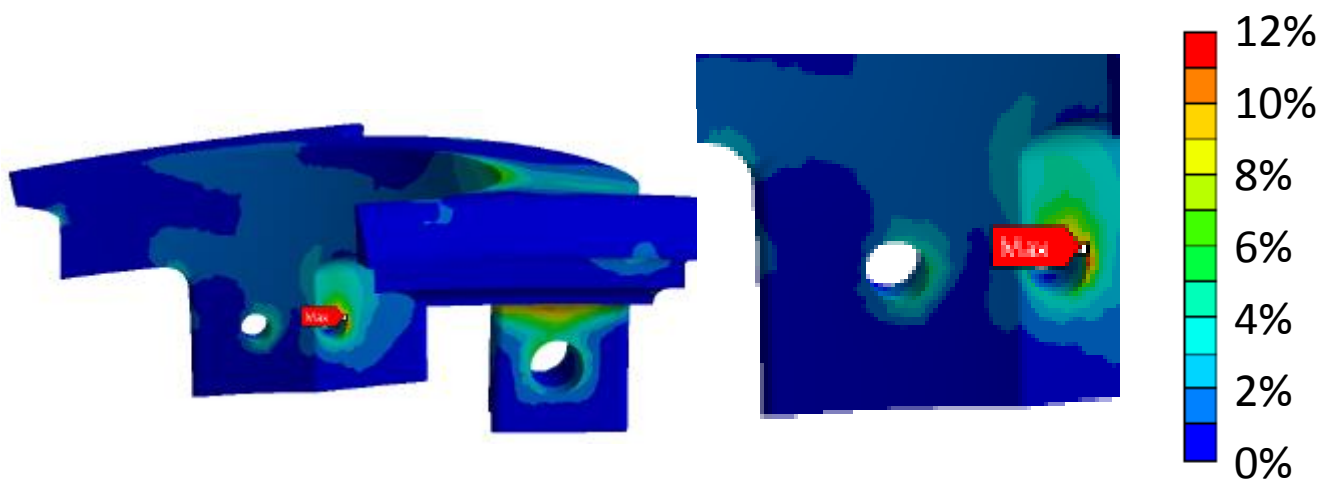


Figure 4.5: left, 3D finite element model of the heat transfer platform; right, close up of the most stressed region, around the trailing edge strut hole. Stresses are given in % of yield strength (90MPa). The safety coefficient under operation at 3000rpm with conservative estimation of the temperature field of the solid is greater than 8.

The deformations under operation are expected to be within 0.1mm, with the most deformed part being the thin appendix at the trailing edge side of the platform's endwall. The estimation is considered conservative as the simulation does not include modeling of the epoxy resin used to glue the edges to the blisk.

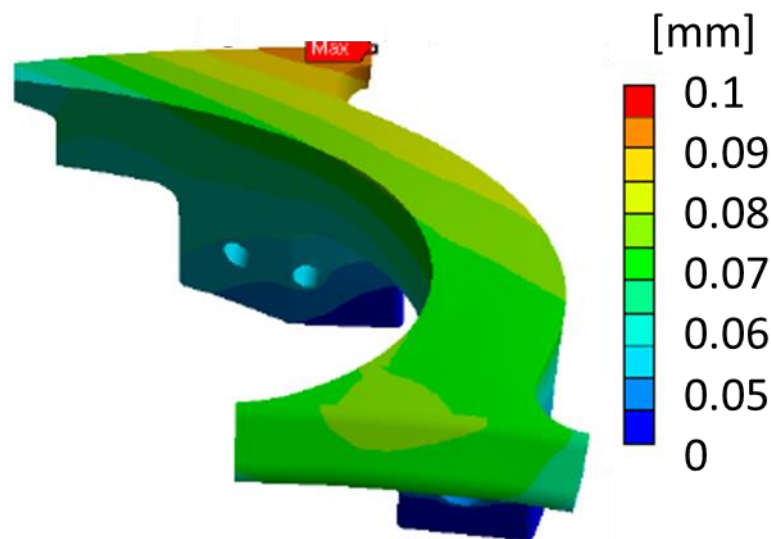


Figure 4.6: deformation distribution of the heat transfer platform under operation at overspeed (3000rpm). The most deformed portion of the part is at the trailing edge of the endwall with 0.1mm deformation. The estimation is conservative not just for the 10% overspeed, but also for the absence in the model of the epoxy resin used to glue the sides of the platform to the blisk.

## 4.2 Design of Electrical Endwall Heaters

Once the substrate material has been defined and its shape designed, the requirements for the thermal management system, i. e. the film heater, must be translated into target heat flux and, at a later step, into constructive characteristics (materials, width of electrical tracks, thickness of the layer, etc.). It is in fact anticipated that the heater will take the shape of a serpentine of uniform track width.

The requirements for the heater are the following:

- to reach a surface temperature of about  $100^{\circ}\text{C}$  (over-temperature of about  $60^{\circ}\text{C}$  with reference to the relative total temperature of the flow) at the design point of the turbine;
- to be powered by a regular DC laboratory power supply (Elektro-Automatik EA-PS 3032-10B: max. power 600W at 150V and 4A);
- to fit within one hub endwall passage

- to present the closest possible spacing between adjacent segments of the serpentine (ideally, the separation between adjacent tracks should not be visible by the infrared camera);

based on a one-dimensional, steady state conductive/convective model, the range of target heat fluxes ( $\sim 1-10\text{kW/m}^2$ ) is determined.

A serpentine of constant width has to be obtained from the film of conductive material that will be deposited on the surface of the PEEK insert. The serpentine will be powered electrically to provide surface heating by Joule effect.

A range of heating track widths is then derived from:

- the maximum thickness of the Nickel layer that can be deposited without incurring in spontaneous cracking and peeling due to residual internal stresses. This is empirically determined to be  $\sim 200\text{nm}$  (see section 4.3.1 );
- the expected electrical resistivity for the Nickel layer, given its maximum thickness and the target substrate temperature range ( $25-120^\circ\text{C}$ ), as documented in literature ( $\sim 20\ \Omega\cdot\text{cm}$ , [108]);

The equation governing the design choice for the geometrical parameters of the heating tracks is:

$$\dot{q}''_{\text{el}} = \left(\frac{i}{w}\right)^2 \frac{\rho}{d} \quad (4.1)$$

which relates width  $w$  and thickness  $d$  of the tracks, the feeding current  $i$  to the heater, the electrical resistivity  $\rho$  of the conductive film and the heat flux produced by Joule effect  $\dot{q}''_{\text{el}}$ .

The final track width of  $1.65\text{mm}$  is chosen for ease of integration of the power connection terminals in the platform.

The turns of the serpentine are kept as close as possible to the fillets of the adjacent blades, in order to exclude from the measurement area the heat flux non-uniformities coming from local current concentrations.



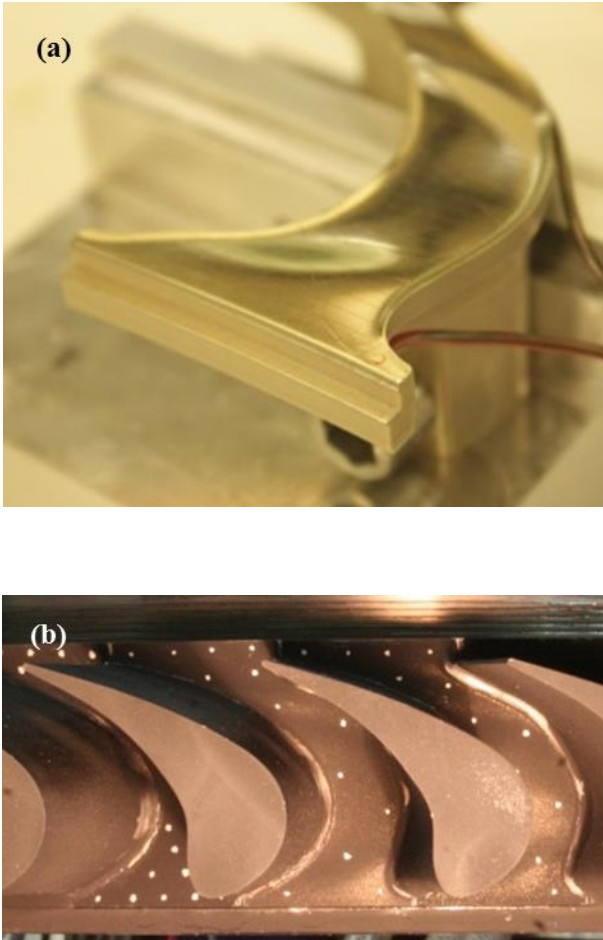


Figure 4.7: heat transfer platform with directly deposited film heater before (a) and after (b) installation on the rotor blisk and application of high-emissivity coating.

## 4.3 Manufacturing of Film Heaters for Contoured Endwalls

The non-zero Gaussian curvature of the endwall surface prevents from installing a two-dimensional film heater, so a bespoke process is developed in order to manufacture a heater directly on the contoured surface of the PEEK substrate. Particularly, a deposition process is required to produce a conductive coating on the polymeric endwall. Several processes exist to accomplish this, for example:

- Electroplating;
- Physical Vapor Deposition (PVD);
- Chemical Vapor Deposition (CVD);

Compared to the other processes, Physical Vapor Deposition offers the advantage of a higher purity of the deposited materials due to the fact that the process takes place in vacuum. The evaporated materials, therefore, have little likelihood of combining with oxygen to form oxides. The purity of the coating results in better control of the physical properties of the layer, especially its electrical resistivity.

Non-conductive impurities result in higher resistivity than expected, thus requiring higher voltage to achieve the same level of current in the serpentine. For this reason, an e-beam vacuum Physical Vapor Deposition process is chosen for this application.

### 4.3.1 Physical Vapor Deposition

Physical Vapor Deposition has stringent requirements concerning the preparation of the substrate material and its compatibility with the coating layer of choice. Special care must be taken when addressing the following points (Mattox [109]):

- surface finish of the substrate material;

- outgassing of the substrate material under vacuum during the deposition process;
- matching of the physical properties of the substrate and the coating. In particular, a substrate with a low Young's modulus, coupled to a layer of material with higher values of elastic modulus might result in mechanical failure of the surficial layer. Similarly, differential thermal expansion – of particular relevance for the target application of this work – might result in excessive tension of the coating at high temperatures, resulting in cracking;
- residual stresses;
- temperature distribution during deposition.

### Surface Quality and Adhesion Testing

Smoothing of the surface is beneficial to the deposition process as it yields denser coatings: since e-beam PVD is a line-of-sight method (i. e., material is deposited on the substrate only in areas that are directly exposed to the crucible), asperities on the surface can produce shadowing effects over the surrounding surface, thus preventing its coverage. Since porosity is undesirable in the conductive film, as it would increase resistivity in an uncontrollable and – possibly - inhomogeneous fashion, a reduction of the residual roughness from the machining of the substrate is in order.

Mechanical methods are not uncommon in the practice of surface preparation of substrates. In particular, a sequence of abrasives with decreasing grit size was employed to finally obtain a surface roughness of  $R_a \sim 30\text{nm}$  (mean roughness) and  $R_z \sim 260\text{nm}$  (mean roughness depth).

The gradual qualitative improvement of the coating with surface smoothing is testified by the profiles and images of Figure 4.8. Adhesion strength was tested by scotch-tape method (see [110, 111]), but due to the low reproducibility of the results depending on the tape used and type of coating and substrate tested (Gray et al. [112]), the approach can only provide qualitative indication of whether the coating will be able to stand the centrifugal loads under operation. Given that the peel-test or scotch-tape test imposes a concentrated shear stress on the coating, rather than a uniform tensile stress approximately normal to the

surface (as expected during actual operation), the indication of the test is considered conservative, and as such the surface quality of the last test piece shown in Figure 4.8 is considered suitable for the deposition of the coating on the final pieces. In this latter case, in fact, detachment of material is sporadic and does not jeopardize the functionality of the surface.

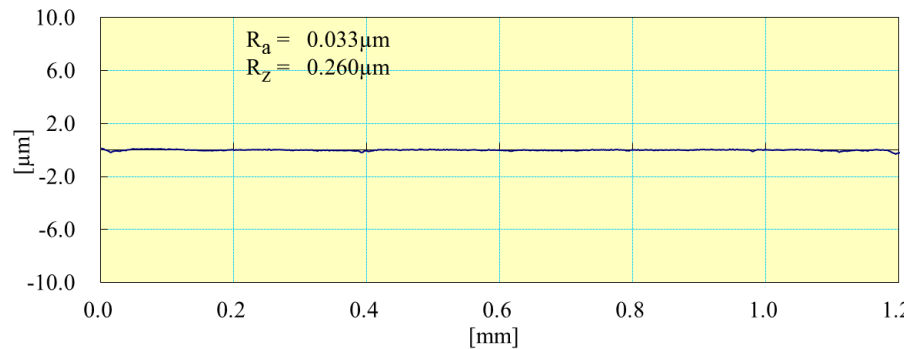
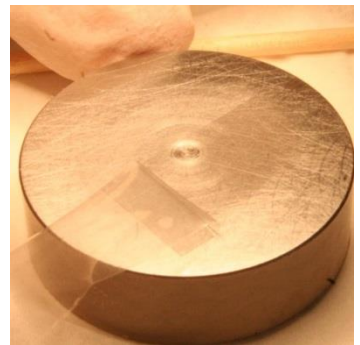
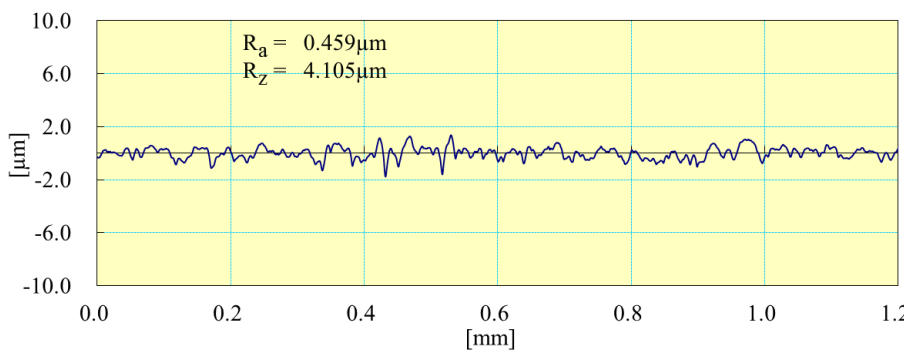
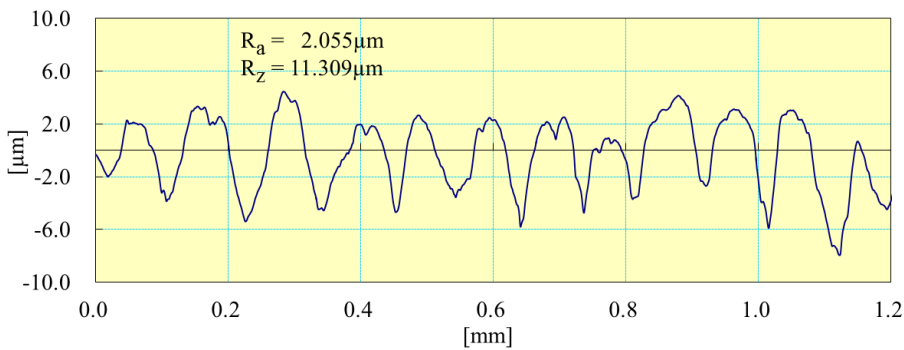


Figure 4.8: adhesion strength of coating on flat PEEK samples increases while porosity decreases with decreasing surface roughness. Adhesion is tested by scotch-tape method (middle-right).

Adhesion is also strongly affected by the thickness of the film and the mechanical properties of the deposited material. In particular, materials with high elastic moduli build up the highest residual stresses after deposition. It is found empirically that film thicknesses exceeding a cumulative value of 220nm (10nm Cr for adhesion, 200nm Ni, 10nm Au for corrosion protection and solderability) spontaneously peel off the substrate after deposition (see later section on residual stresses). This maximum film thickness with the mentioned composition is chosen for the fabrication of the film heater.

### Outgassing of the Substrate

PEEK is known to be vacuum-compatible due to its relatively low outgassing values. The LIGO (Linear Interferometer for Gravitational Observation) team indicates it in their list of authorized materials for application in vacuum, despite with restrictions [113]. However, to further reduce the eventuality of contamination of the deposited material, the parts are pre-evacuated in a separate chamber prior to the deposition process.

### Coating-Substrate Matching

Kim [114] offers a convenient method to classify the combination of substrate and coating based on their failure strain. Two parameters **a** and **b** are defined as follows:

$$\mathbf{a} = \frac{\epsilon_f^f - \epsilon_f^s}{\epsilon_f^f + \epsilon_f^s} = 0.022 \quad (4.2)$$

$$\mathbf{b} = \sqrt[4]{(\epsilon_f^f)^2 + (\epsilon_f^s)^2} = 0.8 \quad (4.3)$$

having indicated with  $\epsilon_f^f = 0.47$  and  $\epsilon_f^s = 0.45$  respectively the strain to failure of the film or coating and of the substrate. It must be noted that the value of strain to failure used in the calculation is the one documented for commercially pure, thick nickel rather than thin film. A value of parameter  $-1 < a < 1$  (4.2) close to 0 as in the present case, indicates similar ductility of the film and the substrate. Systems of this kind are typically suitable for mechanical or structural applications. Considering that the film is required to sustain thermo-mechanical loads during turbine operation,  $a \approx 0$  is desirable. The parameter  $b > 0$  indicates whether the system maintains elastic behavior until fracture or else if plastic deformation takes place before failure occurs. The value obtained for a nickel film on PEEK is indicating ductile behavior. According to the chart depicted in Figure 4.9, the substrate-film system can be classified as Ductile Metal on Ductile Metal (DM/DM), despite the substrate being polymeric, thanks to the remarkable mechanical properties of PEEK.

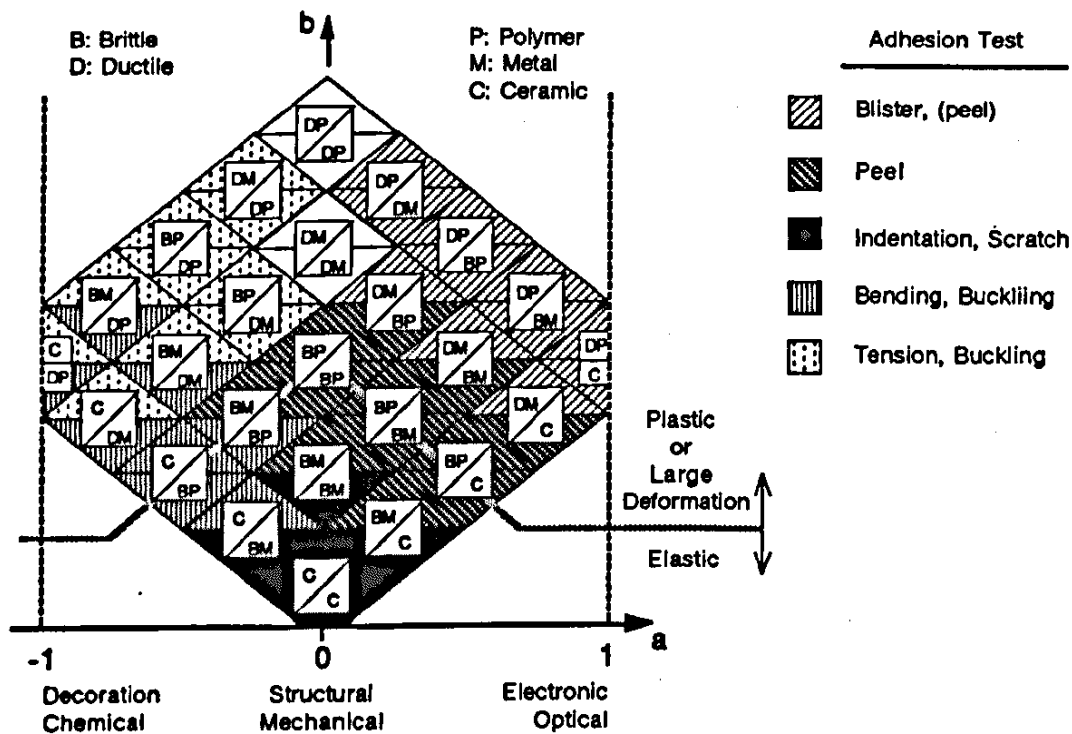


Figure 4.9: film/substrate adhesion classification according to values of parameters  $a$  (eq. 4.2) and  $b$  (eq. 4.3) (Kim [114]).

Aside from the purely mechanical properties of the two materials, another source of stresses for the coating possibly inducing delamination is differential thermal expansion. However, because the coefficient of linear thermal expansion is lower for nickel ( $13 \frac{\mu\text{m}}{\text{m}\cdot\text{K}}$ ) than it is for PEEK ( $50 \frac{\mu\text{m}}{\text{m}\cdot\text{K}}$ ), the film is subject to compressive rather than tensile stresses assuming that no residual stress is present at ambient temperature. In truth (see next section), tensile residual stresses form in the system at ambient temperature because the deposition process occurs at temperatures higher than ambient. These stresses are relieved when the heater is operated and the surface of the part is heated at temperatures closer to the ones experienced during deposition.

### Residual Stresses

Intrinsic stresses in the coating are unavoidable in physical vapor deposition processes (Bagchi and Evans [115]). The multilayer can be designed in order to prevent delamination by satisfying the following condition:

$$\Gamma_i \geq \frac{h \cdot \sigma_R^2}{E \cdot \lambda} \quad (4.4)$$

that is, the interface debond toughness or interface fracture energy  $\Gamma_i$  must be higher than the energy stored in the film of thickness  $h$  and Young's modulus  $E$  due to the residual stresses  $\sigma_R^2$  ( $\lambda \sim 1$  is a cracking number).

The technical difficulty in measuring either  $\Gamma_i$  or  $\sigma_R^2$  makes it practically challenging to make use of eq. 4.4 to design the multilayer. Nonetheless, the inequality explains the physical reason why thicker films ( $h \uparrow$ ) are more likely to break, since they store more energy along their thickness.

For these reasons, systematic testing of the physical vapor deposition of layers of different thicknesses (keeping the composition constant) highlighted the maximum attainable film thickness of 220nm as indicated in the previous section.

### Temperature Distribution During Deposition

It is advisable in the practice of vacuum deposition to keep the substrate at a considerable distance from the crucible to limit its overheating due to radiation [116]. The temperature distribution on the substrate during deposition strongly alters the physical properties of the coating as it affects the outgassing rate of the substrate, the condensation and nucleation of the incoming material and it can produce annealing effects on the already deposited film.

All of the previous considerations have been carefully taken into account in the deposition of the multilayer on the PEEK substrates. In particular, as previously mentioned, the composition and thickness of the multilayer was defined after testing of different configurations. Finally, a 10nm layer of Chromium was deposited first on the PEEK surface as a bonding layer to the substrate. Successively, the 200nm-thick layer of nickel was deposited on top as the bulk of the film heater. Lastly, a 10nm-thick layer of gold is deposited for solderability and limitation of the oxidation of the nickel layer below.

The substrates are rotated at 21rpm during the deposition to reduce the possibility of dis-uniformities due to geometrical shadowing effects. A distance of ~600mm from the crucible is kept to reduce radiant heating from the vapor source. A rate of 0.05nm/s was found to return the most compact film. The machine used is an Evatec BAK501 LL evaporator at the clean room facility of BRNC, IBM, Rüschnikon, Switzerland.

The film was subject to several thermal cycles to alleviate the internal stresses and test its durability.

### 4.3.2 3D Laser Ablation

Under the assumption of uniform thickness and resistivity of the deposited metallic layer, the desired heat flux can be produced by the heater once it is cut in the shape of a serpentine of uniform track width. The desired track width has been determined as explained in section 4.2. The chosen cutting process is laser ablation, for the high spatial accuracy ( $\pm 10\mu\text{m}$  positional error), the minimal in-



vasiveness of the process (the depth of the cuts can be limited to a few micrometers below the surface of the workpiece) and the capability to cope with complex, fully three-dimensional shapes. Also, laser cutting enables to keep the spacing between adjacent tracks of the heater to a minimum, in order for the unheated zone between tracks not to affect significantly the continuity of the heat flux distribution. A picosecond, Nd:YAG, infrared Duetto laser produced by Time-Bandwidth, coupled to a precision traversing system Aerotech A3200 is programmed to follow the shape of the endwall and cut tracks with a width  $w$  of  $1.65\text{mm} \pm 10\mu\text{m}$ . The laser has a beam size of  $55\mu\text{m}$ , corresponding to the final spacing of the adjacent, parallel segments of the serpentine. An alignment procedure is devised to obtain the required accuracy in positioning of the workpiece to ensure that all the tracks are cut at the nominal width.

The workpiece is fixed on a CNC-machined jig presenting dimensional, parallelism and orthogonality tolerances between reference faces (respectively  $\pm 50\mu\text{m}$  and  $0.04^\circ$ ). Circular markers with a diameter of  $0.5\text{mm}$  are machined with a positional accuracy of  $\pm 50\mu\text{m}$  on the surface of the jig.

The relative position of the workpiece in the laser's traversing system's frame of reference ( $x_{\text{las}}\hat{O}_{\text{las}}y_{\text{las}}$  in Figure 4.10) is obtained by means of a micro-camera fixed to the laser head and checked by ablating reference shapes (circles of  $0.6\text{mm}$  in diameter) around the markers. Due to limitations in the optical accessibility, this is done for three of the four markers present on the jig surface. The unit vectors of the planar reference system of the jig are then calculated and a transformation is computed between the traversing system's frame of reference  $x_{\text{las}}\hat{O}_{\text{las}}y_{\text{las}}$  and the corresponding planar reference system of the jig-workpiece assembly  $x_{\text{jig}}\hat{O}_{\text{jig}}y_{\text{jig}}$ . The centers of the markers are hit by the laser with an accuracy of  $0.1\text{mm}$ . As the markers are  $51\text{mm}$  apart, this results in an alignment accuracy of  $0.3^\circ$ .

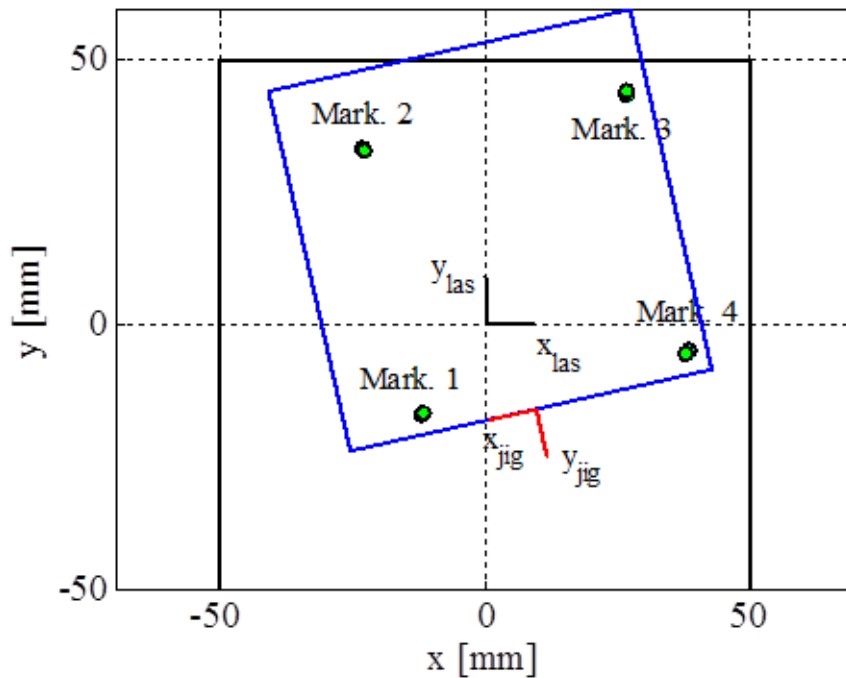


Figure 4.10: schematic illustrating the generic relative position of the jig's reference system (blue) with reference to the one of the laser scanner (black). The misalignment is exaggerated.

The cutting parameters are determined on planar test-pieces of PEEK carrying the same film structure. It is found that electrical separation is achieved with a wide range of parameters so long that the repetition rate of the laser is kept below 50kHz to avoid inter-pulse plasma shielding [117]. A 25kHz repetition rate, with 98% pulse overlap and 50mm/s cutting speed are found to deliver a satisfactory cut through the metallic layer in a single repetition with just 10% of the maximum rated power for the laser (10-15W).

An overall resistance of  $533\Omega$  is measured for the heater at ambient temperature, corresponding to an average value of resistivity for the composite metal layer of  $2.4E-7\Omega\cdot m$ , consistently with what observed in literature for thin-film Nickel layers [108].

High-emissivity paint (Nextel Velvet Coating 811-21, emissivity value 0.98 in the low infrared range) is applied on the top surface of the heaters for the infrared thermography measurements.

## 4.4 Rotating Data Acquisition System

A in-house developed system of wireless data acquisition board is mounted on the rotor of the turbine to acquire the signal coming from the PT100 RTDs embedded in the heat transfer platform and to control the power to the heater. The electronics are specifically designed to be operated on the rotating frame and be able to stand accelerations of up to 15'000g. Nine boards are installed on a specific aluminum fixture mounted at the back of the rotor blisk, with the possibility of stacking up to four boards on top of each other. Each board has four analogue inputs that can be sampled at 200kHz and providing constant feeding current to the temperature sensors. The system can be used also for heat flux gauge measurements, piezoresistive pressure sensors or strain gauges. A thorough characterization of the system is provided by Mansour et al. [118].

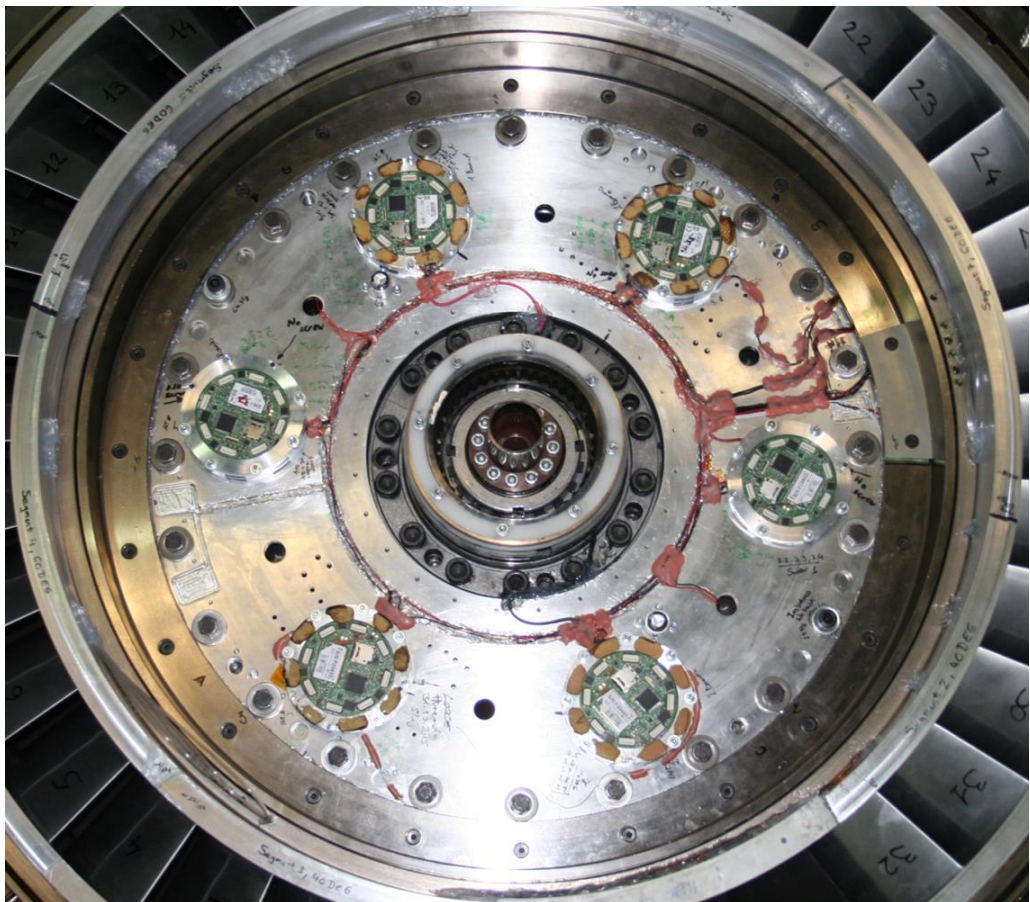


Figure 4.11: the on-board, wireless data acquisition system and power electronics mounted on the rotor during facility assembly.

In order to increase the temperature sensitivity of the measurement chain (PT100 and DAQ boards), the PT100 sensors are connected to a Wheatstone bridge with a  $110\Omega$  precision resistor with a temperature coefficient of  $\pm 10\text{ppm}/^\circ\text{C}$  and a resistance tolerance of  $\pm 0.1\%$ .

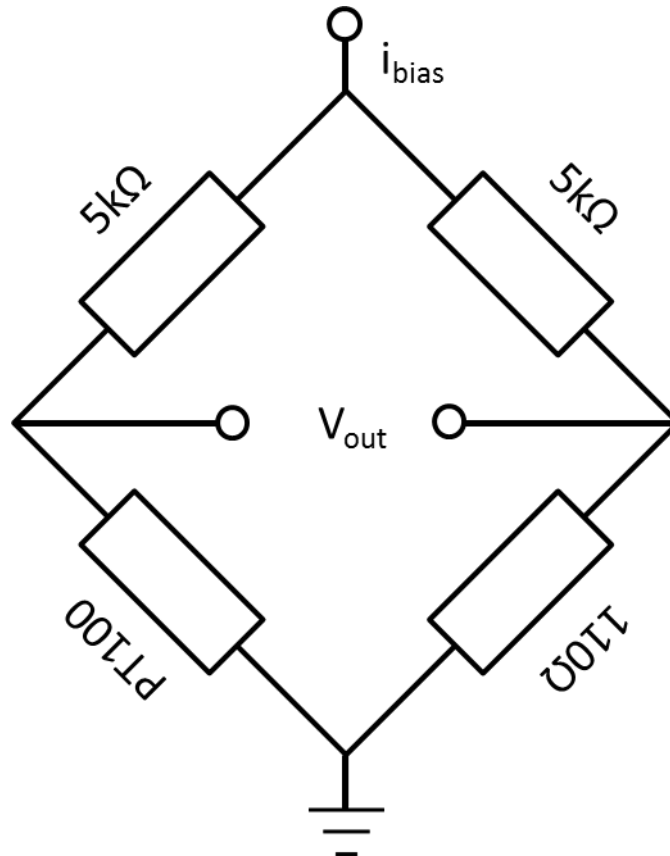


Figure 4.12: Wheatstone bridge configuration for the differential temperature measurements with PT100.

A two/step amplifier multiplies the output voltage  $V_{\text{out}}$  of the Wheatstone bridge by 60 and 32, resulting in a peak-to-peak white noise RMS value of less than  $0.5\text{mV}$ , corresponding to temperature fluctuations of less than  $0.14^\circ\text{C}$ .

#### 4.4.1 PT100 Arrangement

9 PT100 miniaturized resistive temperature transducers (1.6mmx1.2mmx0.8mm, IST AG) are installed in the platform 1mm below the endwall surface. Compatibly with the number of available data acquisition channels and the geometrical constraints posed by the platform design, the number and arrangement of the sensors is defined in order to cover the whole platform from inlet to outlet, as shown in Figure 4.13.

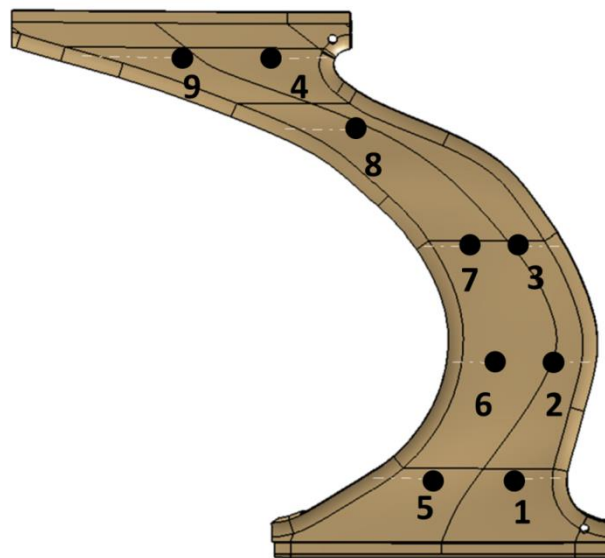


Figure 4.13: distribution of PT100 RTDs below the platform endwall.

## 4.5 Step-Wise Transient Heat Flux Calibration

In order to be able to derive accurately the heat transfer quantities from an iso-energetic setup, it is necessary to verify whether the heat flux provided by the thermal management system can be considered uniform over the surface. In case of unsatisfactory uniformity, a correction method must be found to account for the actual value of heat flux provided locally. This chapter describes a heat flux calibration method specifically developed for this work.

It has been mentioned in the previous chapter (specifically section 4.3.1 ) how several factors during the physical vapor deposition process can affect the uniformity of the film properties and – consequently – the uniformity of the produced heat flux. In particular, one of the hardest variables to control during the vacuum evaporation is the uniformity of the substrate temperature when exposed to a source of radiant heat such as the crucible.

If the substrate presents, in consequence of this, a non-uniform surface temperature during deposition, porosity, electrical resistivity and adhesion of the film to the substrate can be altered.

In particular, the uniformity of the locally generated heat flux can be affected by:

- thickness non-uniformities of the deposited metallic layer;
- resistivity non-uniformities of the deposited material;
- improper electrical separation between tracks after laser ablation.

A procedure was devised in order to test and calibrate for non-uniformities in the electrically generated heat flux, based on a step-wise transient approach. The details of this procedure and its results are presented in this chapter.

The method used presents similarities to the Transient Hot Strip (THS) method developed by Gustafsson et al. [119] in 1979. Gustafsson's method consists of heating samples of solid material by producing a uniform and known heat flux by means of a resistive rectangular strip of uniform thickness. The strip is placed in the middle of two blocks of the material, the properties of which (i.e. thermal conductivity and thermal diffusivity) are to be measured. Heat is produced by Joule effect in a step-wise transient fashion. The change in the resistance of the hot strip is measured over time and related to the local temperature increase.

The temperature increase is finally compared to the analytical solution for an infinitely extended planar heat source.

The hot strip has later been substituted by devices directly evaporated on the samples [120]. The key differences from the THS method are:

- the heat source is at the surface of the solid. The mathematical model used for the evaluation of the heat flux is therefore the one described in the following section 4.5.2 ;
- the substrate onto which the heat source lies is fully three-dimensional;
- the thermal properties (i. e., thermal diffusivity and conductivity) of the substrate are known, so the heat flux provided by the heat source on a point basis is measured instead.

### 4.5.1 Impact of Heat Flux Non-Uniformities on Heat Transfer Measurements

The detrimental effect of unverified assumptions on heat flux distributions and conduction losses in the substrate are well exemplified in the recent work of O'Dowd et al. [121], comparing the steady-state heated foil technique to other infrared-based experimental techniques. The goal of most authors relying on film or foil heaters is to obtain a uniform heat flux boundary condition, regardless of whether the surface temperature is measured with thermocouples (Blair [62], Graziani [57]), by infrared thermography (Lynch [61]) or thermochromic liquid crystals (Simonich [122], Baughn et al. [123]). Moffat [74] demonstrates analytically and verifies experimentally that the heat transfer coefficient  $h$  defined with the adiabatic wall temperature (equation 4.1) is rigorously invariant and independent of thermal boundary conditions. It is, in facts, purely a function of geometrical and fluid mechanics parameters:

$$h = \frac{\dot{q}''_{\text{conv}}}{(T_w - T_{\text{ad}})} \quad (4.5)$$

Given the independence of the heat transfer coefficient from local boundary conditions, if a way is found to measure on a local basis the heat flux provided by

the heating device, it is possible to evaluate the local convective heat flux accurately even in the presence of severe non-uniformities.

### 4.5.2 Theory and Principle

The temperature rise  $\Delta T(t)$  at the surface of a homogeneous, semi-infinite solid with a surficial source of heat flux powered suddenly at a time  $t > t_0$ , is given by:

$$\Delta T(t) = T(t) - T_0 = \frac{2 \cdot q''_{el}}{e} \cdot \sqrt{\frac{t - t_0}{\pi}} \quad (4.6)$$

where  $T(t)$  is the surface temperature at the instant  $t$ ,  $T_0 = T(t_0)$  is the initial temperature at time  $t = t_0$  and  $q''_{el}$  is the heat flux generated by the source. It is immediate, after expressing the temperature rise  $T$  as a linear function of  $\sqrt{t - t_0}$ ,

$$\Delta T = p_1 \cdot \sqrt{t - t_0} + p_2 \quad (4.7)$$

to solve for  $q''_{el}$  by comparing equations (4.6) and (4.7):

$$q''_{el} = \frac{\sqrt{\pi}}{2} \cdot e \cdot p_1 \quad (4.8)$$

Known the thermal effusivity  $e$  of the substrate, the locally produced heat flux  $q''_{el}$  can be calculated under the following assumptions:

- one-dimensionality;
- the source of heat flux is located at the free surface of the solid and in perfect thermal contact with the substrate;
- the initial temperature of the substrate is homogeneous;
- the solid is homogeneous and isotropic.



### 4.5.3 Experimental Setup for Step-Wise Transient Heat Flux Calibration

A simple apparatus is constructed in order to conduct the step-wise transient heat flux calibration: the FLIR SC7300L infrared camera is positioned in front of the heat transfer platform on a test bench. The image resolution matches the one of the measurements performed in the turbine facility (0.32mm/pixel). A solid-state relay is connected to the power supply to the heater and to the digital output of one of the on-board data acquisition devices. The same digital output is connected in parallel to the camera trigger, so that the power to the heater and the recording sequence can be started simultaneously with a maximum time delay of 20ms.

The frame rate of the camera is set to 231frps, the maximum allowed by a full-frame acquisition – with an integration time of 100s and detector gain 1. 1000 frames are recorded for each sequence for a recording time of 4.33s per sequence. Tests are conducted at three different voltage levels: 25V, 35V and 40V. The maximum voltage is limited by the maximum temperature reached by the heater during the test, which must be kept below the glass transition temperature of the PEEK substrate ( $\sim 143^\circ\text{C}$ ). Subsequent tests are performed not earlier than 20 minutes after the previous one in order to ensure that the heat transfer platform has reached a state of thermal equilibrium with the environment.

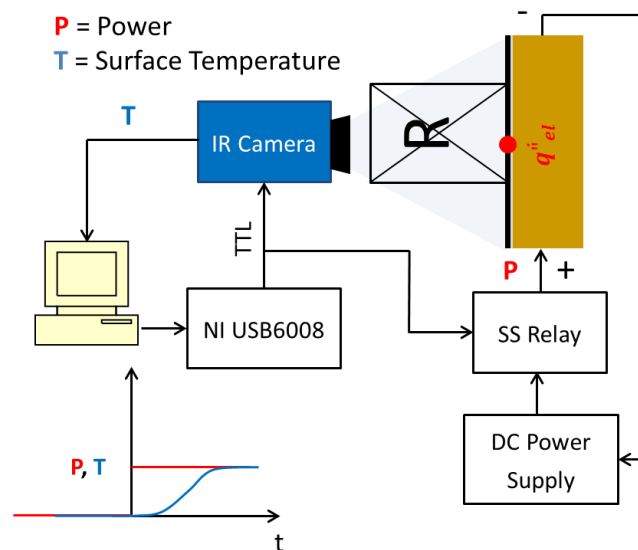


Figure 4.14: schematic of step-wise transient calibration setup

#### 4.5.4 Data Elaboration

The transient temperature increase is mapped onto a mesh of the rotor endwall by means of projective geometry. Further details on the calculations are given in section 2.2. The temperature rise is individually evaluated for each point of the rotor endwall mesh. The linear fit between  $\sqrt{t-t_0}$  and temperature rise is evaluated starting from a time  $t-t_0 > 2 \cdot \tau_{\text{paint}}$ , where  $\tau_{\text{paint}}$  is the thermal diffusivity time constant of the high-emissivity coating covering the heater:

$$\tau_{\text{paint}} = \frac{d_{\text{paint}}^2}{\nu_{\text{paint}}} \quad (4.9)$$

In regions presenting strong gradients in generated heat flux over the surface, conduction starts occurring laterally as soon as a sufficiently high temperature gradient has built up on the surface. This degrades the one-dimensionality of the phenomenon. The portion of signal processed to obtain a linear fit is therefore determined iteratively in order to minimize the root mean squared error of the fit. For each point with a root mean square error (rmse) exceeding  $0.03^\circ\text{C}$ , points are progressively eliminated from the tail of the signal until the rmse falls below the threshold. The value of the threshold corresponds to the average rmse over the endwall prior to the iterative procedure. The result of the iterative procedure is highlighted in Figure 4.17(c): as soon as the temperature increase deviates from the linear behavior due to lateral conduction, the data points are discarded. A map of heat flux is obtained for the whole endwall. Non-uniformities in heat flux production up to 60% of the average value over the whole endwall are detected. Locations of non-uniformities in generated heat flux are found not only in correspondence of the turns of the tracks because of concentrations of the streamlines of the current, but also in the central region of the heater. The reason for this can be attributed to thickness and resistivity non-uniformities in the deposited layer coming from the evaporation process (sect. 4.3.1) and different annealing temperatures of the film due to the complex shape of the part.

The point-by-point scaling factor  $S_q$  is calculated as the ratio between the locally generated heat flux value and the average of this quantity over the complete passage:

$$S_q(\mathbf{x}) = \frac{q''_{el}(\mathbf{x})}{\overline{q''_{el}}} = \frac{q''_{el}(\mathbf{x}) \cdot A_{ew}}{\int_{EW} q''_{el} d\sigma} = \frac{\frac{\sqrt{\pi}}{2} \cdot e \cdot p_1(\mathbf{x}) \cdot A_{ew}}{\frac{\sqrt{\pi}}{2} \cdot e \cdot \int_{EW} p_1 d\sigma} = \frac{p_1(\mathbf{x})}{\overline{p_1}} \quad (4.10)$$

The scaling factor  $S_q$  multiplied by the average heat flux  $\overline{q''_{el}} = i \cdot V / A_{ew}$  returns then the local value of heat flux for each power level.

$$q''_{el}(\mathbf{x}) = S_q(\mathbf{x}) \cdot \frac{P}{A_{ew}} \quad (4.11)$$

It is shown that the scaling factor is independent of the power level by performing tests at three different levels of electrical power, i.e. 1.2W, 2.3W and 3.0W  $\pm 1.6\%$ , respectively corresponding to expected average levels of heat flux of 914W/m<sup>2</sup>, 1752W/m<sup>2</sup> and 2285W/m<sup>2</sup>. The average repeatability of the  $S_q$  values over the passage is within 3.7% in this heat flux range.

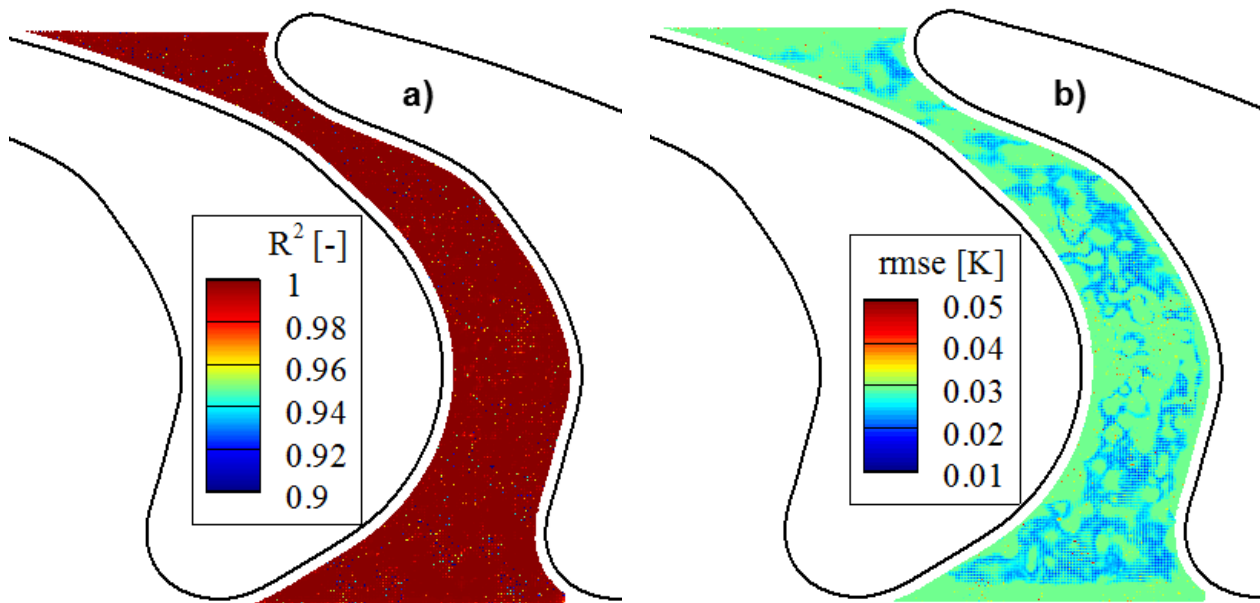


Figure 4.15: distributions of coefficient of determination  $R^2$  a) and of root mean square error b) of the linear fit for the determination of the local heat flux.

A repeatability check is performed between tests recorded before and after the experimental campaign. The resulting scaling factor values fall within less than 3% of each other, as shown in the distribution of Figure 4.16. The differences are attributed to the repeatability of the technique, rather than to modifications of the performance of the film heater. The robustness and suitability of the heater is thus confirmed. Additionally, the stability of the resistance was monitored during every day of operation and is estimated to be  $\sim 1.7\%$ .

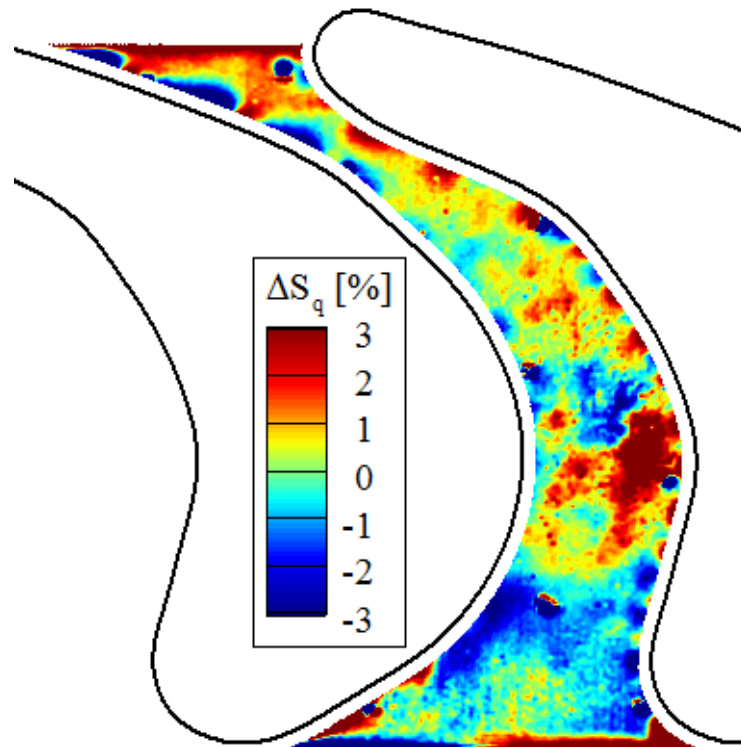


Figure 4.16: differences in the measured scaling factor before and after the experimental campaign are below 3%, confirming the robustness of the film heaters. Differences are attributed to the repeatability of the technique, rather than to physical differences in the heating film.

### 4.5.5 Point-Wise Heat Flux Distribution

The distribution of the scaling factor  $S_q$  is shown in Figure 4.17 together with the corresponding repeatability map calculated by comparing tests performed at different power levels. Uncertainties from the fit procedures are negligible compared to the repeatability errors (one order of magnitude lower in a 95% confidence interval).

No other sources of uncertainty are considered in evaluating the global uncertainty on  $S_q(\mathbf{x})$  other than repeatability and fit errors as, given equation (4.10),  $S_q(\mathbf{x})$  is independent of the thermal properties of the substrate (i.e. its thermal effusivity  $e$ ).

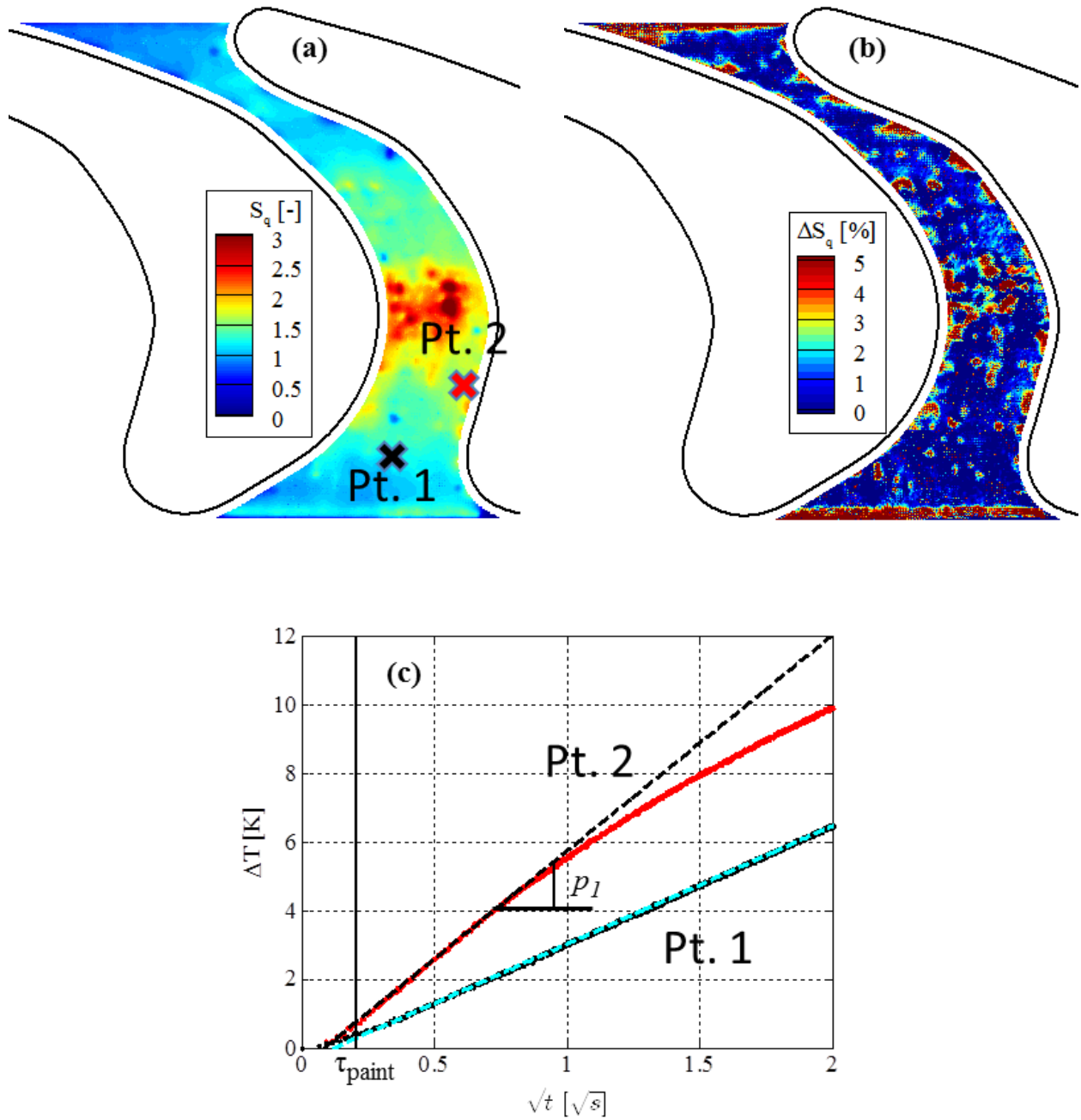


Figure 4.17: map of normalized Joule effect-generated heat flux obtained by means of step-wise transient calibration a). Maximum spread recorded in the range 0.9-2.3kW/m<sup>2</sup> b).

### 4.5.6 Characterization of the Substrate

A thorough characterization of the PEEK material used for the construction of the heat transfer platforms was carried out by means of different measurement techniques. Samples cut out of spare platforms (Figure 4.18) were used for volume, weight, specific heat, thermal diffusivity and thermal conductivity measurements.



Figure 4.18: cylindrical samples of polyether-ether ketone cut out of spare heat transfer platforms for measurements of density, specific heat and thermal diffusivity and conductivity. Squares in the picture are 5mm in side.

The density  $\rho$  of the material is determined indirectly by separately measuring volumes and weights of the samples and assuming homogeneity of the polymer. Volumes are determined by simple geometrical measurements with a Palmer micrometer-screw within  $\pm 0.4\%$  uncertainty. The weight of the samples is then measured on a Mettler-Toledo precision scale with an uncertainty of  $\sim 0.02\%$ . The thermal diffusivity is measured by laser flash method in a Netzsch Laserflash analyzer LFA457 at the EMPA laboratories in Dübendorf, ZH, Switzerland.

Having determined also the specific heat  $C$  of the PEEK by differential scanning calorimetry – also at EMPA Dübendorf – it is possible to determine both the

thermal effusivity  $\mathbf{e}$  and thermal conductivity  $\kappa$  of the material, recalling the following definitions:

$$\mathbf{v} = \frac{\kappa}{\rho \cdot \mathbf{C}} \quad (4.12)$$

$$\mathbf{e} = \sqrt{\kappa \cdot \rho \cdot \mathbf{C}} \quad (4.13)$$

The values obtained with the corresponding uncertainties are reported in Table 6.

Table 6: thermal properties of the PEEK substrate at ambient temperature

Property [Units]	Value
$\mathbf{v}$ [m <sup>2</sup> /s]	$(1.76 \pm 0.06) \cdot 10^{-7}$
$\rho$ [kg/m <sup>3</sup> ]	$1200 \pm 26$
$\mathbf{C}$ [J/(kg · K)]	$1185 \pm 119$
$\mathbf{e}$ [J · K · √s/m <sup>2</sup> ]	$600 \pm 74$
$\kappa$ [W/(m · K)]	$0.252 \pm 0.03$

The thermal property of greatest relevance for the calculation of the heat transfer quantities is the thermal conductivity  $\kappa$ , as the experiments are performed in a steady-state fashion. Transient thermal behavior is, therefore, not of interest during testing. On the other hand, the thermal effusivity  $\mathbf{e}$  plays a role in the agreement between the heating power measured by step-wise transient tests and the electrical power fed to it. The results for the three power levels used are reported in and compared to the measurements of electrical power. The step-wise transient calibration technique appears to underestimate the heating power by about 22.6%.



Table 7: integral value of power  $P_q$  measured by step-wise transient calibration returns consistently lower values than the ones measured by the electrical power-meter  $P_{el}$ .

$P_{el}$ [W]	$P_q$ [W]	$\Delta P$ [%]
1.2	0.9	-22.2
2.3	1.8	-22.3
3.0	2.3	-23.4

The reason for the mismatch is attributed to possible bias in the indirect determination of the thermal effusivity. The error is, in fact, almost constant with power, indicating a possible error in the proportionality coefficient between slope of the fit and heat flux (i. e., the effusivity). However, thanks to the non-dimensionalization performed in eq. (4.10), the uncertainty in the scaling factor  $S_q$  is independent of errors affecting the thermal properties of the substrate.

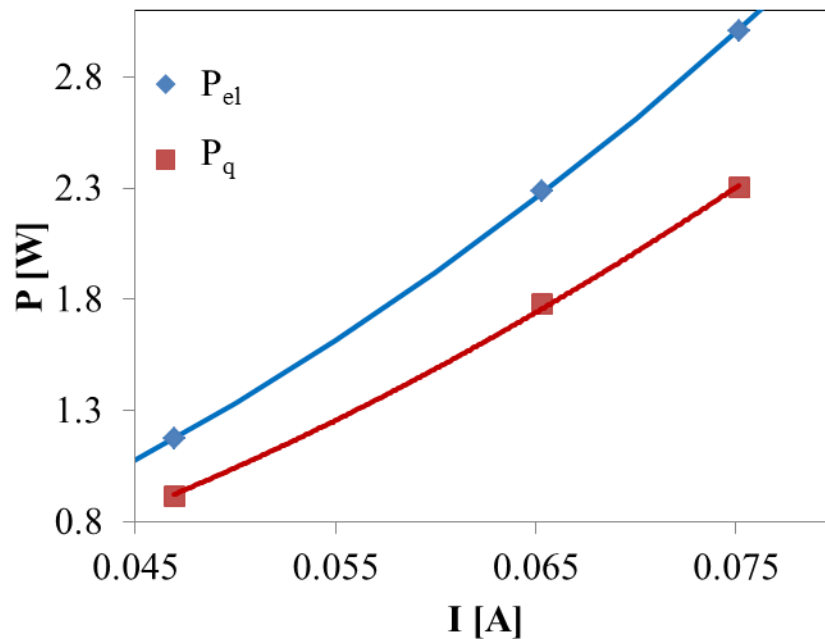


Figure 4.19: the heating power measured by step-wise calibration is consistently  $\sim 22.6\%$  less than the one calculated from the electrical parameters. The mismatch is attributed to a bias in the measured value of thermal effusivity of the substrate.

## 4.6 Measurement Procedure

Once a steady operation of the turbine and the thermal steady state of the platform are reached, data is acquired for 4 levels of average heat flux produced by the heating film, ranging between  $1.7\text{kW/m}^2 \pm 1.6\%$  and  $9.9\text{kW/m}^2 \pm 0.7\%$ . The infrared camera acquisition is synchronized to the rotation of the turbine's shaft by means of an optical trigger. The delay of the frame acquisition with reference to the TTL signal of the turbine's shaft is set so that the platform is centered between the wakes of the upstream stator while its surface temperature is recorded, as shown schematically in Figure 4.20. The estimation is based on the absolute flow angle as measured by a pneumatic 4-hole probe at midspan downstream of the nozzle guide vanes of the turbine. As an additional geometrical reference, the leading edge of the rotor blade sitting on the suction side of the passage is aligned to the trailing edge of a stator vane upstream along the axial direction, while the wake of the neighboring stator vane impinges on the leading edge of the blade on the pressure side of the passage.

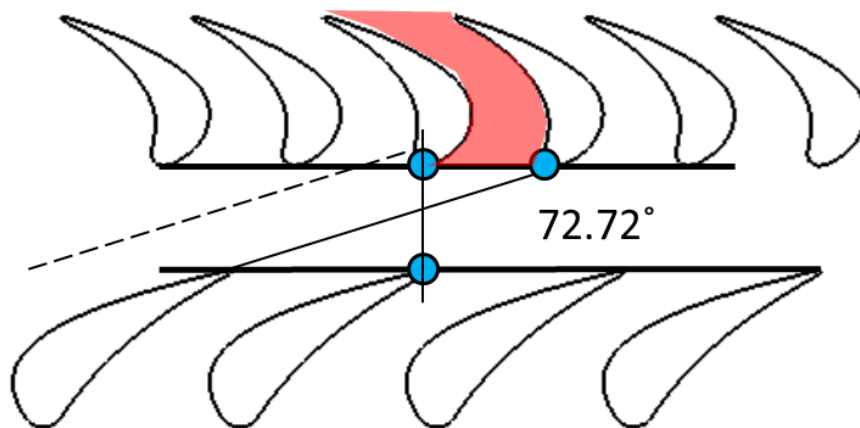


Figure 4.20: stator-rotor geometrical arrangement during image acquisition. The absolute flow angle of  $72.72^\circ$  was measured at design point with a pneumatic 4-hole probe at midspan. The heated platform is centered between the wakes of two stator vanes upstream. For ease of geometrical referencing, the leading edge of the rotor blade on the suction side of the passage is aligned with the trailing edge of a stator vane upstream.

Because of limited optical accessibility, multiple views of the endwall are required to reconstruct the temperature field with sufficient coverage.

Specifically, the inlet portion of the passage until 60% of the axial chord is imaged by positioning the infrared camera at two angles ( $90^\circ$  and  $75^\circ$  with reference to the turbine axis). The outlet portion of the passage is imaged through two smaller ZnSe windows further downstream, traversed circumferentially in 6 different positions. Each recorded sequence consists of 1'000 infrared frames. A sequence is recorded for each of the two camera positions, with two detector integration times:  $10\mu\text{s}$  and  $50\mu\text{s}$ . A total of 16'000 frames is acquired per test case for the inlet portion. An additional 48'000 images are required to cover the outlet region of the passage for each test case. Due to technical difficulties during the measurements, the outlet portion of the passage was only covered for some of the cases presenting purge cavity shaping (chapter 9).

The temperature readings of the PT100 sensors is recorded in intermittent bursts of 5s duration with a sampling rate of 50ks/s.

### 4.6.1 Summary

Accurate knowledge of the heat flux boundary condition provided by the custom-made film heater used in the experiments is crucial for the evaluation of the final results. In order to quantify the locally produced heat flux in a point-wise manner, an experimental technique has been developed allowing the determination over the whole endwall of a non-dimensional parameter  $S_q(\mathbf{x})$ , here denominated “scaling factor”. This parameter is independent of the electrical power fed to the heater and provides a distribution for the non-uniformity in heat flux with respect to the average power per unit surface area.

The uncertainty on  $S_q(\mathbf{x})$  is estimated to be less than 4% on average over the whole endwall.

Coupled with the invariance of the heat transfer coefficient with the thermal wall boundary conditions, the scaling factor allows the measurement of the heat transfer quantities in presence of arbitrary distributions of heat flux on the endwall.



# 5. Uncertainty Analysis

The factors influencing the uncertainty of the heat transfer results obtained from the two experimental setups (iso-thermal setup for stator heat transfer measurements, section 5.1 and iso-energetic for rotor heat transfer measurements, section 5.2) are quite different. The ones playing a role in both experiments change in relevance in dependence of the methodology used.

Each of the critical aspects affecting the accuracy of the measurements in both of the circumstances is addressed in the following sections, with each contribution quantified.

The resulting uncertainty distributions and corresponding average values are also provided.

## 5.1 Uncertainty Analysis for the Stator Endwall Heat Transfer Measurements

### 5.1.1 In-Situ Calibration of the Infrared Camera

The in-situ calibration of the infrared camera (see section 3.4.1 ) serves two purposes:

- prior to installing the ZnSe optics, images of the endwall are acquired at all 48 infrared camera positions to obtain a geometrical calibration from the image referencing of the infrared markers on the measurement area (section 3.4);
- in presence of the ZnSe optics in the optical path, the temperature reading of the camera sensor is related to the temperature value recorded by the PT100 embedded in the stator 2 heat transfer platform. While the turbine is not in operation, the platform is iso-thermal and the PT100 reading can be used to calibrate each pixel of the camera at each of the 48 camera positions, accounting for reflections and transmissivity losses.

Distributions of the fit coefficients are shown in Figure 5.1 a) and b), together with linear fits for the locations marked.

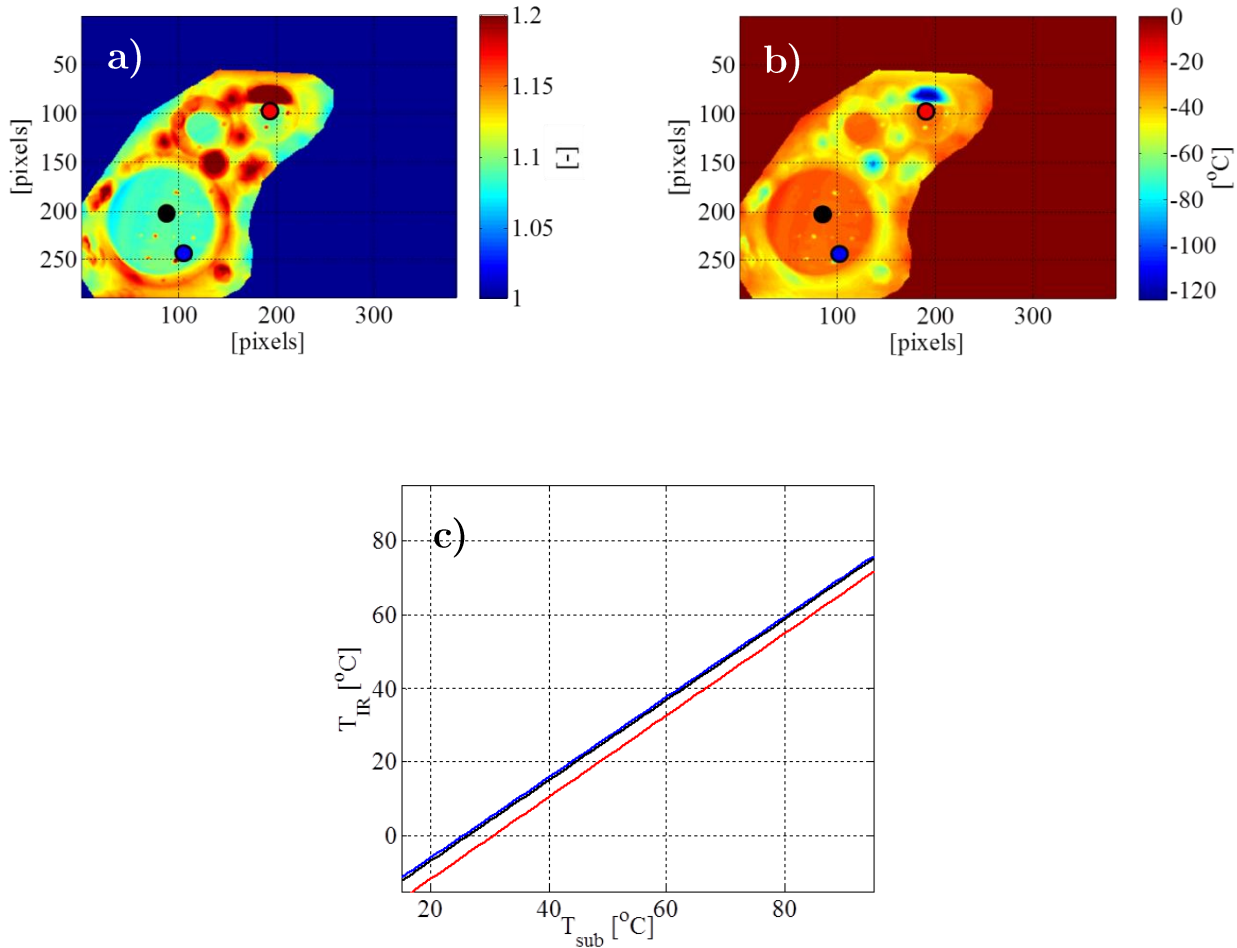


Figure 5.1: distributions of linear fit coefficients for in-situ, pixel-by-pixel temperature calibration with ZnSe windows optics for one of the 48 camera positions. a) proportional coefficient b) offset. c) example of linear calibration curves for the three locations marked in a) and b).

Based on test images, the positioning error of the geometrical reconstruction has been evaluated in 0.3mm (section 2.2).

The temperature calibration excludes the influence of the transmission losses due to the presence of ZnSe windows (a similar approach is followed in the quasi-in-situ calibration of the camera for the rotor measurements, see section 5.2.1 ) and relates the uncertainty in temperature to the calibration error of the PT100 (sec-

tion 5.1.4 ) and the temperature uniformity of the substrate during operation (section 5.1.2 ).

### 5.1.2 Non-Uniformity in the Aluminum Temperature

The non-uniformity of the temperature of the aluminum solid plays a relevant role in the uncertainty propagation, as the conductive heat flux to the endwall surface is calculated according to equation (2.13), based on the assumption of uniform temperature and one-dimensionality.

Strong thermal gradients in the bulk material, in fact, would induce three-dimensional heat conduction within the solid rather than heat flowing to the surface normally to it.

The assumption is therefore verified in two ways:

1. The PT100 data are examined for all temperature steps;
2. 3D FEM analyses based on experimental boundary conditions are performed for multiple water temperatures. The results are then compared to the experimental data from the PT100 RTDs. The purpose of the simulations is two-fold: potentially missing data from temperature transducers can be replaced with information from the FEM results; the temperature field in the solid can be examined in greater detail after validation by means of the RTD values.

The FEM model consists of 720'520 nodes and 2'238'009 elements. All the layers composing the insulating auxiliary wall, including the high-emissivity coating, are modelled.

The experimental boundary conditions applied are:

- wall temperature distributions from the infrared measurements on the endwall;
- convective heat transfer coefficient on the walls of the internal water channels. These are derived from flowrate measurements from the water distribution system and pipe correlations;

- water temperatures on the walls of the internal water channels, also measured in the water distributor.

Additionally, convective heat load distributions are imposed on the lower 30% of the vanes included in the model. These distributions are derived from preliminary CFD simulations performed in ANSYS CFX.

The simulations are performed for water temperature steps corresponding to the ones used for the measurements.

Typical results are shown in Figure 5.2 for the highest operating temperature of the heat transfer platform. At this set point (water temperature  $\sim 90^\circ\text{C}$ ), the non-uniformities in the bulk temperature are the most severe due to conductive heat losses at the leading and trailing edge of the stator segment, despite the presence of POM-C insulation.

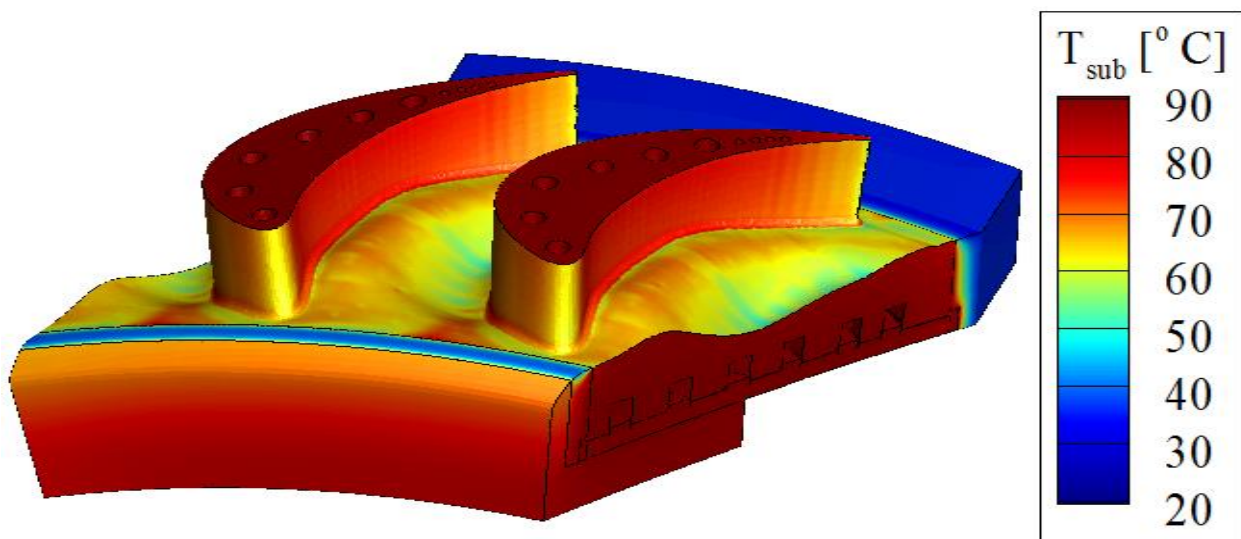


Figure 5.2: 3D FEM results for the evaluation of the bulk temperature non-uniformity in the heat transfer platform. The wall temperature distribution is experimental.

The value of non-uniformity used for the uncertainty analysis is the one portrayed in Figure 5.3 as a function of the water set point. In the worst condition (the highest water set point of  $90^\circ\text{C}$ ), this non-uniformity reaches  $\pm 1^\circ\text{C}$ .



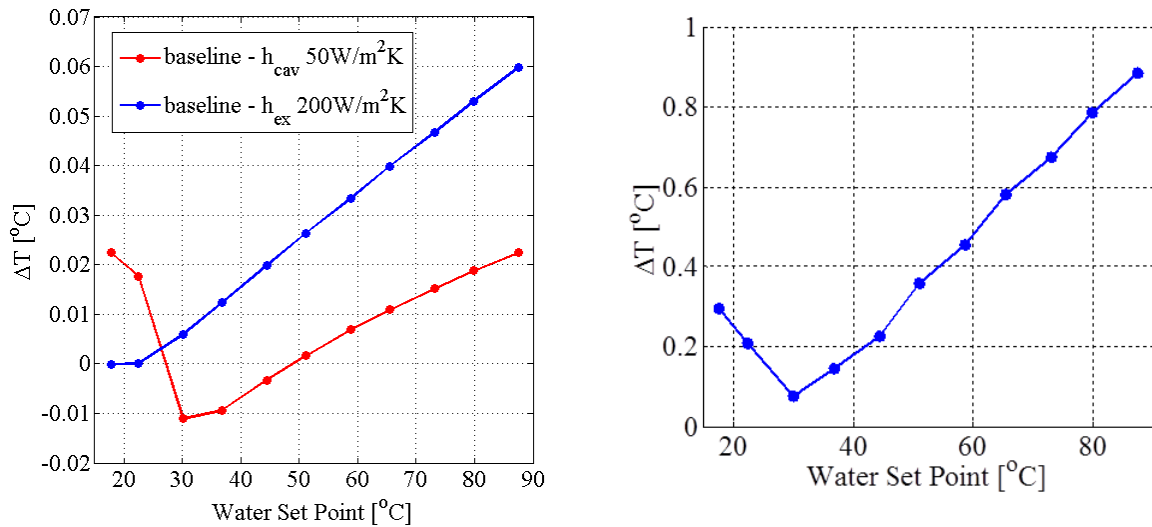


Figure 5.3: left, comparison between baseline FEM simulation with  $h_{cav}$  and  $h_{ex}$  equal to  $100 \text{ W/m}^2\text{K}$  and FEM simulations with altered convective boundary conditions at inlet and outlet of the segment. The sensitivity of the results to the alterations is considered negligible (less than  $0.06^\circ \text{C}$ ). Right, maximum difference between the average experimental PT100 data and all the individual readings is plotted against the water set point. This distribution is used as bulk temperature uncertainty as a function of temperature in the uncertainty analysis.

A dramatic overprediction of the conductive losses at the leading and trailing edge of the platform make the overall results unusable for a reliable calculation of the temperature non-uniformity. However, the simulations are validated by the PT100 readings in the middle of the passage, as visible in the comparison of the laterally averaged values of Figure 5.4.

The sensitivity of the model to the convective heat transfer in the upstream cavity and the downstream support ring is studied, as these are the most uncertain boundary conditions. No significant alteration of the thermal non-uniformity is observed compared to the baseline (cavity heat transfer coefficient  $h_{cav} = 100 \frac{\text{W}}{\text{m}^2\cdot\text{K}}$ , downstream heat transfer coefficient  $h_{ex} = 100 \frac{\text{W}}{\text{m}^2\cdot\text{K}}$ ).

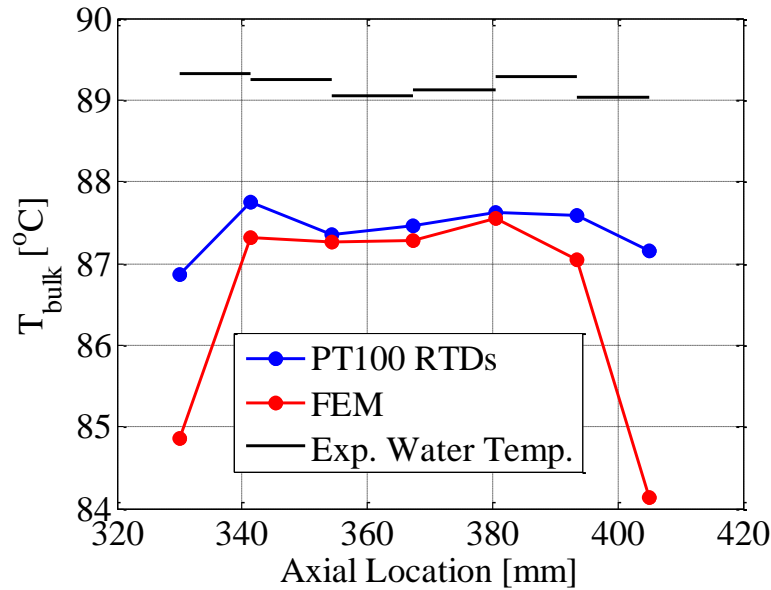


Figure 5.4: comparison between the laterally averaged data for the bulk temperature of the heat transfer platform for the highest water set point ( $\sim 90^\circ\text{C}$ ). The overprediction of the conductive losses at the leading and trailing edge of the platform are evident, however the values at mid-passage show good agreement. As a reference, the water temperature in the water channels used as boundary condition for the FEM is shown in black.

### 5.1.3 Non-Uniformity of the Thermal Resistance of the Insulation

Uncertainties in the thermal properties of the insulating layer directly reflect on the uncertainty in the conductive heat flux to the endwall (equation 2.12) and therefore affect indirectly the heat transfer quantities. As explained in section 3.2.3, given the aggressive, non-axisymmetric endwall contouring of stator 2, the application of the Kapton® auxiliary wall is challenging and prone to air entrainment, despite the reduction in the size of the patches used to approximate the endwall shape. It is therefore necessary to quantify possible deviations in the shape of the endwall profile compared to the nominal one and relate it to local variations in the thermal properties of the insulating layer (thickness or thermal conductivity due to the presence of micro-bubbles of air).

Two methodologies are used to evaluate the quality and the properties of the layer:

- a step-wise laser pulse technique devised by Laveau (see [38]) with the purpose of testing the multilayer for the presence of micro-bubbles
- a differential 3D scanning of the stator segment before and after the application of the multilayer to evaluate the deviation of the multilayer from the nominal geometry. This provides information on the actual thickness of the adhesive layer underneath the Kapton® sheet.

### Surface Thermal Response to Laser Pulses

As extensively described by Laveau ([38, 100]), it is possible to derive the local thermal resistance of a multilayer by exposing it to a step pulse from a laser light source and recording the transient heating of the spot.

In particular, modeling the Kapton®/adhesive and aluminum multilayer as a 2-layer system (the thermal properties of Kapton® and the 3M 467MP adhesive are close, see Table 8 and the thicknesses of paint and adhesive amount to respectively 24% and 40% of the polyimide sheet thickness), the following equation applies (Murphy et al. [124]):

$$T(t) - T_{t=0} = C_c \sqrt{t} \left\{ 1 + \sum_{n=1}^{\infty} 2(-\Gamma)^n \left[ e^{-\frac{n^2 L^2}{\alpha_0 t}} - \frac{nL\sqrt{\pi}}{\sqrt{\alpha_0 t}} \operatorname{erfc}\left(\frac{nL}{\sqrt{\alpha_0 t}}\right) \right] \right\} \quad (5.1)$$

having defined in equation (5.1) the following quantities:

$$C_c = \frac{\varepsilon(1 - R)I}{4\pi^{3/2}e_0} \quad (5.2)$$

$$\Gamma = \frac{e_1 - e_0}{e_1 + e_0} \quad (5.3)$$

Respectively,  $C_c$  of equation 5.2 (Osiander and Spicer [125]) is the incident laser power and  $\Gamma$  is the thermal mismatch factor between layers “0” and “1” of the schematic in Figure 5.5. The thermal effusivities of the layers are indicated with the symbol  $e$ , while  $\varepsilon$  is the surface emissivity,  $R$  the surface reflectivity and  $I$  the laser pulse energy density.

Table 8: thermal properties of Kapton® polyimide (DuPont™) and 3M 467MP adhesive.

Property	Kapton®	3M 467MP	Nextel Velvet Coating 811-21
$\kappa \left[ \frac{\text{W}}{\text{m}\cdot\text{K}} \right]$	0.21	0.17	0.19
$C_p \left[ \frac{\text{J}}{\text{kg}\cdot\text{K}} \right]$	1'090	1'000	1'000
$\rho \left[ \frac{\text{kg}}{\text{m}^3} \right]$	1'420	1'012	2'000
$\nu \left[ \frac{\text{m}^2}{\text{s}} \right]$	$1.36\cdot 10^{-7}$	$1.68\cdot 10^{-7}$	$0.95\cdot 10^{-7}$
$e \left[ \frac{\text{W}\cdot\sqrt{\text{s}}}{\text{m}^2\cdot\text{K}} \right]$	570	415	616

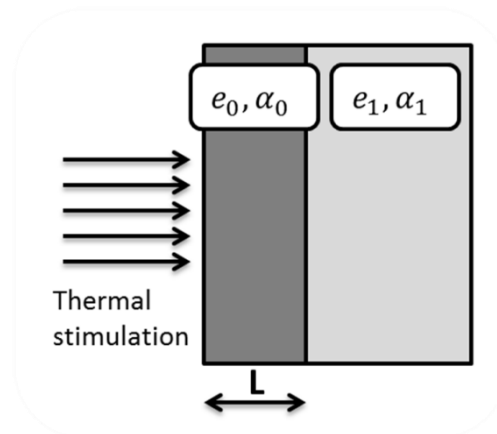


Figure 5.5: schematic of a two layer system exposed to surficial thermal stimulation (e. g. laser pulse).

The temperature rise is, therefore, proportional to the laser pulse energy density  $I$ . However, it is possible to define a normalized temperature rise or “thermal contrast”  $C_{\text{ratio}}(t)$ :

$$C_{\text{ratio}}(t) = \frac{T(\mathbf{x}, t) - T(\mathbf{x}, t=0)}{T(\mathbf{x}_{\text{ref}}, t) - T(\mathbf{x}_{\text{ref}}, t=0)} \quad (5.4)$$

Where the temperature rise as a function of time for an arbitrary spot  $\mathbf{x}$  on the endwall is normalized by the temperature rise of a reference point  $\mathbf{x}_{\text{ref}}$  for which the thermal properties of the layer correspond to the nominal values, i. e., no detachment or air entrainment has taken place.

In virtue of the normalization, provided that the temperature rise is induced by the same light source, at the same distance and with the same optical arrangement, the thermal contrast  $C_{\text{ratio}}(t)$  is theoretically independent of the pulse energy density  $I$ .

The thermal contrast  $C_{\text{ratio}}(t)$  can be related to air thickness below the insulating layer by means of the experimental calibration by Laveau [38]: a calibration block with CNC machined pockets modeling air bubbles with varying thicknesses is covered with the same multilayer used on the stator segment. The thermal contrast of this calibration block is mapped with the laser pulse technique and related to the known thickness of the air bubbles (Figure 5.6). The measured thermal contrast on the segment is therefore translated into a distribution of air thickness below the insulating layer.

The calibration plate carries artificial air bubbles of thickness ranging between 10 and 50 $\mu\text{m}$ . The method is therefore to be considered calibrated for these values of air thickness. Because different lateral conduction effects or natural convection within the air bubble may occur for thicknesses outside of the calibration range, data showing air thicknesses beyond this interval are to be attentively considered.

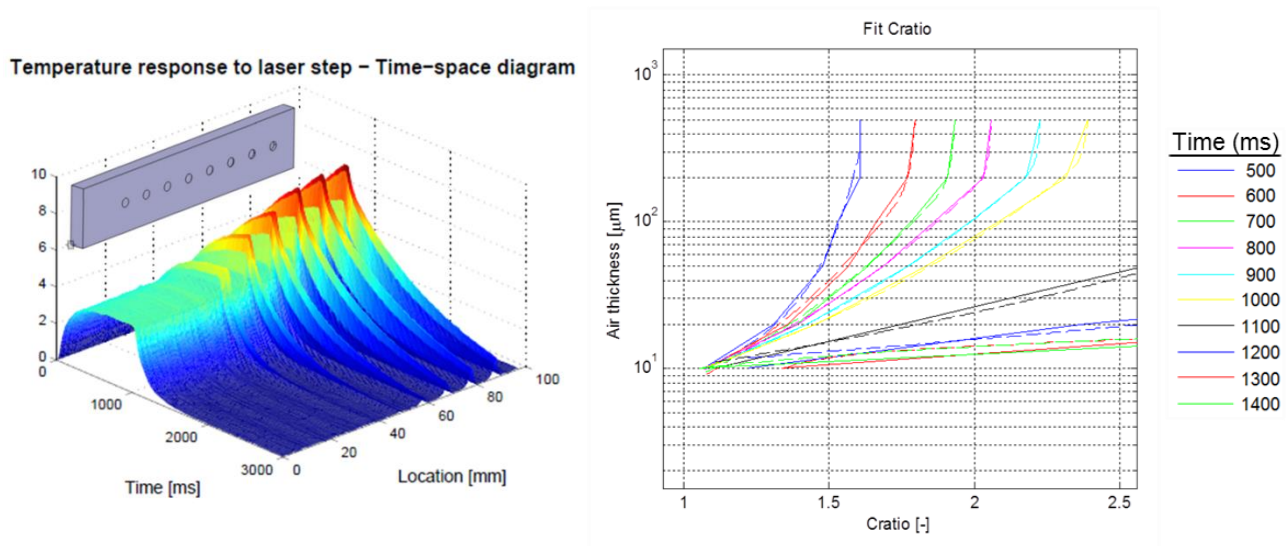


Figure 5.6: left, temperature rise as function of space and time for the calibration plate; right, the measured thermal contrast (solid lines) is used to derive fitting curves (dashed lines) relating thermal contrast to air thickness (Laveau [38]).

Because of the limited optical accessibility to the endwall of the segment, the traversing system used for the measurements (section 3.4) is adapted for use in the calibration procedure. The robot arm traverses the calibration plate and the segment, while the infrared camera and the laser are fixed to an optical table. The robot places adjacent points of the endwall at the focus of the camera and waits for the data collection to be completed before moving to the next position. The positions are defined by means of a Matlab program, calculating the robot coordinates after a spatial calibration similar to the one described in section 3.4.1

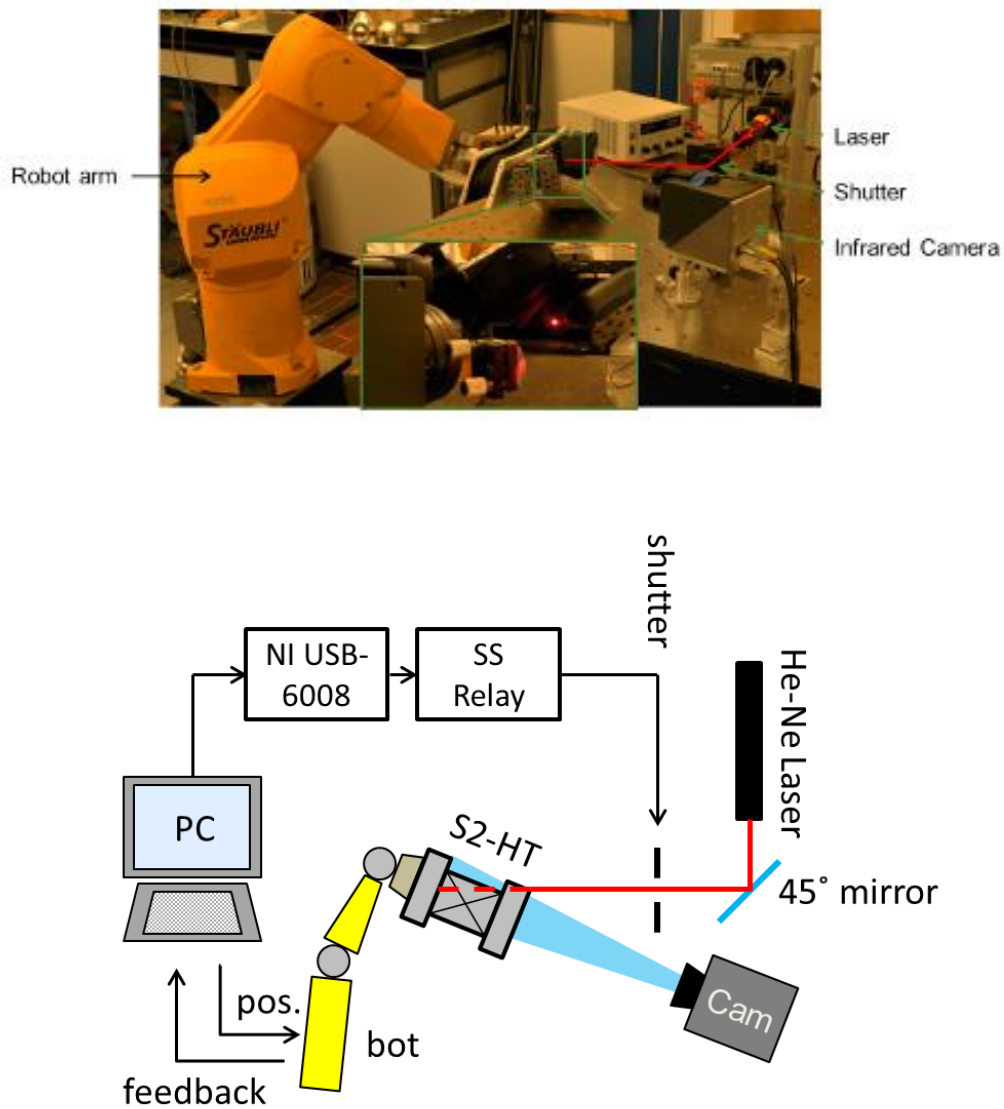


Figure 5.7: top, the setup for thermal diffusivity measurement during operation; bottom, the schematic of the setup. A computer controls the position of the robot and starts the laser irradiation and the camera acquisition once the segment is in the desired location.

The results are projected on a triangular mesh of the endwall, also used to determine the robot positions for the data collection and are displayed in Figure 5.8.

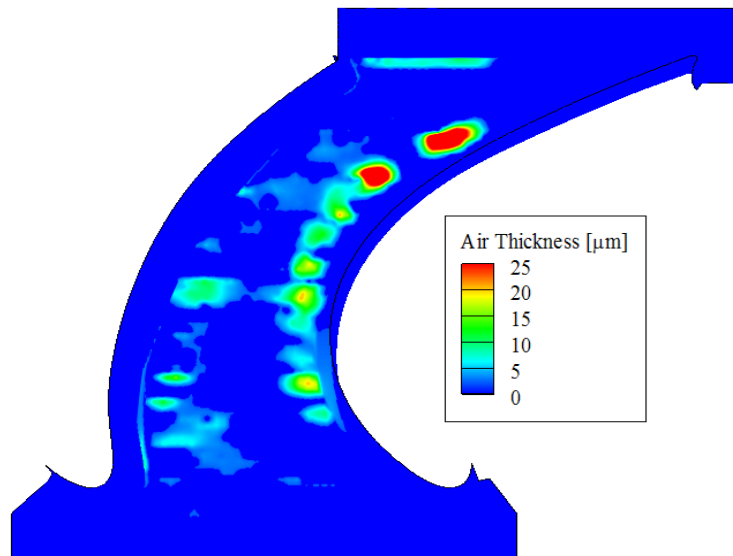


Figure 5.8: thermal thickness derived from the thermal contrast measurements and translated to equivalent air thickness.

It is found that, when correcting the heat transfer data for air entrainment as specified by the distribution of Figure 5.8, the heat transfer coefficient contours are overcorrected and do not match the levels in the unaffected regions (blue in Figure 5.8). The additional “thermal thickness” detected is therefore imputed to locally thickened adhesive.

In order to reconstruct the physical additional thickness of the adhesive, a comparative 3D scan of the part with and without insulating layer is performed and the results are presented in the following section.

### Differential 3D Scan of the Stator Segment

The stator segment is optically scanned with an ATOS Professional system by GOM. A scan is performed before and after the application of the insulating multilayer of Kapton® and adhesive, with the objective of obtaining a point-wise distribution of thickness of the layer over the endwall.

The scan of the bare aluminum segment is necessary to account for manufacturing deviations from the nominal geometry specified in the CAD model.



The highest deviations ( $\sim 80\mu\text{m}$ ) are found in correspondence of the fillets, which are not included in the measurement area (Figure 5.9).

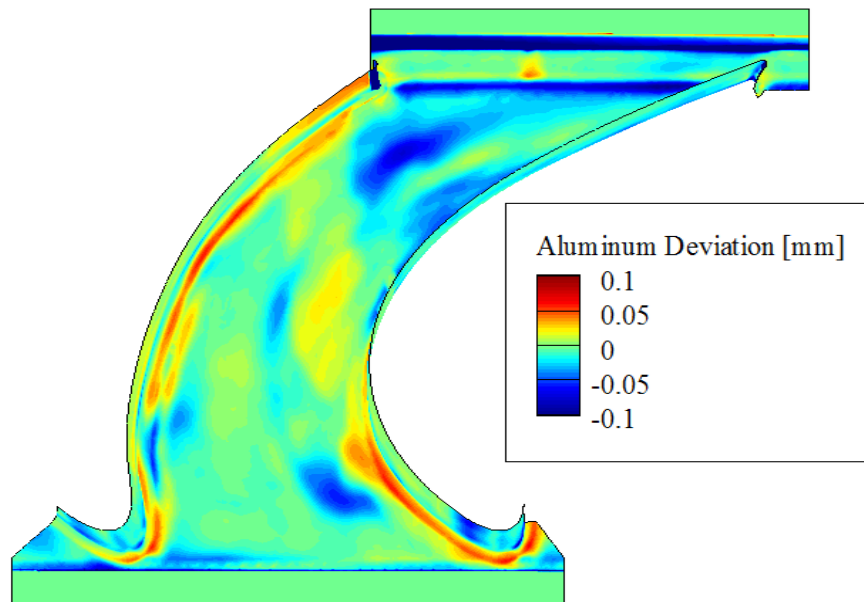


Figure 5.9: deviation of the actual, CNC machined part with reference to the nominal CAD geometry.

Anywhere else, the geometry lies within the requested manufacturing tolerances of  $\pm 50\mu\text{m}$ .

The direct comparison of the cloud of points obtained by the 3D scanner and the CAD is carried out in the GOM Workbench, which allows alignment of the two data sets.

By difference, the map of is recovered, showing the deviation of the insulating multilayer from the nominal geometry (Figure 5.10).

The information of Figure 5.10 is used to correct the heat transfer results based on the actual thermal resistance of the insulating layer point-by-point.

However, because the method has a minimum resolution of  $20\mu\text{m}$ , only data showing an additional thickness of the insulating layer beyond this value is considered for the correction of the heat transfer data.

The distribution of additional thickness to be added to the default value is shown in Figure 5.11.

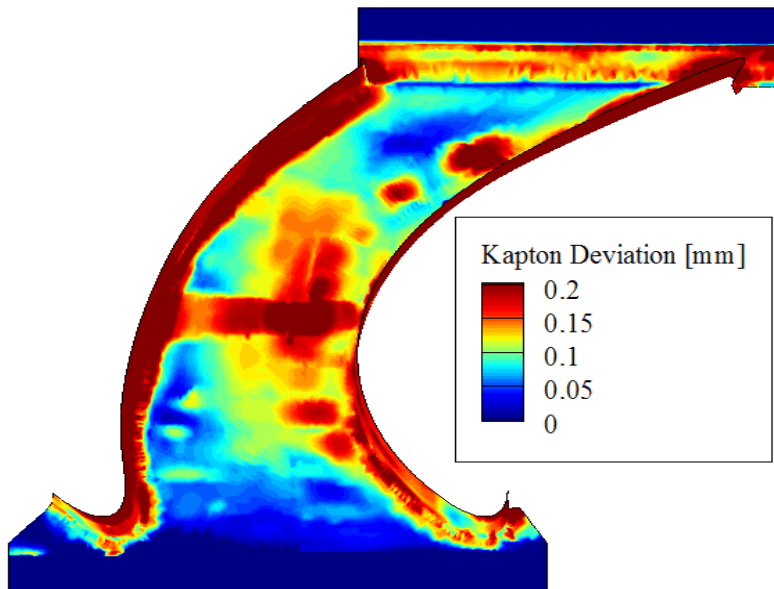


Figure 5.10: distribution of deviation between the insulating multilayer (paint/Kapton®/adhesive) and the nominal CAD geometry of the endwall segment. The discrepancies are attributed to thickened adhesive in locations of difficult attachment of the layer to the aluminum substrate due to strong local curvature.

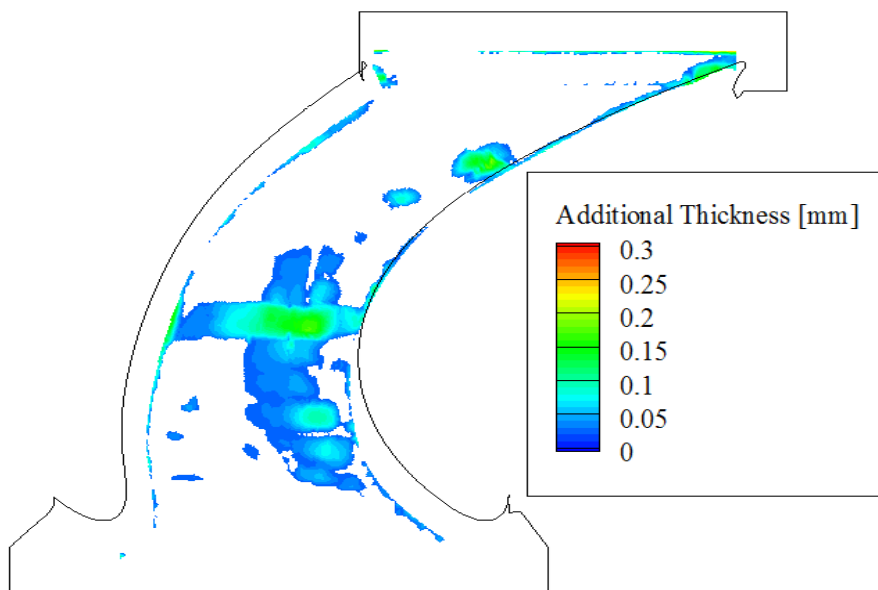


Figure 5.11: distribution of additional thickness in the insulating layer of adhesive/Kapton®/paint. Results are blanked for values below the resolution of the 3D scanner: 20 $\mu$ m.

The additional thickness distribution is added to nominal thickness of the insulating layer (205 $\mu\text{m}$ ). It is assumed that the adhesive layer presents non-uniformities due to a redistribution of the material after its gluing on the endwall and thermal cycling. The altered thermal resistance of the layer results in a matching of the contour levels of heat transfer coefficient with the surrounding values.

The 20 $\mu\text{m}$  resolution of the scanner contributes by  $\sim 0.5\%$  to the global uncertainty in Nusselt number in the locations where the correction is applied.

#### 5.1.4 PT100 Calibration Error

All of the 52 PT100 RTDs integrated in the aluminum solid are calibrated at once in LEC's calibration oven, by stepping the temperature of the chamber at 10 different levels for 3 cycles. The average values for the cycles is considered to define a quadratic calibration curve for each sensor, starting from the reference values acquired by two high-precision, reference RTDs inside the chamber kept in the proximity of the segment during calibration.

The average error of the calibration curve is less than 0.05  $^{\circ}\text{C}$  (for a confidence level of 95%).

#### 5.1.5 Final Uncertainty Distributions for Stator Endwall Results

The perturbation method by Moffat [126] enables the analysis of the propagation of the uncertainties from all sources to the final results of Nusselt number  $\text{Nu}$  and adiabatic wall temperature  $T_{\text{aw}}$  (see Figure 5.12 and Figure 5.13). The most relevant parameters affecting the heat transfer coefficient results are – as anticipated – the thermal and geometrical characteristics of the insulating layer: thermal conductivity and thickness of adhesive, Kapton<sup>®</sup> and paint, respectively accounting for 5.6 to 18.0% and 14.3 to 17.4% of the overall average error. Despite the surface temperature  $T_{\text{IR}}$  reading having little effect on the heat transfer

coefficient, it is by far the main contributor to the uncertainty in adiabatic wall temperature  $T_{aw}$  (it accounts for more than 63% of the error).

An additional uncertainty parameter is considered for the additional adhesive thickness reconstructed by means of 3D scanning ( $dt_{p,add}$ ).

Table 9: individual contributions to overall uncertainty levels in heat transfer coefficient  $h$  and adiabatic wall temperature  $T_{aw}$ .

		$h$	$T_{aw}$
$\delta t_{adh}$ [%]	adh. thickness	18.0	3.8
$\delta k_{kap}$ [%]	Kapton® th. cond.	17.4	2.9
$\delta t_P$ [%]	paint thickn.	14.5	3.8
$\delta k_P$ [%]	paint th. cond.	14.4	2.9
$\delta k_{adh}$ [%]	adh. thickn.	14.3	2.9
$\delta t_{kap}$ [%]	Kapton® thickn.	9.1	3.7
$\delta t_{add}$ [%]	add. adh. thickn.	5.6	3.4
$\delta T_s$ [%]	solid temperature	1.3	3.2
$\delta t_{p,add}$ [%]	add. paint thickn.	1.3	3.2
$\delta T_{t,in}$ [%]	tot. inlet temp.	1.3	3.7
$\delta T_{IR}$ [%]	surf. temp.	1.3	63.1
$\delta \varepsilon$ [%]	surf. emissivity	1.3	3.4

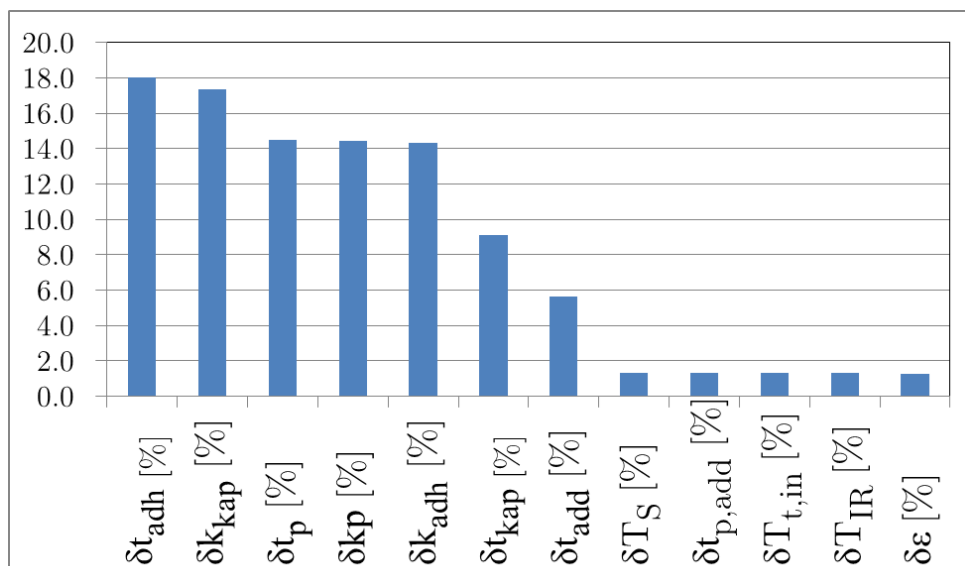


Figure 5.12: histogram of contributions to global average uncertainty in heat transfer coefficient.

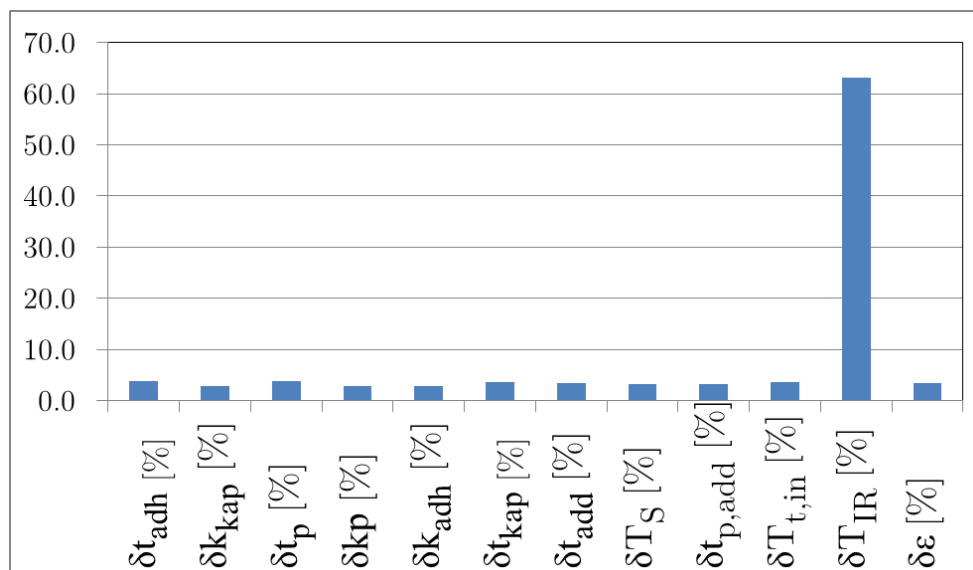


Figure 5.13: histogram of contributions to global average uncertainty in adiabatic wall temperature. The surface temperature measured by the infrared camera is the main source of uncertainty.

The contributions of the main factors result in the distributions shown in Figure 5.14, respectively for Kapton® thermal conductivity and adhesive thickness.

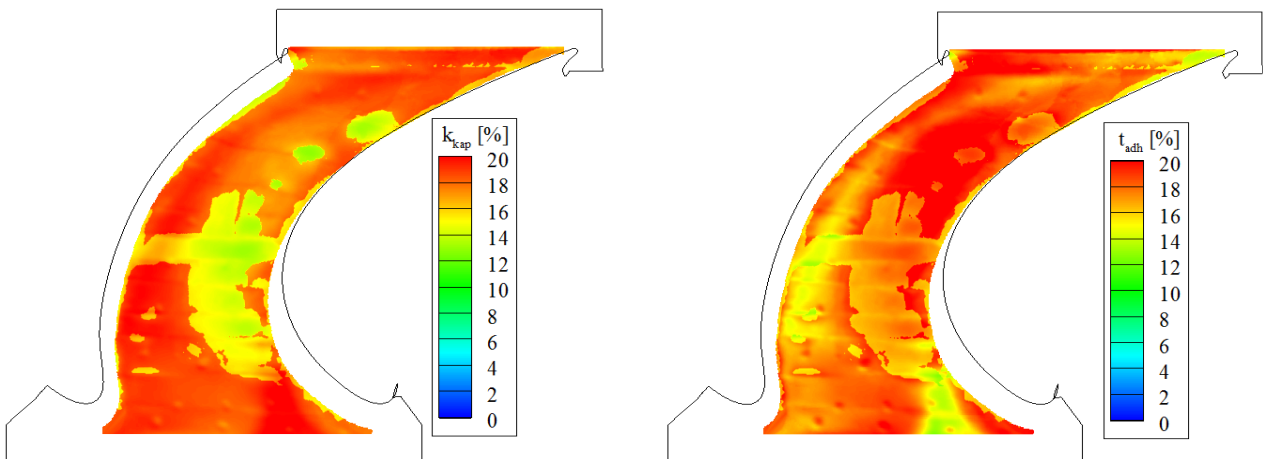


Figure 5.14: left, contribution of uncertainty in Kapton® thermal conductivity to global uncertainty in heat transfer coefficient; right, contribution of uncertainty nominal adhesive thickness to global uncertainty in heat transfer coefficient.

The relative contribution of the uncertainty in the nominal values of the properties of the layer drops in correspondence of the locations where the additional adhesive thickness is detected. In these locations, in fact, a major contributor to the uncertainty is the resolution of the 3D scanning methodology presented in section 5.1.3 .

The distributions in Figure 5.15 show the impact of the uncertainty in additional adhesive thickness determined by differential 3D scanning on the global level of uncertainty in heat transfer coefficient (left) adiabatic wall temperature (right) in percentage of the local value of global uncertainty.

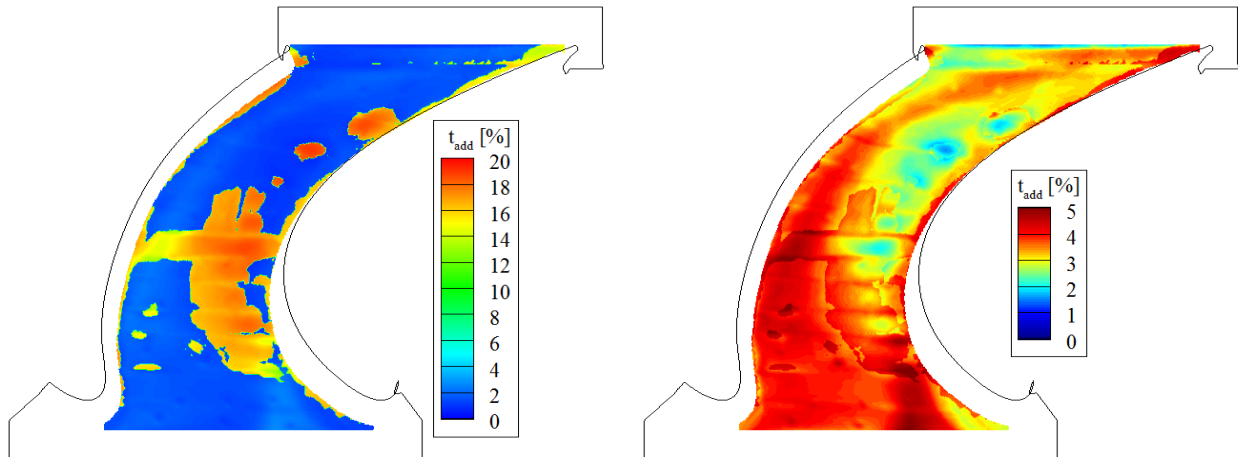


Figure 5.15: the additional adhesive thickness measured by differential 3D scanning of the heat transfer platform is used only at locations for which the threshold given by the method's resolution is exceeded. In these locations, essentially concentrated at mid-passage, the uncertainty in the measured value of additional thickness contributes to the global uncertainty in heat transfer coefficient by up to 20%.

As far as the adiabatic wall temperature is concerned, the wall temperature is on average the most relevant contributor to its uncertainty. The distribution of its impact, shown in Figure 5.16, highlights how the highest uncertainty is reached in correspondence of the highest levels of heat transfer coefficient. This can be explained by the fact that the excursion in surface temperature for these locations is reduced by the higher heat load. Therefore, the same uncertainty in wall temperature propagates more severely to the calculation of the intercept of the linear fit (section 2.3.1 ).

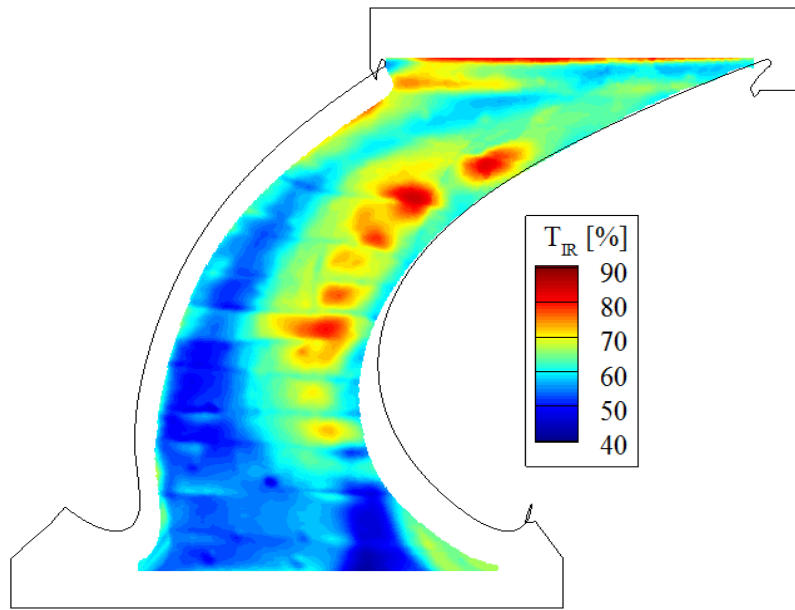


Figure 5.16: the impact of the uncertainty in wall temperature measured by infrared camera is the highest in locations of lower wall temperature excursion (i. e., where the heat transfer coefficient is the highest). Values are expressed in percentage of the global local uncertainty in adiabatic wall temperature.

The final distributions of uncertainty for the design point test case with 0.8% injection ratio are presented in Figure 5.17. On average, the uncertainty in Nusselt number over the endwall area is 9.7%, while the uncertainty in adiabatic wall temperature is of 0.71K.

Clearly, where the adhesive thickness correction is introduced, the uncertainty in Nusselt number is higher. Its effect, however, is limited to a  $\sim 0.5\%$  increase compared to surrounding levels.



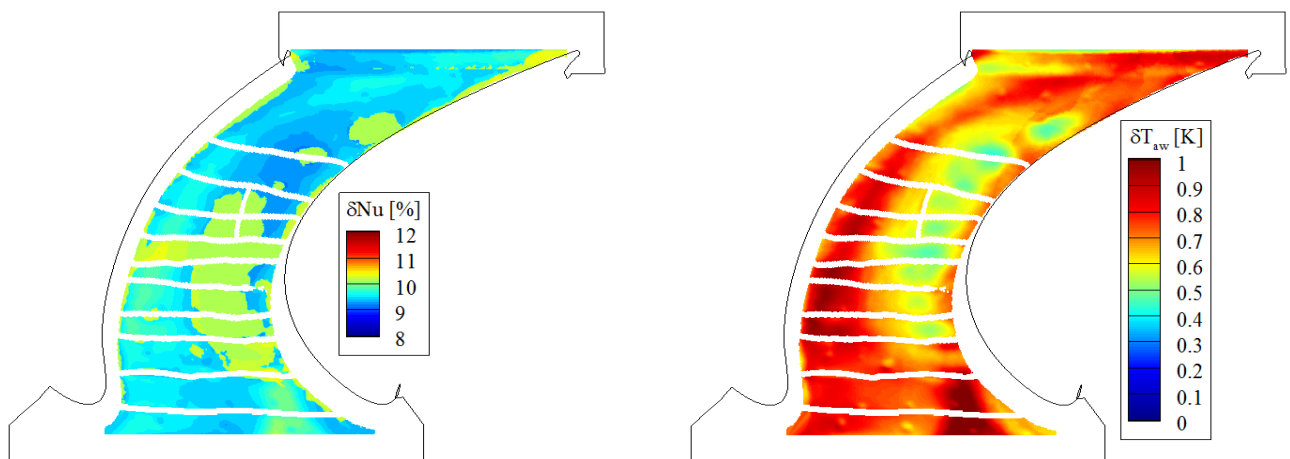


Figure 5.17: final distributions of uncertainty for design point with injection ratio IR of 0.8% for Nusselt number (left) and adiabatic wall temperature (right). The average values of uncertainty are, respectively, 9.7% for the former and 0.71K for the latter.

## 5.2 Uncertainty Analysis for the Rotor Endwall Heat Transfer Measurements

The purpose of this section is to provide details on the diverse sources of errors affecting the precision and accuracy of the heat transfer measurements performed on the rotating frame of reference.

Differently than in the previous section, because of the different technique, the thermal characteristics of the top layer covering the endwall do not contribute significantly to the overall uncertainty.

It can be anticipated that the uncertainty in the determination of the heat transfer quantities, i.e. heat transfer coefficient and adiabatic wall temperature essentially propagates from the following three main factors:

- errors in the determination of the endwall temperature (section 5.2.1 ).
- errors in the determination of the electrical heat flux provided at the end-wall (section 5.2.2 );
- errors in the determination of the conductive losses through the insulating substrate (section 5.2.3 ).

However, these three main factors themselves are indirectly measured. Therefore, in order to provide indications on how to possibly improve the quality of the final results, each direct contributor to the final uncertainty must be individually addressed.

The following paragraphs provide a quantification of these contributions.

## 5.2.1 Errors in Surface Temperature

### Mitigation of Errors due to Trigger Jittering

The impact of this procedure on the accuracy of the temperature data is shown in Figure 5.18. The maximum value of the standard deviation between frames is reduced by a factor 2.3. Furthermore, the area affected by standard deviation values greater than 5% is reduced from 12.3% to 5.3% of a frame and limited to the region closer to the edges of the heated endwall (that is, the area covered by standard deviation values beyond 5% drops by 330 times).

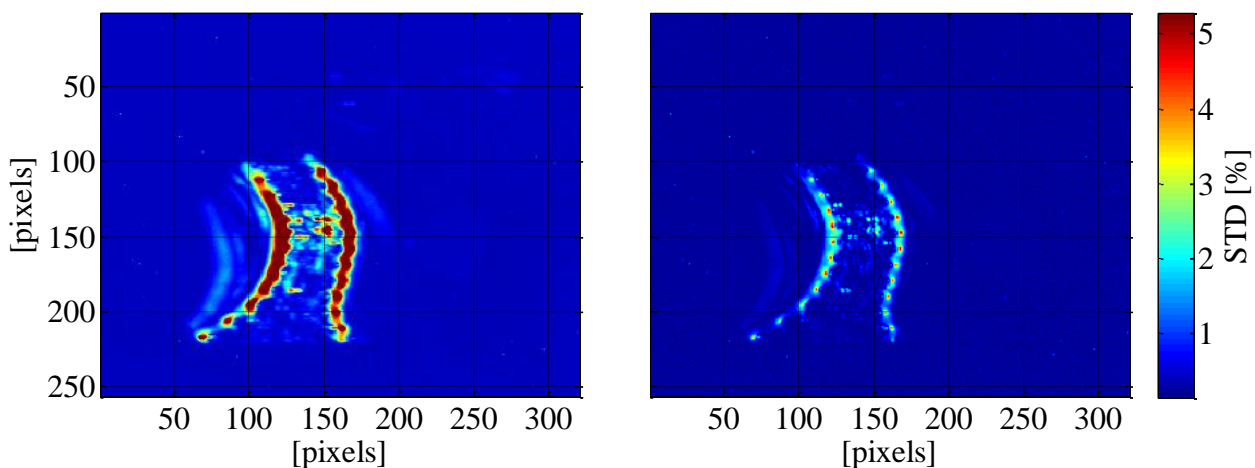


Figure 5.18: standard deviation of a sequence of infrared images before and after registration. Areas with standard deviation values beyond 5% are reduced by a factor of  $\sim 330$ . The maximum value is reduced by 2.3 times.

### Impact of Image Reconstruction Procedure

The frequency spectra-based image reconstruction procedure described and validated in section 2.2 reaches the goal of producing infrared frames with an iso-

tropic spatial resolution of 0.36mm/pixel while maintaining the detector fill within the recommended operational range of the camera for the temperature interval measured (section 2.1.5 ). However, the combination of the two data sets with different camera sensitivity levels introduce an error that, in section 2.2, was conservatively estimated to be of 0.46K based on the average value calculated on a rectangular region of interest including the hottest pixels in the frame.

By projecting the error distributions for all views onto the rotor endwall mesh and averaging the values in the region where the distributions overlap, it is possible to obtain a point-by-point map of the error introduced by the reconstruction procedure (Figure 5.19).

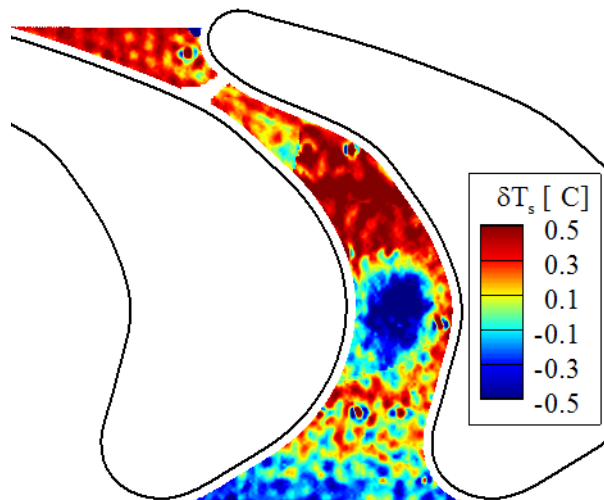


Figure 5.19: error distribution over the rotor endwall due to the frequency-based image reconstruction procedure (see section 2.2). Minimum value XXK, maximum XXK, root mean square value over the endwall is 0.27K.

The surface temperature appears to be underestimated in the centre of the passage, where the temperatures are the highest due to the heat flux non-uniformities detected in chapter 0, while it is mostly overestimated elsewhere.

The error distribution ranges from a minimum of -1.19K to a maximum of 1.18K. However, it can be seen how most of the passage (88%) has error values that are within  $\pm 0.5$ K.

As a result, the average error over the passage is within  $\pm 0.27$ K.

### Errors due to Radiative Losses through IR Transparent Optics

The semi in situ calibration procedure explained in section 2.1.5 ensures that the transmissivity losses through the infrared transparent optics in ZnSe are accounted for. However, the actual transmissivity  $\tau$  of the optics has been estimated by running two calibrations with and without Zinc-Selenide windows interposed between the infrared camera and the black-body radiative source.

The transmissivity can be calculated as:

$$\tau \approx \left( \frac{T_{\text{BB, ZnSe}}}{T_{\text{BB, NoZnSe}}} \right)^4 \quad (5.5)$$

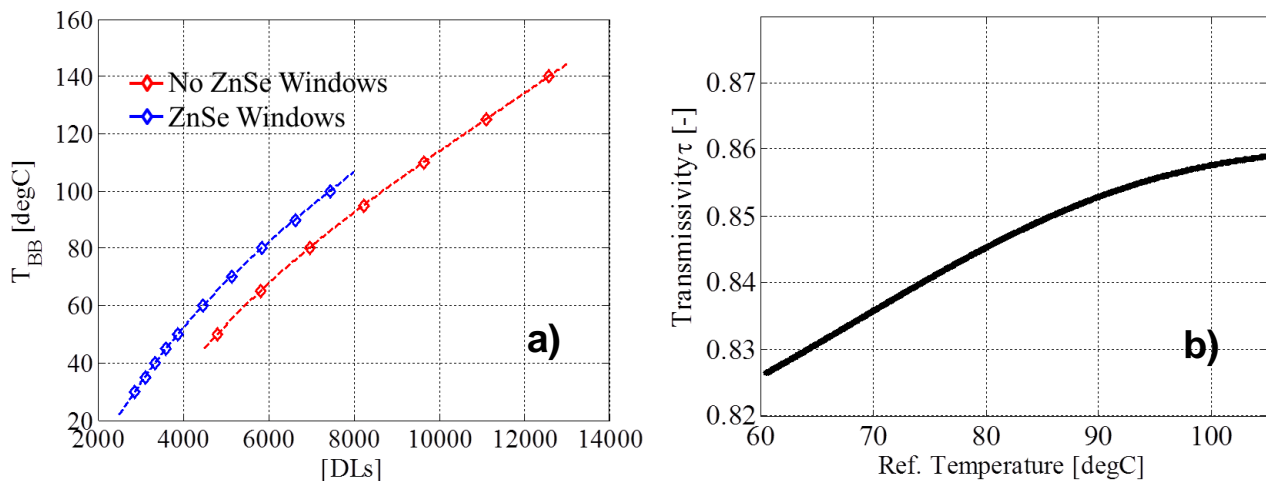


Figure 5.20: comparison of calibration curves with and without ZnSe windows in the optical path a); transmissivity of the ZnSe optics as a function of black body surface temperature b).

### IR Camera Calibration Errors

There are essentially three sources of errors arising from the calibration of the infrared camera with a reference radiative source:

- Errors in the fitting curve calculated from the acquired data points;
- Errors in the uniformity of the temperature over the surface of the radiative source – the reference temperature value is calculated as an average over such surface;
- Errors in the stability of the temperature of the reference surface, as it is assumed for it to be stationary over the averaging time.

The 4<sup>th</sup> order polynomial calibration curve shown in Figure 2.10 presents a root mean square error of less than 0.04 °C.

The non-uniformity in temperature over the surface of the radiative source is evaluated as two times the standard deviation of the temperature measured by the camera over the pixels considered for the averaging (corresponding to a 95% confidence level). These pixels are chosen to exclude optical disturbances introduced by the surface architecture of the ISOTECH Graybody source, which presents concentric circular ridges affecting the apparent emissivity of the surface. The pixels considered for the averaging constitute 63% of the active surface of the radiative source visible through the main ZnSe window. The temperature non-uniformity is shown as a function of the reference temperature in Figure 5.21.

The maximum value of non-uniformity in the range of interest for the rotor heat transfer measurements is of 0.55 °C and is reached at 75 °C, while the minimum is of 0.13 °C at 45 °C. On average, the temperature non-uniformity over the range of interest is of 0.36 °C.

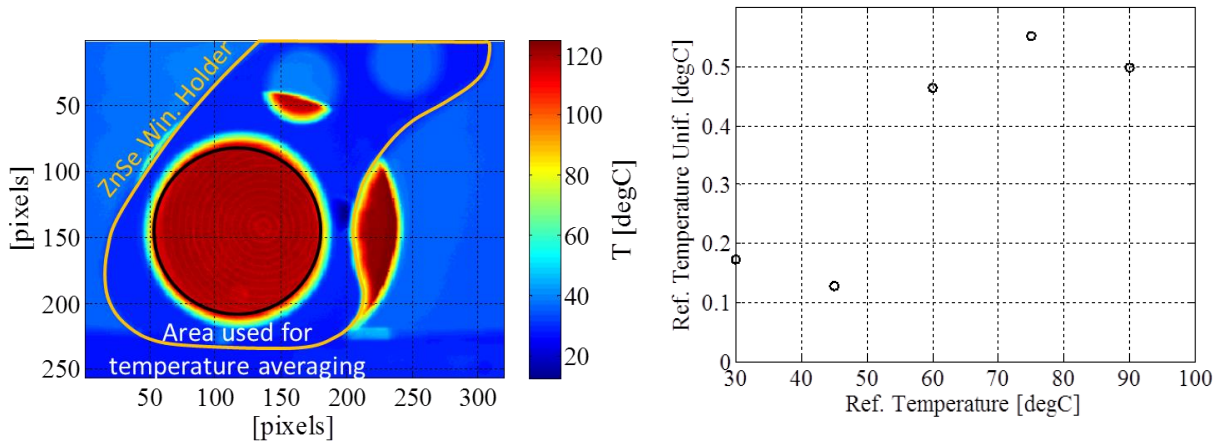


Figure 5.21: a) typical frame from the IR camera calibration data set with the area considered for temperature averaging highlighted in black and the outer contour of the ZnSe window holder highlighted in orange. b) non-uniformity in reference temperature as a function of reference temperature.

The calibration error and the image reconstruction error are combined to produce an average value over the endwall of 0.45K.

## 5.2.2 Errors in the determination of the electrical heat flux provided at the endwall

Based on equation (4.11), the errors in the estimation of the electrical heat flux provided by the film heater propagate from the uncertainties in the power readings and the scaling factor  $S_q$  measured in chapter 4.5 to account for non-uniformities.

Errors in the surface area are neglected as the platforms are manufactured with tolerances within  $\pm 50\mu\text{m}$  over a nominal surface area of the endwall greater than  $1'300\text{mm}^2$ , corresponding to an error of less than 200ppm (see section 5.2.5 ).

The relative error on the electrical heat flux can be quantified as:

$$\frac{\delta \dot{q}''_{el}}{\dot{q}''_{el}} = \frac{\delta S_q}{S_q} + \frac{\delta P}{P} \quad (5.6)$$

The highest uncertainties in power  $P$  are detected for the lowest power level (1.56% at 2.24W, see Table 10).

Table 10: electrical parameters and corresponding measurement uncertainties for all power levels.

Step	i [A]	di [A]	V [V]	dV [V]	P [W]	dP [W]	dP [%]
1	0.064	0.001	35	0.005	2.24	0.04	1.56
2	0.092	0.001	50	0.005	4.60	0.05	1.09
3	0.136	0.001	75	0.01	10.20	0.08	0.74
4	0.153	0.001	85	0.01	13.01	0.09	0.65

This uncertainty level, summed to the local uncertainty in value of the scaling factor  $S_q$  (Figure 4.17(b)), results in an average uncertainty of 5.3% over the whole passage. The uncertainty in electrical heat flux is the second most relevant contributor to the overall uncertainty (22% of the overall uncertainty) after that coming from the conduction loss estimation (70% of the overall uncertainty).

### 5.2.3 Errors in the determination of the conductive losses through the insulating substrate.

The local conductive heat loss is evaluated based on the readings of the 9 PT100 RTDs and the thermal properties of the substrate according to equation (2.12), where  $T_w$  is the wall temperature measured at the normal projection on the endwall of the PT100 location and  $T_{sub}$  is the substrate temperature read by the PT100 thermometer. For each heat flux level, an average value of conductive loss is calculated over the passage and used in the energy balance (2.11).

The sources of error in the evaluation of this average quantity are three-fold:

- thermal conductivity of the substrate material (PEEK);

- errors in the calibration of the PT100 and noise affecting the read-out of the detected values during the operation of the turbine;
- spatial variations of the quantity over the endwall.

### **Errors in the determination of the thermal conductivity of the substrate material**

The value of the thermal conductivity of PEEK is determined indirectly by separately measuring its thermal diffusivity  $\nu$ , density  $\rho$  and specific heat  $C$  and rearranging equation (4.12) into:

$$\kappa = \rho \cdot C \cdot \nu \quad (5.7)$$

Details on the experimental methodologies used to measure the different quantities and the related uncertainties are given in section 4.5.6 . The available data for the specific heat is restricted to the temperature range 80-130 ° C. It is therefore necessary to extrapolate the values to ambient temperature. The extrapolation is carried out by means of a linear fit, based on the behavior reported by Riviere et al [127] in the temperature range of interest. An uncertainty on the values of  $\kappa$  of 12% is determined by analytical error propagation.



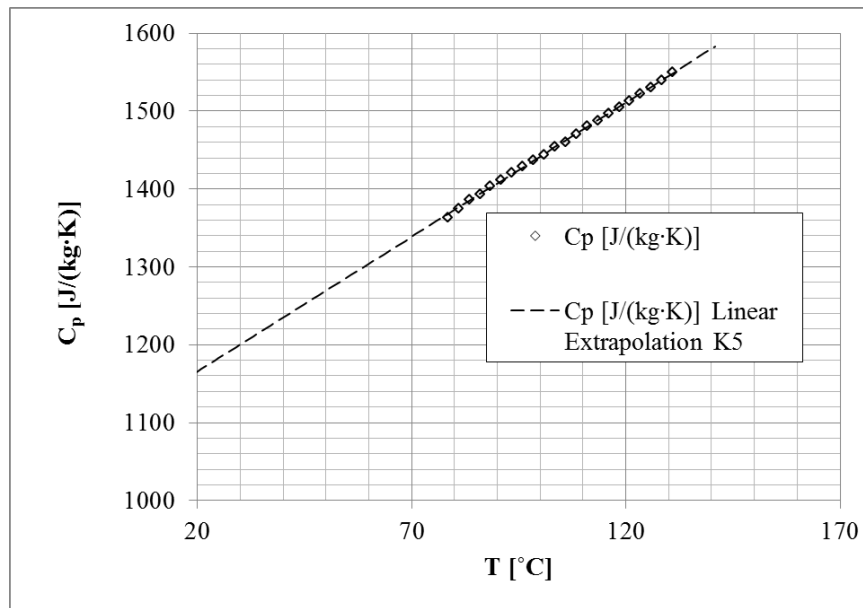


Figure 5.22: DSC data for specific heat of PEEK  $C_p$  as a function of temperature and linear extrapolation to ambient temperature.

### Errors in the calibration and read-out of the RTDs readings

The calibration of the 9 PT100 RTDs embedded in the heat transfer platform is performed by placing the instrumented platform in a calibration oven, varying the temperature of the chamber in steps of 10-20 °C. The temperature range covered is between 22 and 113 °C, wider than the operating range of the heat transfer platforms (from room temperature ~25 °C to 90 °C). The chamber is kept at constant temperature until thermal equilibrium is reached between the PEEK and the environment of the oven.

The reference temperature is provided by two RTDs located in the chamber with a spread of less than 0.35K.

The calibration curves are calculated as second order polynomial fits.

For all sensors, the mean error of the calibration curves in the calibration range is of 0.62K.

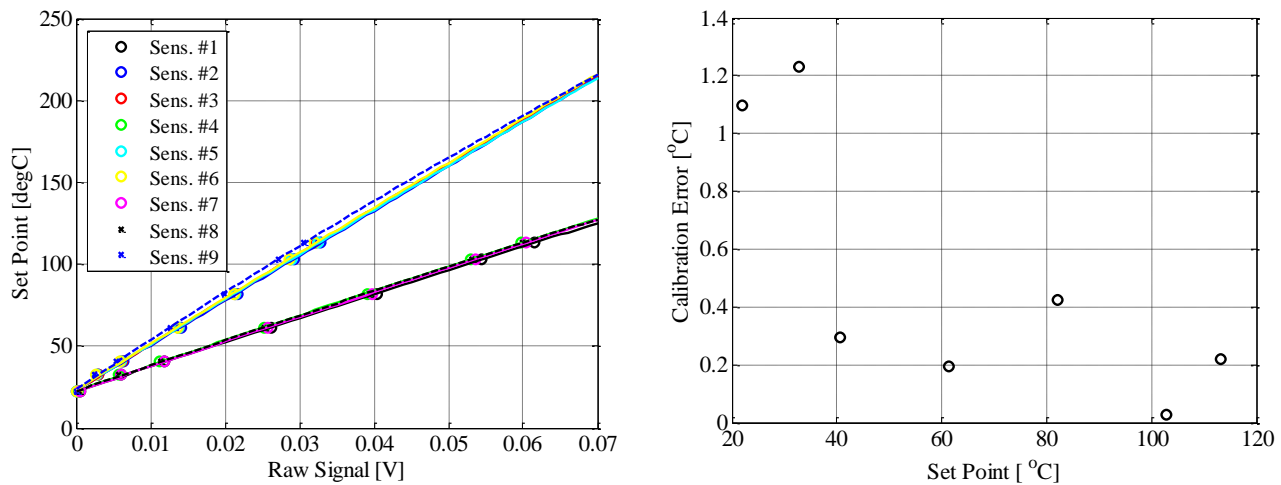


Figure 5.23: calibration curves of the 9 PT100 embedded in the rotor HT platform (left); average calibration error over all sensors as a function of temperature (right). The average error is of 0.62K over the calibration range.

### Non-uniformities of the conductive losses

The conduction loss through the substrate is calculated at the locations where the PT100 are installed in terms of percentage of the surface heat flux provided by the endwall heater, based on equation (2.12).

The average values fall between 1.6% and 6.8% for the nominal operating point and between 11.2% and 18.7% for the off-design condition, depending on the location for which the loss is calculated.

Because in the final energy balance, a single average value for the whole endwall is used, the non-uniformity in conduction loss constitutes a source of uncertainty. This non-uniformity is up to twice the average value used for both operating conditions. The conduction losses are therefore varied up to double of the value recorded for both cases when applying Moffat's [126] perturbation method.

The other sources of uncertainty on the conductive losses (thermal conductivity and temperature readings) are considered negligible compared to the contribution of the non-uniformity ( $\sim 100\%$  of the conductivity loss itself).

However, for a relative estimation of uncertainty, the non-uniformity contribution to the uncertainty in conduction losses reduces to 55% of the value measured for the cases at the nominal operating point.

### 5.2.4 Final Uncertainty Distributions for Rotor Endwall Results

The average uncertainty contributions summarized thus far are collected in the following Table 11:

Table 11: average uncertainty values on measurement inputs.

Q.ty	Unc. Contrib.	Value
$T_s$	$dT_{s,cal}$	0.36K
	$dT_{s,img\ rec}$	0.27K
	<b><math>dT_{s,total}</math></b>	<b>0.45K</b>
$q''_{el}$	$dS_q$	
	$dP$	1.6%
	<b><math>dq''_{el}</math></b>	<b>5.3%</b>
$q''_{cond}$	$d\kappa$	12%
	$dT_{sub}$	0.32K
	<b><math>dq''_{cond}</math></b>	<b>~5% <math>q''_{tot}</math> (DP)</b> <b>~14% <math>q''_{tot}</math> (Part-Load)</b>
Others	$d\varepsilon$	2%
	$dT_{t,rel}$	1K

The overall uncertainty on Nusselt number and non-dimensional adiabatic wall temperature is evaluated by successively perturbing the relevant inputs by their respective uncertainties using Moffat's [126] method.

Overall, the average uncertainty on the Nusselt number value over the whole passage is 9.0% and 0.42K on the adiabatic wall temperature. The final uncertainty distributions for the nominal operating condition are shown in Figure 5.24, the adiabatic wall temperature uncertainty being non-dimensionalized with the dynamic temperature at rotor inlet (4.7K).

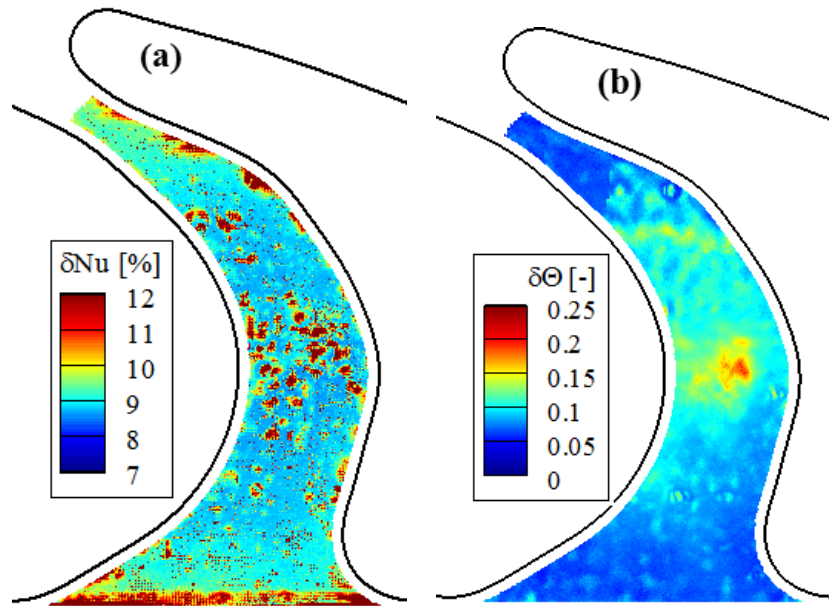


Figure 5.24: overall uncertainty in Nusselt number (a) and in non-dimensional adiabatic wall temperature (b) for the nominal operating condition.

A detailed overview of the individual contributions to the average overall uncertainty in Nusselt number is given in Table 12 and shown in Figure 5.25. Similarly, the contribution to the uncertainty in non-dimensional adiabatic wall temperature  $\Theta$  is given in Table 13 and Figure 7.1.

It can be seen that the main contributors to the uncertainty are, in both cases:

- conductive losses;
- variability of the scaling factor  $S_q$  with different power levels;
- surface temperature  $T_s$ .

Uncertainties on current  $i$ , voltage  $V$ , surface emissivity  $\varepsilon$  and relative total inlet temperature  $T_{t,rel}$  have negligible effect on the final global uncertainty due to the high precision of their measurement. This indicates that improvements in the uncertainty of the technique can be obtained by determining with higher precision the conduction losses (finer calibration of the RTDs, increasing the depth of their installation to maximize the surface-to-substrate temperature difference) and by developing surface heaters with lower non-uniformities.

## 5.2 Uncertainty Analysis for the Rotor Endwall Heat Transfer Measurements 151

Table 12 relative contributions to the uncertainty in Nusselt number

$T_s$ [%]	$q''_{\text{cond}}$ [%]	$S_q$ [%]	$i$ [%]	$V$ [%]	$\varepsilon$ [%]	$T_{t,\text{rel}}$ [%]
5.6	70.3	22.4	0.4	0.0	0.4	0.9

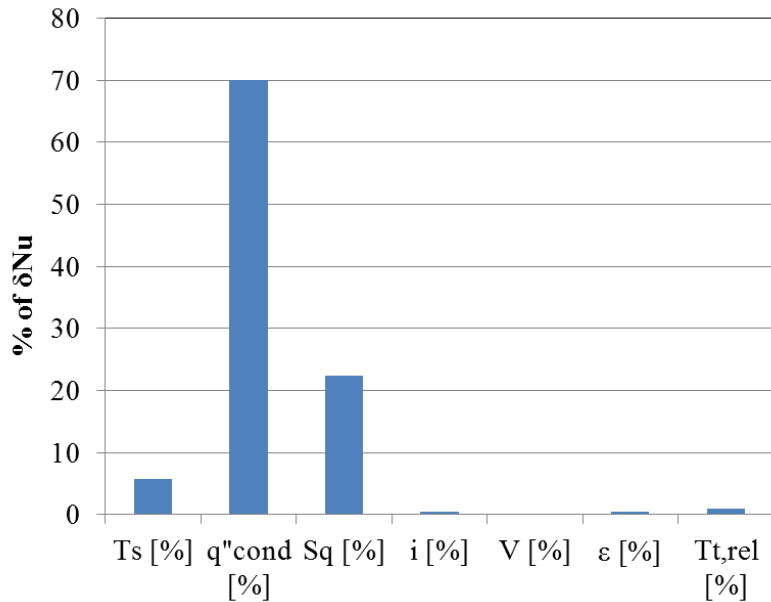


Figure 5.25: relative contribution to the total uncertainty on Nusselt number.

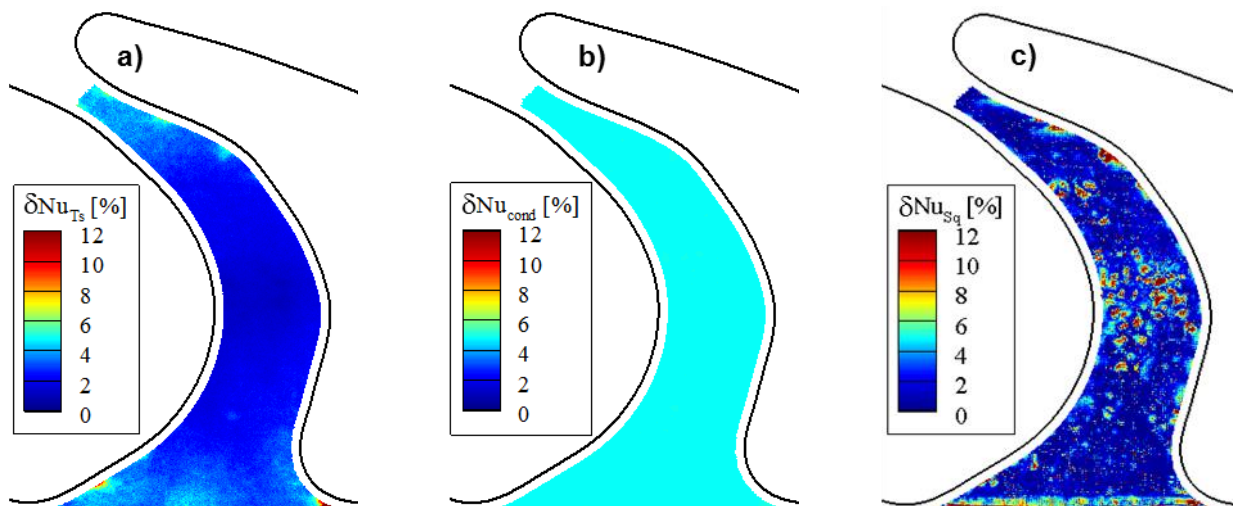


Figure 5.26: point-wise contributions to the uncertainty in Nusselt number due to uncertainties in a) surface temperature  $T_s$ , b) conduction losses  $q''_{\text{cond}}$ , c) scaling factor  $S_q$ .

Table 13: relative contributions to the uncertainty in adiabatic wall temperature

$T_s$ [%]	$q''_{\text{cond}}$ [%]	$S_q$ [%]	$i$ [%]	$V$ [%]	$\varepsilon$ [%]	$T_{t,\text{rel}}$ [%]
71.5	26.9	0.0	1.5	0.0	0.0	0.1

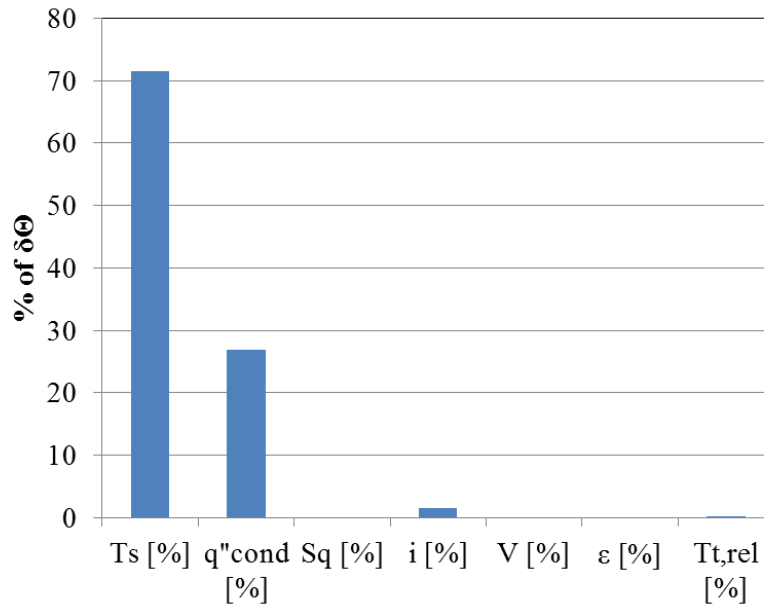
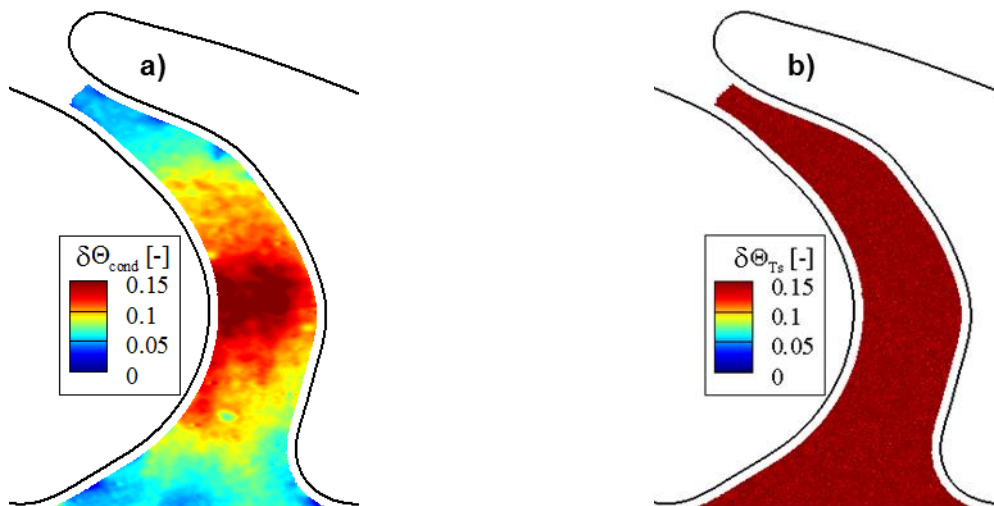


Figure 5.27: relative contribution to the total uncertainty on adiabatic wall temperature.

Figure 5.28: point-wise contributions to the uncertainty in non-dimensional adiabatic wall temperature due to uncertainties in a) conduction losses  $q''_{\text{cond}}$ , b) surface temperature  $T_s$ .

### 5.2.5 Geometry Errors due to Manufacturing Tolerances

The heat transfer platform is checked for compliance to the nominal geometry. A 3D scan of the part is performed with a GOM ATOS system and compared to a CAD model. The data corresponding to the precision jig holding the part are used as a reference for aligning the clouds of points. The comparison is performed in the GOM Inspect V7.5 SR2. The result is shown in Figure 5.29. Deviations are found to be within  $\pm 0.15\text{mm}$  of the nominal geometry within the measurement area.

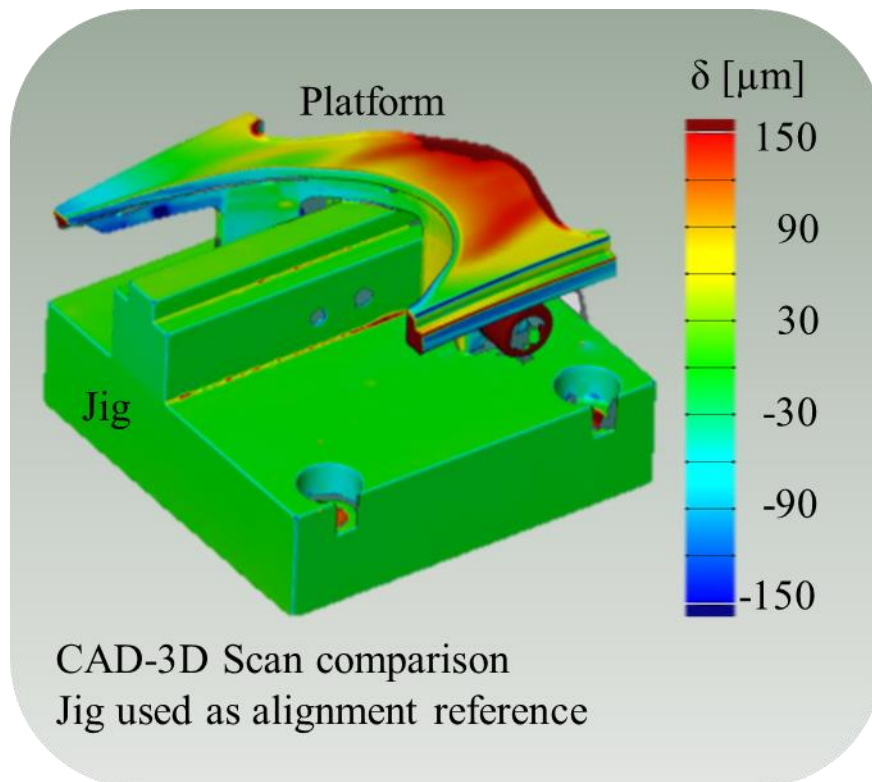


Figure 5.29: comparison between nominal CAD geometry of the heat transfer platform and the actual component. The precision aluminum jig acts as a geometrical reference for the superposition of the data. Deviations are  $< 0.1\text{mm}$  in the measurement area.





## 6. Heat Transfer Measurements on the Stator Endwall

The setup and methodology described in chapters 2 and 3 are used to perform measurements on the second stator's endwall at different operating conditions of the turbine.

The operating conditions investigated are summarized in Table 14. The focus is, first of all, to assess the repeatability of the technique by comparing measurements performed on different days for the same operating condition: design point. Secondly, the patterns observed experimentally are related to three-dimensional flow features in the passage with the help of unsteady CFD simulations. Finally, the change in the distribution of the heat transfer quantities, particularly the convective heat transfer coefficient in non-dimensional form, is studied when altering the operation of the machine by reducing the core mass flow rate and varying in both directions the incidence of the flow on the rotor blade.

Design Point and Part Load conditions are the same as in Table 3.2

Table 14: operating conditions during stator 2 heat transfer measurements.

	Design Point	Part Load	Design Point (Rep.)	Inc. +
$n$ [rpm]	2'700	2'700	2'700	1'900
$\dot{m}$ $\left[\frac{\text{kg}}{\text{s}}\right]$	11.73	8.39	11.72	8.38
IR [%]	0.81	0.80	0.82	0.79
$\beta$ [-]	1.65	1.33	1.65	1.30
$T_{t,in}$ [ $^{\circ}$ C]	54.63	54.75	54.72	54.63
$T_{t,in,S2}$ [ $^{\circ}$ C]	30.18	38.76	30.24	40.90
$T_w$ steps [-]	11	11	11	10
$Re_{C_{ax},S2ex}$ [-]	410k	220k	410k	295k

Aerodynamic experimental data acquired with 4 and 5-hole pneumatic probes as well as with FRAP (Fast Response Aerodynamic Probes, see Kupferschmied et al. [128] and Pfau et al. [129]) by Regina complement the observations deriving from the heat transfer data. 38 radial by 41 circumferential points are acquired at intervals of 1.4% span and  $0.25^\circ$ . Data from pneumatic probes is naturally time-averaged due to the transmission of pressure waves along the pneumatic tubes to the Keller pressure transducers.

## 6.1 Nominal Operating Point and Comparison to CFD

The first set of data presented in this section is the one acquired at the nominal operating condition. The general patterns observed experimentally are described for this condition and related to expectations from previous research in the field of stator heat transfer. The repeatability of the technique is assessed to further comment on the significance of the observed variations. Finally, a comparison with the results of unsteady CFD simulations is provided to relate the experimental results to the highly complex, fully three-dimensional flow field in the stator passage.

The results for the nominal operating condition are shown in Figure 6.1 both in terms of Nusselt number distribution and in terms of adiabatic wall temperature referred to the total temperature of the flow at the inlet of stator 2.

In order to assess the repeatability of the technique, the measurements are performed twice in different days for this particular condition.

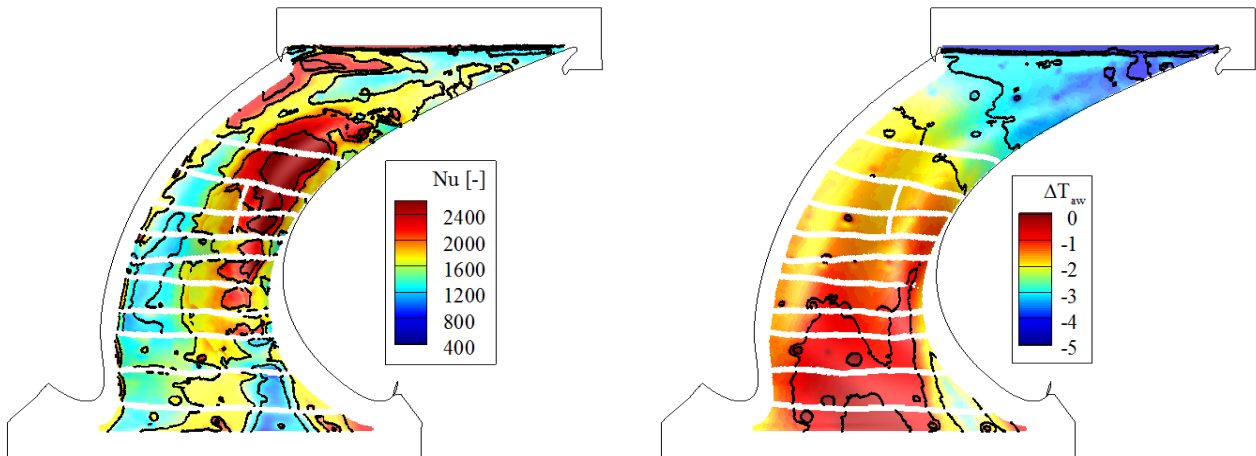


Figure 6.1: left, Nusselt number distribution for the nominal operating point with an injection ratio of 0.8%; right, adiabatic wall temperature distribution referred to the total temperature at stator 2 inlet for the same operating condition.

The Nusselt number distribution is consistent within 4.7% on average over the whole endwall, with extreme excursions between -15% and +30% localized at the inlet of the passage, towards the suction side of the blade.

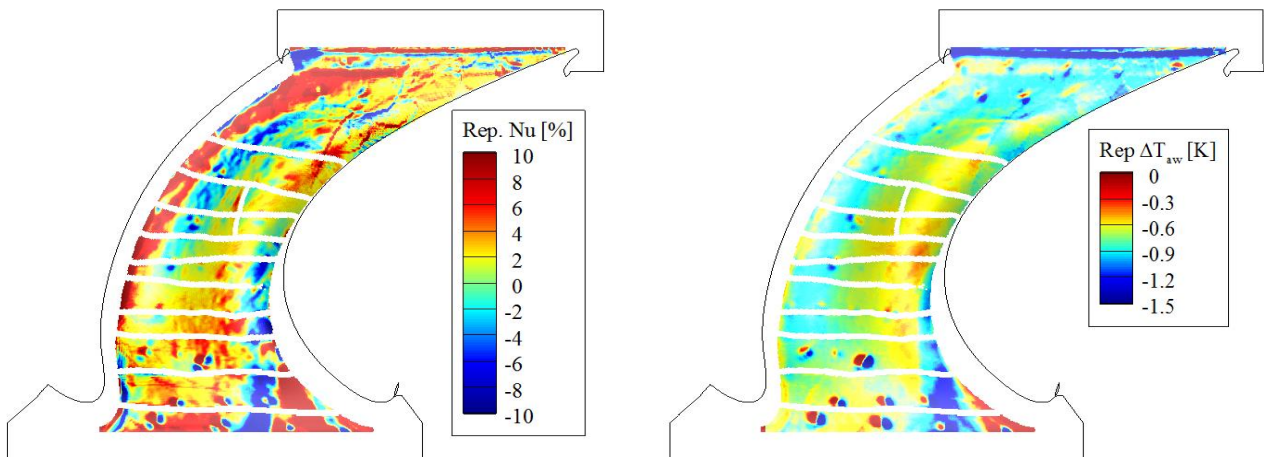


Figure 6.2: left, point-wise repeatability check for the Nusselt number distribution at the nominal operating condition; right, repeatability check for the adiabatic wall temperature distribution for the same condition. Average values over the endwall are 4.7% and 0.69K.

The repeatability distributions, together with the uncertainty distributions presented in section 5.1.5 (Figure 5.17) are essential to make a judgment on the significance of the changes observed when varying operating conditions (see following sections).

However, before moving to the evaluation of the differences in the distributions of the heat transfer quantities in the different test cases, a detailed description of the results for the rated operating condition – taken as reference – is in order.

The adiabatic wall temperature distribution clearly shows the cooling of the flow with its expansion along the passage. The endwall profiling appears effective in keeping the isothermal curves towards the throat normal to the main direction of the flow. Typically, in high-pressure turbines with cylindrical endwalls and strong secondary flows, the migration of the passage vortex to the suction side alters the temperature and pressure profiles tilting the isotherms and isobars towards the axial direction.

On the other hand, understanding the Nusselt number distribution demands a more detailed examination of the flow patterns induced by the aggressive end-wall contouring.

Typically, in cascade heat transfer – either linear or annular – the highest heat transfer levels are encountered at the stagnation point of the vane and in correspondence with the rolling up of the pressure side leg of the horseshoe vortex. The signature of its migration and merger with the passage vortex is normally evident in the presence of cylindrical endwalls and the acceleration of the flow along the passage contributes significantly to the increase of the heat transfer coefficient towards the outlet (Blair [56], Laveau et al. [72]).

In the present case, instead, a region of high heat transfer is visible downstream of mid-chord, close to the suction side. Furthermore, regions showing low heat transfer coefficient values are present at the very inlet of the passage towards the suction side and all along the pressure side of the vane. No clear signature of the pressure leg of the horseshoe vortex is present and the acceleration of the flow through the passage does not appear to significantly increase the Nusselt number.

Moreover, the Nusselt number distribution defies expectations concerning the effect of the endwall profiling. Specifically, the highest heat transfer is recorded in correspondence of the trough of the endwall contouring, while a lower level is measured over the hill on the pressure side. The deceleration induced by the wider cross-sectional area encountered by the flow in the trough is therefore not sufficient to decrease the local shear stress and – consequently – the local heat transfer.

For a better understanding of the relationship between the heat transfer patterns and the strongly three-dimensional flow in presence of aggressive endwall contouring, unsteady CFD simulations were conducted (A. Cocina, [130]) based on experimental aero-thermal boundary conditions.

### 6.1.1 Numerical Setup

A passage-centered mesh of 1.8miO node is created for a single pitch of the second stator. For a satisfactory resolution of the velocity gradient at the wall, the first cell height is limited to values lower than the local viscous unit ( $y^+ < 1$  everywhere on the endwall). The experimental, unsteady boundary conditions are imposed at the inlet plane in terms of 2D distributions per each time step. 2 simulations are run with adiabatic and isothermal boundary conditions in order to compute the adiabatic wall temperature from the former and the heat flux corresponding to the prescribed temperature difference from the latter.

The boundary conditions applied are summarized in Table 15.

Table 15: boundary conditions for the unsteady heat transfer CFD simulations performed by Cocina [130].

Inlet BCs	Outlet BCs	Wall BCs
Total pressure	Static pressure at the hub	Adiabatic/Isothermal (90 ° C)
Total temperature	Static pressure at the tip	
Axial Mach number		
Yaw		
Pitch		
Turbulent length scale		
Turbulent intensity		

It is of interest to focus the attention on the inflow to the blade row, presented in form of time-averaged total pressure loss coefficient in the stationary frame in Figure 6.3. The total pressure coefficient is defined as follows:

$$C_{pt} = \frac{p_t - p_{s,ex}}{p_{t,in} - p_{s,ex}} \quad (6.1)$$

where  $p_t$  is the local value of total pressure on the measurement plane,  $p_{t,in}$  is the average total pressure at turbine inlet and  $p_{s,ex}$  is the static pressure at turbine exit.

Because of the presence of the upstream blade rows, the inflow boundary condition is highly non-uniform. In a time-averaged fashion, the wake and the hub secondary flows of the first stator are clearly visible in the total pressure loss coefficient distribution (regions 1 and 3 in Figure 6.3), together with the high losses introduced by the tip leakage vortex of the rotor blade at the outer radius (regions 2 in Figure 6.3).

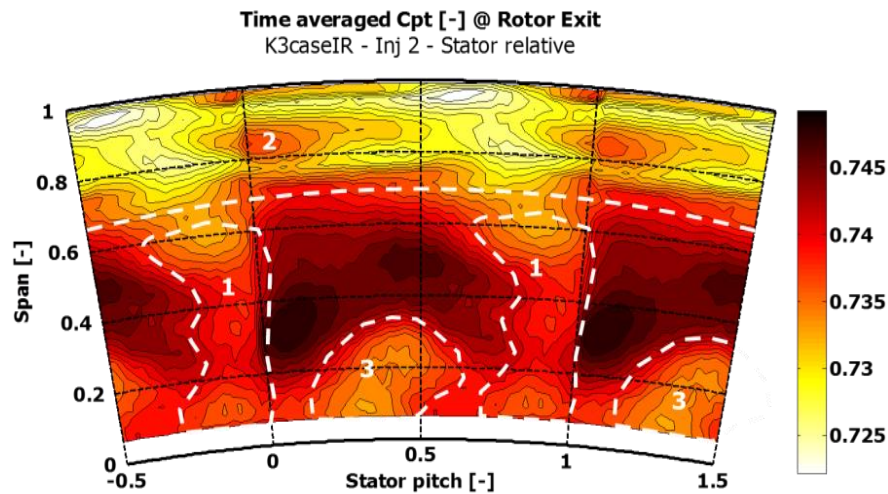


Figure 6.3: experimental, time averaged distribution of total pressure loss coefficient  $C_{p,t}$  (eq. 6.1) in the stator-relative frame. Stationary flow features such as the wakes (1) of the upstream vanes of the first stator and the hub passage vortices (3) are still visible downstream of the rotor. The annular region (2) of lowest total pressure is a marker of the presence of highly lossy tip leakage vortices.

The solver used is the URANS MULTI3 solver internally developed at the Laboratory for Energy Conversion at ETH Zurich.

An unsteady solution with 20 time steps and 1200 sub-iterations (i. e., iterations per time step) is calculated.

Convergence is checked based on monitoring points for static pressure, wall temperatures and heat flux. Variations in heat flux at each time step for the selected monitoring point are less than 1.3% when increasing the sub-iterations from 800 to 1200.

The simulation is therefore considered converged after 1200 sub-iterations.

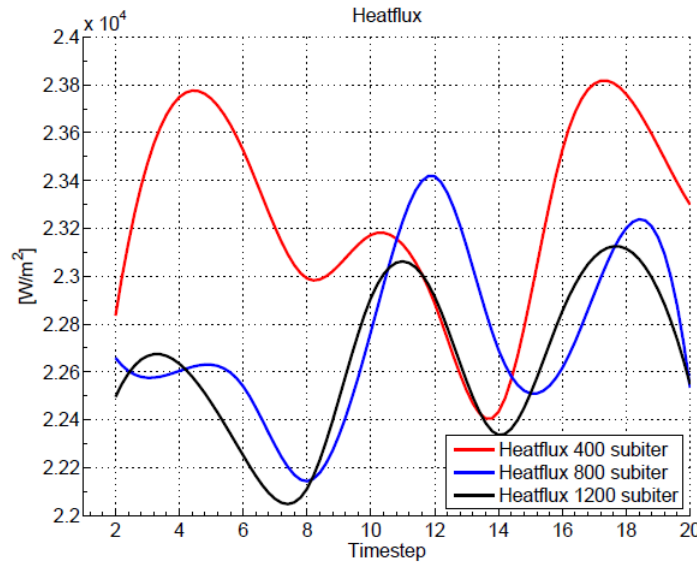


Figure 6.4: the heat flux at each time step for the selected monitoring point varies within 1.3% when increasing the number of sub-iterations from 800 to 1'200 (Cocina [130]). Convergence therefore is inferred after 1'200 sub-iterations.

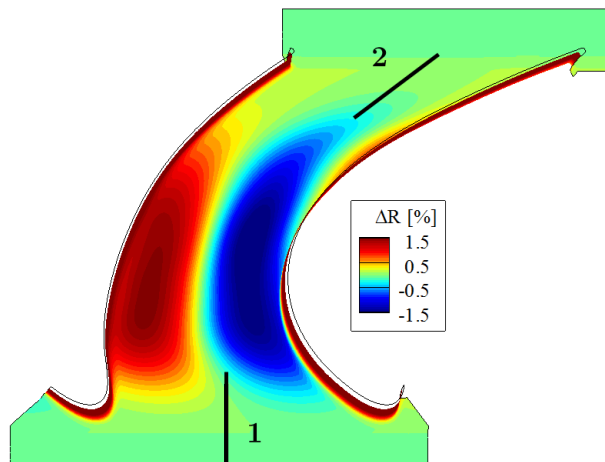
### 6.1.2 CFD Results

The heat transfer patterns are consistently observed in the CFD results (Figure 6.7) as well as in the measurements shown in Figure 6.1. The regions highlighted in Figure 6.7 can be recognized easily in the experimental Nusselt number distribution. However, the absolute value of the Nusselt number is reduced in the predictions due to the assumption of smooth walls for solver stability reasons.

It has been shown how increases in heat transfer of up to 40-60% can be detected in regions with high flow acceleration (such as the throat of the passage), if an equivalent sandgrain roughness of 30-60 $\mu\text{m}$  is introduced on the surface [100].

The high-emissivity paint used in this study falls, in fact, in this range of roughness ( $R_z = 45\text{-}60\mu\text{m}$ ).





Location	Ra [ $\mu\text{m}$ ]	Rz [ $\mu\text{m}$ ]
1	8.46	45.63
2	8.29	59.54

Figure 6.5: locations of roughness measurement on the endwall (left), values of average and peak-to-peak roughness (right)

The qualitative agreement of the results, especially with reference to the Nusselt number distribution (Figure 6.7), confirms the observation that the effect of endwall profiling on heat transfer does not relate directly to the locally increased static pressure and reduced velocity in the trough towards the suction side or to the locally reduced static pressure and increased velocity towards the pressure side.

The highest rates of heat transfer are found in the region labeled as “B” in Figure 6.7, on the suction side of the passage. A smaller region, triangular in shape and close to the inlet of the passage (labeled “A” in Figure 6.7) presents lower values of Nusselt number. The regions “C” and “D” are adjacent to each other and graze the pressure side of the passage and suggest the presence of a vortical structure increasing the heat transfer with its downwash motion in “D” while lowering it with its upwash motion in “C” (Eibeck [131]). The described patterns can be recognized in the experimental Nusselt number distribution of Figure 6.1.

In fact, the predicted endwall pressure distribution shown in Figure 6.6 confirms that, despite the aggressive contouring, the pressure difference between the pressure and suction side of the passage is still relevant and the isobars are far from being aligned with the normal to the main flow direction. Clearly, the strong

turning of the flow induced by the vanes exacerbates this (in excess of  $105^\circ$  based on mass-averaged pneumatic probe data at the inlet and outlet planes).

A strong passage vortex is therefore to be expected.

Additionally, the higher acceleration of the flow on the suction side of the passage corresponds to a stronger wall shear stress, resulting in higher heat transfer rates, as observed also experimentally.

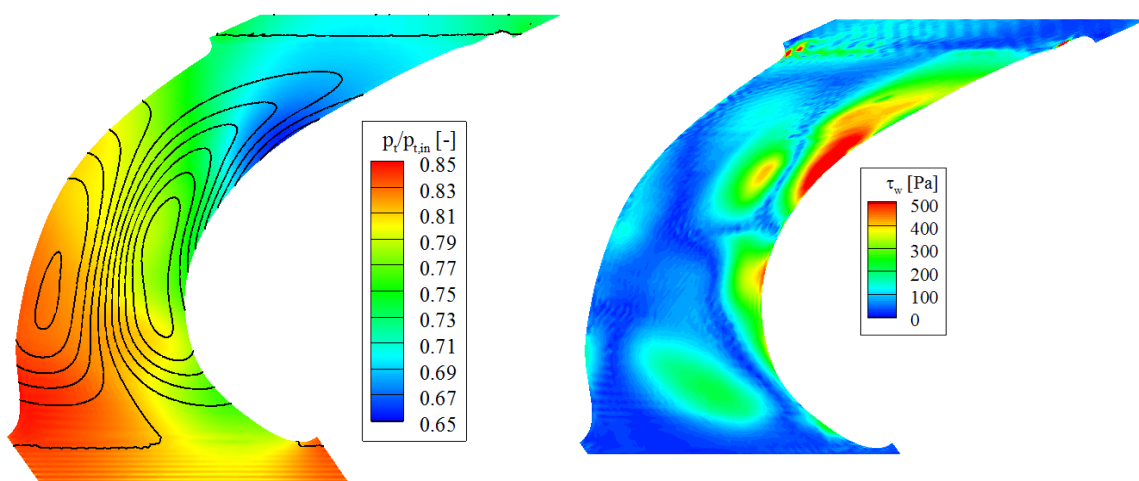


Figure 6.6: left, distribution of pressure normalized by the total inlet pressure with iso-levels of endwall radius. The iso-bars do not realign normally to the main flow direction: the pressure difference between the pressure and suction side of the passage is still severe. The flow accelerates more strongly on the suction side of the passage, thus there generating the highest wall shear stress (right) and, consequently, higher heat transfer.

The preliminary considerations based on the endwall static pressure distribution of Figure 6.6 are supplemented by the visualization in three-dimensions of the vortical structures in the passage (Figure 6.8). It appears that the pressure leg of the horseshoe vortex, with its core at around 24% of the span, stays close to the pressure surface and at maintains its spanwise location through the whole passage. The suction leg, instead, strengthened by the passage vortex and by the merger with the upstream secondary flows coming from the first stator (see region 3 in Figure 6.3), occupies a much lower spanwise location, closer to the endwall. Furthermore, the iso-surface of streamwise vorticity shown in Figure

6.8 encloses a much stronger and bigger vortex on the suction side than on the pressure side (maximum streamwise vorticity value respectively  $\sim 3'600\text{s}^{-1}$  and  $\sim 1'800\text{s}^{-1}$ ).

The presence of such structure on the suction side justifies the higher rates of heat transfer on the suction side of the passage. While the Nusselt number distribution agrees qualitatively with the experimental results, the evolution of the adiabatic wall temperature in the experiment seems to follow a uniform expansion along the mean line of the passage and not to be significantly affected by the stronger acceleration on the suction side.

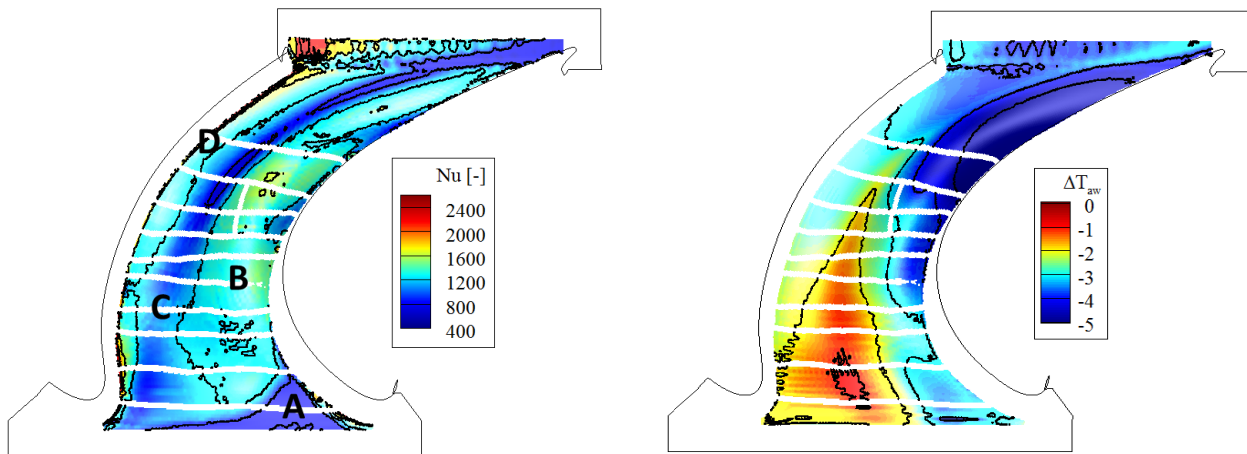


Figure 6.7: left, predicted Nusselt number distribution over the stator endwall for the nominal operating condition; right, adiabatic wall temperature distribution referred to the total temperature at stator 2 inlet.

Despite the significantly smaller size and strength and its distance from the endwall, the pressure leg of the horseshoe vortex (highlighted by the “A” red circle in Figure 6.8) does play a role in determining the heat transfer patterns on the endwall. As anticipated, the regions labeled as “C” and “D” in Figure 6.7 can be related respectively to the upwash and downwash motion induced by this vortical structure.

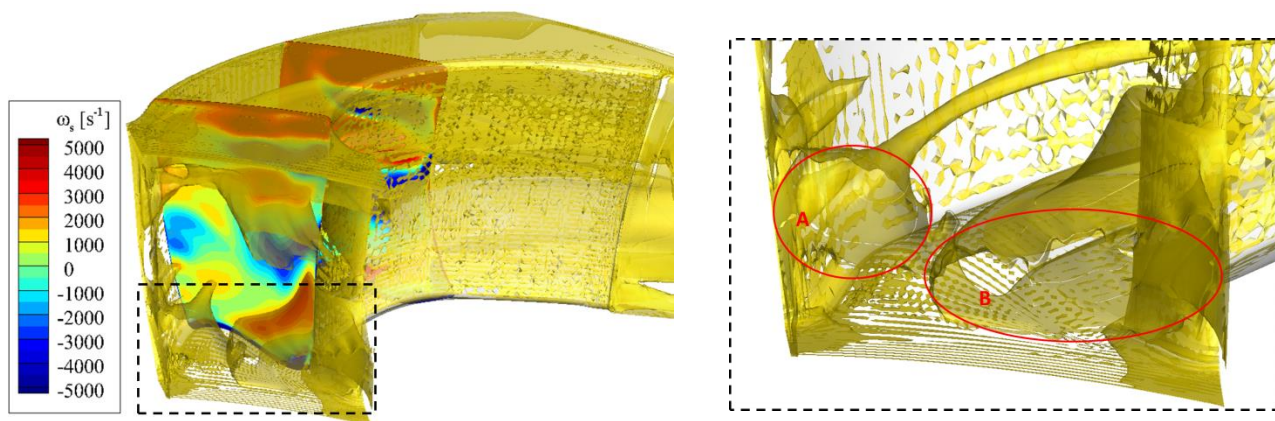


Figure 6.8:left, predicted iso-surfaces of streamwise vorticity of  $1'500\text{s}^{-1}$  and contours on axial planes of the same quantity across the second stator; right, detail of the pressure leg of the horseshoe vortex (A) and suction leg of the horseshoe vortex (B). It is evident how the suction leg is bigger, stronger and closer to the hub endwall, thus justifying the higher levels of heat transfer recorded both experimentally and computationally.

In conclusion, the distributions of heat transfer quantities measured experimentally are validated qualitatively by the time-averaged results of the unsteady CFD predictions. The increased Nusselt number on the suction side of the passage is related to the presence of a strong suction leg of the horseshoe vortex, combined with a significant cross-flow due to the high pressure difference between pressure and suction side of the passage (the turning induced by the vanes is beyond  $105^\circ\text{C}$  on average) and strengthened further by the hub secondary flows coming from the first stator upstream. The lower pressure in this area also relates to stronger flow acceleration, resulting in the stronger drop in adiabatic wall temperature observable in the computational results, but not as strongly in the experimental distribution.

## 6.2 Off-Design Conditions

Two off-design conditions are tested for their effect on the stator 2 hub endwall heat transfer.

The first is obtained by reducing the mass flow rate by 28.5% while keeping the rotational speed of the rotor constant at 2'700rpm. This produces a reduction in Reynolds number through the 1.5 stage and a negative incidence on the rotor blade of about  $12^\circ$ .

The second is obtained by the same reduction in core mass flow rate, but with an additional reduction of the rotational speed of the rotor to 1'800rpm. This results in the same reduction in Reynolds number, but coupled with an increased incidence on the rotor blade and, consequently, a higher work extraction through the rotor.

More parameters of these operating conditions are given in Table 14.

In the following paragraphs, the effects of these changes in operation are described.

### 6.2.1 Reduced Reynolds Number and Rotor Incidence

The reduction of the mass flow rate determines a decrease in axial velocity. Because the direction of the absolute velocity vector is essentially unaltered and the rotational speed is kept constant, this results in a negative incidence of the relative velocity of the flow onto the leading edge of the rotor blade. The velocity triangles drawn based on mass-averaged pneumatic probe data and shown in Figure 6.9 are consistent with this expectation.

The mass-averaged relative flow angle  $\beta$  decreases from  $53.70^\circ$  to  $41.76^\circ$  on average along the whole span, determining a negative incidence  $i = -11.94^\circ$  (typical uncertainty value for pneumatic probes  $<0.7\%$ ).

Two effects therefore must be considered when examining the heat transfer patterns on the stator 2 endwall: a reduction in Reynolds number of 47%, coupled with a reduced work extraction across the rotor due to the lower turning. Aero-

dynamically, the reduction in speed and loading results in much lower total pressure losses through the blade rows. This can be verified by examining the time-averaged inlet boundary condition to the second stator in Figure 6.10.

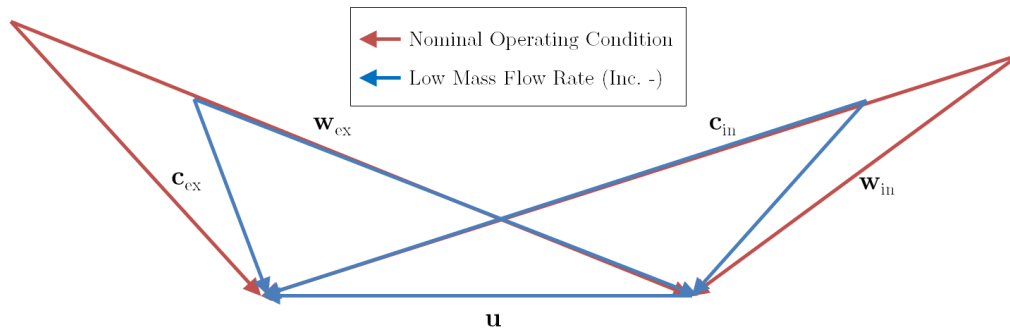


Figure 6.9: velocity triangles based on pneumatic probe data for the nominal operating condition and the reduced mass flow rate operation. The inclination of the relative velocity vector  $w_{in}$  at the inlet of the rotor shows the negative incidence of the latter.

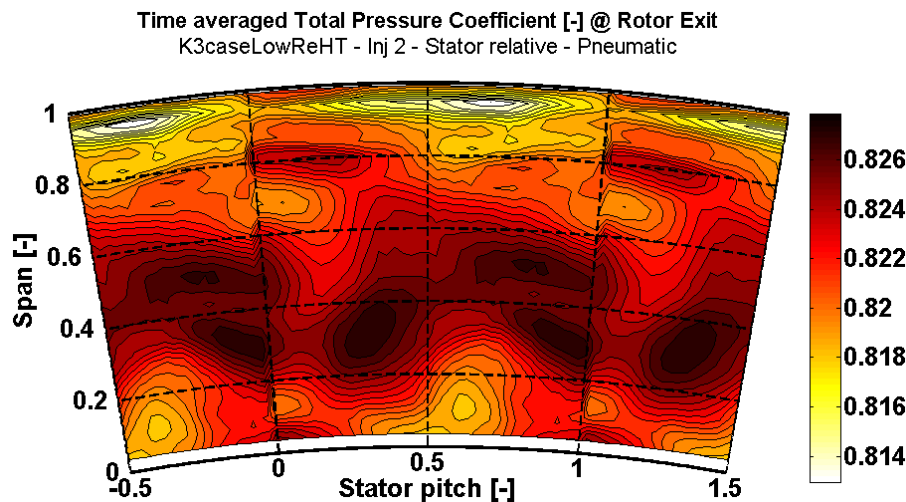


Figure 6.10: experimental, time averaged distribution of total pressure coefficient  $C_{p,t}$  (eq. 6.1) in the stator-relative frame for part-load condition at the inlet of the second stator. Compared to the distribution for the nominal operation of Figure 6.3,  $\sim 10\%$  lower total pressure losses are recorded. The wakes of the upstream vanes of the first stator and the hub passage vortices are still visible downstream of the rotor, but are more mixed out than at design point. The region of lowest total pressure at the outermost radii is a marker of the presence of the tip leakage vortices. These, too, are weaker and occupy a smaller fraction of cross-sectional area than at the rated condition.



Compared to the total pressure coefficient distribution for the nominal operating point (Figure 6.3), the overall value of the total pressure loss coefficient is  $\sim 10\%$  higher. More in detail, the wakes of the first stator are partially mixed out at part-load, while still very recognizable at design point (region 1 in Figure 6.3). The losses due to the tip leakage vortex through the rotor are confined to more outer radii (region 2 in Figure 6.3), as consistent with a reduced loading of the rotor. The secondary flows from the stator 1 also occupy a smaller cross-sectional area and appear more mixed in the circumferential direction.

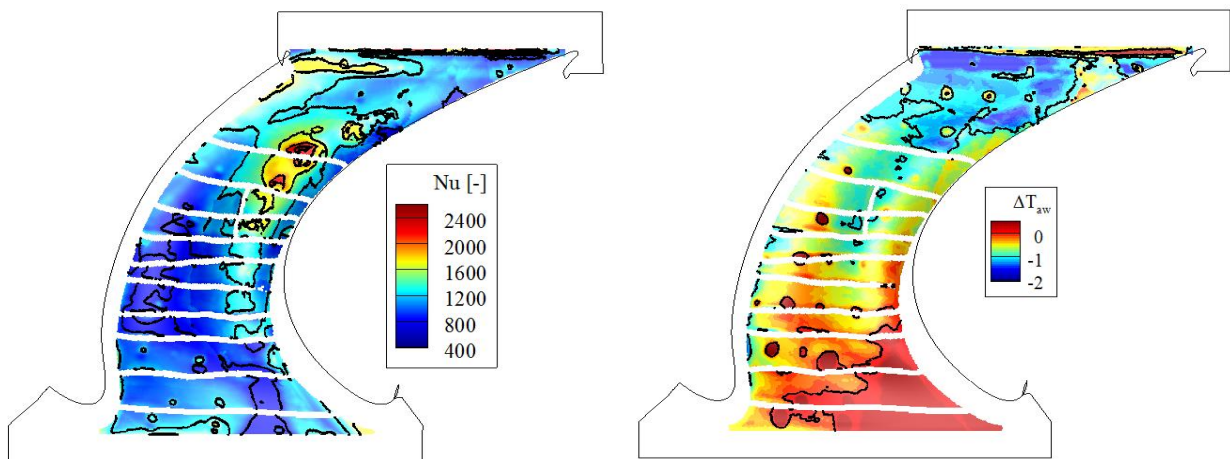


Figure 6.11: left, Nusselt number distribution for the off-design condition with reduced mass flow rate and negative rotor incidence. Injection ratio of 0.8%; right, adiabatic wall temperature distribution referred to the total temperature at stator 2 inlet for the same operating condition.

When observing the heat transfer quantities distributions (Figure 6.11) for the part-load condition, in fact, we find evidence of the aerodynamic effects described so far.

First of all, a general – expected – reduction in the heat transfer rates is evident in the Nusselt number distribution compared to the full load operation (Figure 6.1). Secondly, the average adiabatic wall temperature increases following the total temperature at the inlet of the vane row (that is, the contours of adiabatic wall temperature start from a close to 0K value at the inlet of the passage).

Qualitatively, the heat transfer patterns are quite similar to the one observed at design point, characterized by a stronger heat transfer rate close to the suction side of the passage.

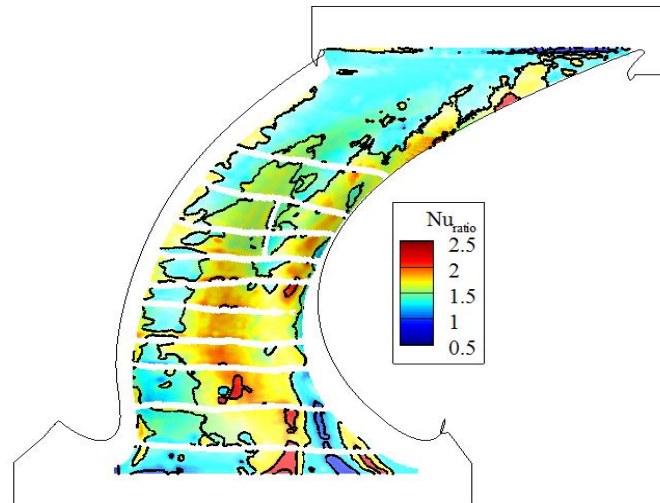


Figure 6.12: point-by-point distribution of ratio of Nusselt number between the nominal operating condition and the part-load condition. Two main regions are clearly distinguishable: a first one, close to the suction side of the passage and occupying the trough of the endwall, affected by the pressure leg of the horseshoe vortex and the passage vortex, presenting higher values of  $Nu_{ratio}$  (1.70 on average) and a second one, grazing the pressure side of the passage along the hill of the endwall and covering most of the outlet of the passage with an average value of  $Nu_{ratio} = 1.34$ .

From a more quantitative point of view, it is of interest to consider the ratio of Nusselt number between the two test cases, which can be compared to the ratio calculated from a 1D correlation for flat plates grazed by a flow with the same inlet Reynolds number as the two cases considered.

The calculation returns the following:

$$Nu_{ratio} = \frac{Nu_{Des. Pt.}}{Nu_{Off-Des.}} = \left( \frac{Re_{Des. Pt.}}{Re_{Off-Des.}} \right)^\alpha = \begin{cases} 1.37 & \text{for } \alpha=0.5 \text{ (laminar)} \\ 1.66 & \text{for } \alpha=0.8 \text{ (turbulent)} \end{cases} \quad (6.2)$$



The two values calculated, respectively for the laminar and turbulent case, have remarkable agreement with the average values detected in the two main regions of the passage observed in Figure 6.12, respectively above and below a threshold level of 1.5 (light blue, average value 1.34 and yellow, average value 1.70).

Two kinds of considerations can be made: one pertaining to the turbulent or laminar nature of the endwall boundary layer, one more strictly concerning the flow structures acting in the passage.

It has been shown by Schubauer and Skramstad [132] how a favorable pressure gradient suppresses oscillations in boundary layers on a flat plate. In turbomachinery flows, it has similarly been observed how the intermittence in the boundary layer decreases with the acceleration of the flow, starting from a high level at the inlet (Moore and Gregory-Smith [133]). A highly turbulent region is found by Moore and Gregory-Smith around the separation line between the passage vortex and the suction side leg of the horseshoe vortex, while the boundary layer is predominantly laminar proceeding downstream towards the throat. Turner [134], additionally, observes no transition taking place on the pressure side of the airfoil used for his experimental and computational study.

The distribution of  $Nu_{ratio}$  of Figure 6.12 is consistent with these observations, suggesting the presence of a laminar boundary layer all along the pressure side of the passage, expanding to cover the whole trailing edge area due to the favorable pressure gradient and of a turbulent boundary layer close to the suction side.

As a confirmation of the reduction in turbulence intensity through the second stator, the mass-averaged profiles of turbulence intensity are shown at the inlet and at the outlet of the vane row, as measured by FRAP (K. Regina, Figure 6.13). The turbulence intensity level is reduced by 41% on average over the whole span.

The strong difference in the scaling of the heat transfer rates with Reynolds number highlights the importance of correctly estimating the local level of turbulence in the passage. From a computational point of view, boundary layer transition modeling is one of the most challenging tasks, particularly in complex turbomachinery flows. Experimental validation is therefore essential also for this specific aspect.

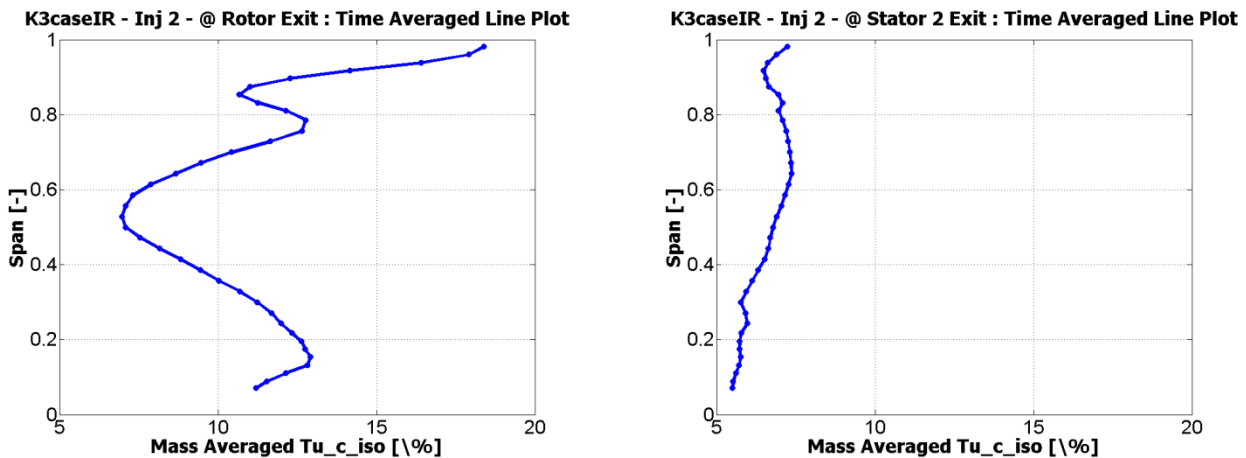


Figure 6.13: mass-averaged profiles of turbulent intensity at the inlet (left) and at the outlet (right) of the stator 2 vane row. Clearly, the acceleration and expansion of the flow through the vane row promotes laminarization of the flow, reducing the turbulence intensity on average from 11.17% to 6.55%.

The possible laminarization of the flow towards the outlet of the passage also justifies the observation that the acceleration does not appear to increase the local Nusselt number as would be expected and as is observed experimentally on the rotor endwall (see chapter 7). This further highlights the importance of reliably predicting the transition or laminarization of the boundary layer for cooling optimization purposes.

Furthermore, as previously explained, the suction leg of the horseshoe vortex and the hub passage vortex play a substantial role in driving the convective heat transfer in correspondence of the suction side of the passage and of the trough of the endwall.

The higher heat transfer rate at design point compared to the part-load operation can be justified by the strengthening of the secondary flows of the second stator on the part of the ones coming from the first. As previously shown, these structures are still distinguishable at the inlet to the second stator (Figure 6.3 and Figure 6.10) and their strength and size are much reduced at part-load and therefore contribute less to the strengthening of the secondary flows in the passage of stator 2.

### 6.2.2 Reduced Reynolds Number with Increased Rotor Incidence

The second off-design condition presents, due to a reduction in the rotational speed of the rotor combined with the reduction in mass flow rate, an increase in incidence on the rotor blade of  $\sim 4^\circ$  and, therefore, a much increased turning and work extraction taking place through the rotor compared to the previously described part-load condition (negative incidence of  $\sim -12^\circ$ ). The load coefficient increases from 2.34 for design point to 2.59 for this off-design condition (10.6% increase).

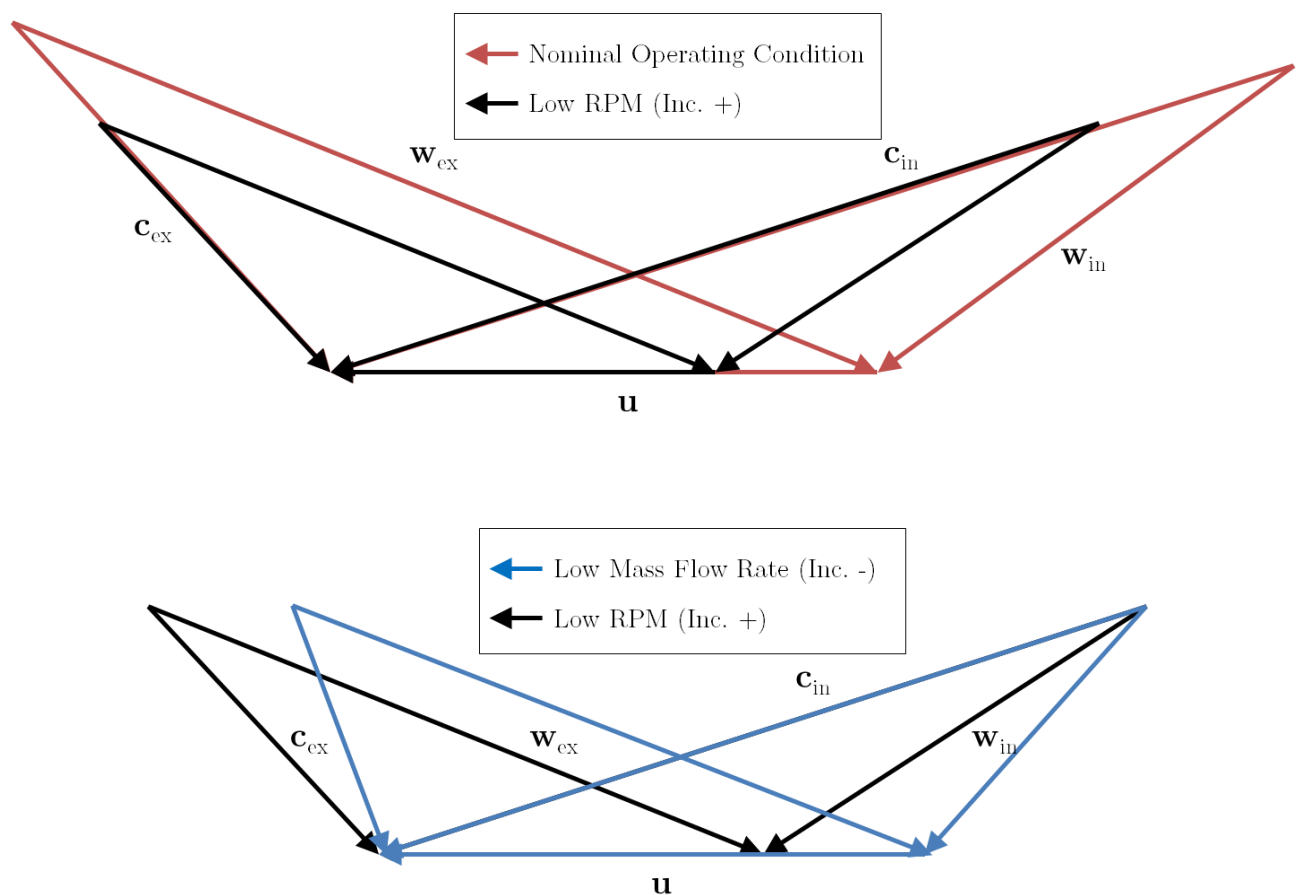


Figure 6.14: top, velocity triangles based on pneumatic probe data for the nominal operating condition and the reduced mass flow rate operation with reduced rotational speed. The relative velocity vector  $w_{in}$  at the inlet of the rotor shows a slightly positive incidence for the off-design condition; bottom, velocity triangles based on pneumatic probe data for the two off-design conditions. The difference in incidence of the relative velocity vector  $w_{in}$  at the inlet of the rotor is evident.

This is illustrated by the velocity triangles shown in Figure 6.14. For the nominal and part-load operating conditions the diagrams are based on pneumatic probe data. For the positive incidence off-design operation, the velocity triangles are drawn based on the assumptions of: same inflow condition at the rotor as in the part-load condition, constant axial velocity through the rotor and negligible radial component of velocity and no deviation from the metal angle at the exit.

The difference in incidence is particularly evident when comparing the two off-design operating conditions (Figure 6.14, bottom).

The velocity triangles are essentially similar between the nominal operating condition and the increased incidence operation (Figure 6.14, top).

Similar considerations can be made concerning the qualitative patterns presented by the heat transfer quantities distributions as what previously discussed both concerning the nominal operation and the part-load condition.

However, it should be noted that the overall Nusselt number level is higher than in the part-load condition: on average by 23%.

A reason for this increase can be found in the strengthened rotor secondary flows due to the increased loading.

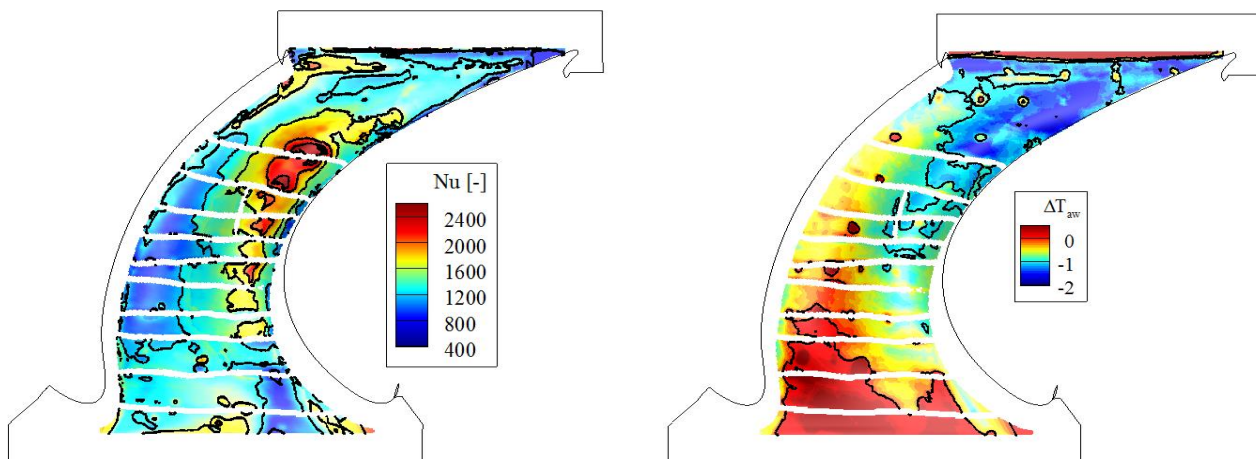


Figure 6.15: left, Nusselt number distribution for the off-design condition with reduced mass flow rate and positive rotor incidence (reduced rotational speed). Injection ratio of 0.8%; right, adiabatic wall temperature distribution referred to the total temperature at stator 2 inlet for the same operating condition.

For this case, the correlation used in (6.2) returns respectively 1.18 for the laminar case and 1.30 for the turbulent boundary layer.

Again, two regions are evident in the distribution of Nusselt number ratio of Figure 6.16, having determined a threshold of 1.2. The average values in these two distinct regions do appear to correspond to the 1D correlation estimation: respectively 1.12 and 1.30. However, the proximity of the two values (10% difference) does not allow making a conclusive statement on whether which scaling is appropriate or whether the higher value of Nusselt number ratio is to be attributed to higher turbulence. Nonetheless, it can be observed that the higher heat transfer rates at design point are now recorded in a region that includes the pressure side of the passage. This might indicate that the passage vortex is significantly stronger in this case than it is at the off-design condition with increased rotor incidence.

The comparable levels of heat transfer at the very inlet of the passage can be caused by the enhanced unsteadiness of the flow due to the stronger secondary flows of the rotor passage, enhanced by the higher loading.

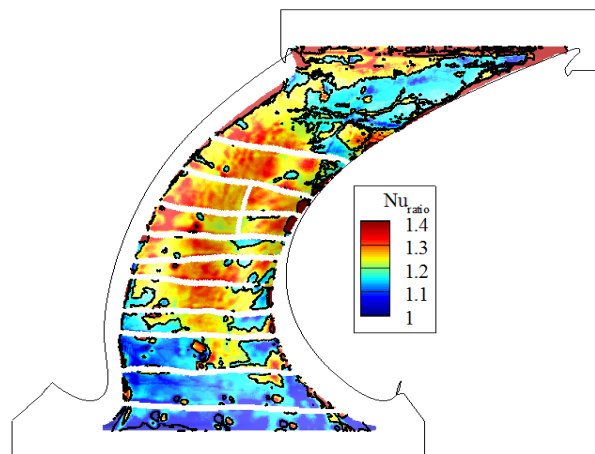


Figure 6.16: point-by-point distribution of ratio of Nusselt number between the nominal operating condition and the off-design operating condition with increased rotor incidence.

## 6.3 Summary

- The heat transfer coefficient distribution on the endwall of the second stator is essentially driven by the combination of the suction leg of the horseshoe vortex and the hub passage vortex, strengthened by the still appreciable traces of the secondary flows of the first stator.

This applies to all operating conditions studied.

- The distributions of Nusselt number, with the highest values in the trough of the contoured endwall and the lowest on the hill, defy the expectations of the role of non-axisymmetric endwall profiling on heat transfer.

This suggests that optimization of the endwall for heat transfer is not relevant and that management of the incoming secondary flows from upstream rows is more critical.

- When comparing the nominal operating condition to the part-load condition, the role of turbulence in determining the local rate of heat transfer is highlighted: a laminarization of the flow appears to take place due to the favorable pressure gradient, thus reducing the exponent of the scaling of Nusselt number as a function of the Reynolds number. I. e., the Nusselt number increases by a factor of  $\sim 1.4$  for a laminar boundary layer with a rise in Reynolds number of 47%, while the factor increases to  $\sim 1.7$  for a turbulent boundary layer.
- This fact, consistent with previous observation, underlines strongly the necessity of appropriate modeling of boundary layer transition for design purposes and, consequently, experimental validation (e. g., by means of intermittence measurements).
- The unsteadiness from the rotor directly upstream influences the distribution of Nusselt number when loading on the blade is increased, thus inducing stronger secondary flows in the rotating frame. However, these appear to influence essentially the inlet of the passage, up to  $\sim 30\%$  of the axial chord. In this region, in fact, the heat transfer rate is comparable between the nominal operating condition and the high-loading condition with reduced mass flow rate, despite the lower Reynolds number. After 30% of the chord, however, the rate is 30% lower at off-design as prescribed by 1D turbulent correlations.

# 7. Heat Transfer Measurements on Contoured Rotor Endwalls

In the current chapter, a first set of experimental results is presented, demonstrating the effect of changes in the overall operation of the turbine on the rotor endwall heat transfer. The results are complemented by results from CFD simulations. A detailed estimation of the uncertainties is provided.

Data is acquired for two operating conditions with different purge flow injection ratios. The main operating parameters are summarized in Table 3.2.

The two operating conditions are the nominal operating point at a pressure ratio of 1.65 and a mass flow rate of 11.7kg/s and a part-load condition with reduced pressure ratio (1.33) and mass flow rate (8.3kg/s). The implications of off-loading the turbine will be discussed in section 7.2.

Three injection ratio IR settings are used in the measurements: 0.0% (i. e., no purge injection), 0.8% and 1.2% of the main mass flow.

In this chapter, results from the nominal operating point will be examined first. Nusselt number distributions and adiabatic wall temperature distributions will be analyzed and the observed trends related to flow features and phenomena documented in the open literature. After having thus demonstrated the sensitivity of the measurement technique, the effects of off-design operation on the heat loads will be described. Finally, the changes in purge air injection ratio during nominal operation and at off-design condition will be discussed and conclusion will be drawn concerning the effectiveness of rim seal leakage flow as rotor hub platform coolant and the effects on the signatures left by the rotor hub passage secondary flows with increasing injection ratios.

## 7.1 Heat Transfer Measurements at Nominal Operating Condition

The tested geometry was optimized for aerodynamic efficiency at the nominal operating condition described by the parameters in the left column of Table 3.2.

In this section, heat transfer results for this operating condition are examined and interpreted by comparing them to the open literature. The results are also complemented by CFD predictions performed by Siemens (section 7.1.1).

The Nusselt number distribution (Figure 7.1(a)) shows the following expected features:

- the start of the thermal boundary layer at the very front of the passage. This derives from the fact that at this axial location the heated endwall begins;
- a high heat transfer region towards the leading edge and pressure side of the blade, which is attributed to the presence of the stagnation point and the formation of the pressure side leg of the horseshoe vortex;
- a triangular region where the heat transfer coefficient is lower towards the inlet, downstream of the start of the thermal boundary layer;
- the increase in heat transfer due to the flow acceleration going towards the throat of the passage.

Similar observations have been reported in literature for studies performed in linear cascades (Blair [56], Graziani et al. [57], Goldstein et al. [69]).

Additionally, a region of lower heat transfer is observed between  $\sim 40$  and  $\sim 60\%$  of the axial extent of the passage. This is attributed to the detachment of the rotor hub passage vortex from the endwall and its migration to higher radial locations. This behavior is consistent with what typically observed in studies concerning rotor secondary flows such as Regina et al. [40], Jenny et al. [41] and Ong et al. [42]. Unsteady aerodynamic data collected on the same turbine configuration confirm the radial migration of the rotor hub secondary flows [43].

The low heat transfer level in the region is then explained by the presence of low-momentum fluid in the wake of the detaching hub passage vortex. The flow



acceleration and expansion is evident in the distribution of non-dimensional adiabatic wall temperature  $\Theta$  for the design point (Figure 7.1(b)).  $\Theta$  is defined as:

$$\Theta = (T_{aw} - T_{t,rel}) / \frac{w_{\infty,in}^2}{2 \cdot C_{p,in}} \quad (7.1)$$

That is, as the difference between the adiabatic wall temperature  $T_{aw}$  and the mass-averaged relative total inlet temperature  $T_{t,rel}$ , non-dimensionalized by the relative dynamic temperature  $\frac{w_{\infty,in}^2}{2 \cdot C_{p,in}}$ .

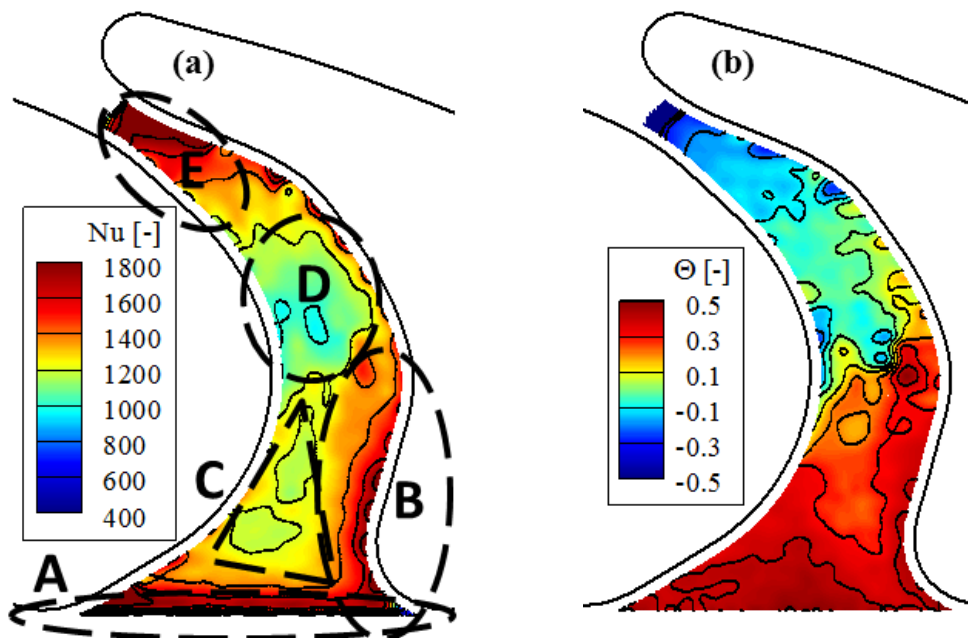


Figure 7.1: Nusselt number distribution for design condition and injection ratio 0.8% (a). Regions of the distribution corresponding to specific flow features are highlighted. I. e.:

- A: start of the thermomechanical boundary layer;
- B: high heat transfer region due to stagnation point on the leading edge and formation of pressure leg of horseshoe vortex;
- C: wedge-like low heat transfer region;
- D: low momentum fluid downstream of the wake of the detaching hub passage vortex produces low heat transfer;
- E: flow acceleration towards the throat results in increasing Nusselt numbers.

adiabatic wall temperature referred to the total relative rotor inlet temperature for design conditions and injection ratio 0.8% (b).

### 7.1.1 Comparison with CFD Predictions

As explained in section 1.1.4 , experimental data on rotor endwall heat transfer are particularly valuable for CFD validation. For this reason, the experimental data are complemented with simulations run by Siemens AG. The results are compared and possible explanations for the disagreement, where present, are provided.

#### Computational Setup

Transient CFD simulations were performed by Siemens AG on a 20° sector of the complete 1.5 stage turbine, including the hub cavity (see schematic of Figure 7.2). The mesh was generated in AutoGrid5™ by Numeca. Approximately 2 million cells were used for each passage with an average  $y^+ < 1$ . The simulations were conducted in ANSYS CFX v15.0 with experimental boundary conditions:

- total pressure and total temperature at the inlet;
- static pressure at the outlet;
- an injection ratio  $IR=0.8\%$  for the cavity flow;
- two uniform endwall heat flux values for the Nusselt number calculation;
- an endwall equivalent sandgrain roughness of  $k_s=12\mu\text{m}$ , representative of the high-emissivity coating.

The Shear Stress Transport turbulence model (SST) and a temporal resolution of 50 time steps per rotor pitch were used. Three complete rotor revolutions ensure a converged aerodynamic flow field with adiabatic walls. An additional revolution was then conducted for each of the two wall heat flux boundary conditions. The results shown are derived from data that was time-averaged over this last revolution.

For comparison, also a steady state result is shown, derived from a mixing plane model. Mesh, boundary conditions and turbulence settings are identical to the transient setup.

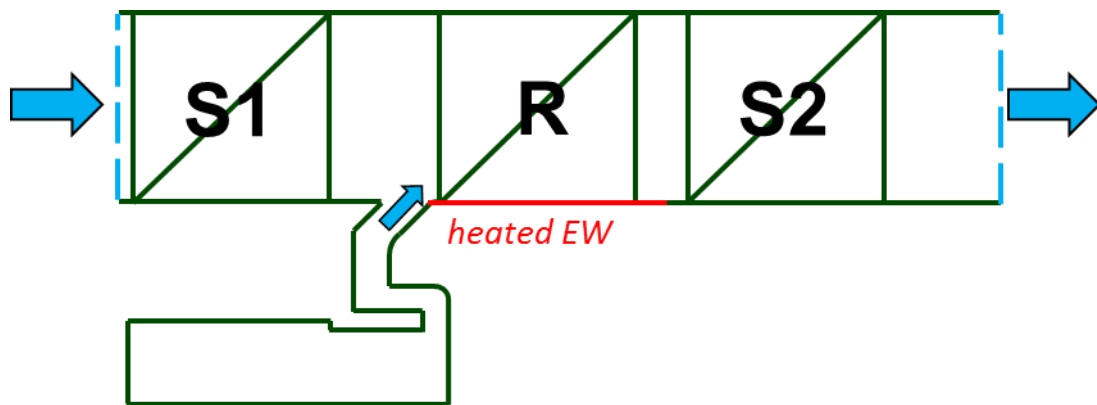


Figure 7.2: schematic of the computational domain (axial cut). All blade rows and rim seal cavity are included in the model. The heat flux boundary condition is applied to the sole rotor endwall as occurs in the experimental setup.

### Agreement of Experimental Results and Predictions

Both predictions and experimental data for IR0.8% show the following features:

- a high heat transfer region on the pressure side of the passage due to the horseshoe vortex formation;
- the increase of Nusselt number due to flow acceleration;
- two regions of lower heat transfer close to the inlet and downstream of the migration of the passage vortex towards the suction side of the passage.

Notice that the start of the boundary layer is not present in the CFD results, because the uniform heat flux boundary condition is imposed from further upstream in the model, compared to the start of the heated platform used in the experiments. The general underestimation of the heat transfer level is attributed to the effect of wall roughness, not properly captured by the simulations. An estimation of the non-dimensional sandgrain roughness can be given according to equation 6.8, based on the measured values for the sandgrain roughness  $k_s$  of the endwall, the mass-averaged relative velocities  $w$  (measured by aerodynamic probes), Fanning's friction factor  $f$  (see previous section 7.3) and the kinematic viscosity of air  $\nu$  at the mass-averaged static conditions measured at inlet and outlet of the rotor. The values are  $\sim 13$  at the inlet of the passage and  $\sim 20$  at the outlet and fall – according to Ligrani and Moffat's [27] classification –, in two different roughness regimes: respectively hydrodynamically smooth and transitionally rough. This can explain, in particular, the divergence of the two corresponding laterally averaged Nusselt number curves in Figure 7.4.

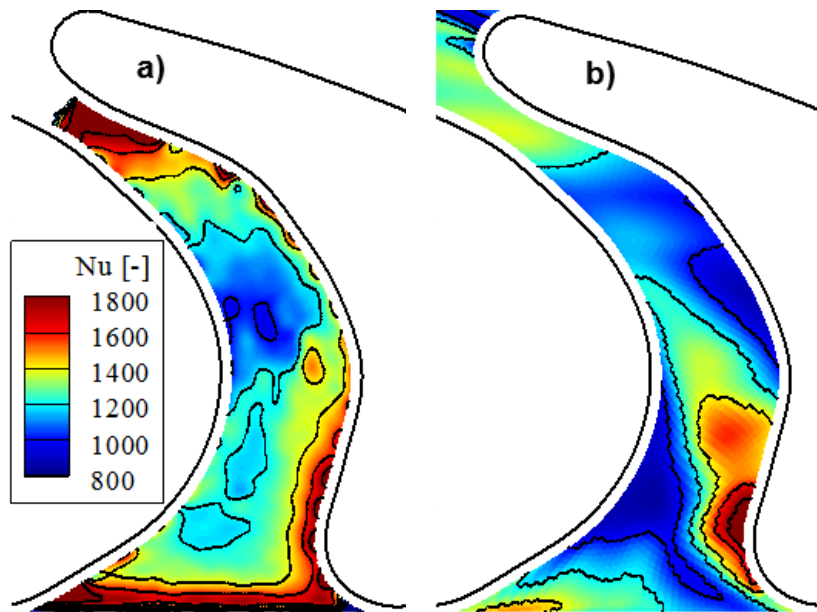


Figure 7.3: comparison of Nusselt number distributions from experiments a) and transient CFD b) for IR0.8%

The circumferentially averaged Nusselt number profiles of Figure 7.4 show good agreement between the experimental data and the unsteady simulations until about 50% of the axial extent of the passage. From this point on, the flow acceleration becomes of relevance and the increase in heat transfer due to the thinner boundary layer is underpredicted. The discrepancy is attributed to a not captured wall roughness effect. The steady CFD simulation tends to overpredict the heat transfer significantly (20-30%). The comparison is completed with a flat plate correlation for turbulent boundary layers on surfaces with uniform heat flux:

$$\text{Nu} = 0.03 \cdot \text{Pr}^{0.6} \cdot \text{Re}_x^{0.8} \cdot \frac{C_{ax}}{x} \quad (7.2)$$

The correlation matches the experiments in the initial part of the passage (until ~15-20% of its axial extent), until secondary flows and flow acceleration occur.

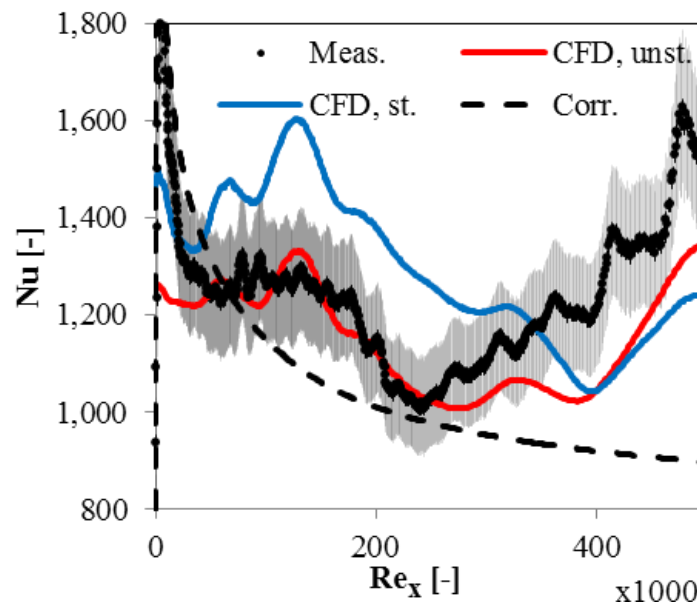


Figure 7.4: circumferentially averaged Nusselt number profiles. Shaded area represents experimental uncertainty.

The different level of agreement with the experimental results of the steady and unsteady CFD predictions indicates that:

- despite being computationally more expensive, running unsteady simulations pays off by returning heat transfer coefficient results 30% more accurate than steady simulations;
- conversely, steady state experiments in cascades, by not including the unsteady effects induced by the rotor-stator interaction, might lead to incorrect results. It is therefore recommendable to validate CFD predictions against experimental data collected in rotating facilities.

## 7.2 Effect of Off-Design Operation

Results are now presented also for the second of two operating conditions summarized in Table 3.2, i. e. the off-design or part-load condition with a reduced pressure ratio (1.33 instead of 1.65) and mass flow rate (8.5kg/s instead of 11.65kg/s).

The change of these two parameters essentially affects the results because of a reduction in Reynolds number and a negative incidence of the flow on the rotor blades ( $\sim -12.3^\circ$ ).

The reduction of mass flow rate translates in an almost proportional reduction of the axial component of velocity. The result is negative incidence of the flow on the leading edge of the rotor blade, as shown in Figure 7.6. At mid-span, the incidence angle is calculated to be  $-12.3^\circ$ . At lower spanwise locations, such as 10% span, this value reduces to  $-10.5^\circ$ . A profile of incidence angle is shown in Figure 7.5. The incidence angle over the span is estimated by comparing the relative flow angle distribution at design point with the one at off-design condition. Data was obtained from 5-hole probe measurements at the inlet of the rotor.

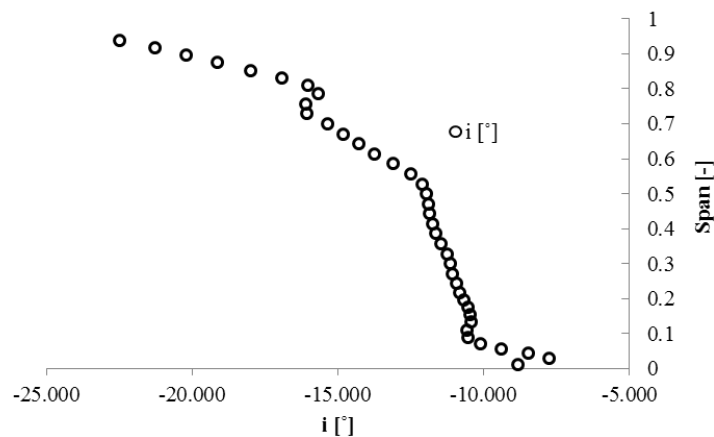


Figure 7.5: radial profile of incidence calculated as the difference between the relative flow angle at design point and the relative flow angle at off-design condition starting from pneumatic probe measurements performed at rotor inlet.

Still, the stagnation point moves to the suction side of the airfoil increasing locally the static pressure. As a consequence, the coolant exiting the rim seal cavity will enter the passage closer to its center than at design point.

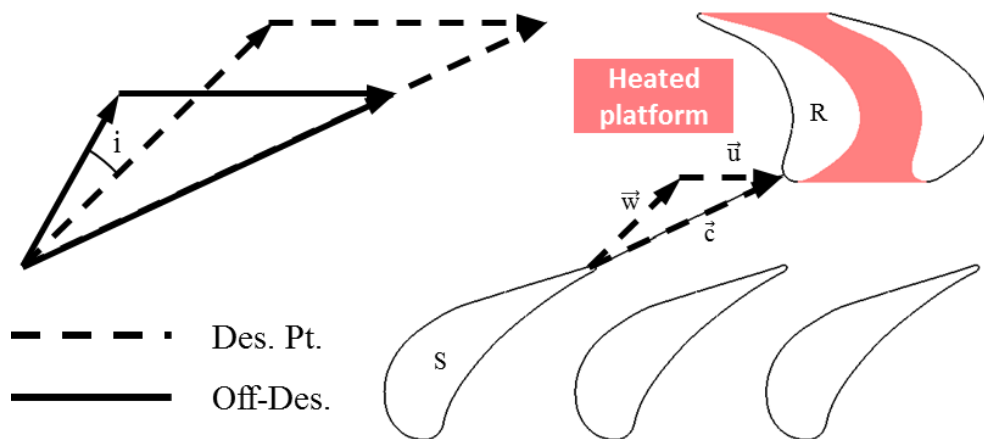


Figure 7.6: velocity triangles at design point and off-design condition based on pneumatic probe, mass-averaged data at rotor exit. The reduction in mass flow rate results in negative incidence on the rotor quantified in  $-12.3^\circ$  at mid-span

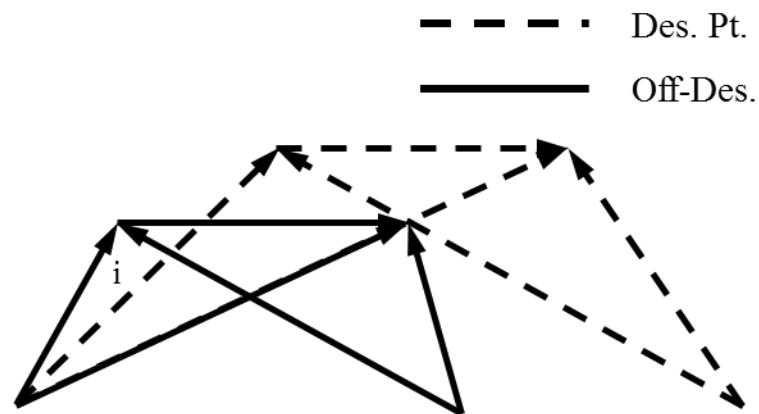


Figure 7.7: the load coefficient is strongly reduced when passing from the design condition to the part-load (off-design) condition.

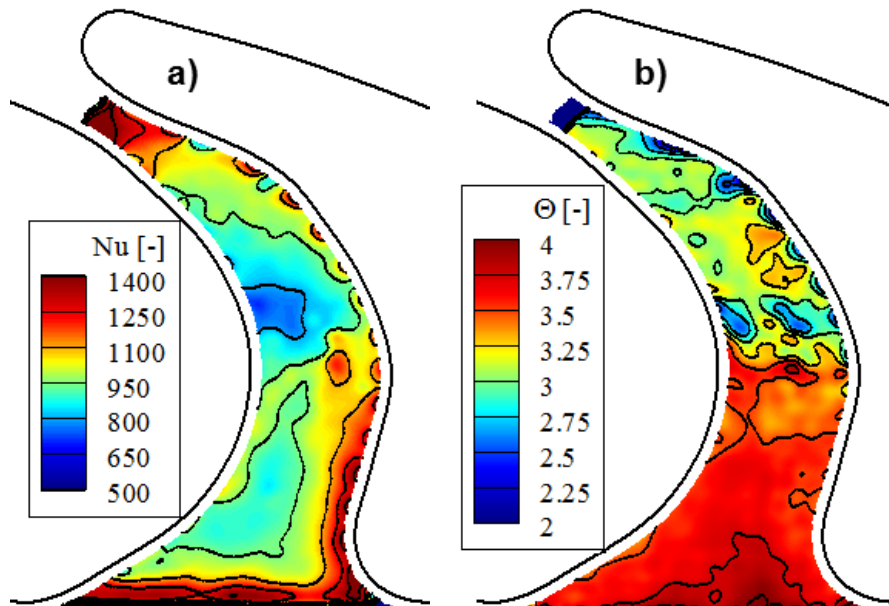


Figure 7.8: Nusselt number distribution for off-design condition and injection ratio 0.0% (a) non-dimensional adiabatic wall temperature b).

The features outlined in the description of the Nusselt number distribution for the nominal operating condition are still visible at part-load. High heat transfer levels are again detected at the start of the heated platform, towards the pressure side of the blade in the aft-portion of the passage and approaching the throat. A triangular region of lower heat transfer (even more clearly defined in the off-design case) pointing towards downstream is also found in the first 50% of the passage, followed by another area with lower heat transfer levels, possibly following the detachment of the hub passage vortex from the endwall. The non-dimensional adiabatic wall temperature distribution also qualitatively matches what found at design point.

Clearly, both Nusselt number values and adiabatic wall temperature values are affected by the change in operating condition. The former especially because of Reynolds number effect, the second due to the flow expanding less through the first stator.



Based on the turbulent correlation for a flat plate with uniform heat flux [106], it is possible to estimate the effect of the reduction in Reynolds number on the heat transfer coefficient:

$$\text{St}_{\text{ratio}} \approx \left( \frac{\text{Re}_{\text{Des. Pt.}}}{\text{Re}_{\text{Off-Des.}}} \right)^{-0.2} = 0.9 \quad (7.3)$$

The Reynolds numbers in eq. 7.3 are the ones calculated at rotor exit as reported in Table 3.2: operating conditions of the LISA facility during heat transfer measurements. A comparison between the cases is shown as a ratio of Stanton numbers in Figure 7.9(b). The ratio is defined as:

$$\text{St}_{\text{ratio}} = \frac{\text{St}_{\text{Des. Pt.}}}{\text{St}_{\text{Off-Des}}} \quad (7.4)$$

The values of  $\text{St}_{\text{ratio}}$  shown in Figure 7.9(b) approach this estimate towards the throat of the passage.

A sharp contrast in the  $\text{St}_{\text{ratio}}$  that could be related to boundary layer transition is not observable.

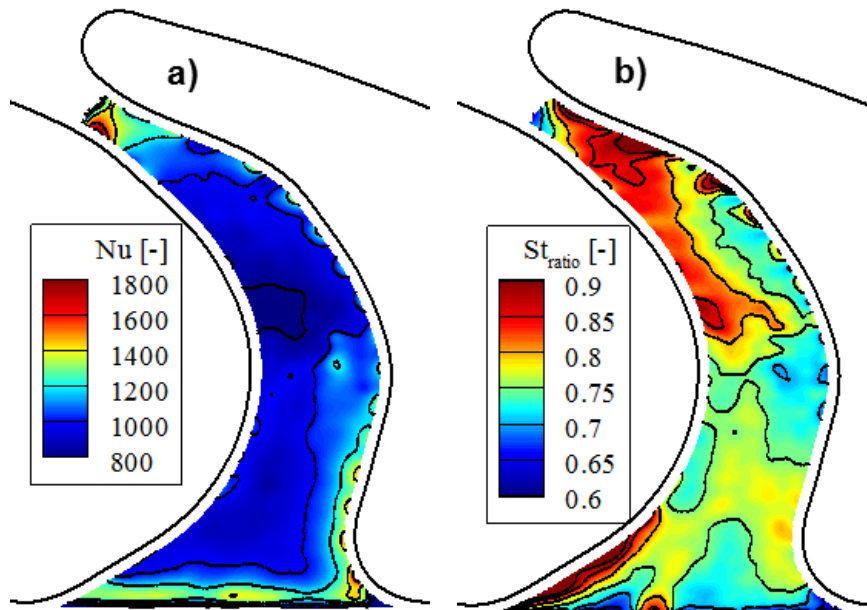


Figure 7.9: Nusselt number distribution for off-design condition and injection ratio 0.8% (a) ratio of Stanton number between design and off-design operating condition (b).

The Nusselt number distribution at part load (Figure 7.9a)) does not qualitatively differ from the one shown for full load operation (Figure 7.8a)), despite the negative incidence at off-design condition. On the other hand, the Stanton number distribution of Figure 7.9b) suggests that, in relative terms, the effect of secondary flows at the inlet is stronger for the off-design condition. This might be justified by either stronger vortices, lower radial location of the secondary flows due to off-loading or the effect of the negative incidence.

The laterally averaged profiles also show a decrease of Nusselt number beyond the uncertainties.

Several flow effects are still visible in the laterally averaged Nusselt number profiles in Figure 7.10(a). In particular:

- the typical decay of Nusselt number as present also in flat plate cases due to the start of the thermal boundary layer and its development;
- between 20 and 40% of the axial extent of the passage, the decrease is interrupted by the presence of the secondary flows;

- at 55% of the axial chord, the heat transfer increases due to the acceleration of the flow in the passage.

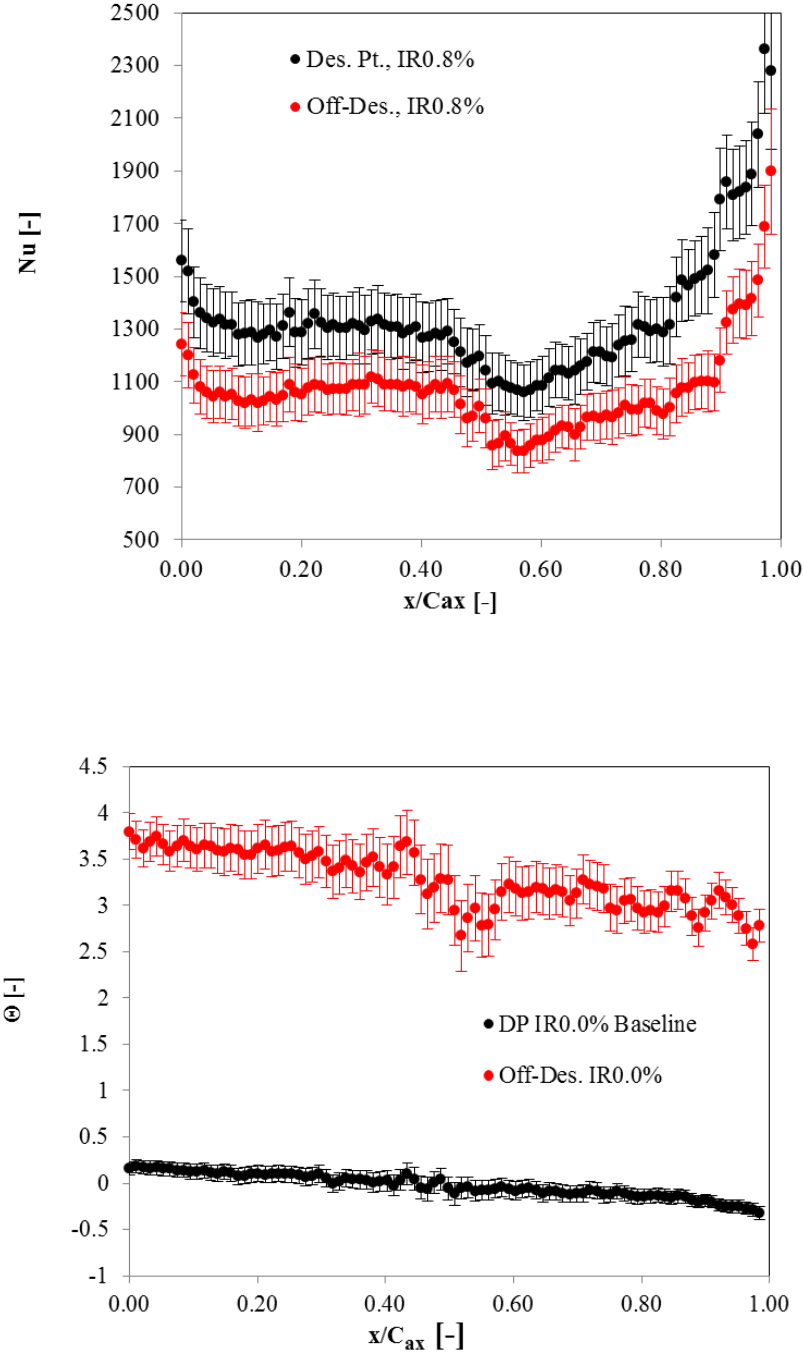


Figure 7.10: Laterally averaged Nusselt number profiles for design point and part-load operating condition.

### 7.3 Effect of Roughness

The effect of roughness is non-negligible on the presented results. Roughness was measured by means of a mechanical profilometer Mitutoyo SJ-210 at two locations on the endwall (see Figure 7.12). Because of the high-emissivity coating on the heat transfer platforms, the following values of roughness were measured:

Table 16: Roughness values measured on the endwall of the heat transfer platform for the contoured case

Locations	Ra [ $\mu\text{m}$ ]	Rz [ $\mu\text{m}$ ]
Loc. 1	6.7	45.6
Loc. 2	6.2	39.5

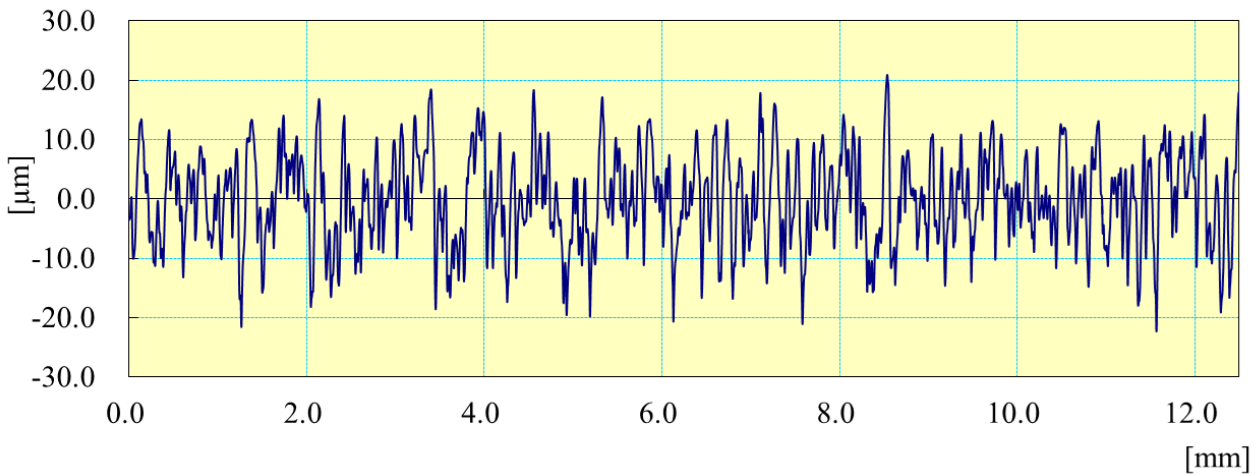


Figure 7.11: typical roughness profile for location 2 shown in Figure 7.12.

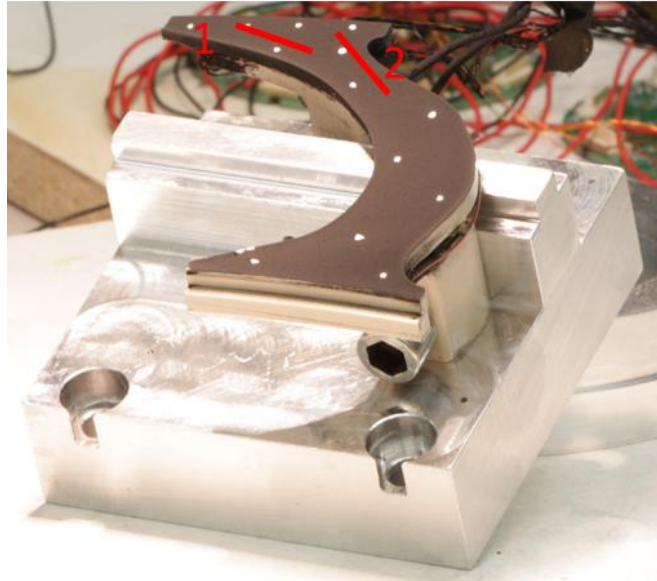


Figure 7.12: location of roughness measurements on the rotor endwall (highlighted in red) before heat transfer platform assembly in rotor.

Assuming  $k = R_z$  as roughness parameter (see Bons et al. [135]) and following van Rij's correlation [136], a value of  $k_s^+ = 1.97 \cdot R_z$  can be calculated based on the following equations:

$$k_s^+ = \frac{k_s \cdot u_\tau}{\nu} \quad (7.5)$$

$$u_\tau = \sqrt{\frac{\tau_w}{\rho}} \quad (7.6)$$

$$\tau_w = \frac{f \cdot \rho \cdot w^2}{2} \quad (7.7)$$

By substitution of eq. (7.7) in eq. (7.6) and again in eq. (7.5) we obtain:

$$k_s^+ = \frac{k_s \cdot w}{\nu} \cdot \sqrt{\frac{f}{2}} \quad (7.8)$$

where  $k_s$  is the equivalent sandgrain roughness,  $u_\tau$  is the friction velocity,  $\tau_w$  is the wall shear stress,  $\nu$  is the air kinematic viscosity,  $\rho$  is the air density,  $w$  is

the mass-averaged rotor-relative flow velocity and  $f$  is Fanning friction factor evaluated according to Chen [137]. Equation (7.8) is the definition of the non-dimensional roughness.

The values of  $k_s^+$  are respectively 28 and 47. Both values at the outlet falls in the transitionally rough regime, according to the classification of Nikuradse [138] (transitionally rough regime for  $5 < k_s^+ < 70$ ). The effect of roughness on flow and heat transfer is, therefore, not negligible and its correct prediction can affect the agreement between CFD and experiments, particularly where the flow is the fastest, since the value of non-dimensional roughness almost doubles across the passage. It has been shown in similar geometries, in fact, that CFD tends to underpredict the increase in heat transfer coefficient coming from the higher penetration of the roughness elements in the boundary layer [17].

## 7.4 Summary

It is estimated that the experimental technique developed for this work is capable of returning Nusselt number distributions accurate within  $\pm 9\%$  and adiabatic wall temperature distributions accurate within  $\pm 0.35\text{K}$  (average numbers over whole endwall).

The technique is demonstrated to be sensitive not only to strong changes in the operation of the turbine – especially implying reductions in Reynolds number – but also to local flow features on the endwall.

The observed features are consistent to what expected from previous observation available in the open literature.

It was observed that a reduction in Reynolds number produces the expected drop in Nusselt number, but does not qualitatively alter its distribution.

Negative incidence also does not strongly influence the general distribution of the heat transfer quantities.

A set of computational results are compared to the experiments and enable the following considerations:

- as already observed in cascades, the effect of roughness on heat transfer is not well captured by the CFD predictions in presence of strong accelerations (i. e., towards the exit of the passage);
- unsteady simulations predict Nusselt numbers within the experimental uncertainty, while steady simulations show an overprediction of up to 30%.

It is concluded that

- the additional computational cost of unsteady simulations is worth when accuracy is required;
- experimental results acquired in rotating machines and, therefore, including the unsteady effects of the rotor-stator interaction can provide a more reliable benchmark against which to validate CFD codes for heat transfer in turbomachinery.





## 8. Effect of Purge Air Injection on the Heat Load Distributions

The general purpose of rim seal leakage flow or purge flow has already been illustrated in the introductory section 1.2.4 . The purge flow is leaked through the cavities present between rotating and stationary organs to prevent the ingestion of hot gases below the platform, where sensitive mechanical components such as the shaft and bearings may otherwise suffer from overheating.

Whilst the detrimental impact of the purge air on the aerodynamic performance of the rotor has been extensively documented, its global impact on the heat load, with special reference to Nusselt number distributions, has not been observed – to the best of the author’s knowledge – in the rotating frame. Only cooling effectiveness distributions, either in cascades or in rotating facilities, can be found in the open literature.

In this chapter, results are presented for the two injection rate settings of 0.8% and 1.2% referred to the reference case with no purge air injection (0.0%) for both nominal and part-load operating conditions. Variations in Nusselt number and adiabatic wall temperature with respect to the designated reference cases are related to purge flow aerodynamics as documented in the open literature and conclusions are drawn on the effectiveness of purge air as rotor endwall coolant. Significant differences are observed in the distributions for design point and part-load conditions. An interpretation is offered on the basis of known effects of off-loading on rotor endwall aerodynamics.

## 8.1 Definitions

As already mentioned, results are presented in terms of differences with reference to a designed reference case, i. e. the same overall operating condition of the machine, but with no purge flow injection. Variations in Nusselt number and adiabatic wall temperatures are shown respectively in terms of percentage of the reference Nusselt number (Figure 8.3a) and Figure 8.4a)) and a non-dimensional temperature difference  $\theta$  (Figure 8.3b) and Figure 8.4b)). The two quantities are defined as:

$$\Delta Nu = \frac{Nu - Nu_{0.0\%}}{Nu_{0.0\%}} \cdot 100 \quad (8.1)$$

$$\theta = \frac{T_{aw} - T_{aw,0.0\%}}{T_{t,rel,purge} - T_{t,rel,MAIN}} \quad (8.2)$$

In eq. (8.2),  $T_{aw}$  is the local adiabatic wall temperature for the test case of interest,  $T_{aw,0.0\%}$  is the adiabatic wall temperature of the reference test case with no purge flow injection,  $T_{t,rel,purge}$  and  $T_{t,rel,MAIN}$  are respectively the rotor-relative total temperatures of the purge flow and of the main flow, obtained by means of probe measurements. The definition enables a qualitative assessment of the cooling effect of the purge flow over the endwall. In the current study, density ratios are not representative of cooling conditions in actual engines, being in the order of 1. The impact of this limitation on the results is discussed in section 8.3. The cavity flow actually presents a slightly higher rotor-relative total temperature than the main flow, as shown in Figure 8.1. The total temperature difference at the denominator of eq. (8.2):

$$T_{tot,rel,purge} - T_{tot,rel,MAIN} \quad (8.3)$$

increases proportionally – for design conditions – with the injected mass flow rate. The value calculated at zero purge flow rate are used to calculate  $\theta$

according to eq. (8.2). For the part-load condition, the same trend is assumed to hold when offset to cross the only datum available (off-design condition with purge flow injection rate 0.8%).

The values used are summarized in Table 17.

Table 17: rotor-relative total temperature differences used for non-dimensionalization according to eq. (6.4)

Operating Condition	$T_{\text{tot,rel,purge}} - T_{\text{tot,rel,MAIN}}$
Design Point	$(2.16 \pm 0.2)\text{K}$
Off-Design Condition	$(1.58 \pm 0.2)\text{K}$

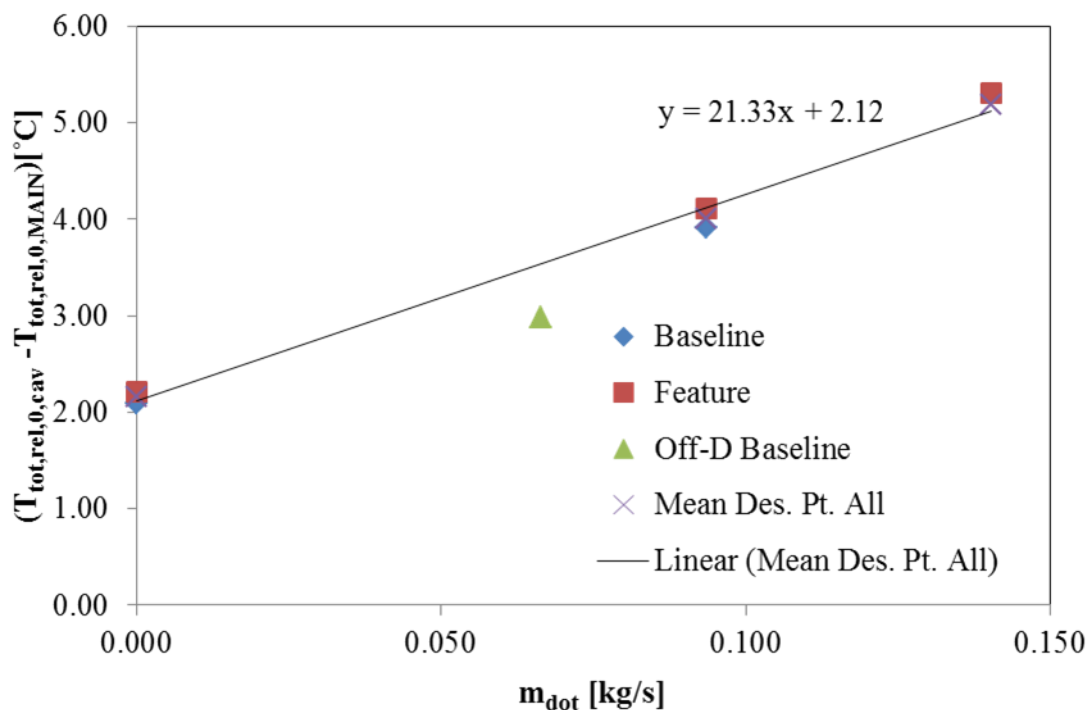


Figure 8.1: the relative total temperature difference between cavity flow and main flow increases proportionally with the injected mass flow. The values calculated based on the linear trends at 0 purge injection rate are used to non-dimensionalize the adiabatic wall temperature difference.

## 8.2 Effect of Purge Air Injection on the Heat Load Distributions at Design Point

In this section, results are presented for varying purge flow injection ratio  $IR$  (eq. 3.1) while operating the turbine at its nominal operating point. Variations of Nusselt number on a point-wise basis are shown in Figure 8.3a) and Figure 8.4a), respectively for  $IR0.8\%$  and  $IR1.2\%$ , while laterally averaged profiles of Nusselt numbers are presented for all cases in Figure 8.6a).

Differences in Nusselt number induced by different rates of purge air injection are generally within the measurement uncertainties both on a local and on a circumferentially averaged basis. Nonetheless, at the very inlet of the passage, close to the suction side of the rotor blade, pairs of islands presenting increases up to 20% of the reference case and decreases of the order of 5% are consistently observed in both Nusselt number distributions recorded for  $IR0.8\%$  and  $IR1.2\%$ . The patterns suggest a strengthening of the suction side leg of the horseshoe vortex producing an increase of heat transfer due to the downwash acceleration and a milder decrease corresponding to the upwash acceleration. Similar effects have been observed in turbulent boundary layers perturbed by longitudinal vortices (Eibeck et al. [131]). Moreover, increases up to 20% are also recorded closer to the pressure side of the blade and affecting a wider area spanning towards the suction side. This can be related to the strengthening of the passage vortex due to the entrainment of purge flow. Additionally, it is worth noting that the area of Nusselt number increase in the proximity of the pressure side of the blade has a lesser axial extent in the  $IR1.2\%$  case. This suggests an earlier lift-off of the passage vortex due to the higher radial momentum of the purge flow. This last circumstance is confirmed by the pitch angle profiles of Figure 8.2. It is clear that the injection of purge flow from the cavity increasingly pushes the main flow towards higher radial spanwise locations with greater injection ratios. The influence of purge air on pitch angle is felt up until 50% of the span due to the additional blockage to the incoming main flow.

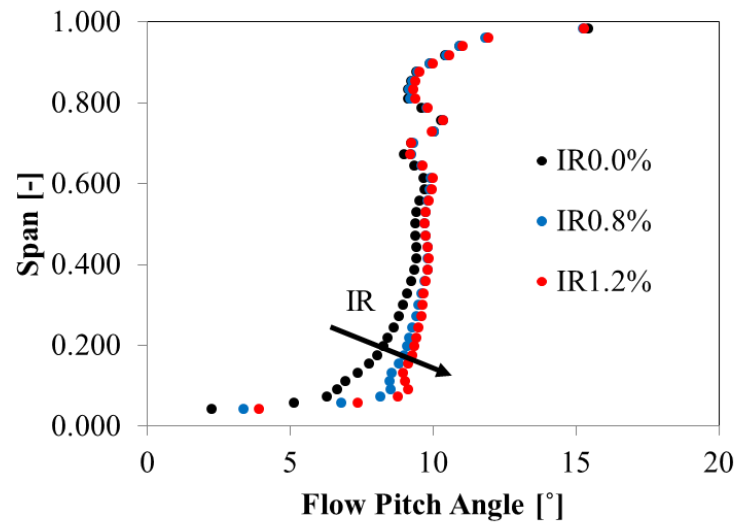


Figure 8.2: mass-averaged flow pitch angle profiles for baseline purge flow cavity geometry at design point. The influence of purge air in increasing the flow pitch angle is clear up until almost 50% of the span and – of course – especially at the endwall.

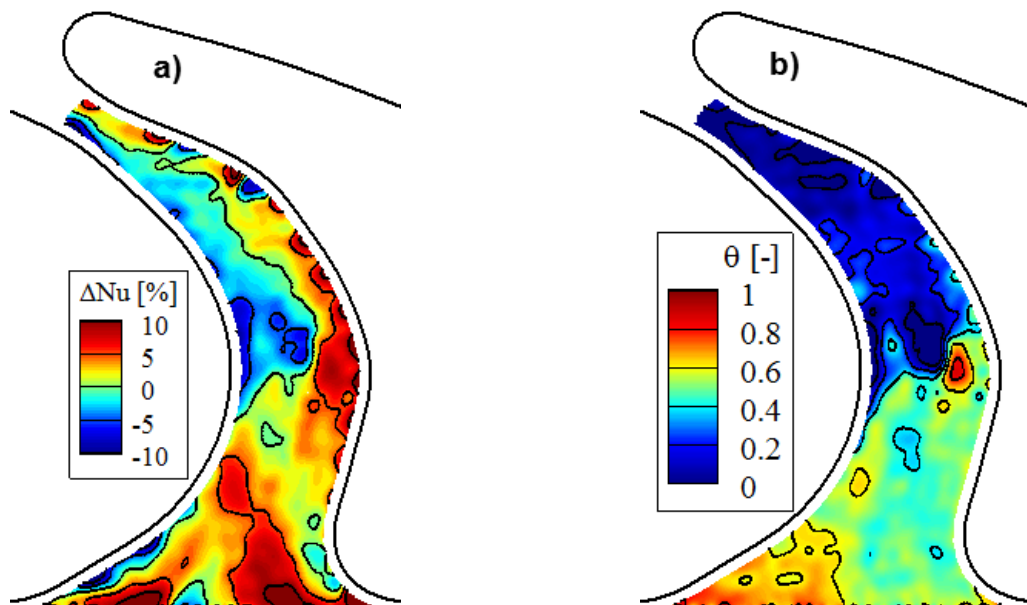


Figure 8.3: comparison between reference case (design point, IR=0.0%) and IR=0.8%. Nusselt number relative difference a) and non-dimensional adiabatic wall temperature difference (eq. (8.2)) b).

For both of the cases presented, the distributions of non-dimensional adiabatic wall temperature difference (Figure 8.3b) and Figure 8.3b)) underline how the purge flow is most effective as coolant in the proximity of the suction side of the rotor blade. This is expected due to the static pressure being lower towards this side of the passage and – therefore – favorable for purge flow ejection locally. Furthermore, this is consistent with observations made in past studies (section 1.2.4 ). In this location, the effect of purge air manifests itself as a local increase of the adiabatic wall temperature because of the difference in relative total temperature between rim seal leakage flow and the main flow (section 8.1 and Table 17). Respectively, the increase is of 0.67 times the difference between the rotor-relative total temperatures of the cavity flow and the main flow for an IR0.8% and of 0.82 times for an IR1.2%.

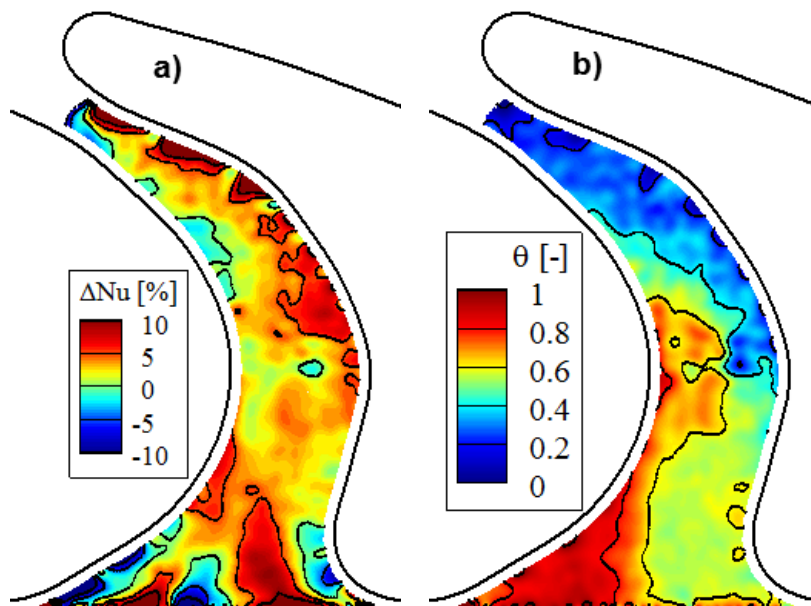


Figure 8.4: comparison between reference case (design point, IR=0.0%) and IR=1.2%. Nusselt number relative difference a) and non-dimensional adiabatic wall temperature difference (eq. (8.2)) b).

The local character of the adiabatic wall temperature variation highlights how the purge air has a potential application as coolant for specific rotor endwall locations (i. e., inlet of the passage towards the suction side of the blade).

On a circumferentially averaged basis, Figure 8.6a) shows negligible impact of the purge air injection on the Nusselt number distribution, while differences are still well distinguishable in Figure 8.6b) on the non-dimensional adiabatic wall temperature  $\Theta$ , especially towards the inlet and until  $\sim 30\%$  of the rotor blade axial chord  $C_{ax}$ .

The tendency of the purge flow to exit towards the suction side of the passage is not only confirmed by previous study on purge flow aerodynamics and cooling effectiveness (see section 1.2.4 ), but also finds experimental evidence in the non-uniform distribution of normalized static pressure at the purge flow cavity exit shown in Figure 8.5.

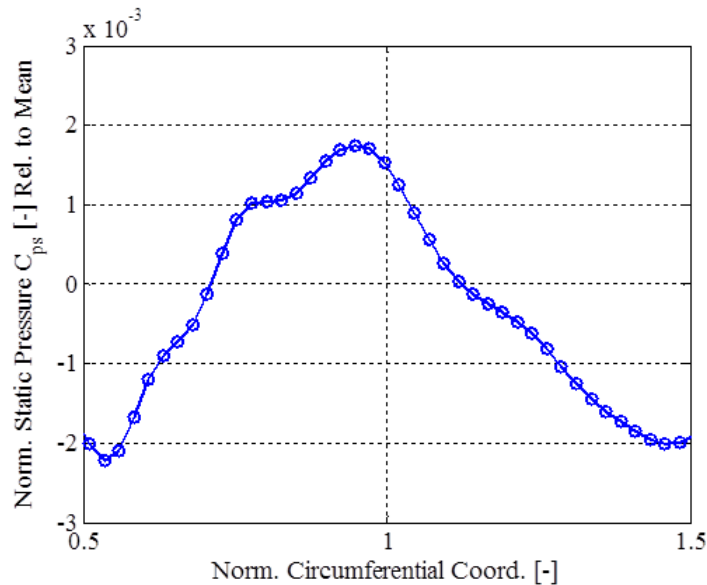


Figure 8.5: rotor-relative, normalized static pressure distribution referred to the mean value over three rotor pitches for the nominal operating point with  $IR=0.8\%$ . The existence of preferential location of purge flow ejection in the passage is confirmed. The lower static pressure induced by the suction surface ( $x\sim 0.55$ ) of the airfoil rapidly recovers due to the potential field of the pressure side.

A sharp gradient of static pressure towards the suction side of the passage (lower  $x$  coordinates) suggests preferential purge injection in that area of the passage.

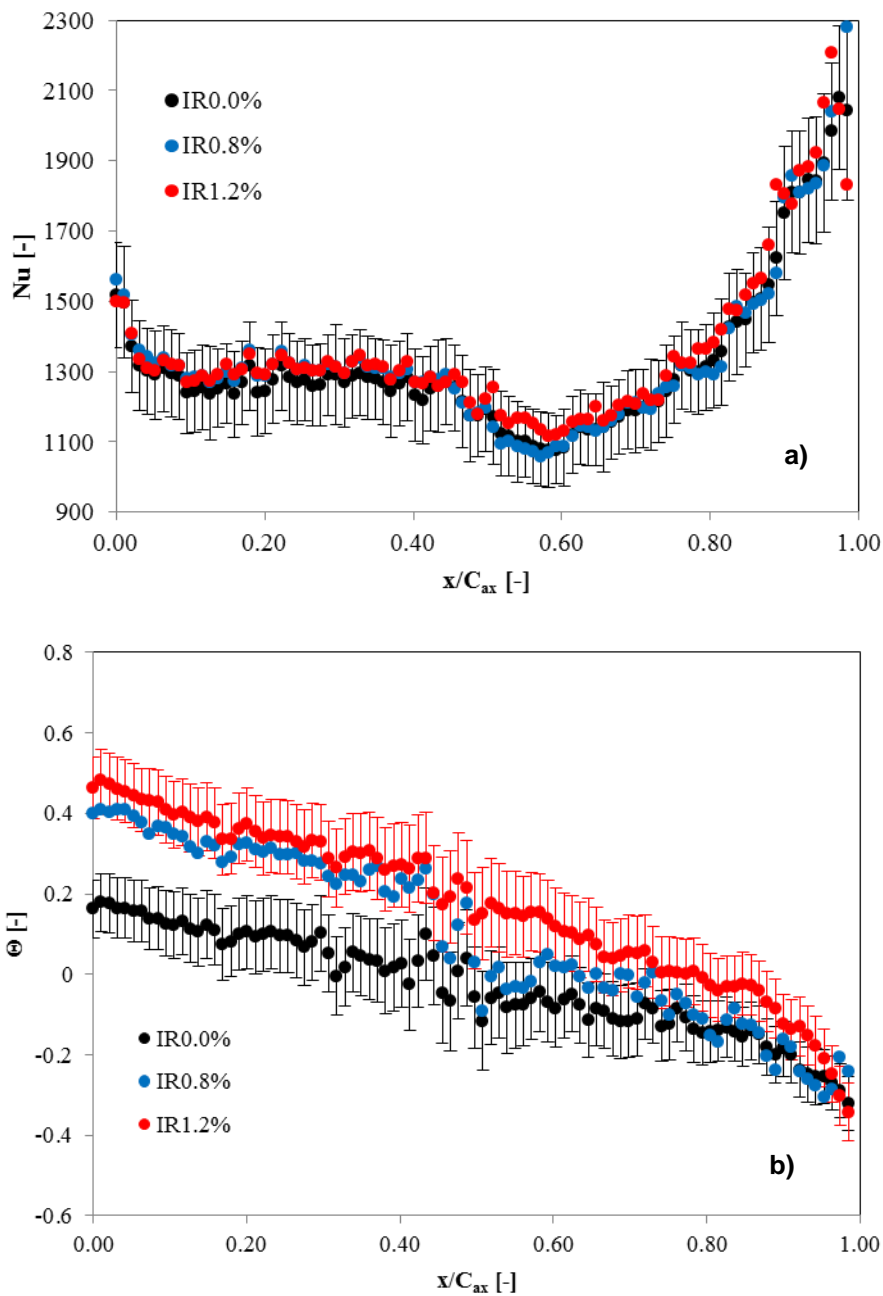


Figure 8.6: circumferentially averaged Nusselt number for all test cases a); circumferentially averaged non-dimensional adiabatic wall temperature b), Error bars represent a 95% confidence interval.



## 8.3 Effect of Unitary Density Ratio

A conclusive statement of the impact of the purge air total temperature on the local fluid dynamics would require a parametric study of the aerodynamics with varying purge temperatures. Such an investigation falls beyond the scope of the current work. However, the problem can be reduced to the effect of density ratio  $DR = \rho_c/\rho_m$ . Several film cooling papers can be found in literature documenting how blowing ratio  $BR = (\rho_c \cdot u_c)/(\rho_m \cdot u_m)$  and momentum flux ratio  $I = (\rho_c \cdot u_c^2)/(\rho_m \cdot u_m^2)$  are more relevant to the mechanics and performance of the cooling flow than the sheer density ratio. In particular, an exhaustive review is given by Bogard and Thole [139]. Indeed, with a low density ratio, only one other scaling parameter among momentum flux ratio and blowing ratio can be simultaneously matched to the engine operation. In the case of the present paper, the parameter rigorously matched is the blowing ratio, proportional to the injection ratio  $IR$  (eq. 3.1). The blowing ratio  $BR$  scales the convective heat transport, as this is proportional to  $\rho_c \cdot u_c \cdot C_p$ . The momentum flux ratio  $I$  being lower as a result of the low density ratio  $DR$ , the coolant has lower penetration in the main flow than in fully scaled operating condition. On the other hand, provided that the momentum flux ratio  $I$  does not induce the coolant to detach from the surface, its effect on the general dynamics is not particularly relevant otherwise. For these reasons, and due to the technical difficulties of simulating a representative density ratio, copious literature is available on film cooling or purge flow studies performed with density ratios close to unity (e. g.: Gao et al. [58], Lynch and Thole [60]).

## 8.4 Effect of Purge Air Injection on the Heat Load Distributions at Off-Design Conditions

The effect of reducing mass flow rate and turbine load coefficient on the main flow aerodynamics has been discussed in section 7.2. However, operating the turbine at part-load also affects the modes of interaction between the main flow and the rim seal leakage flow.

According to Schobeiri et al. [21], decreasing the incidence on the rotor blade (as it happens in the case in study,  $i = -12.3^\circ$ ) results in two main effects:

- 1) the strength of the secondary flows is reduced due to lower turning;
- 2) the incoming cooling film is injected closer to the pressure side and exhibits a lower tendency to migrate towards the suction side while flowing through the passage. This results in a higher coverage of the coolant on the endwall. This effect is to be attributed to the displacement of the stagnation point towards the suction side and the decrease of the pressure gradient between pressure and suction side of the passage.

Snedden et al. [140] study computationally and experimentally the performance of a generically contoured stage compared to one with cylindrical endwalls and find that the migration of the passage vortex towards outer radii is encouraged by higher loading of the blade row. Kang et al [71] observe that higher Reynolds numbers induce span-wise migration of the passage vortex in linear cascades. Conversely, it can be stated that when off-loading the blades, the secondary flows adheres to the endwall longer.

These findings are helpful to interpret the trends observed in this study, in particular when analyzing the distributions of non-dimensional adiabatic wall temperature difference  $\theta$  (eq. 8.2).

Before doing so, however, it is useful to provide the Nusselt number distribution and non-dimensional adiabatic wall temperature distribution for the reference case (Figure 8.7).

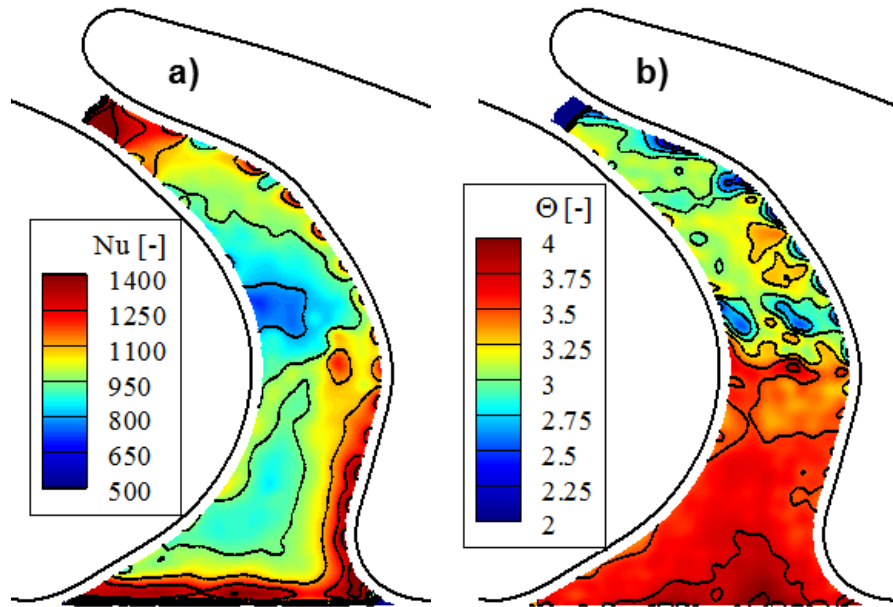


Figure 8.7: Nusselt number distribution (a) and non-dimensional adiabatic wall temperature for off-design condition and injection ratio 0.0% (b).

Considerations about the results shown in Figure 8.7 are analogous to the ones discussed in section 7.2, as the variation of purge injection rate (0.0% instead of 0.8%) does not qualitatively alter the main trends observable on the endwall distributions.

However, when analyzing the relative differences in Nusselt number distributions and adiabatic wall temperature, significant changes in the patterns can be observed compared to the corresponding distributions obtained at the nominal operating point.

Figure 8.8 shows the  $\Delta Nu$  (eq. 8.1) and  $\theta$  (eq. 8.2) distributions for  $IR = 0.8\%$ .

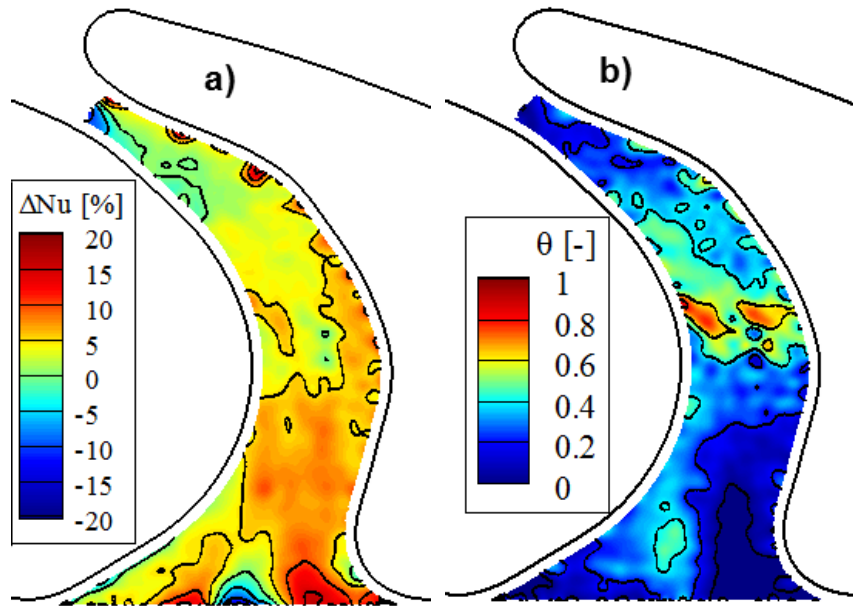


Figure 8.8: comparison between reference case (off-design, IR=0.0%) and IR=0.8%. Nusselt number relative difference a) and non-dimensional adiabatic wall temperature difference (eq. (8.2)) b).

Compared to the same injection rate setting at design condition, the purge flow seems to be affecting more strongly the heat transfer coefficient distribution when off-loading the blades. In fact, increases between 10 and 15% are observable for IR0.8% compared to the reference case with no purge injection (Figure 8.8).

When increasing the injection ratio to 1.2% of the core mass flow (Figure 8.9), the increases in Nusselt number reach up to  $\sim 20\%$  and affect much wider areas than in the design point case with the same injection ratio (Figure 8.3). That is, as expected, the introduction of leakage flow in the passage strengthens the rotor hub secondary flows, i. e. the pressure leg of the horseshoe vortex and the passage vortex and it does so more severely than at design point.

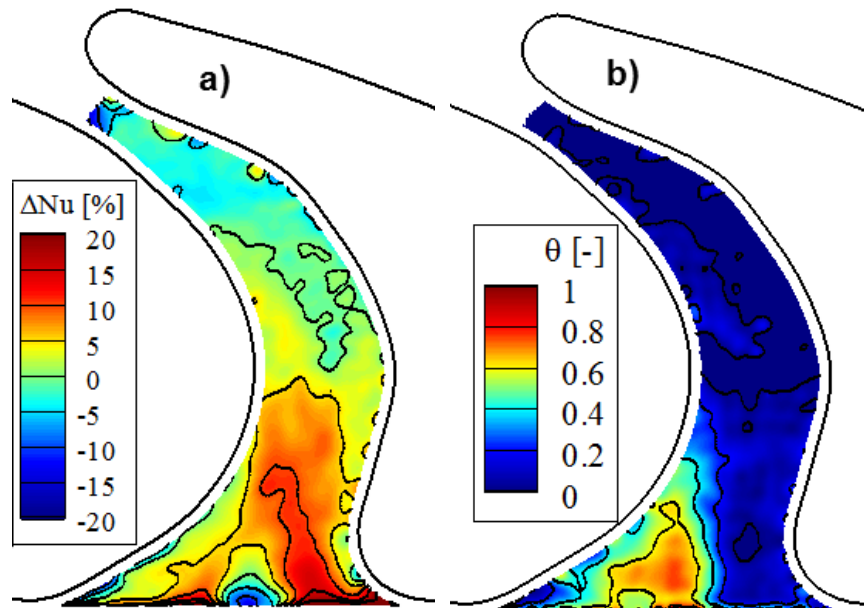


Figure 8.9: comparison between reference case (off-design, IR=0.0%) and IR=1.2%. Nusselt number relative difference a) and non-dimensional adiabatic wall temperature difference (eq. (8.2)) b).

Based on the considerations at the beginning of this section and keeping in mind the aerodynamic effects of purge flow described in section 1.2.4 of the introduction, two main reasons for these observations can be given:

- 1) the wider and clearer signature of the secondary flows on the endwall distribution of Nusselt number difference at part-load derives from their lower spanwise position, consistently with the observations of Snedden [140] and Kang [71];
- 2) the increase in Nusselt number difference with increasing injection ratio is consistent with already observed at design point and follows from the strengthening of the secondary flows due to more severe mixing losses.

The increase in purge flow injection rate appears also to be affecting the adhesion of the passage vortex to the endwall. Both the  $\Delta Nu$  distribution and the  $\theta$  distributions, in fact, point towards the hypothesis of an earlier lift-off of the hub passage vortex with increased injection ratio: the increases in  $\Delta Nu$  and  $\theta$  extend on smaller areas and closer to the inlet for the IR1.2% case.

Finally, similarly as what already observed for design point, at the inlet of the passage, areas showing positive variations in Nusselt number are juxtaposed with zones of opposite sign. These are typical signatures of the strengthening of vortical structures – as previously discussed (section 8.2) – suggesting that the purge air exits in a vortex in the same circumferential location indicated by the distributions of non-dimensional wall temperature difference: still towards the suction side of the blade, but closer to the center of the passage than in the design condition.

Focusing now on the distributions of non-dimensional adiabatic wall temperature difference, especially at the inlet of the passage on the suction side, it is possible to observe how the trace of the purge flow moves towards the center of the passage at part-load, compared to the design point data (see Figure 8.10).

Clearly, the signature of the purge air injection stops adhering to the suction side of the blade and is found more aligned to the axial direction, suggesting a different angle of the cavity flow when entering the passage.

This observation can be also partially justified by the displacement of the stagnation point towards the suction side of the blade due to negative incidence (section 7.2).

Finally, the purge flow appears to be less effective in cooling the endwall at off-design condition, as demonstrated by the lower values of  $\theta$  in the passage. This is attributed to an increased momentum ratio  $I$  at part-load, as explained further on.

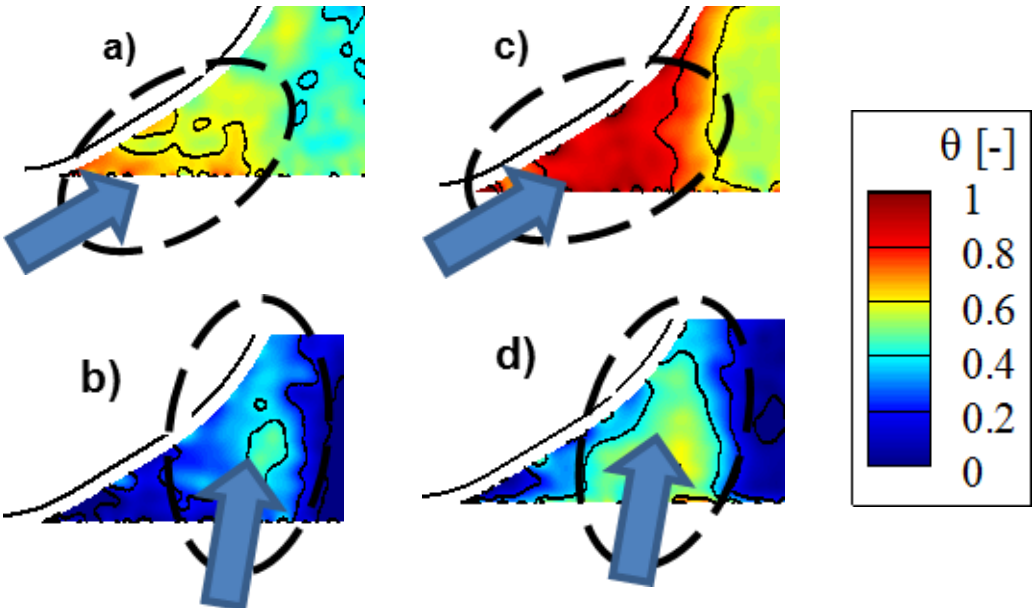


Figure 8.10: detail of the endwall in the proximity of the suction side of the blade under different conditions:

- a) Design point,  $\theta$  for IR0p8%
- b) Off-design condition,  $\theta$  for IR0p8%
- c) Design point,  $\theta$  for IR1p2%
- d) Off-design condition,  $\theta$  for IR1p2%

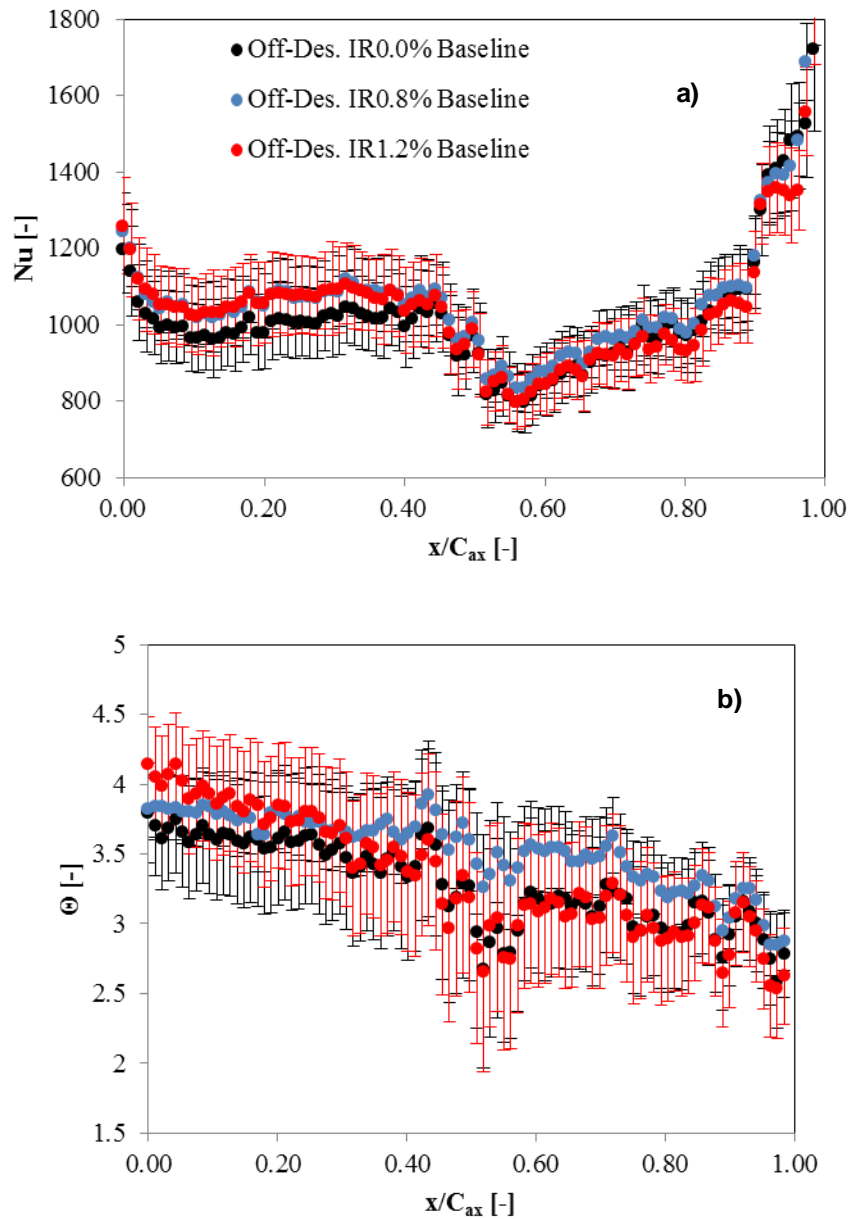


Figure 8.11: circumferentially averaged Nusselt number for all test cases a); circumferentially averaged non-dimensional adiabatic wall temperature b), Error bars represent a 95% confidence interval.

Again, the effect on the laterally averaged Nusselt number profiles is within the uncertainty bands. The circumferentially averaged Nusselt number is about 4% higher with a 1.2% injection ratio than with no purge injection until 30% of the axial extent of the passage. The uncertainty in the same region, though, is of  $\sim \pm 10\%$ . Compared to design point with no purge injection, the off-design condi-



tion with the highest purge flow rate still presents Nusselt number values 20% lower.

Concerning the laterally averaged profiles of non-dimensional adiabatic wall temperature, no relevant differences are observable for varying injection ratio. Figure 8.8b) and Figure 8.9b) show, in fact, that the effect of the purge flow on the wall temperature is strictly limited to the suction side of the inlet of the passage for part-load condition. At full load, as shown in Figure 8.3b) and Figure 8.4b), the effectiveness of the purge flow is more widely spread to the complete inlet portion of the passage and only drops after 40% of its axial extent. An interpretation of this phenomenon can be given in the following terms: the change in main flow speed results in roughly a 10% increase in momentum ratio, which in turn results in a higher penetration of the purge air towards higher spanwise positions. This can explain the reduced effectiveness of purge flow on the endwall: rim seal leakage flow migrates faster towards outer radii and mixes with the main flow. Where secondary flows are present, more purge air is entrained by the upwash motion of the vortices than what occurs at full load, when a greater part of the purge air adheres to the endwall.

It is of interest, on the other hand, to compare the off-design condition with maximum purge flow injection ratio (1.2%), to the design point operating condition with no purge flow on a point-wise basis (Figure 8.12)

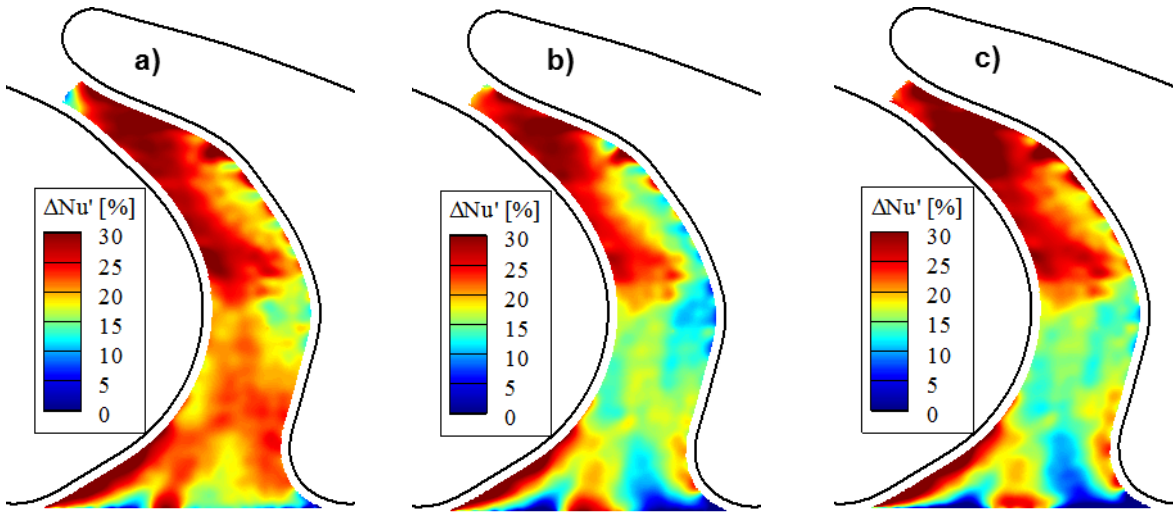


Figure 8.12: relative differences in Nusselt number on a point-wise basis between design point operation with no purge flow injection and off-design condition with varying purge flow injection ratio: 0.0% a), 0.8% b), 1.2% c). If with no purge injection the Nusselt number for full-load is  $\sim 30\%$  higher in most of the passage, areas of nearly equivalent heat transfer coefficient are observed at the very inlet of the passage for higher injection ratio at part-load. This suggests that the stronger adhesion of the secondary flows to the endwall and their higher intensity due to the purge flow injection at off-design condition produce significant effects.

In Figure 8.12,  $\Delta Nu'$  is defined as in the following equation 8.4:

$$\Delta Nu' = \frac{Nu_{DP,IR0.0\%} - Nu_{OffD,IRX.X\%}}{Nu_{DP,IR0.0\%}} \cdot 100 \quad (8.4)$$

It is expected for the heat loads at design point to be generally higher than at off design condition due to the higher Reynolds number (see section 7.2, equation 7.2). On the other hand, the expected increase in heat transfer coefficient of about 20-30% is only achieved after  $\sim 40\%$  of the axial extent of the passage, due to the flow acceleration. At the very inlet of the passage, instead, regions appear where the Nusselt numbers are comparable for the two cases. The better adhesion of the secondary flows to the endwall due to off-loading and their strength-

ening because of purge flow injection produce local Nusselt numbers at off-design conditions as high as the ones detected at design point. If coupled with comparable main flow temperatures, this could result in critical hot spots even at operating conditions normally considered less demanding for the engine.

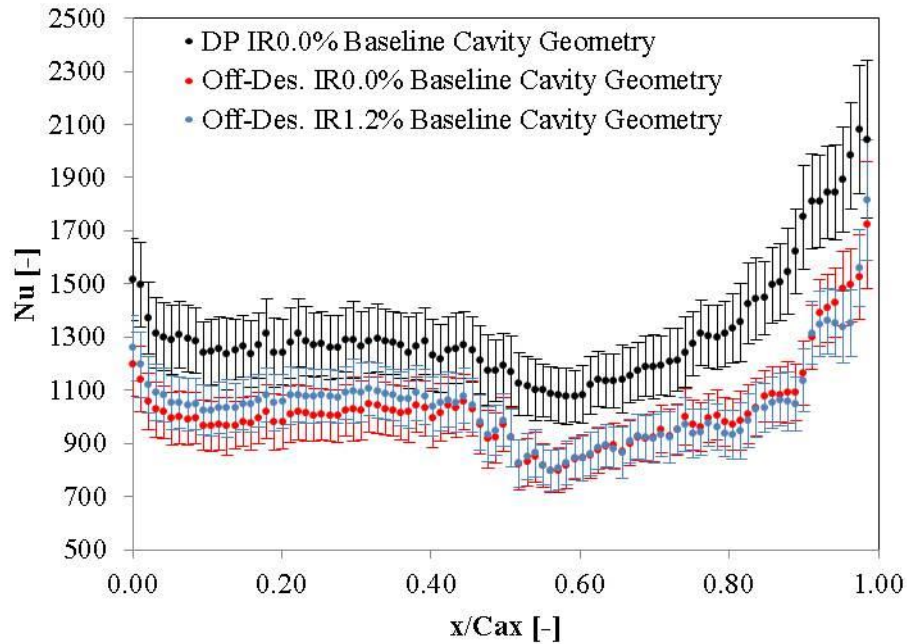


Figure 8.13: circumferentially averaged Nusselt number distributions for design condition with no purge injection (black), and off-design condition with no purge injection (red) and with 1.2% injection ratio (blue). Despite an increase of  $\sim 4\%$  at the inlet, the Nusselt number distribution for off-design condition does not reach the levels measured for design point.

At off-design condition, differently than at higher loading, the adiabatic wall temperature also is not strongly affected by the purge injection. On the other hand, on a local basis, increases in Nusselt number are of the order of twice the uncertainty (up to  $\sim 20\%$  increases) in wider regions than what observed at design conditions. It can be concluded that the sensitivity of heat transfer to purge injection is then higher when off-loading the turbine.

## 8.5 Summary

The main conclusions of the current chapter can be summarized as follows:

- at design point, the effect of purge flow on the Nusselt number distribution falls within the measurement uncertainty. However, the observed trends show a change in the secondary flow patterns and, particularly, a strengthening effect of purge air injection on the horseshoe vortex and passage vortex;
- at the nominal operating point, purge flow has a relevant effect on the heat fluxes close to the suction side of the rotor passage, up to  $\sim 30\%$  of its axial extent. It does alter, in fact, the adiabatic wall temperature by bringing it closer to its own rotor-relative total temperature. An increase in the local adiabatic wall temperature of  $67\%$  of the temperature difference between cavity flow and main flow is reported for an injection ratio of  $0.8\%$ . The increase grows to  $82\%$  for an injection ratio of  $1.2\%$ . These results suggest that purge flow can effectively be used as rotor platform coolant in the specific region of the passage close to the suction side of the rotor blade;
- at off-design condition, the sensitivity of the heat load to purge flow injection variations is shown on the Nusselt number distributions rather than in the adiabatic wall temperature distribution. This behavior is opposite to the one observed at design point. Reasons for this are found in a better adhesion of the secondary flows to the endwall on one hand and in an earlier lift-off of the purge flow from the endwall on the other. This latter phenomenon is due to a change in momentum ratio  $I$  with respect to nominal operation;
- the location of preferential injection of the purge flow at part-load operation shifts towards the center of the passage, consistently with the displacement of the stagnation point to the suction side of the blade due to negative incidence;
- the spatial resolution and sensitivity of the IR-based technique developed for this work are sufficient to detect local effects of purge air on the heat transfer quantities on the rotor endwall.

## 9. Rim Seal Cavity Exit Shaping and its Effects on Coolant Distribution

It has been explained how the main reason why purge flow affects aerodynamic performance of the blade rows lies in mixing losses of colder, low-momentum fluid with the main flow (section 1.2.4 ). In particular, the mismatch in momentum is most severe in the swirl component. The main flow, in fact, presents high swirl components of velocity, especially at the outlet of the stator vanes, while the rim seal leakage flow, except for a mild circumferential velocity induced by friction with the rotor disk, mainly carries a radial component of momentum. At the lower spans, this results in negative incidence on the leading edge of the rotor blade, reduction of work extraction and strengthening of secondary flows. Furthermore, the blockage effect introduced by the purge flow results in a mass redistribution over the complete span, thus altering the coupling between flow field and blade profile over the complete radial extend of the blade.

In the most advanced designs, an attempt is made to shape the cavity exit to overcome these shortcomings or at least to minimize their effect on performance, whilst maintaining the effectiveness of purge flow in preventing hot gas ingestion. The benefits of the very same design under study in this chapter have been quantified and analyzed by Schädler et al. [141]. The effect of this practice, though, is not limited in the reduction of the mixing losses, but also affects the distribution of the purge flow on the endwall and, as a consequence, its effectiveness as platform coolant.

In this chapter, experimental results show how the cooling effectiveness distribution is altered by the introduction of so-called “purge control features” in the cavity design as opposed to the axisymmetric baseline cavity shown in Figure 3.3.

## 9.1 Design Principles of Rim Seal Cavity Exit Shaping

Schädler et al. [141] describe the design intent of the purge control features used in this study. The purge control features consist of grooves both on the stator side of the cavity exit and on the rotor side. The general intention is to reduce the mixing losses introduced by the strong shear between the low-momentum cavity flow and the main flow. This is achieved differently on the two sides of the cavity exit (Figure 9.1).

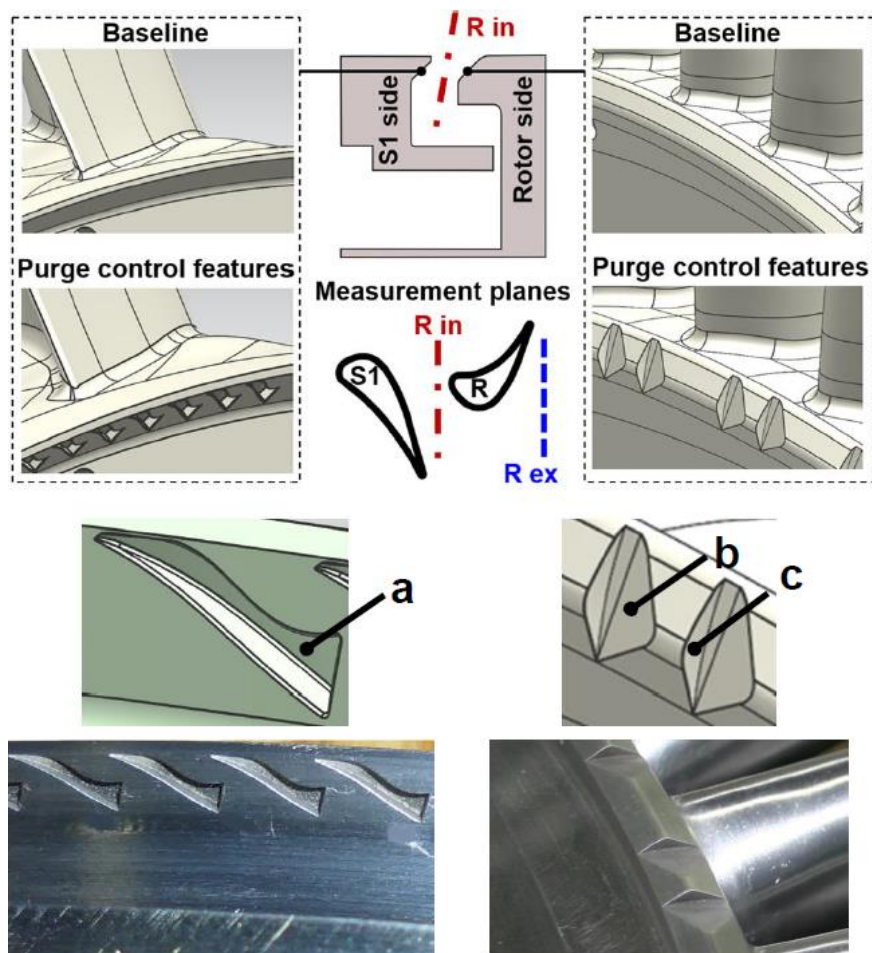


Figure 9.1: comparison between baseline cavity geometry and purge control features on stator (left) and rotor side (right). Indications of inlet and outlet planes of the rotor ( $R_{in}$  and  $R_{ex}$ ) (Schädler et al. [141]).

On the stator side (left side of Figure 9.1), grooves angled with reference to the radial direction increase the swirl component of velocity of the purge air and promote its acceleration thanks to a variable depth of the groove decreasing in the flow direction (Figure 9.1, a).

On the rotor side (right side of Figure 9.1), the features aim at actively increasing the purge momentum in the circumferential direction (Figure 9.1, groove b) and, additionally, preventing hot gas ingestion by imparting a stronger radial component of velocity to the cavity flow (Figure 9.1, surface c).

Overall, the velocity of the rim seal leakage flow is increased to match more closely the swirl component of velocity of the main flow, without increasing the hot gas ingestion.

## 9.2 Effects of Rim Seal Cavity Exit Geometry on endwall Cooling at Design Condition

Results are presented in relative terms of Nusselt number relative difference  $\Delta Nu$  and non-dimensional adiabatic wall temperature difference  $\theta$  as in chapter 8, based on the definitions (8.1) and (8.2).

The reference case for the calculation of the Nusselt number differences and the non-dimensional adiabatic wall temperature differences is the case with purge control features (that is, with rim seal cavity exit shaping), but no net purge flow injection ( $IR = 0.0\%$ ).

For the sake of consistency and comparability, the color scale of the contour plots is the same as the one used in chapter 8 for the corresponding plots for the baseline configuration.

The first striking observation can be made by considering the distributions of Nusselt number differences for the nominal operating condition.

Compared to the axisymmetric rim seal cavity geometry, the increases in Nusselt number due to an increase in purge flow injection to  $0.8\%$  of the main

mass flow rate are much less severe: less than 10% and generally closer to 5% instead of reaching values of up to ~15%.

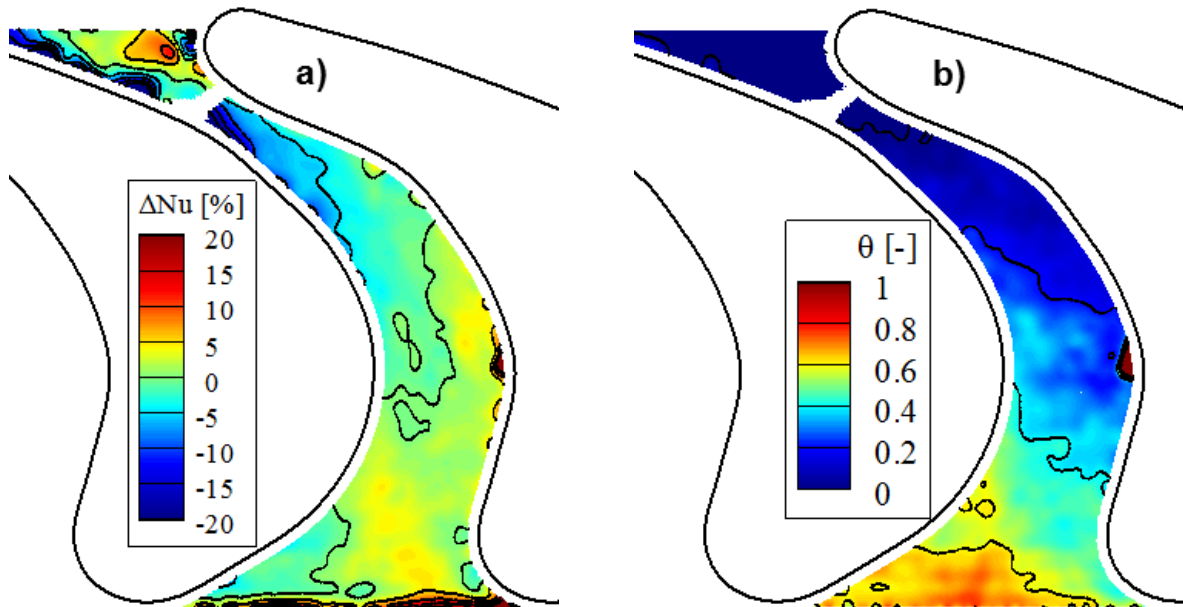


Figure 9.2: comparison between reference case (design point, IR=0.0%) and IR=0.8%. Nusselt number relative difference a) and non-dimensional adiabatic wall temperature difference (eq. (9)) b).

Even when the injection ratio reaches 1.2%, the increases in Nusselt number at the inlet of the passage (i. e., where the pressure leg of the horseshoe vortex lies) do not reach the 10% mark.

These results indicate that the increased momentum of the rim seal leakage flow determines the hub secondary flows not to be strengthened as much by the injection of purge flow.

The benefit of this is twofold:

- on the aerodynamic side, it reduces the efficiency deficit introduced by the purge flow, as stated by Schädler in the aforementioned paper [141] (Figure 9.3);



- on the heat transfer side, the enhancement of heat transfer coefficient determined by the purge flow is
  - o less severe overall;
  - o less concentrated on specific spots related to the trace on the endwall of the hub secondary flows. From a structural point of view, a more uniform increase of Nusselt number reduces the thermal gradients in the material and the consequent mechanical stresses.

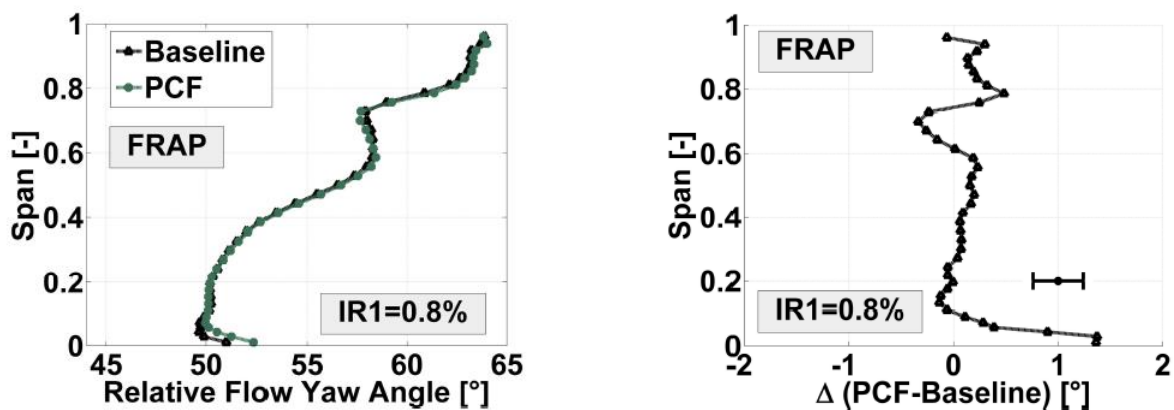


Figure 9.3: comparison of mass- and circumferentially averaged relative flow yaw angle profiles at rotor inlet. Span-wise distributions (left) and difference between baseline and purge control features (PCF) as shown by Schädler et al. [141]

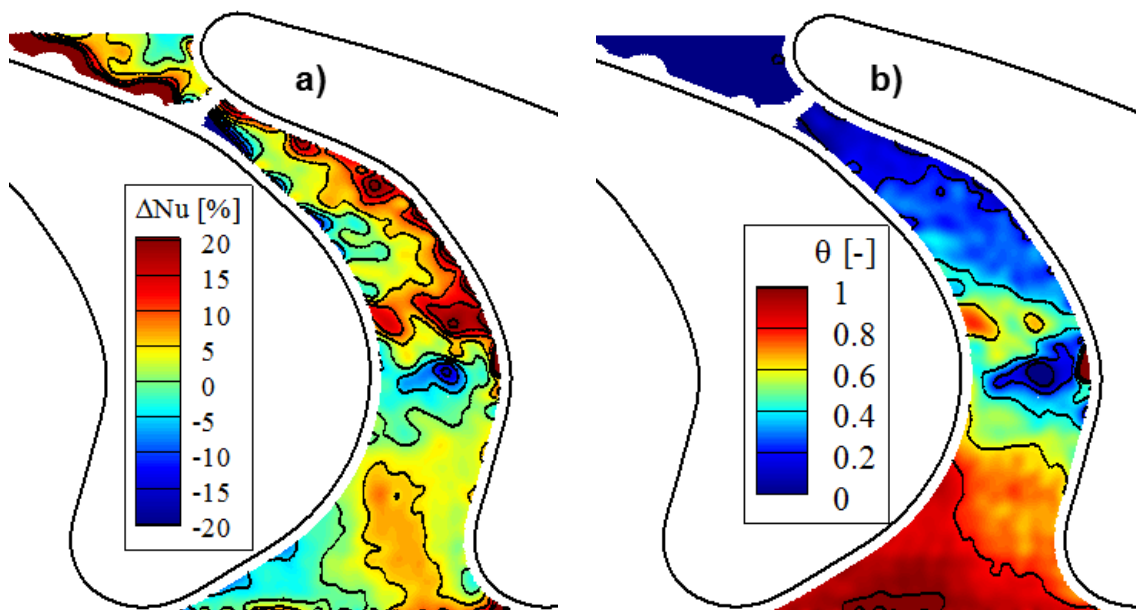


Figure 9.4: comparison between reference case (Des. Pt., IR=0.0%) and IR=1.2%. Nusselt number relative difference a) and non-dimensional adiabatic wall temperature difference (eq. (8.2)) b).

More information on the mode and location of injection of purge air can be obtained by the observation of the non-dimensional adiabatic wall temperature difference distributions.

The purge flow appears to leave a much more uniform signature at the inlet of the passage, instead of being preferentially ejected towards the suction side of the blade.

As for the Nusselt number distribution, the fact of having a more even distribution of cooling effectiveness can benefit structurally the rotating part reducing the thermal gradients in the metal and, therefore, the mechanical stresses arising from differential thermal expansion.

Furthermore, the more uniform cooling effectiveness at the inlet may allow the reduction or the elimination of film cooling holes in this area of the rotor passage, thus reducing the mass flow rate of by-pass air spilled from the upstream compressor for cooling purposes.

For this operating condition, the purge flow cavity shaping enables the rim seal leakage flow to exert the double function of preventing hot gas ingestion in the cavity and cooling effectively the hub endwall.

On a laterally averaged basis (Figure 9.5), the effects are comparable to the axisymmetric purge cavity: that is, negligible effect on Nusselt number distribution, but relevant on the adiabatic wall temperature. Also in absolute terms, the laterally averaged values between baseline and purge control features are indistinguishable at design point.

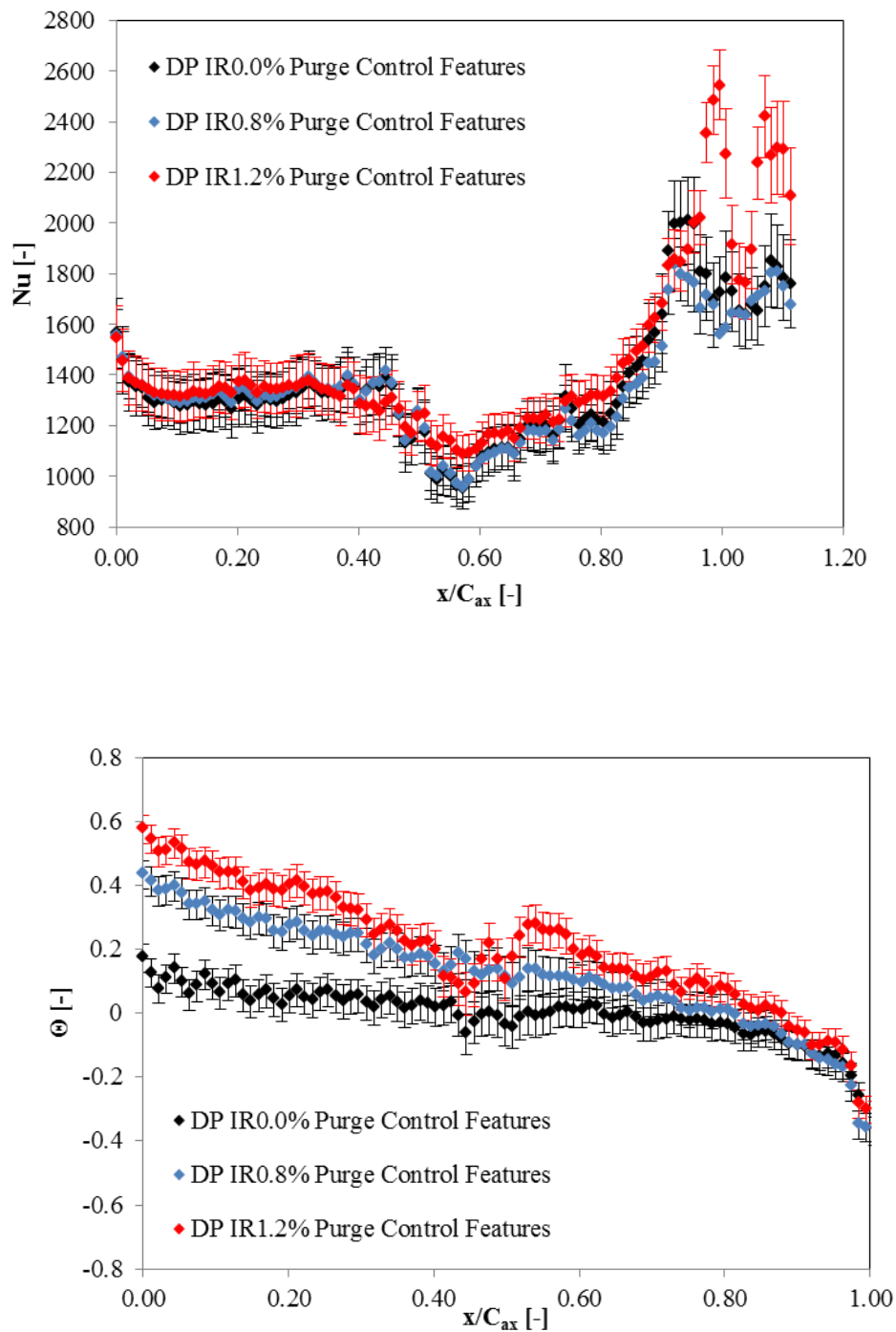


Figure 9.5: laterally averaged profiles of Nusselt number (top) and non-dimensional adiabatic wall temperature (bottom). Negligible effect of purge air injection for the former, but relevant shift of wall temperature as in baseline cavity geometry case.

### 9.3 Effects of Rim Seal Cavity Exit Geometry on endwall Cooling at Off-Design Condition

From the analysis of the heat transfer results at part-load, very different conclusions can be drawn concerning the effectiveness of the purge control features in redistributing evenly the coolant on the endwall, than the ones offered in the previous section on their performance at design point.

If, in fact, the strengthening of the secondary flows by the purge flow is significantly reduced at design point due to the lower mixing losses, at part-load condition the trace of the stronger horseshoe vortex (its pressure side leg, specifically), is much more visible with increases in Nusselt number of up to 10-15% at  $IR = 0.8\%$  and 15-20% at  $IR = 0.8-1.2\%$ .

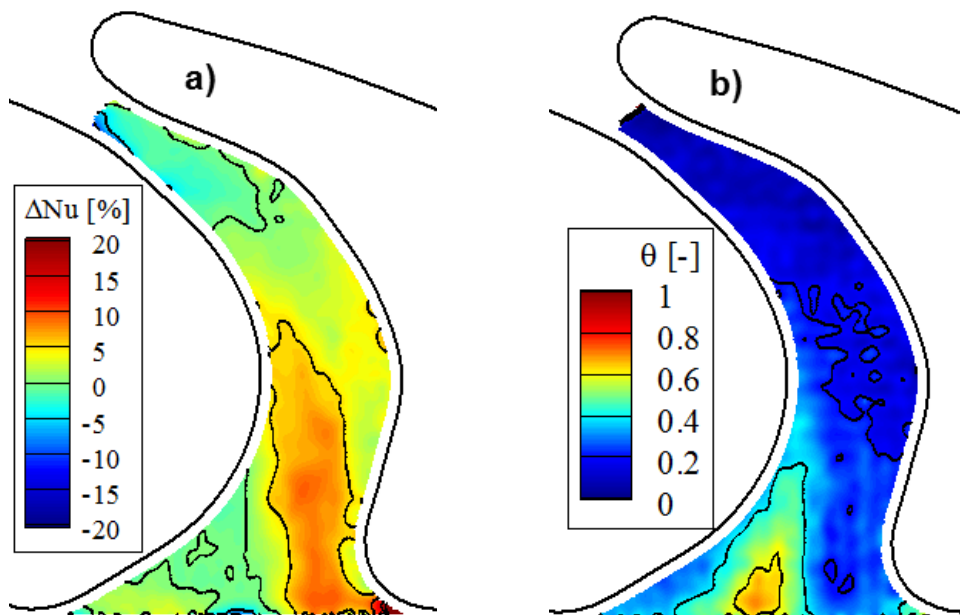


Figure 9.6: comparison between reference case (part-load condition,  $IR=0.0\%$ ) and  $IR=0.8\%$ . Nusselt number relative difference a) and non-dimensional adiabatic wall temperature difference (eq. (8.2)) b).

Furthermore, the distributions of  $\theta$  (Figure 9.6 b), Figure 9.7 b)) clearly indicate that the ejection of the purge flow occurs on the suction side of the passage, driven by the favorable pressure gradient, very differently than for nominal operation, during which the leakage flow is purged over the whole circumferential extent of the passage.

The reason for this can be looked for in the lower spanwise position of the secondary flows due to off-loading of the turbine as previously stated for the baseline configuration (Snedden [140], Kang [71]).

Also, the signature of the horseshoe vortex extinguishes at earlier axial locations, again suggesting an earlier lift-off of the vertical structure from the endwall induced by the increased purge flow injection.

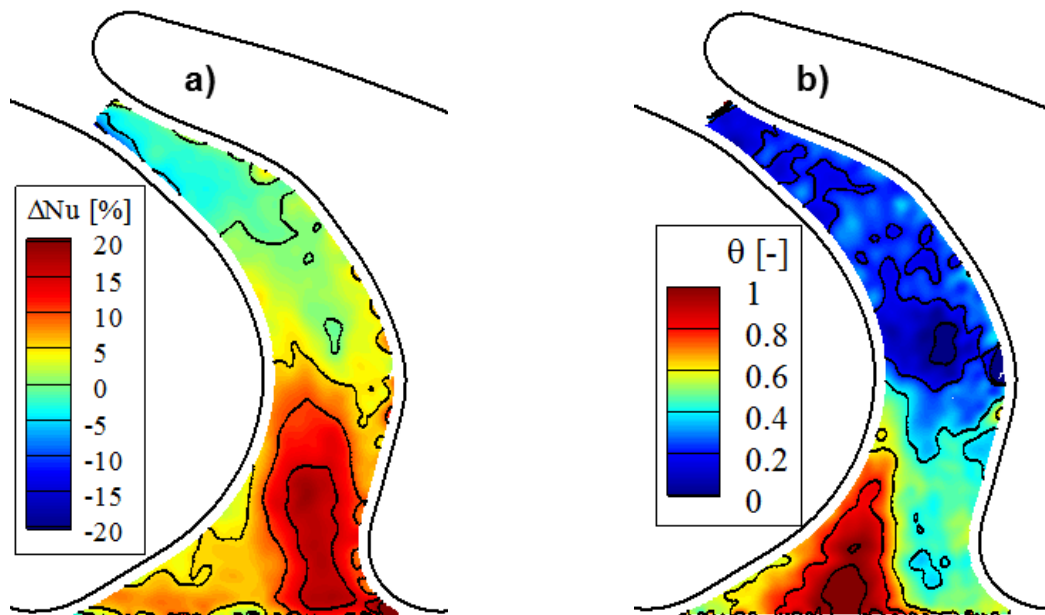


Figure 9.7: comparison between reference case (part-load condition, IR=0.0%) and IR=1.2%. Nusselt number relative difference a) and non-dimensional adiabatic wall temperature difference (eq. (8.2)) b).

When considering the laterally averaged profiles of Nusselt number and non-dimensional adiabatic wall temperature, it is possible to observe that the injec-

tion of purge flow affects in an appreciable manner both quantities, despite the Nusselt number profiles still being within the measurement uncertainty band.

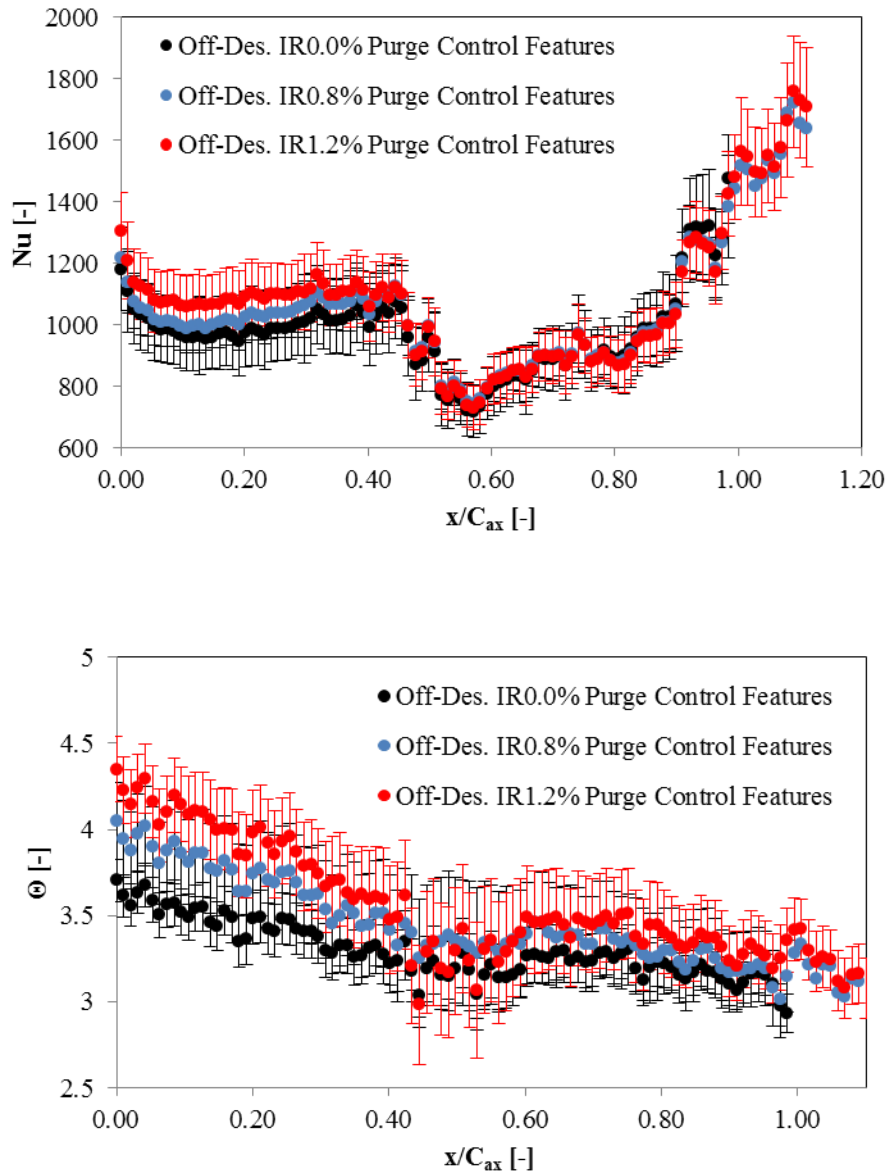


Figure 9.8: laterally averaged profiles of Nusselt number (top) and non-dimensional adiabatic wall temperature (bottom). Despite still being within the measurement uncertainties, the differences in Nusselt number induced by the introduction of purge air in the passage are more visible for part-load operation than for the nominal operating point. Differently than for the baseline cavity geometry, non-dimensional adiabatic wall temperatures are still appreciable at off-design.

## 9.4 Integral Cooling Effectiveness Comparison of Purge Control Features and Axisymmetric Cavity Geometry

By defining threshold values for the minimum cooling effectiveness desired (as stated when defining the non-dimensional adiabatic wall temperature difference  $\theta$ , eq. (8.2), this quantity can be assimilated to the cooling effectiveness of the purge flow), it is possible to integrate the surface area of the endwall that is cooled with the desired level under different injection ratios and operating conditions.

The following plots describe the variation of the cooled surface area of the endwall with a threshold levels for  $\theta$  of 0.5.

The variation of the cooled surface area with the injection ratio is compared for the two different cavity designs at both full and part load (Figure 9.9).

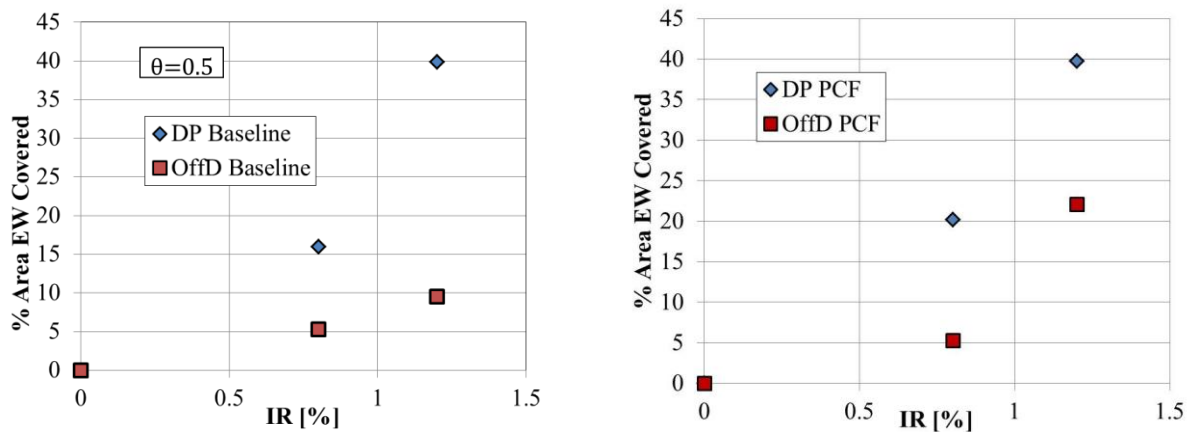


Figure 9.9: surface area cooled with a value of non-dimensional adiabatic wall temperature difference ( $\sim$ cooling effectiveness) in percentage of total endwall surface area for the baseline, axisymmetric cavity geometry (left) and purge control features (right) for both operating conditions.

For both cavity geometries, the coverage of the endwall by the coolant is more than 3 times greater at the rated operating condition, except for the maximum IR with non-axisymmetric cavity geometry ( $\sim$ 2 times greater). This is consistent

with a lower radial penetration of the purge flow, pressed more strongly towards the endwall by the higher momentum of the main flow.

At the rated operating condition, the purge control features are mildly more effective in spreading the cooling flow on a wider area for an  $IR = 0.8\%$ . However, the distributions of section 9.2 show that the coolant is more uniformly spread at the inlet of the passage compared to the baseline cavity geometry. In this circumstance, the advantage of having a shaped cavity lies in less severe temperature gradients and, therefore, in lower thermomechanical stresses on the part and improved durability. On the other hand, as already anticipated in section 9.3, at part-load operation the purge control features (PCFs) appear to lose their effectiveness from the heat transfer point of view. The plot on the right of Figure 9.10, shows how the endwall coverage is reduced by 4 times for an  $IR = 0.8\%$  and by 2 for  $IR = 1.2\%$  with the purge control features at part-load.

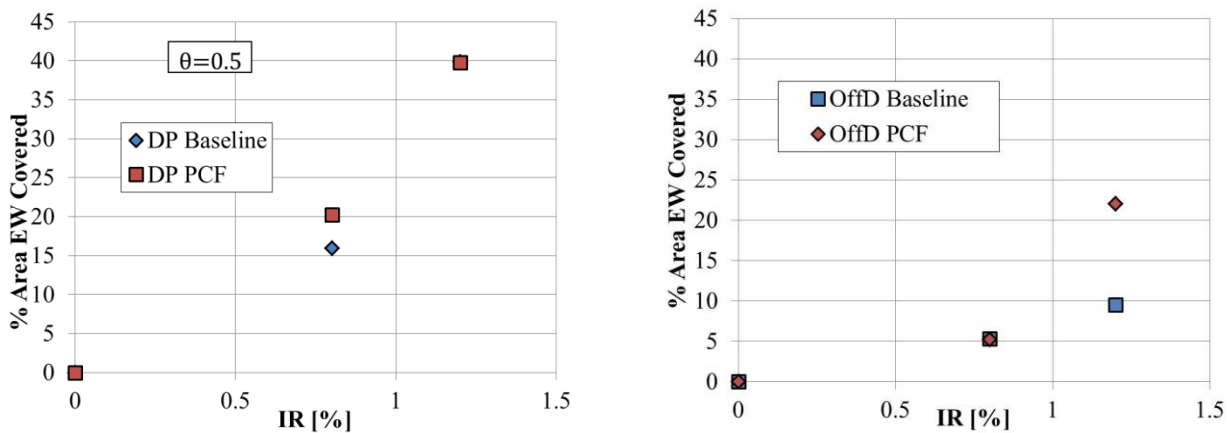


Figure 9.10: percentage of endwall surface area cooled at a level of non-dimensional adiabatic wall temperature difference greater than 0.5 for the nominal operating condition (left) and part-load (right). Comparisons between values for baseline, axisymmetric cavity geometry and purge control features.



## 9.5 Summary

Non-axisymmetric purge flow cavity shaping aims at reducing the mixing losses introduced by purge flow injection. However, this chapter presents results on its effect on endwall heat transfer. The relevance of the observations lies in the fact that an improvement in purge flow cooling effectiveness can lead to a reduction in the mass flow rate of coolant bled from the upstream compressor. Consequently, the overall efficiency of the machine can be increased while safeguarding its reliability and mechanical integrity.

The purge control features added to the rim seal cavity prove beneficial at the nominal operating condition for two reasons:

- the reduction in mixing losses and negative incidence due to increase swirl results in a milder increase in strength and size of the secondary flows with higher injection ratios. Therefore, the signature of the strengthened hub passage vortex on the Nusselt number distribution is not as significant as with the axisymmetric cavity geometry;
- the higher swirl of the purge flow also contributed to its more uniform spreading over the inlet portion of the rotor hub endwall. The purge flow is therefore more effective in cooling this portion of the passage. Resorting to film cooling might thus be limited for this region and under these operating conditions;

On the other hand, the purge control features lose their effectiveness when the engine is operated at part-load. In this case, in fact, the purge flow resumes its typical behavior, with preferential ejection towards the suction side of the passage.

This is confirmed in integral terms by the percentage of endwall surface area cooled with a level of adiabatic wall temperature difference ( $\sim$ cooling effectiveness) greater than 0.5. The coverage is reduced by a factor between 4 and 2 when operating the machine at part-load condition, while it is maintained essentially unvaried at design point.

The main advantage – in heat transfer terms – of using a shaped purge injection cavity is, together with the reduction in strength of the secondary flows, a more

uniform temperature field at the inlet of the passage, reducing thermal gradients and improving the durability of the components.

However, the presented results suggest that a cavity geometry optimized for multiple operating conditions of the engine has the potential to enable a reduction in the mass flow rate of coolant required to manage the metal temperature of the rotor endwall.

# 10. Summary, Conclusions and Outlook

## 10.1 Summary

The energy market requires of gas turbine manufacturers to design and produce more efficient engines able to operate flexibly with moderate maintenance-related costs. The present work is part of the joint industrial and academic effort in developing such engines, with particular focus on the heat loads on the rotor endwall, one of the most thermo-mechanically solicited portions of the machine. Especially, the aim of this work was to produce experimental evidence of the variation of the aforementioned thermal loads with the operating condition of the machine. Measurements were performed on stationary and rotating components, in presence of realistic leakage flows and unsteady effects due to the stator-rotor interaction.

Additionally, the high-resolution data acquired in this study constitutes a database for the validation of Computational Fluid Dynamics (CFD) codes, used in the design of gas turbines.

In order to achieve the aforementioned goals, a novel experimental setup and method was developed for measurements on the rotor, comprising of a custom heat transfer platform with directly deposited film heaters, rapid infrared thermography, frequency-based, quantitative image reconstruction tools and a step-wise transient heat flux calibration procedure.

The observed heat transfer patterns, complemented with aerodynamic data and unsteady CFD predictions, are interpreted with reference to the effect of the flow features acting in the passages.

### **Experimental Setup and Methods**

The measurements of heat transfer quantities (Nusselt number and adiabatic wall temperature) with high resolution and in the rotating frame of reference required the development of specific measurement equipment, calibration methods and data processing tools. Specifically:

- design, manufacturing and calibration of a custom-made heat transfer platform carrying directly deposited and laser-cut film heaters;
- development of a calibration method for quantitative evaluation heat flux generated by the newly developed film heater on a point-wise basis;
- a frequency-based, quantitative image reconstruction procedure for the combination of multi-integration time data sets with the double goal of eliminating high-frequency noise and counteract the effects of motion blurring.

Overall, the developments introduced in this work can find wider applications than heat transfer measurements in turbomachinery.

The thermal management technology (i. e. the directly deposited, three-dimensional film heaters) can be applied to virtually any complex geometry, enabling measurements on all sorts of surfaces in turbomachinery, electronics, braking technology or others.

The heat flux calibration method can be applied to any iso-energetic setup to verify the assumption of heat flux uniformity and reduce the measurement uncertainties.

The image processing tools can allow imaging of rapidly moving objects overcoming the limitations of the cameras currently available on the market and reducing the costs associated to the experiments (no need for overly sensitive cameras).

### **Secondary Flows from the Upstream Stator Strengthen the Signature of the Second Stator Pressure Side Horseshoe Vortex**

Despite the presence of the rotor, the impact of the time-averaged hub endwall secondary flows formed in the first vane row still have a relevant and localized impact on the Nusselt number distribution on the endwall of the second stator. It appears, in fact, that the vortical structures enhance the suction leg of the horseshoe vortex and, consequently, the heat transfer coefficient on the suction side of the passage. This effect is more relevant in terms of heat loads than the acceleration imposed to the flow by the expansion through the second vane row or than the deceleration imposed by the endwall contouring in this part of the passage.

In fact, the highest levels of Nusselt number are recorded in the trough of the endwall towards the suction side of the passage rather than at the throat.

### **Secondary Flows from the Upstream Rotor Increase Heat Transfer at the Inlet of the Second Stator**

When loading the rotor at off-design condition (load coefficient increases by 10.6% from 2.34 to 2.59), the strengthened secondary flows and consequent unsteadiness increase the heat load on the first 30% of the axial extent of the passage. The heat transfer rates under these conditions, despite the reduction in Reynolds number of ~30%, are of comparable entity at the inlet of the passage.

### **Endwall Contouring Effect on Heat Loads**

The experimental and computational distributions of heat transfer quantities contradict the expectations of the effect of contouring. The highest levels of Nusselt number are recorded in correspondence of the trough of the passage, towards the suction side, while the lowest ones are observed on the hill of the passage towards the pressure side.

It can therefore be concluded that the effect of flow deceleration in the trough and acceleration on the hill and the respective decrease and increase in wall shear stress play a secondary role on the Nusselt number patterns compared to the evident effect of the secondary flows – especially on the suction side of the passage.

There is therefore no reason to optimize the endwall contouring for heat transfer for vane rows downstream of the first stage. Management of the incoming unsteady and vortical flow can bring higher rewards in thermal management.

### **Boundary Layer Laminarization due to Acceleration Reduces Heat Transfer Rate at the Outlet of the Passage**

The observation that the scaling of the Nusselt number with Reynolds evolves from a turbulent flat plate correlation to a laminar one when moving downstream through the passage suggests that the expansion on the flow and its con-

sequent acceleration promotes relaminarization of the boundary layer, thus reducing the heat transfer rates towards the throat. In fact, the outlet portion of the passage typically presents the highest heat transfer coefficient values precisely due to the strong acceleration taking place at the throat and the high wall shear stress. In the case studied in this work, however, the highest Nusselt numbers are instead observed on the suction side of the passage and tend to decrease towards the outlet.

Additionally, the lower heat transfer rates also observed on the pressure side of the passage are consistent with previous experimental observation of low intermittance and absence of laminar to turbulent transition on the pressure side of cascades.

From these results, an indication of further work in correct modeling of laminar to turbulent transition and relaminarization of the flow in turbomachinery applications can be derived.

### **Recommendation for Unsteady CFD for Heat Transfer Predictions on the Rotor**

By successfully performing high-resolution measurements (0.32mm/pixels for a total of ~3700 measurement points over the area of interest) of Nusselt number distributions in a rotating facility and comparing the experimental data to steady and unsteady computations it was concluded that neglecting unsteady effects (such as the unsteadiness induced by the stator-rotor interaction) leads to errors of up to 30% in the heat transfer coefficient.

It is therefore recommended to validate CFD codes by using data obtained from rotating facilities rather than cascades and, furthermore, to rely on time-averaged data from unsteady CFD predictions rather than on steady-state simulations for the design and optimization of cooling schemes on the rotor endwall.

However, the distributions of heat transfer quantities do not present significant qualitative differences to what previously observed in cascades.

At part-load operation, similar heat transfer patterns are observed and the reduction in heat transfer coefficient is essentially related to a Reynolds number effect.

### **Effect of Purge Flow on Rotor Endwall Heat Transfer**

The injection of purge flow through the rim seal cavity has a double effect on the rotor endwall heat transfer:

- due to mixing losses and negative incidence with respect to the rotor blade, purge air enhances the strength and size of the hub secondary flows. This effect is detrimental, but in a limited area of the passage (i. e. toward the suction side of the blade) is compensated by a lower adiabatic wall temperature;
- the purge flow acts as coolant over the endwall, but mainly in the proximity of the suction side of the passage. Its effectiveness is also strongly variable with the operating condition, so film cooling must complement its action;
- at part-load condition, the secondary flows tend to adhere more to the rotor endwall. Their strengthening due to purge flow injection leaves therefore more significant traces on the heat transfer patterns. Depending on the momentum ratio between the purge air and the main flow, the cooling effectiveness of the purge air can also be reduced at part-load. Attention should therefore be paid during the design process at simulating thermal loads at off-design conditions including realistic models of the cavities if operating temperatures comparable to the ones at design point are expected.

### **Rim Seal Cavity Shaping Enhances Effectiveness only at Design Point**

A non-axisymmetric rim seal cavity design was tested in this work with the objective of observing its effect on the heat loads on the rotor endwall, compared to the axisymmetric design.

The blading was left unaltered thanks to a modular design of the facility.

It was found that, at design point, an increased swirl component of velocity of the purge flow promoted higher and more evenly spread values of cooling effectiveness in the inlet portion of the passage.

Furthermore, thanks to the reduced negative incidence and mixing losses, the increase in Nusselt number due to the strengthening of the secondary flows was less severe than with an axisymmetric cavity design.

However, the usual behavior of the rim seal leakage flow resumed at part-load condition, with purge air preferentially leaking towards the suction side of the passage and visible signatures of a stronger hub passage vortex.

In order to take advantage of the potential of a non-axisymmetric cavity design for reduction in coolant mass flow rate, its geometry should be optimized for multiple operating conditions.

## 10.2 Concluding Remarks and Main Contributions

### 10.2.1 Stator Endwall Heat Transfer

Thermal management of downstream stators from the main flow-path side benefits the most from improved aerodynamic design. Specifically, the following points play a more relevant role on endwall heat transfer:

- management of secondary flows from upstream blade and vane rows ;
- reduction of unsteadiness from the upstream rotor;
- boundary layer transition and re-laminarization in the passage,

than attempting to achieve improvements in thermal performance by means of adding thermal constraints on top of aerodynamic ones when designing the end-wall shape.

### 10.2.2 Rotor Endwall Heat Transfer

- Accurate prediction of thermal loads must rely on unsteady simulations in order to more faithfully capture the absolute values of heat transfer coefficient;
- purge flow can effectively act as coolant in limited portions of the endwall even when ejected from axisymmetric rim seal cavities;
- improvements in the effectiveness of purge flow as endwall coolant can be achieved if non-axisymmetric designs of such cavities are adopted;



- in general, for a single non-axisymmetric rim seal cavity design to achieve improvements in thermal performance over a range of engine operating conditions it is required to carefully design the lip features. The design tested in the current study, in fact, proved to be sensitive to off-design operation.

## 10.3 Outlook

The technique developed in this work can be employed as-is for further studies on cavity and endwall shape optimization with the goal of minimizing the thermal loads on the rotor hub platform.

Matching the density ratios of actual engines would require heating of the main flow beyond 100 °C, and therefore a complete redesign of the system because of the more challenging thermo-mechanical conditions for the rotating equipment and because of a shift in the spectral range of the infrared emission.

However, it would still be desirable to equip the research facility LISA with a cooling system for the purge flow, so to assess systematically the effect of varying density ratios on the aerothermodynamics of the rotor endwall.

A double purpose setup coupling heat transfer platforms with pressure sensitive paint passages would allow a one-to-one, fully experimental comparison of heat transfer patterns and in-passage flow field.

Also, given the role of turbulence and transition on the heat transfer patterns, boundary layer intermittence measurement would provide a valuable complement to the heat load distributions.

Even without resorting to additional equipment, the technique can be adapted for measurements on other areas of the rotor, for example the blade tip, also critical for heat transfer for the presence of tip leakage vortices.

For this specific application, the higher linear velocity of the body needs to be accounted for in the infrared camera acquisition parameters (integration time) and the image processing (motion blurring).

Another area of interest is the lateral surfaces of the blades, which could also be equipped with directly deposited film heaters thanks to the manufacturing pro-

cess developed in the present work. Clearly, the mechanical integration of the heated blade and the optical accessibility to its surface would require significant effort.

It must be said that data acquired with heat flux gauges on the airfoil have proven quite reliable, but the signatures of the spanwise migration of the secondary flows cannot be observed but with a high-resolution, optical technique.

Additional topics of research can derive from the goal of improving the technique in itself.

First and foremost, a better process control during the film heater deposition would prove beneficial in the levels of heat flux uniformity obtained over the surface of interest. Possible areas of improvement in this regard are:

- if the physical vapor deposition is maintained, a systematic assessment of the performance of the evaporator should be carried out to quantify the effect of parameters such as crucible – to – sample distance, sample angle and rotation on the uniformity of the deposited layer;
- other deposition processes can be explored to obtain higher uniformity of the film.

The benefit of a higher uniformity essentially lies in a wider extension of the heat flux ranges usable during the experiments.

The accuracy of the step-wise heat flux calibration – still recommended to improve the uncertainty in the final results despite lower non-uniformity values – can be improved in absolute terms by measuring more accurately the thermal properties – especially the thermal capacity – of the substrate material.

From the image processing side, a parametric study on the integration times used for the frequency-based recombination could bring a benefit in terms of temperature uncertainty and smoothness of the contours. Also, the empirical determination of the cutoff wavelength of the filter by minimization of the error can be complemented by a numerical/analytical evaluation of the zeros of the Point-Spread Function used for deconvolution.

# Bibliography

- [1] B. Salehnasab, E. Poursaeidi, S. Mortazavi, and G. Farokhian, "Hot corrosion failure in the first stage nozzle of a gas turbine engine," *Engineering Failure Analysis*, vol. 60, pp. 316-325, 2016.
- [2] "World Energy Outlook 2015," International Energy Agency 2015.
- [3] "Annual Energy Outlook 2014 with Projections to 2040," U. S. Energy Information Administration, Washington DC, U.S.A. 2014.
- [4] "Long-Term Market: Current Market Outlook 2016-2035," Boeing 2016.
- [5] "Airbus Global Market Forecast 2016-2035," Airbus 2016.
- [6] "IATA Annual Review 2016," International Air Transport Association, [www.iata.org](http://www.iata.org) 2016.
- [7] J.-C. Han, S. Dutta, and S. Ekkad, *Gas turbine heat transfer and cooling technology*: CRC Press, 2012.
- [8] M. K. Chyu, "Recent advances in turbine heat transfer—with a view of transition to coal-gas based systems," *Journal of Heat Transfer*, vol. 134, p. 031006, 2012.
- [9] M. G. Dunn, "Convective Heat Transfer and Aerodynamics in Axial Flow Turbines," *Journal of Turbomachinery*, vol. 123, pp. 637-686, 2001.
- [10] CFM. (2016, 27.01.2017). *CFM, The Power of Flight*. Available: <https://www.cfmaeroengines.com/engines/leap/>
- [11] K. Kyprianidis, *Future Aero Engine Designs: An Evolving Vision*, 2011.
- [12] "Siemens achieves breakthrough with 3D printed gas turbine blades," ed. <https://www.siemens.com/press/PR2017020154PGEN>: Siemens AG, 2017.
- [13] R. S. Bunker, "Gas Turbine Heat Transfer: Ten Remaining Hot Gas Path Challenges," *Journal of Turbomachinery*, vol. 129, pp. 193-201, 2006.
- [14] J. D. Denton, "Some limitations of turbomachinery CFD," in *ASME Turbo Expo 2010: Power for Land, Sea, and Air*, 2010, pp. 735-745.
- [15] M. Schobeiri and S. Abdelfattah, "On the reliability of RANS and URANS numerical results for high-pressure turbine simulations: a benchmark experimental and numerical study on performance and interstage flow behavior of high-pressure turbines at design and off-design conditions using two different turbine designs," *Journal of Turbomachinery*, vol. 135, p. 061012, 2013.
- [16] K. Regina, "High-Pressure Turbines with Novel Airfoils and End Walls Operating under Engine Representative Aero-Thermodynamic Effects," Diss., Eidgenössische Technische Hochschule ETH Zürich, Nr. 22633, 2015.

- [17] E. Lutum, F. Cottier, M. E. Crawford, B. Laveau, and R. S. Abhari, "A computational investigation of the effect of surface roughness on heat transfer on the stator endwall of an axial turbine," *Proceedings of the Institution of Mechanical Engineers, Part A: Journal of Power and Energy*, vol. 229, pp. 454-464, 2015.
- [18] F. Duchaine, A. Corpron, L. Pons, V. Moureau, F. Nicoud, and T. Poinsot, "Development and assessment of a coupled strategy for conjugate heat transfer with Large Eddy Simulation: Application to a cooled turbine blade," *International Journal of Heat and Fluid Flow*, vol. 30, pp. 1129-1141, 12//2009.
- [19] P. G. Tucker, "Computation of unsteady turbomachinery flows: Part 2—LES and hybrids," *Progress in Aerospace Sciences*, vol. 47, pp. 546-569, 10//2011.
- [20] J. C. Rodriguez, P.; Brunelli, M.; Custer, C.; Carpenter, C., "High Fidelity CHT CFD for Gas Turbine Heat Transfer Applications," in *Global Power and Propulsion Forum*, Zurich, 2017.
- [21] M. Schobeiri, K. Lu, and M. Rezasoltani, "Effect of non-axisymmetric contouring on performance and film cooling of a rotating turbine endwall subjected to the secondary air purge: A combined numerical and experimental study," *Proceedings of the Institution of Mechanical Engineers, Part A: Journal of Power and Energy*, p. 0957650915594724, 2015.
- [22] A. G. Hansen, H. Z. Herzig, and G. R. Costello, "A visualization study of secondary flows in cascades," DTIC Document1953.
- [23] L. Langston, M. Nice, and R. Hooper, "Three-dimensional flow within a turbine cascade passage," *Journal of Engineering for Power*, vol. 99, pp. 21-28, 1977.
- [24] T. Simon and J. Piggush, "Turbine endwall aerodynamics and heat transfer," *Journal of propulsion and power*, vol. 22, pp. 301-312, 2006.
- [25] L. S. Langston, "Secondary Flows in Axial Turbines—A Review," *Annals of the New York Academy of Sciences*, vol. 934, pp. 11-26, 2001.
- [26] M. Schobeiri, *Turbomachinery flow physics and dynamic performance*: Springer, 2005.
- [27] J. Schlienger, A. I. Kalfas, and R. S. Abhari, "Vortex-Wake-Blade Interaction in a Shrouded Axial Turbine," *Journal of Turbomachinery*, vol. 127, pp. 699-707, 2005.
- [28] P. Jenny, "Interaction mechanisms between rim seal purge flow and profiled end walls in a low-pressure turbine," ETH, 2012.

- [29] R. P. Dring and H. D. Joslyn, "The Relative Eddy in Axial Turbine Rotor Passages," in *ASME 1983 International Gas Turbine Conference and Exhibit*, 1983, pp. V001T01A010-V001T01A010.
- [30] G. Riollet, "Curved channels through which a gas or vapour flows," ed: Google Patents, 1970.
- [31] A. Morris and R. Hoare, "Secondary loss measurements in a cascade of turbine blades with meridional wall profiling," in *American Society of Mechanical Engineers, Winter Annual Meeting, Houston, Tex*, 1975, p. 1975.
- [32] M. Atkins, "Secondary losses and end-wall profiling in a turbine cascade," *I Mech. E C*, vol. 255, pp. 29-42, 1987.
- [33] M. G. Rose, "Non-axisymmetric endwall profiling in the HP NGV's of an axial flow gas turbine," in *ASME 1994 International Gas Turbine and Aeroengine Congress and Exposition*, 1994, pp. V001T01A090-V001T01A090.
- [34] J. Hartland, D. Gregory-Smith, N. Harvey, and M. Rose, "Non-Axisymmetric Turbine End Wall Design: Part II—Experimental Validation," in *ASME 1999 International Gas Turbine and Aeroengine Congress and Exhibition*, 1999, pp. V001T03A050-V001T03A050.
- [35] G. Ingram, D. Gregory-Smith, M. Rose, N. Harvey, and G. Brennan, "The effect of end-wall profiling on secondary flow and loss development in a turbine cascade," in *ASME Turbo Expo 2002: Power for Land, Sea, and Air*, 2002, pp. 135-145.
- [36] G. I. Mahmood and S. Acharya, "Measured endwall flow and passage heat transfer in a linear blade passage with endwall and leading edge modifications," in *ASME Turbo Expo 2007: Power for Land, Sea, and Air*, 2007, pp. 917-930.
- [37] A. K. Saha and S. Acharya, "Computations of Turbulent Flow and Heat Transfer Through a Three-Dimensional Nonaxisymmetric Blade Passage," *Journal of Turbomachinery*, vol. 130, pp. 031008-031008-10, 2008.
- [38] B. Laveau, R. S. Abhari, M. E. Crawford, and E. Lutum, "High Resolution Heat Transfer Measurement Technique on Contoured Endwall With Non-Uniform Thermal Resistance," in *ASME Turbo Expo 2015: Turbine Technical Conference and Exposition*, 2015, pp. V05BT13A023-V05BT13A023.
- [39] F. Puetz, J. Kneer, A. Schulz, and H.-J. Bauer, "A New Test Facility to Investigate Film Cooling on a Non-Axisymmetric Contoured Turbine Endwall: Part I—Introduction and Aerodynamic Measurements," in *ASME*

- Turbo Expo 2015: Turbine Technical Conference and Exposition*, 2015, pp. V02AT38A005-V02AT38A005.
- [40] J. Kneer, F. Puetz, A. Schulz, and H.-J. Bauer, "A New Test Facility to Investigate Film Cooling on a Non-Axisymmetric Contoured Turbine Endwall: Part II — Heat Transfer and Film Cooling Measurements," p. V05BT12A015, 2015.
- [41] R. Royce, *The jet engine*: John Wiley & Sons, 2015.
- [42] B. V. Johnson, R. Jakoby, D. E. Bohn, and D. Cunat, "A Method for Estimating the Influence of Time-Dependent Vane and Blade Pressure Fields on Turbine Rim Seal Ingestion," *Journal of Turbomachinery*, vol. 131, pp. 021005-021005-10, 2009.
- [43] K. Reid, J. Denton, G. Pullan, E. Curtis, and J. Longley, "The effect of stator-rotor hub sealing flow on the mainstream aerodynamics of a turbine," in *ASME Turbo Expo 2006: Power for Land, Sea, and Air*, 2006, pp. 789-798.
- [44] J. Ong, R. J. Miller, and S. Uchida, "The effect of coolant injection on the endwall flow of a high pressure turbine," *Journal of Turbomachinery*, vol. 134, p. 051003, 2012.
- [45] G. Paniagua, R. Dénos, and S. Almeida, "Effect of the Hub Endwall Cavity Flow on the Flow-Field of a Transonic High-Pressure Turbine," *Journal of Turbomachinery*, vol. 126, p. 9, 2004.
- [46] P. Schuepbach, R. S. Abhari, M. G. Rose, T. Germain, I. Raab, and J. Gier, "Effects of Suction and Injection Purge-Flow on the Secondary Flow Structures of a High-Work Turbine," *Journal of Turbomachinery*, vol. 132, pp. 021021-021021, 2010.
- [47] P. Jenny, R. S. Abhari, M. G. Rose, M. Brettschneider, K. Engel, and J. Gier, "Unsteady Rotor Hub Passage Vortex Behavior in the Presence of Purge Flow in an Axial Low Pressure Turbine," *Journal of Turbomachinery*, vol. 135, p. 051022, 2013.
- [48] B. R. Green, R. M. Mathison, and M. G. Dunn, "Time-Averaged and Time-Accurate Aerodynamic Effects of Rotor Purge Flow for a Modern, One and One-Half Stage High-Pressure Turbine—Part II: Analytical Flow Field Analysis," *Journal of Turbomachinery*, vol. 136, p. 011009, 2014.
- [49] L. Balling, "Fast cycling and rapid start-up: new generation of plants achieves impressive results," *Modern power systems. San Francisco CA*, vol. 31, pp. 35-41, 2011.
- [50] I. Popović and H. P. Hodson, "The Effects of a Parametric Variation of the Rim Seal Geometry on the Interaction Between Hub Leakage and

- Mainstream Flows in High Pressure Turbines," *Journal of Engineering for Gas Turbines and Power*, vol. 135, p. 112501, 2013.
- [51] A. M. Basol, A. Raheem, M. Huber, and R. S. Abhari, "Full-Annular Numerical Investigation of the Rim Seal Cavity Flows Using GPU's," p. V02DT44A034, 2014.
- [52] P. S. Rebholz, S. Krebietke, R. S. Abhari, and A. I. Kalfas, "Turbine Aerodynamic Low-Frequency Oscillation and Noise Reduction Using Partial Shrouds," *Journal of Propulsion and Power*, vol. 32, pp. 1067-1076, 2016/09/01 2016.
- [53] R. Schädler, A. I. Kalfas, R. S. Abhari, G. Schmid, and S. S. Völker, "Modulation and Radial Migration of Turbine Hub Cavity Modes by the Rim Seal Purge Flow," *Journal of Turbomachinery*, 2016.
- [54] M. G. Turner, "Multistage turbine simulations with vortex-blade interaction," in *ASME 1995 International Gas Turbine and Aeroengine Congress and Exposition*, 1995, pp. V001T01A074-V001T01A074.
- [55] S. D. Hunter and S. R. Manwaring, "Endwall Cavity Flow Effects on Gaspath Aerodynamics in an Axial Flow Turbine: Part I—Experimental and Numerical Investigation," in *ASME Turbo Expo 2000: Power for Land, Sea, and Air*, 2000, pp. V001T03A111-V001T03A111.
- [56] M. Blair, "An experimental study of heat transfer and film cooling on large-scale turbine endwalls," in *ASME 1974 International Gas Turbine Conference and Products Show*, 1974, pp. V01AT01A033-V01AT01A033.
- [57] R. Graziani, M. F. Blair, J. Taylor, and R. Mayle, "An experimental study of endwall and airfoil surface heat transfer in a large scale turbine blade cascade," *Journal of Engineering for Power*, vol. 102, pp. 257-267, 1980.
- [58] Z. Gao, D. Narzary, and J.-C. Han, "Turbine blade platform film cooling with typical stator-rotor purge flow and discrete-hole film cooling," *Journal of Turbomachinery*, vol. 131, p. 041004, 2009.
- [59] L. M. Wright, S. A. Blake, D.-H. Rhee, and J.-C. Han, "Effect of Upstream Wake With Vortex on Turbine Blade Platform Film Cooling With Simulated Stator-Rotor Purge Flow," *Journal of Turbomachinery*, vol. 131, p. 021017, 2009.
- [60] S. P. Lynch and K. A. Thole, "Heat Transfer and Film Cooling on a Contoured Blade Endwall With Platform Gap Leakage," in *ASME Turbo Expo 2015: Turbine Technical Conference and Exposition*, 2015, pp. V05BT12A037-V05BT12A037.

- [61] S. P. Lynch, N. Sundaram, K. A. Thole, A. Kohli, and C. Lehane, "Heat transfer for a turbine blade with nonaxisymmetric endwall contouring," *Journal of Turbomachinery*, vol. 133, p. 011019, 2011.
- [62] M. F. Blair, "An experimental study of heat transfer in a large-scale turbine rotor passage," in *ASME 1992 International Gas Turbine and Aeroengine Congress and Exposition*, 1992, pp. V004T09A012-V004T09A012.
- [63] R. Abhari, G. Guenette, A. Epstein, and M. Giles, "Comparison of time-resolved turbine rotor blade heat transfer measurements and numerical calculations," in *ASME 1991 International Gas Turbine and Aeroengine Congress and Exposition*, 1991, pp. V004T09A018-V004T09A018.
- [64] R. S. Abhari and A. Epstein, "An experimental study of film cooling in a rotating transonic turbine," in *ASME 1992 International Gas Turbine and Aeroengine Congress and Exposition*, 1992, pp. V004T09A018-V004T09A018.
- [65] M. G. Dunn, W. J. Rae, and J. L. Holt, "Measurement and Analyses of Heat Flux Data in a Turbine Stage: Part II—Discussion of Results and Comparison With Predictions," *Journal of Engineering for Gas Turbines and Power*, vol. 106, pp. 234-240, 1984.
- [66] M. G. Dunn, W. J. Rae, and J. L. Holt, "Measurement and Analyses of Heat Flux Data in a Turbine Stage: Part I—Description of Experimental Apparatus and Data Analysis," *Journal of Engineering for Gas Turbines and Power*, vol. 106, pp. 229-233, 1984.
- [67] R. Dénos and G. Paniagua, "Influence of the hub endwall cavity flow on the time-averaged and time-resolved aero-thermodynamics of an axial HP turbine stage," in *ASME Turbo Expo 2002: Power for Land, Sea, and Air*, 2002, pp. 207-217.
- [68] M. Rezasoltani, M. T. Schobeiri, and J. C. Han, "Experimental Investigation of the Effect of Purge Flow on Film Cooling Effectiveness on a Rotating Turbine With Non-Axisymmetric Endwall Contouring," p. V03BT13A033, 2013.
- [69] R. J. Goldstein and R. A. Spores, "Turbulent Transport on the Endwall in the Region Between Adjacent Turbine Blades," *Journal of Heat Transfer*, vol. 110, pp. 862-869, 1988.
- [70] R. J. Boyle and L. M. Russell, "Experimental Determination of Stator Endwall Heat Transfer," *Journal of Turbomachinery*, vol. 112, pp. 547-558, 1990.



- [71] M. B. Kang, A. Kohli, and K. Thole, "Heat transfer and flowfield measurements in the leading edge region of a stator vane endwall," *ASME J. Turbomach*, vol. 121, pp. 558-568, 1999.
- [72] B. Laveau, R. S. Abhari, M. E. Crawford, and E. Lutum, "High Resolution Heat Transfer Measurements on the Stator Endwall of an Axial Turbine," *Journal of Turbomachinery*, vol. 137, pp. 041005-041005, 2014.
- [73] A. de la Loma, G. Paniagua, D. Verrastro, and P. Adami, "Transonic Turbine Stage Heat Transfer Investigation in Presence of Strong Shocks," *Journal of Turbomachinery*, vol. 130, p. 031019, 2008.
- [74] R. J. Moffat, "What's new in convective heat transfer?," *International Journal of Heat and Fluid Flow*, vol. 19, pp. 90-101, 4// 1998.
- [75] A. Rogalski, "New material systems for third generation infrared photodetectors," in *Opto-Electronics Review* vol. 16, ed, 2008, p. 458.
- [76] C. Meola and G. M. Carlomagno, "Recent advances in the use of infrared thermography," *Measurement science and technology*, vol. 15, p. R27, 2004.
- [77] G. M. Carlomagno and G. Cardone, "Infrared thermography for convective heat transfer measurements," *Experiments in Fluids*, vol. 49, pp. 1187-1218, 2010.
- [78] V. Scherer, S. Wittig, G. Bittlinger, and A. Pfeiffer, "Thermographic heat transfer measurements in separated flows," *Experiments in fluids*, vol. 14, pp. 17-24, 1993.
- [79] A. Schulz, "Infrared thermography as applied to film cooling of gas turbine components," *Measurement Science and Technology*, vol. 11, p. 948, 2000.
- [80] G. Cardone, T. Astarita, and G. Carlomagno, "Heat transfer measurements on a rotating disk," *International Journal of Rotating Machinery*, vol. 3, pp. 1-9, 1997.
- [81] O. Lyons, D. Murray, and A. Torrance, "Air jet cooling of brake discs," *Proceedings of the Institution of Mechanical Engineers, Part C: Journal of Mechanical Engineering Science*, vol. 222, pp. 995-1004, 2008.
- [82] M. Siroux, S. Harmand, and B. Desmet, "Experimental study using infrared thermography on the convective heat transfer of a TGV brake disk in the actual environment," *Optical Engineering*, vol. 41, pp. 1558-1564, 2002.
- [83] T. Astarita, G. Cardone, and G. Carlomagno, "Spiral vortices detection on a rotating disk," in *Proceedings of 23rd congress international council aeronautical sciences, paper n. ICAS2002-3.6*, 2002.
- [84] T. Astarita and G. Cardone, "Convective heat transfer on a rotating disk with a centred impinging round jet," *International Journal of Heat and Mass Transfer*, vol. 51, pp. 1562-1572, 4// 2008.

- [85] N. Afshordi and J. Magueijo, "Critical geometry of a thermal big bang," *Physical Review D*, vol. 94, p. 101301, 11/18/ 2016.
- [86] T. Astarita and G. M. Carlomagno, *Infrared thermography for thermo-fluid-dynamics*: Springer Science & Business Media, 2012.
- [87] R. Tustison and R. L. Gentilman, "Current and emerging materials for LWIR external windows," in *32nd Annual Technical Symposium*, 1989, pp. 25-34.
- [88] H. A. Gebbie, W. R. Harding, C. Hilsum, A. Pryce, and V. Roberts, "Atmospheric Transmission in the 1 to 14 $\mu$  Region," in *Proceedings of the Royal Society of London A: Mathematical, Physical and Engineering Sciences*, 1951, pp. 87-107.
- [89] J. Lohrengel and R. Todtenhaupt, "Warmeleitfähigkeit, Gesamtemissionsgrade und spektrale Emissionsgrade der Beschichtung Nextel-Velvet-Coating 811-21 (RAL 900 15 tiefschwarz matt)," *PTB Mitteilungen Forschen und Prüfen*, vol. 106, pp. 259-264, 1996.
- [90] J. Gengenbach, S. Kabelac, and L. Koirala, "Measurement of Directional Spectral Emissivities of Microstructured Surfaces," in *17th European Conference on Thermophysical Properties (ECTP), Bratislava, Slovakia, Sept*, 2005, pp. 5-8.
- [91] W. Herschel, "Experiments on the Solar, and on the Terrestrial Rays that Occasion Heat; With a Comparative View of the Laws to Which Light and Heat, or Rather the Rays Which Occasion Them, are Subject, in Order to Determine Whether They are the Same, or Different. Part I. By William Herschel, LL. D. F. R. S.," *Philosophical Transactions of the Royal Society of London*, vol. 90, pp. 293-326, 1800.
- [92] R. C. Jones, "Performance of Detectors for Visible and Infrared Radiation," in *Advances in Electronics and Electron Physics*. vol. Volume 5, L. Marton, Ed., ed: Academic Press, 1953, pp. 1-96.
- [93] M. Ochs, T. Horbach, A. Schulz, R. Koch, and H. Bauer, "A novel calibration method for an infrared thermography system applied to heat transfer experiments," *Measurement Science and Technology*, vol. 20, p. 075103, 2009.
- [94] L. B. Lucy, "An iterative technique for the rectification of observed distributions," *The astronomical journal*, vol. 79, p. 745, 1974.
- [95] W. H. Richardson, "Bayesian-Based Iterative Method of Image Restoration\*," *JOSA*, vol. 62, pp. 55-59, 1972.

- [96] R. J. Hanisch, R. L. White, and R. L. Gilliland, "Deconvolution of Hubbles Space Telescope images and spectra," in *Deconvolution of images and spectra (2nd ed.)*, A. J. Peter, Ed., ed: Academic Press, Inc., 1996, pp. 310-360.
- [97] D. S. Biggs and M. Andrews, "Acceleration of iterative image restoration algorithms," *Applied optics*, vol. 36, pp. 1766-1775, 1997.
- [98] A. P. Dempster, N. M. Laird, and D. B. Rubin, "Maximum Likelihood from Incomplete Data via the EM Algorithm," *Journal of the Royal Statistical Society. Series B (Methodological)*, vol. 39, pp. 1-38, 1977.
- [99] Z. Wang, A. C. Bovik, H. R. Sheikh, and E. P. Simoncelli, "Image quality assessment: from error visibility to structural similarity," *Image Processing, IEEE Transactions on*, vol. 13, pp. 600-612, 2004.
- [100] B. E. Laveau, "Investigation of the heat transfer patterns on the vane endwall of an axial turbine," ETH Zurich, 2014.
- [101] O. Faugeras, Q.-T. Luong, and T. Papadopoulos, *The geometry of multiple images: the laws that govern the formation of multiple images of a scene and some of their applications*: MIT press, 2004.
- [102] H. Werschnik, T. Ostrowski, J. Hilgert, M. Schneider, and H.-P. Schiffer, "Infrared thermography to study endwall cooling and heat transfer in turbine stator vane passages using the auxiliary wall method and comparison to numerical simulations," *Quantitative InfraRed Thermography Journal*, vol. 12, pp. 219-236, 2015/07/03 2015.
- [103] G. Paniagua, R. Dénos, and S. Almeida, "Effect of the Hub Endwall Cavity Flow on the Flow-Field of a Transonic High-Pressure Turbine," *Journal of Turbomachinery*, vol. 126, p. 578, 2004.
- [104] K. Regina, A. Kalfas, R. Abhari, A. Lohaus, S. Voelker, and T. auf dem Kampe, "Aerodynamic Robustness of End Wall Contouring Against Rim Seal Purge Flow," in *ASME Turbo Expo 2014: Turbine Technical Conference and Exposition*, 2014, pp. V02CT38A027-V02CT38A027.
- [105] T. Germain, M. Nagel, I. Raab, P. Schüpbach, R. S. Abhari, and M. Rose, "Improving Efficiency of a High Work Turbine Using Nonaxisymmetric Endwalls— Part I: Endwall Design and Performance," *Journal of Turbomachinery*, vol. 132, pp. 021007-021007-9, 2010.
- [106] W. M. Kays, M. E. Crawford, and B. Weigand, *Convective heat and mass transfer*: Tata McGraw-Hill Education, 2012.
- [107] J.-Y. Bouguet. *Camera Calibration Toolbox for Matlab*. Available: <http://www.vision.caltech.edu/bouguetj/>
- [108] B. Johnson, "Electrical resistivity of copper and nickel thin-film interconnections," *Journal of Applied Physics*, vol. 67, pp. 3018-3024, 1990.

- [109] D. M. Mattox, "Chapter 2 - Substrate ("Real") Surfaces and Surface Modification," in *Handbook of Physical Vapor Deposition (PVD) Processing (Second Edition)*, ed Boston: William Andrew Publishing, 2010, pp. 25-72.
- [110] A. International, "ASTM D 3359-97," ed. West Conshohocken, Pennsylvania, USA, 1997.
- [111] A. International, "Standard Test Methods for Measuring Adhesion by Tape Test," ed. West Conshohocken, Pennsylvania, USA: ASTM International, 2009.
- [112] K. N. Gray, S. E. Buckley, and G. L. Nelson, "Assessing measurement standards for coating adhesion to plastics," *Modern Paint Coatings*, vol. 75, pp. 160-162, 1985.
- [113] D. Coyne, "LIGO vacuum compatible materials list."
- [114] K. Kim, "Mechanics of the peel test for thin film adhesion," in *MRS Proceedings*, 1988, p. 31.
- [115] A. Bagchi and A. Evans, "The mechanics and physics of thin film decohesion and its measurement," *Interface Science*, vol. 3, pp. 169-193, 1996.
- [116] D. M. Mattox, "Chapter 1 - Introduction," in *Handbook of Physical Vapor Deposition (PVD) Processing (Second Edition)*, ed Boston: William Andrew Publishing, 2010, pp. 1-24.
- [117] R. Penttilä, H. Pantsar, and P. Laakso, "Picosecond laser processing—material removal rates of metals," in *Proceedings of the 11th NOLAMP Conference in Laser Processing of Materials*, 2007, pp. 502-512.
- [118] M. Mansour, P. Rebholz, A. Kalfas, and R. S. Abhari, "An On-Board Wireless Multi-Sensor Measurement System for Rotating Turbomachinery Application," 2015.
- [119] S. E. Gustafsson, E. Karawacki, and M. N. Khan, "Transient hot-strip method for simultaneously measuring thermal conductivity and thermal diffusivity of solids and fluids," *Journal of Physics D: Applied Physics*, vol. 12, p. 1411, 1979.
- [120] S. E. Gustafsson, "Transient plane source techniques for thermal conductivity and thermal diffusivity measurements of solid materials," *Review of scientific instruments*, vol. 62, pp. 797-804, 1991.
- [121] D. O. O'Dowd, Q. Zhang, L. He, P. M. Ligrani, and S. Friedrichs, "Comparison of Heat Transfer Measurement Techniques on a Transonic Turbine Blade Tip," *Journal of Turbomachinery*, vol. 133, p. 021028, 2011.
- [122] J. C. Simonich and R. J. Moffat, "New technique for mapping heat-transfer coefficient contours," *Review of Scientific Instruments*, vol. 53, pp. 678-683, 1982.

- [123] J. Baughn, R. Takahashi, M. Hoffman, and A. McKillop, "Local heat transfer measurements using an electrically heated thin gold-coated plastic sheet," *Journal of heat transfer*, vol. 107, pp. 953-959, 1985.
- [124] J. C. A. Murphy, L. C.; Maclachan Spicer, J. W., in *Principles of photothermal detection in solids*, ed New York: Elsevier, 1992, pp. 41-94.
- [125] R. Osiander and J. W. M. Spicer, "Time-resolved infrared radiometry with step heating. A review," *Revue Générale de Thermique*, vol. 37, pp. 680-692, 1998/09/01 1998.
- [126] R. J. Moffat, "Describing the uncertainties in experimental results," *Experimental thermal and fluid science*, vol. 1, pp. 3-17, 1988.
- [127] L. Riviere, N. Caussé, A. Lonjon, É. Dantras, and C. Lacabanne, "Specific heat capacity and thermal conductivity of PEEK/Ag nanoparticles composites determined by Modulated-Temperature Differential Scanning Calorimetry," *Polymer Degradation and Stability*, vol. 30, p. 1e7, 2015.
- [128] P. Kupferschmied, P. Köppel, W. Gizzi, C. Roduner, and G. Gyarmathy, "Time-resolved flow measurements with fast-response aerodynamic probes in turbomachines," *Measurement Science and Technology*, vol. 11, p. 1036, 2000.
- [129] A. Pfau, J. Schlienger, A. I. Kalfas, and R. S. Abhari, "Unsteady, 3-Dimensional Flow Measurement Using a Miniature Virtual 4 Sensor Fast Response Aerodynamic Probe (FRAP)," pp. 307-315, 2003.
- [130] A. Cocina, "Simulations of Heat Transfer in Gas Turbines for Comparison with Experimental Data," MSc Mechanical Engineering Semester Project Report, Dept. of Mech. and Process Engineering, ETH Zurich, Zurich, 2014.
- [131] P. Eibeck and J. Eaton, "Heat transfer effects of a longitudinal vortex embedded in a turbulent boundary layer," *Journal of Heat Transfer*, vol. 109, pp. 16-24, 1987.
- [132] G. B. Schubauer and H. K. Skramstad, "Laminar-boundary-layer oscillations and transition on a flat plate," NATIONAL AERONAUTICS AND SPACE ADMINISTRATION WASHINGTON DC1948.
- [133] H. Moore and D. Gregory-Smith, "Transition effects on secondary flows in a turbine cascade," in *ASME 1996 International Gas Turbine and Aeroengine Congress and Exhibition*, 1996, pp. V001T01A035-V001T01A035.
- [134] A. B. Turner, "Local heat transfer measurements on a gas turbine blade," *Journal of Mechanical Engineering Science*, vol. 13, pp. 1-12, 1971.
- [135] J. P. Bons, R. P. Taylor, S. T. McClain, and R. B. Rivir, "The many faces of turbine surface roughness," in *ASME Turbo Expo 2001: Power for Land, Sea, and Air*, 2001, pp. V003T01A042-V003T01A042.

- 
- [136] J. A. Van Rij, B. Belnap, and P. Ligrani, "Analysis and experiments on three-dimensional, irregular surface roughness," *Journal of fluids engineering*, vol. 124, pp. 671-677, 2002.
- [137] N. H. Chen, "An explicit equation for friction factor in pipe," *Industrial & Engineering Chemistry Fundamentals*, vol. 18, pp. 296-297, 1979.
- [138] J. Nikuradse, "Laws of flow in rough pipes," in *VDI Forschungsheft*, 1933.
- [139] D. Bogard and K. Thole, "Gas turbine film cooling," *Journal of propulsion and power*, vol. 22, pp. 249-270, 2006.
- [140] G. Snedden, D. Dunn, G. Ingram, and D. Gregory-Smith, "The Performance of a Generic Non-Axisymmetric End Wall in a Single Stage, Rotating Turbine at On and Off-Design Conditions," in *ASME Turbo Expo 2010: Power for Land, Sea, and Air*, 2010, pp. 1069-1080.
- [141] R. Schädler, A. I. Kalfas, R. S. Abhari, G. Schmid, T. auf dem Kampe, and S. B. Prabhu, "Novel High-Pressure Turbine Purge Control Features for Increased Stage Efficiency," *GPPF 2017*, 2017.

# A. Nomenclature

## Symbols

$A_{ew}$	Endwall surface area	$[m^2]$
AR	Aspect ratio	$[-]$
b	Wien's displ. Constant	$[m \cdot K]$
$B_\lambda$	Spectral radiance	$[\frac{W}{sr \cdot m^2 \cdot Hz}]$
c	Absolute flow velocity	$[m/s]$
C	Chord	$[m]$
$C_{1,2}$	Const. SSIM	$[-]$
$C_p$	Thermal capacity	$[\frac{J}{kg \cdot K}]$
d	thickness	$[m]$
$D^*$	Normalized detectivity	$[\frac{cm \cdot \sqrt{Hz}}{W}]$
e	Thermal effusivity	$[J \cdot K \cdot \sqrt{s} / m^2]$
E	Young's modulus	$[GPa]$
f	Fanning's friction factor	$[-]$
$\Delta f$	Eq. noise bandwidth	$[Hz]$
F	Fourier transform	
G	Thermal conductance	$[\frac{W}{m^2 \cdot K}]$
h	Conv. heat transfer coeff.	$[\frac{W}{m^2 \cdot K}]$
i	Electric current	$[A]$
I	Sharp image	
IR	Injection ratio	$[\%]$

$j^*$	Radiant emittance	$[\frac{W}{m^2}]$
$k$	Blur kernel	[-]
$k_B$	Boltzmann's const.	$[\frac{m^2 \cdot kg}{s^2 \cdot K}]$
$k_S$	Sandgrain roughness	[m]
$k_S^+$	Non-dim. Sandgrain roughness	[-]
$M$	Mach number	[-]
$M$	No. pixels x	[-]
$\dot{m}$	Mass flow rate	[kg/s]
$n$	Rotational speed	[rpm]
$N$	No. pixels y	[-]
$n_{iter}$	Number of iterations	[-]
$Nu$	Nusselt number	[-]
$p$	Pressure	[Pa]
$P$	Electrical power	[W]
$Pr$	Prandtl number	[-]
$\dot{q}''$	Heat flux	$[W/m^2]$
$R$	Radius	[m]
$R_a$	Average roughness	[m]
$Re$	Reynolds number	[-]
$R_z$	Peak-to-peak roughness	[m]
$S$	Span	[m]
$S_q$	Heat flux scaling factor	[-]
$St$	Stanton number	[-]
$t$	Time	[s]
$T$	Temperature	[K]
$u$	Blade velocity	[m/s]
$u_\tau$	Friction velocity	[m/s]



V	Voltage	[V]
w	Relative velocity	[m/s]
y	Blurred image	
$y^+$	Non-dimensional viscous unit	[-]
<b>Greek</b>		
$\beta$	Pressure ratio	[-]
$\Gamma_i$	Interface fracture energy	[J]
$\varepsilon$	emissivity	[-]
$\kappa$	Thermal conductivity	$[\frac{W}{m \cdot K}]$
$\eta_c$	Efficiency Carnot Cycle	[-]
$\lambda$	wavelength	[m]
$\mu$	Mean intensity	
$\nu$	Thermal Diffusivity	[m <sup>2</sup> /s]
$\rho$	Density	[kg/m <sup>3</sup> ]
$\rho$	Electrical resistivity	[kg/m <sup>3</sup> ]
$\sigma$	solidity	[-]
$\sigma_R$	Residual stress	[MPa]
$\sigma_{s/y'_n}$	Contrast s vs. $y'_n$	[-]
$\sigma_{sy'_n}$	Correlation s & $y'_n$	[-]
$\Sigma$	Surface area of detector	[m <sup>2</sup> ]
$\tau$	Th. Diffusivity Time constant	[s]
$\tau_w$	Wall shear stress	[Pa]
$\Theta$	Non-dim. Adiab. Wall Temp.	[-]
$\Phi$	Flow coefficient	[-]
$\theta$	Non-dim. Adab. Wall temp. diff.	[-]
$\Psi$	Load coefficient	[-]
$\Omega$	Solid angle	[sr]

**Subscripts**

aw	adiabatic wall
ex	Outlet of blade/vane row
in	Inlet of blade/vane row
rel	relative
s	surface
stat	static
tot	total quantity

**Abbreviations**

CFD	Computational Fluid Dynamics
MSSIM	Mean Structure Similarity Index
Nd:YAG	neodymium-doped yttrium aluminium garnet
NEP	Noise-equivalent power
SSIM	Structure Similarity Index

## **B. List of Publications**

### **Journal Publications**

S. Lazzi Gazzini, R. Schädler, A. I. Kalfas, R. S. Abhari, Infrared Thermography With Non-Uniform Heat Flux Boundary Conditions On The Rotor Endwall Of An Axial Turbine, Measurement Science and Technology, Vol. 28, Issue 2, Feb 2017, p. 025901

S. Lazzi Gazzini, R. Schädler, A. I. Kalfas, R. S. Abhari, G. Schmid, S. Hohenstein, E. Lutum, Effect of Purge Air On Rotor Endwall Heat Transfer Of An Axial Turbine, accepted for publication in the Journal of the Global Power and Propulsion Society



# C. Curriculum Vitae

## Personal Information

Sebastiano Lazzi Gazzini, born 11<sup>th</sup> April 1987 in Rome, Italy.

## Professional Experience

2012 – 2017 Research assistant and doctoral student, Laboratory for Energy Conversion, Dept. of Mechanical and Process Engineering, ETH Zurich

2011 – 2012 Research collaborator, Dept. of Mechanics and Aeronautics, Università degli studi di Roma “la Sapienza”, Italy

2011 (9 months) Lean Manufacturing Intern, GE Oil and Gas Nuovo Pignone SpA, Florence, Italy

## Education

2010 – 2012 MSc Mechanical Engineering, Università degli studi di Roma “la Sapienza”

2008 – 2010 BSc Mechanical Engineering, Università degli studi di Roma “la Sapienza”